

**Universität  
Rostock**



Traditio et Innovatio

# **Rydberg excitons in external fields**

**Dissertation  
zur Erlangung des akademischen Grades  
doctor rerum naturalium (Dr. rer. nat.)  
der Mathematisch-Naturwissenschaftlichen Fakultät  
der Universität Rostock**

**vorgelegt von**

**Ma. Sc. Sjard Ole Krüger, geb. am 6. Mai 1987 in Hamburg**



Dieses Werk ist lizenziert unter einer  
Creative Commons Namensnennung - Nicht-kommerziell -  
Weitergabe unter gleichen Bedingungen 4.0 International Lizenz.

**Erster Gutachter:** Prof. Dr. Stefan Scheel, Universität Rostock  
**Zweiter Gutachter:** Prof. Dr. Jörg Main, Universität Stuttgart

**Eröffnung des Promotionsverfahrens:** 25. November 2020  
**Termin des Kolloquiums:** 19. Februar 2021



## Abstract

Cuprous oxide ( $\text{Cu}_2\text{O}$ ) has been at the forefront of multiple fields of semiconductor research since the early twentieth century. In particular, it has been an important material to basic exciton research, as it was the first material in which the existence of semiconductor Wannier excitons was demonstrated experimentally. In the last decade, the excitons of  $\text{Cu}_2\text{O}$  gained renewed interest due to the observation of Rydberg excitons with principal quantum numbers up to  $n = 28$ . This thesis gauges the influence of the complex valence-band structure on the Rydberg excitons of the yellow series. The derived wave functions and energies are then used to calculate excitonic Van der Waals potentials as well as effective strain potentials as a means to induce trapping potentials for the excitons. Furthermore, an analysis of the transition matrix-elements of excitonic transitions between states of the yellow, green and blue series is provided. It is shown that regimes may exist, in which the dipole approximation breaks down. Finally, the influence of a possible background of charged impurities on the excitonic absorption spectra is assessed.



## Zusammenfassung

Seit der Frühzeit der Halbleiterforschung ist Kupferoxydul ( $\text{Cu}_2\text{O}$ ) ein wichtiges Material der Grundlagenforschung. Dies gilt besonders für die Exzitonenforschung, in der es das erste Material war, in welchem die Existenz von Wannierexzitonen experimentell nachgewiesen wurde. Im letzten Jahrzehnt erlangten diese Exzitonen erneuerte Aufmerksamkeit aufgrund der Beobachtung von Rydbergexzitonen mit Hauptquantenzahlen bis zu  $n = 28$ . In dieser Arbeit wird zuerst der Einfluss der komplexen Struktur des Valenzbandes auf die Exzitonen der gelben Serie untersucht. Mit den so gewonnen Wellenfunktionen und Eigenenergien werden daraufhin Exzitonische Van-der-Waals-Potentiale berechnet und die Anwendung effektiver Strainpotentiale zur Lokalisierung von Rydbergexzitonen untersucht. Darüberhinaus enthält die Arbeit eine Analyse der für exzitonische Interserienübergänge relevanten Übergangsmatrixelemente für Übergänge zwischen den Zuständen der gelben, grünen und blauen Serie. Diese zeigen, dass es Bereiche geben kann in denen die Dipolapproximation zusammenbricht. Schlussendlich wird der Einfluss von geladenen Störstellen auf die exzitonischen Absorptionsspektren untersucht.



# Contents

<b>1. Introduction</b>	<b>1</b>
<b>2. Theoretical preliminaries</b>	<b>5</b>
2.1. Group theory . . . . .	5
2.1.1. Space groups and point groups . . . . .	6
2.1.2. Representations . . . . .	7
2.1.3. Coupling coefficients . . . . .	9
2.2. Fundamentals of semiconductor physics . . . . .	10
2.2.1. Semiconductor solid-state theory . . . . .	12
2.2.2. The $k \cdot p$ method . . . . .	17
2.2.3. Excitons . . . . .	24
2.3. Cuprous oxide . . . . .	27
2.3.1. Band structure . . . . .	28
2.3.2. Excitons . . . . .	29
2.3.3. Phonons . . . . .	33
<b>3. Yellow series quantum defects</b>	<b>35</b>
3.1. Numerical approach . . . . .	35
3.1.1. Multi-band picture . . . . .	36
3.1.2. Two-band picture . . . . .	37
3.1.3. Wave functions . . . . .	41
3.2. Band structure . . . . .	42
3.3. Results . . . . .	43
3.3.1. Conclusion . . . . .	46
3.4. Excitonic Van der Waals potentials . . . . .	47
<b>4. Strain traps for Rydberg excitons</b>	<b>51</b>
4.1. Continuum mechanics . . . . .	52
4.1.1. Hertzian contact theory . . . . .	54
4.2. Band structures of strained crystals . . . . .	57
4.3. Band-gap shift . . . . .	59
4.4. Binding energy shift . . . . .	63
4.5. Conclusion . . . . .	66

<b>5. Excitonic transitions beyond the dipole approximation</b>	<b>67</b>
5.1. Excitonic inter-series transitions . . . . .	68
5.1.1. Theory of excitonic inter-series transitions . . . . .	71
5.1.2. Yellow-green transitions . . . . .	75
5.1.3. Yellow-blue transitions . . . . .	79
5.1.4. Conclusion . . . . .	82
5.2. Transformational properties of Laguerre-Gaussian modes under $O_h$ symmetry . . . .	83
<b>6. Influence of charged impurities</b>	<b>87</b>
6.1. Interaction of Rydberg excitons with charged impurities . . . . .	89
6.1.1. The Holtsmark distribution . . . . .	90
6.1.2. Stark spectra . . . . .	92
6.2. Results . . . . .	95
6.3. Conclusion . . . . .	98
<b>7. Summary &amp; Outlook</b>	<b>99</b>
<b>A. Important tables</b>	<b>101</b>
A.1. Material properties of $\text{Cu}_2\text{O}$ . . . . .	101
A.2. Excitonic binding energies . . . . .	102
<b>B. Group theoretical tables</b>	<b>105</b>
B.1. Point group symmetries of $\text{Cu}_2\text{O}$ . . . . .	105
B.2. Character table of $O_h$ . . . . .	107
B.3. Multiplication table of $O_h$ . . . . .	109
B.4. Compatibility and lattice harmonics . . . . .	110
B.4.1. Compatibility of $O_h$ with respect to $O(3)$ . . . . .	110
B.4.2. Compatibility of $D_{2h}$ with respect to $O(3)$ . . . . .	117
B.4.3. Compatibility of $C_{2h}$ with respect to $O(3)$ . . . . .	118
B.5. The continuous rotation group $O(3)$ . . . . .	119
B.5.1. Spherical harmonics . . . . .	120
<b>C. Excitonic inter-series transitions</b>	<b>121</b>
C.1. Yellow-green inter-band matrix elements . . . . .	121
C.2. Extended Waters basis . . . . .	123
C.3. Evaluation of real-space integrals . . . . .	125
<b>D. List of publications</b>	<b>127</b>
D.1. Published papers . . . . .	127
D.2. Submitted papers . . . . .	128
D.3. Conference contributions . . . . .	128

**Bibliography**

**133**



# Acronyms

**bcc** body centered cubic. 13, 27, 28

**BEC** Bose-Einstein condensation. 1, 2, 51

**BSW** Bouckaert-Smoluchowski-Wigner. 5, 108

**cw** continuous wave. 3, 33

**DFG** Deutsche Forschungsgemeinschaft. 145

**fcc** face centered cubic. 13, 27, 28

**FEM** finite element method. 55, 56

**FWHM** full width half maximum. 32, 33, 92

**GGA** generalised gradient approximation. 28

**OAM** orbital angular momentum. 3, 68

**sc** simple cubic. 13, 16

**sDFT** spin density-functional theory. 28, 29, 80, 145

**SHG** second harmonic generation. 93





# Chapter 1.

## Introduction

The copper oxide  $\text{Cu}_2\text{O}$  (called **cuprous oxide**) has been at the forefront of multiple fields of semiconductor research since the first observation of its photo conductivity by A. Pfund in 1916 [1] and the rectifying properties of Cu-Cu<sub>2</sub>O contacts by L. O. Grondahl in the early 1920s [2]. The latter constituted one of the first observations of rectification in spatially extended metal-semiconductor junctions leading to a quick industrial adaptation of the technology and use until the 1950s [3, 4]. Their study led to the formulation of the semi-classical theory of the Schottky<sup>1</sup> barrier [5, 6] and to Cu<sub>2</sub>O being one of the first pure materials broadly accepted as a semiconductor.

From the early 1950s on, Cu<sub>2</sub>O gained renewed interest due to the first observation of Wannier excitons by Hayashi *et al.* [7] as well as E. F. Gross [8, 9], who observed the yellow series ( $n_{\text{max}} = 8$ ), the green ( $n_{\text{max}} = 5$ ) as well as the blue and violet series (both up to  $n_{\text{max}} = 2$ ). Excitons as the fundamental electronic excitation of band-gapped crystals had been predicted by J. Frenkel [10, 11] and G. H. Wannier [12] in the 1930s for two different limiting cases. Frenkel described tightly bound electron-hole pairs with binding energies on the order of 1 eV and spatial separations comparable to the size of the unit cell, which can typically be found in organic semiconductors. Wannier excitons, on the other hand, describe the opposing limit of weakly bound electron-hole pairs with separations of many lattice constants and binding energies typically below 100 meV. In this limit, the crystal background can be treated as a uniform dielectric and the problem is described by the Wannier equation which in the simplest model (the so called effective-mass approximation) is formally equivalent to the Schrödinger equation of the hydrogen atom. The excitons do then appear as a Rydberg series below the band gap  $E_g$ , showing the characteristic dependence on the principal quantum number  $E_n = E_g - Ry^* n^{-2}$ . In Cu<sub>2</sub>O, all excitons but the excitonic ground states fall rather unambiguously into the category of Wannier excitons. Only the  $1S$  states could be considered intermediates between Frenkel and Wannier excitons.

For the longest time, the research has focused on these excitonic ground states. The long-lived  $1S$  paraexciton, for example, was considered a prime candidate for the realisation of Bose-Einstein condensation (BEC) in excitonic systems, due to the low exciton-mass on the order of

---

<sup>1</sup>It shall be noted here, that Walter H. Schottky resided in Rostock as a professor of theoretical physics from 1923 until 1927. The relevant publications do, however, fall into the time after his stay in Rostock, beginning in 1929 [5].

the free electron mass, 3 – 5 orders of magnitude lower than that of typical atoms. Although this greatly reduces the critical density  $n_c \propto (Tm)^{3/2}$  for BEC formation [13, 14], there has been no unambiguous experimental observation to this day [15]. The main limiting factor is the two-exciton Auger decay in which one exciton recombines, giving its energy to the second exciton, ionising it [16]. Thereby, the Auger decay hinders the formation of an excitonic BEC in two ways, by reducing the density of excitons and heating the crystal at the same time.

Due to the large excitonic Rydberg energy of  $\sim 86$  meV, the yellow series of cuprous oxide has always had a rather large number of observable excitonic resonances. The original experiments performed by E. F. Gross already reached as high as the  $8P$  [9], which was improved to  $12P$  in the 1990s [17]. Recently, however, a rather large leap has been achieved, pushing the maximum principal quantum number first up to  $n_{\max} = 25$  [18] and later to  $n_{\max} = 28$  [19] as well as the orbital quantum number up to  $\ell = 5$  [20]. The largest of these excitons reach diameters of  $\sim 2.5 \mu\text{m}$  and have been dubbed Rydberg excitons due to the observation of an intensity-dependent bleaching of the resonances which has been interpreted as a Rydberg blockade. In the Rydberg blockade, one atom excited to a Rydberg state shifts the transition to the same state out of resonance on nearby atoms, effectively blocking the excitation of these atoms. Due to the strong dipole-dipole interaction of the Rydberg atoms, which in turn is a result of the large polarisability of these states increasing with  $n^7$  [21, 22], blockade radii on the order of tens of  $\mu\text{m}$  are routinely achievable [23, 24]. The Rydberg blockade is well known and frequently exploited in atomic Rydberg physics, a field of research which has reached a great degree of maturity within the last two decades. Experiments on cold, interacting Rydberg atoms are, however, expensive and subtle to set up. The sophisticated trapping and cooling techniques needed to perform such experiments can be exchanged for a liquid-helium cryostat and the natural localisation due to both the crystal boundaries and the finite size of the laser spot in experiments on Rydberg excitons, leading to cheaper and simpler experimental setups and greater potential for integration. This is not to say that trapping potentials might not be useful for Rydberg excitons as well, as both effects do currently only permit localisation on length scales of 30 to  $100 \mu\text{m}$ , far bigger than both the spatial extensions and the estimated blockade radii of the Rydberg excitons.

The observation of so many consecutive excitonic resonances provided the unique opportunity to study the excitonic fine structure. It has been observed early on, that the small but systematic deviation from an ideal Rydberg series can be cast into quantum defects  $\delta_{n,\ell}$ , which behave similar to those known from alkali Rydberg atoms. These observations were explained by the central-cell corrections, first and foremost the nonparabolicity of the valence band [25, 26, 27] but also the anisotropy as well as the polaronic corrections to the electron-hole interaction potential [28]. Furthermore, the absorption spectra show additional broad peaks between the Rydberg excitons which have been interpreted as signatures of a quantum coherent excitation of two consecutive excitonic resonances [29].

Just like their atomic counterparts, Rydberg excitons have been shown to be very sensitive to their environment. One environmental influence which has been investigated in great detail is the presence of an electron-hole plasma [30, 31]. It is virtually impossible to prevent the generation of such a plasma, as both the background of phonon-assisted absorption into the  $1S$ -states [32] and the main decay channel of the Rydberg excitons via a phonon-scattering process [33] create a population of  $1S$ -excitons which undergoes Auger decay and leaves behind an electron-hole plasma. Furthermore, disorder induced, e.g., by impurities or optical phonons induces an exponential decay of the band gap allowing the direct excitation of unbound electron-hole pairs even below the nominal band gap [34, 35, 36]. The investigations have shown that the main influence of such a plasma is a lowering of the band gap which affects the excitonic resonances only weakly until the band gap crosses a resonance. At this point the corresponding exciton becomes ionised and vanishes into an absorption continuum. As the plasma densities depend strongly on the excitation intensity, these processes can lead to an intensity dependent bleaching, which is hard to distinguish from a Rydberg blockade in the continuous wave (cw) experiments performed thus far.

Other environmental influences that have sparked considerable interest are the dipole-dipole interaction of Rydberg excitons [37] as well as the influence electric and magnetic fields. For example, the possibility to observe excitonic giant-dipole states in crossed electric and magnetic fields has been investigated theoretically [38, 39], as well as the spectra of Stark excitons [40, 41], magnetoexcitons [42] and excitons in a background of charged impurities [43]. Finally, multiple proposals have been put forward, e.g. to use the Rydberg excitons for the implementation of masers [44, 45] or the creation of topological spin phases in lattice potentials [46].

In this work, different phenomena will be investigated which can broadly be summarised under the title “Rydberg excitons in external fields”. These will entail the possibility of inhomogeneous strain as a means to trap Rydberg excitons in Chapter 4 and the theory of optical transitions beyond the dipole approximation in Chapter 5, including transitions from the Rydberg states of the yellow series to those of the green and blue series as well as the excitation of yellow Rydberg excitons using orbital angular momentum (OAM) light. Finally, the influence of a background of charged impurities on the excitonic spectra will be discussed in Chapter 6. First, however, Chapter 2 will lay out the fundamentals of group theory, semiconductor physics as well as the properties of cuprous oxide and its excitons. Chapter 3 will outline the numerical solution of the anisotropic, nonparabolic exciton problem and the calculation of the excitonic van der Waals potentials based on the derived eigenenergies and wave functions. An outlook and a summarising discussion is given in the final Chapter 7. The material constants used in this thesis are summarised in App. A.1.



## Chapter 2.

# Theoretical preliminaries

### 2.1. Group theory

To a physicist, group theory is the mathematical language of symmetry. This Section will focus on its application to quantum mechanics in general and solid state theory in specific. Here, the knowledge about symmetries of the Hamiltonian allows one to make far-reaching statements about the transformational properties of the eigenstates, their degeneracy and selection rules.

In solid state physics, there are four main types of symmetries of interest: translational symmetries, rotational symmetries, the  $SU(2)$  (spin-)symmetry inherited from the Pauli equation [47] and time-inversion symmetry. Of most immediate interest to this work are the rotational symmetries described by the point group of a crystal and the double group of combined rotational and  $SU(2)$  symmetry. A short discussion on the connection of the point group of  $Cu_2O$  to the space group, which is the group of combined rotational and translational symmetries, will be given in Sec. 2.3. The discussion in this Section will be limited to unitary symmetries (i.e. symmetries that conserve scalar products), which includes all the aforementioned types of symmetries except time inversion. This Section will give a short introduction into the main concepts of group theory and define important terms and relations used in the following. For a more in-depth introduction the reader is referred to Refs. [48, 49, 50].

The crystallographic group theory is plagued with a variety of different notational conventions, most notably the Schoenflies and Hermann-Maguin notation for the crystallographic point and space groups as well as the Koster [50] and the Bouckaert-Smoluchowski-Wigner (BSW) notation [51] for the irreducible representations of the point groups. We will stick to the Schoenflies and the Koster notations in this work. Table B.2 contains the transcription between the Koster and the BSW notation for the point group  $O_h$ .

**Definition 1** (Group). A group  $G$  is a set of elements  $\{a, b, c, \dots\}$ , with a multiplicative mapping  $ab : G \times G \mapsto G$ , fulfilling the following axioms:

1. **Closure:**  $ab \in G \forall a, b \in G$
2. **Associativity:**  $(ab)c = a(bc) \forall a, b, c \in G$
3. **Identity element:**  $\exists e \in G : ae = ea = a \forall a \in G$
4. **Inverse element:**  $\forall a \in G \exists a^{-1} \in G : aa^{-1} = a^{-1}a = e$ .

A group is called **abelian** if it fulfils the additional axiom:

5. **Commutativity:**  $ab = ba \forall a, b \in G$ .

A subset  $H$  of  $G$  fulfilling the axioms 1.–4. is called a **subgroup** of  $G$ .

An important property of a group is its **order**  $g$ , i.e. the number of its elements. Groups with infinite order do exist as well, a special case of which are the **Lie-groups**, i.e. continuous symmetry groups such as the rotation groups  $SO(3)$  and  $O(3)$  or the translation group of free space. Another important concept are the **conjugacy classes** which are subsets of  $G$  defined as follows: two elements of  $a, b \in G$  belong to the same conjugacy class if there exists a  $c \in G$  such that  $a = c^{-1}bc$ . Thereby, every element of the group does unambiguously belong to exactly one conjugacy class.

### 2.1.1. Space groups and point groups

The space group of a crystal is the group of all its spatial symmetries  $\{\alpha, \tau\}$  consisting of combined rotations and translations  $\alpha$  and  $\tau$ , respectively. They transform any function  $f(\mathbf{r})$  according to

$$\{\alpha, \tau\} f(\mathbf{r}) = f(\alpha^{-1} \cdot (\mathbf{r} - \tau)). \quad (2.1)$$

The subset of pure translations  $\{\mathbf{1}, \mathbf{R}_n\}$  forms a subgroup of the space group and is called the **Bravais lattice** of the crystal. The group of rotational symmetries of this Bravais lattice is called the **holoedra group** of the crystal and the 14 Bravais lattices can be classed into 7 **crystal systems** according to it [48].

The pure rotations  $\alpha$  present in the space group form the **point group** of the crystal which, in general, is not a symmetry group of the crystal. If it is, the crystal is called **symmorphic** and the space group is the product of the translation group and the point group. Examples for symmorphic crystals are all elemental crystals without a basis, i.e. with only one atom per lattice site. For non-symmorphic crystals, some rotational symmetries do only map the crystal onto itself in combination with a nontrivial translation (i.e. a translation that by itself is not a symmetry of the crystal). It should be noted that for crystals with a basis, the point group is not necessarily identical to the

holoedral group, but it must be one of its subgroups. There are 230 crystallographic space groups with 32 different point groups in three dimensions [48, 50].

### 2.1.2. Representations

A **representation**  $\Lambda$  of a group  $G$  is defined as a set of matrices  $D_\Lambda(a) \in \mathbb{C}^{n \times n}$ , one for each  $a \in G$ , whose multiplications follow the multiplication table of the group, i.e.

$$D_\Lambda(a) \cdot D_\Lambda(b) = D_\Lambda(ab) \quad \forall a, b \in G. \quad (2.2)$$

The parameter  $n$  is called the dimension of the representation. If the mapping between the elements of the group and the representation matrices is bijective, the representation matrices form a group that is isomorphic to  $G$  and are called a **faithful representation**.

If two representations  $\Lambda_\alpha, \Lambda_\beta$  of a group are known, additional ones can be constructed via

$$D_{\Lambda_\gamma}(a) = D_{\Lambda_\alpha}(a) \otimes D_{\Lambda_\beta}(a), \quad (2.3)$$

$$D_{\Lambda_\delta}(a) = \begin{pmatrix} D_{\Lambda_\alpha}(a) & \mathbf{0} \\ \mathbf{0} & D_{\Lambda_\beta}(a) \end{pmatrix}. \quad (2.4)$$

The shorthand notations used to refer to these operations are, respectively,  $\Lambda_\gamma = \Lambda_\alpha \otimes \Lambda_\beta$  and  $\Lambda_\delta = \Lambda_\alpha \oplus \Lambda_\beta$ . Another way to construct new representations from known ones is via similarity transformations  $D_{\Lambda_\epsilon}(a) = \mathbf{A}^{-1} \cdot D_{\Lambda_\alpha}(a) \cdot \mathbf{A}$  with some invertible  $\mathbf{A} \in \mathbb{C}^{n \times n}$ . The representations are then called **equivalent**  $\Lambda_\epsilon \sim \Lambda_\alpha$ .

A representation  $\Gamma$  is called **irreducible** if there exists no similarity transformation to transform all the matrices to the same block-diagonal form as in Eq. (2.4). It can be shown that the number of inequivalent, irreducible representations of any finite group is equal to the number  $r$  of its conjugacy classes. The continuous rotation group  $\text{SO}(3)$  has a countably infinite number of irreducible representations which can be labelled by the orbital quantum number  $\ell$  and have dimension  $2\ell + 1$ , respectively.

Every representation of a group can be decomposed into an equivalent sum of irreducible representations. The decomposition of products of irreducible representations into sums of irreducible representations, in particular, are given as the **multiplication tables** of the irreducible representations (see Tab. B.3 for  $O_h$ ). The connection of these decompositions to the **characters**  $\chi_\Lambda(a) = \text{Tr}[D_\Lambda(a)]$  of the representations is discussed in App. B.2.

In quantum mechanics, the term representation is often used synonymously with an eigenspace of the Hamiltonian that owes its degeneracy to the symmetry of the Hamiltonian. Let  $\mathcal{H}$  be a Hamil-

tonian with symmetry group  $G$  and  $V$  the eigenspace with an orthonormal basis  $|1_V\rangle, |2_V\rangle, \dots, |N_V\rangle$  and an eigenenergy  $E_V$ . By applying the symmetry operations  $a \in G$  via the operators  $\hat{S}_a$

$$\hat{S}_a \mathcal{H} |i_V\rangle = \mathcal{H} \hat{S}_a |i_V\rangle = E_V \hat{S}_a |i_V\rangle, \quad (2.5)$$

it is clear that  $\hat{S}_a |i_V\rangle$  is an eigenvector of the Hamiltonian from the same eigenspace. The eigenspace is thus invariant and in the case of unitary symmetries, the transformation of the basis can be expressed as

$$\hat{S}_a |i_V\rangle = \sum_{j=1}^N \mathcal{D}_{j,i}(a) |j_V\rangle. \quad (2.6)$$

The unitary matrices

$$\mathcal{D}_{j,i}(a) = \langle j_V | \hat{S}_a | i_V \rangle \quad (2.7)$$

have to fulfil the representation property Eq. (2.2) and motivate the nomenclature. The symmetry of the Hamiltonian implies that every eigenspace must be degenerate according to the dimension of its irreducible representation. Any higher degeneracy is either coincidental or indicative of additional symmetries<sup>1</sup>.

It is often convenient to choose the bases of invariant vector spaces belonging to the same irreducible representation in such a way that they transform in the same way, i.e. that the transformation matrices  $\mathcal{D}(a)$  coincide. The particular choice is somewhat arbitrary and tends to be defined in terms of exemplary basis functions, given in the character tables (see Tab. B.2). These basis functions will be called the **rows of the irreducible representation** in the following. In the case of the infinite rotation groups the rows are generally labelled by the magnetic quantum number<sup>2</sup>  $m$ .

The most basic irreducible representation every group possesses is the one-dimensional identity representation  $\Gamma_1$  with  $\mathcal{D}_{\Gamma_1}(a) = 1$  for all  $a \in G$ . This representation corresponds to states or operators which are invariant under all symmetry transformations, e.g. the Hamiltonian, which has the full symmetry by definition. The specialisation for the group  $\text{SO}(3)$  is the representation  $\Gamma_{\ell=0}$  corresponding to all rotationally symmetric states and operators.

Another important concept in group theory is that of **compatibility**. Let  $\Gamma_\alpha$  be an irreducible representation of the group  $G$  and  $H$  a subgroup of  $G$ . The set  $\{\mathcal{D}_{\Gamma_\alpha}(a) : a \in H\}$  clearly forms

<sup>1</sup>A famous example of the latter would be the hydrogen atom in which the obvious  $\text{O}(3)$  symmetry is responsible for the  $(2\ell + 1)$ -fold degeneracy with respect to the magnetic quantum number  $m$ . The degeneracy with respect to the orbital quantum number  $\ell$  is induced by a hidden, dynamical  $\text{SO}(4)$ -symmetry [52] which depends crucially on both the parabolic dispersion of the electron and the  $1/r$  Coulomb potential. It is therefore broken in more complicated systems such as Rydberg excitons or the alkali Rydberg atoms and the degeneracy is lifted.

<sup>2</sup>Sometimes, homogeneous polynomials of order  $\ell$  are used instead, for example  $\{x, y, z\}$  for  $\ell = 1$  or  $\{(2z^2 - x^2 - y^2)/\sqrt{6}, (x^2 - y^2)/\sqrt{2}, yz, zx, xy\}$  for  $\ell = 2$ .



a representation of  $H$ . The decomposition  $\Gamma_\alpha(G) \mapsto \sum_\beta \Gamma_\beta(H)$  into irreducible representations of  $H$  is then given by the compatibility table of  $H$  with respect to  $G$  (see e.g. Tab. B.4 for the compatibility table of  $O_h$  with respect to  $O(3)$ ). In quantum mechanics, the compatibility relations indicate the splitting of degenerate manifolds under a corresponding reduction of symmetry. As all crystallographic point groups are subgroups of  $O(3)$ , linear combinations of its basis functions, the spherical harmonics  $Y_\ell^m(\phi, \theta)$ , can be constructed which transform like the rows of the point groups' irreducible representations. These are called **lattice harmonics** [53, 48, 54] in general and **cubic harmonics** in the case of the point group  $O_h$  [55, 56]. The cubic harmonics up to  $\ell = 6$  are given in App. B.4.

### 2.1.3. Coupling coefficients

Let  $|\Gamma_\alpha, i\rangle$  and  $|\Gamma_\beta, j\rangle$  be the bases for two invariant Hilbert spaces corresponding to the irreducible representations  $\Gamma_\alpha$  and  $\Gamma_\beta$  and transforming according to the particular choice of basis functions for these two representations. The  $|\Gamma_\alpha, i\rangle$  and  $|\Gamma_\beta, j\rangle$  are assumed to be vectors of some Hilbert space here, but the discussion is readily extensible to invariant operator spaces as it only hinges on the transformational properties. The product states do then transform like

$$\begin{aligned} \hat{S}_a |\Gamma_\alpha, i\rangle |\Gamma_\beta, j\rangle &= \sum_{k=1}^n \sum_{l=1}^{n'} \mathcal{D}_{k,i}^{\Gamma_\alpha}(a) \mathcal{D}_{l,j}^{\Gamma_\beta}(a) |\Gamma_\alpha, k\rangle |\Gamma_\beta, l\rangle \\ &= \sum_{\tau=1}^{nn'} \left[ \mathcal{D}^{\Gamma_\alpha}(a) \otimes \mathcal{D}^{\Gamma_\beta}(a) \right]_{\tau, \nu} |\Gamma_\alpha, \tau\rangle |\Gamma_\beta, \tau\rangle \end{aligned} \quad (2.8)$$

where  $\nu \triangleq \{i, j\}$  and  $\tau \triangleq \{k, l\}$  are compound indices. Clearly, the representation of the space spanned by all products is  $\Gamma_\alpha \otimes \Gamma_\beta$ , which will in general be reducible. If this is the case, the matrices  $\mathcal{D}^{\Gamma_\alpha}(a) \otimes \mathcal{D}^{\Gamma_\beta}(a)$  can be brought to a block-diagonal form as in Eq. (2.4) via a unitary transformation. The coefficients  $\langle \Gamma_\alpha, i; \Gamma_\beta, j | \Gamma_\gamma, k \rangle_\mu$  of the unitary transformation for which the block matrices take the form implied by the rows of the irreducible representations are called **coupling coefficients** or **Clebsch-Gordan coefficients** in the case of the infinite rotation groups. The index  $\mu$  accounts for the fact that  $\Gamma_\gamma$  might appear more than once in  $\Gamma_\alpha \otimes \Gamma_\beta$  which would imply that there are multiple linearly independent combinations of product states transforming like the row  $k$  of  $\Gamma_\gamma$ . Symmetrised products can then be constructed via

$$|\Gamma_\gamma, k\rangle_\mu = \sum_{i,j} \langle \Gamma_\alpha, i; \Gamma_\beta, j | \Gamma_\gamma, k \rangle_\mu |\Gamma_\alpha, i\rangle |\Gamma_\beta, j\rangle. \quad (2.9)$$

A comprehensive list of coupling coefficients for all 32 crystallographic point groups can be found in Ref. [50].

One important application of these coupling coefficients is the so called **Wigner-Eckart theorem**. Let  $\hat{O}_j$  be an operator transforming like the  $j$ th row of the irreducible representation  $\Gamma_\beta$  and  $|R, \Gamma_\alpha, i\rangle$  as well as  $|R', \Gamma_\gamma, k\rangle$  two states with the rows  $i, k$  of the irreducible representations  $\Gamma_\alpha, \Gamma_\gamma$  and  $R, R'$  labelling all other quantum numbers. The Wigner-Eckart theorem states that the corresponding matrix element can be written as

$$\langle R, \Gamma_\alpha, i | \hat{O}_j | R', \Gamma_\gamma, k \rangle = \sum_{\mu=1}^M \langle R, \Gamma_\alpha | \hat{O} | R', \Gamma_\gamma \rangle_\mu \langle \Gamma_\beta, j; \Gamma_\gamma, k | \Gamma_\alpha, i \rangle_\mu^* \quad (2.10)$$

with the reduced matrix elements  $\langle R, \Gamma_\alpha | \hat{O} | R', \Gamma_\gamma \rangle_\mu$ , the complex conjugated coupling coefficients  $\langle \Gamma_\beta, j; \Gamma_\gamma, k | \Gamma_\alpha, i \rangle_\mu^*$  and the multiplicity  $M$  of the irreducible representation  $\Gamma_\alpha$  in the decomposition of  $\Gamma_\beta \otimes \Gamma_\gamma$ . Notably, if  $M$  is zero, the matrix element has to vanish<sup>3</sup>. It is often possible to derive selection rules based solely on this observation and the multiplication table of the irreducible representations (see, e.g. Tab. B.3). Another important aspect is the fact that the reduced matrix elements do not depend on the rows  $i, j$  and  $k$  of the irreducible representations while the coupling coefficients are completely determined by the transformational properties of the operator and the states. This can be exploited to minimise the number of independent free parameters in, say, perturbation theoretical calculations.

## 2.2. Fundamentals of semiconductor physics

This Section is based on the introductory chapters of the books [57, 58, 59, 60, 61]. For a more comprehensive discussion, the reader is referred to these resources as well as Refs. [62, 63].

A semiconductor can be defined as a material with a conductivity between that of a conductor and an insulator, typically in the range between  $10^{-2} \Omega \text{ cm}$  and  $10^9 \Omega \text{ cm}$ . An important result of solid state physics is the observation that only partially filled bands may contribute to the conductivity of a crystal, while bands that are either completely filled or completely empty may not. This motivates the classification based on the size of the main band gap<sup>4</sup> which allows for a more rigid distinction between conductors (materials without a band gap) and semiconductors<sup>5</sup> (materials with a band gap  $E_g \lesssim 3 \text{ eV}$ ). The distinction between semiconductors and insulators, however, is still fuzzy. Semiconductors as well as insulators possess only bands that are either completely filled or completely empty in their ground state. Due to their lower band gap, however, semicon-

<sup>3</sup>A more basic derivation of this result relies on the fact that the scalar product of two vectors has to vanish by symmetry, if they correspond to different rows of two (possibly identical) irreducible representations  $\langle R, \Gamma_\alpha, i | R', \Gamma_\gamma, k \rangle \propto \delta_{\Gamma_\alpha, \Gamma_\gamma} \delta_{i,k}$  [49]. Thus, if the vector  $\hat{O}_j | R', \Gamma_\gamma, k \rangle$  does not contain any component transforming like  $|\Gamma_\alpha, i\rangle$ , the corresponding matrix element has to vanish.

<sup>4</sup>At this point, it shall suffice to define the band gap as the energy difference between the highest occupied electronic state and the lowest unoccupied state at 0 K. The Fermi energy  $E_f$  can be loosely defined as the energy below which all states are filled and above which all states are empty at 0 K.

<sup>5</sup>Zero-gap semiconductors do exist as well (e.g. graphene). For those, the conduction and valence band touch at the Fermi-energy  $E_f$ .

ductors can be thermally or optically excited, resulting in an intermediate conductivity at room temperature. A schematic of the classification is shown in Fig. 2.1.

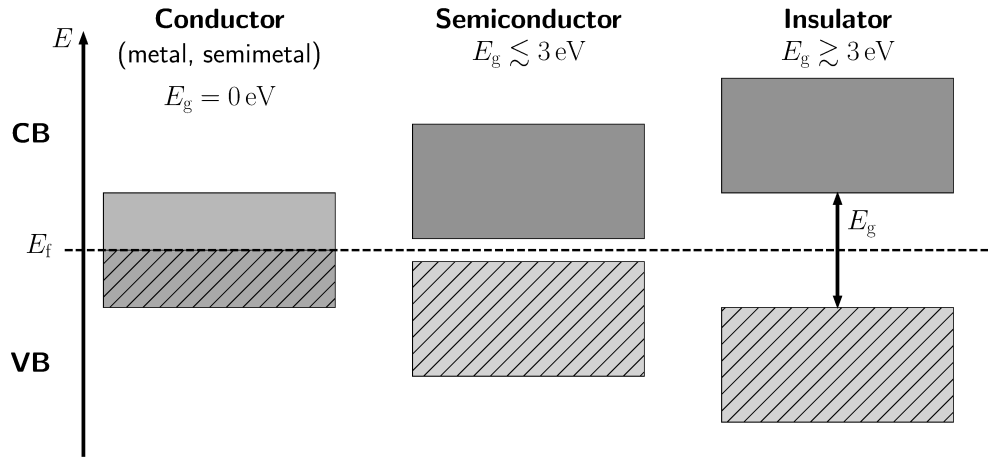


**Figure 2.1.:** Classification of materials based on the main band gap between the filled valence band (VB, light grey) and empty conduction band (CB, dark grey). Hatched areas indicate occupied states.

The susceptibility to external and internal influences is one of the main reasons why semiconductors have a wide range of technological applications. Their electronic and optical properties tend to be tunable by factors that can be integrated into manufacturing processes such as doping by impurities, straining of the crystal or the fabrication of heterostructures. The most important semiconductors for industrial applications are the elemental group IV semiconductors silicon (Si) and germanium (Ge). Although diamond does not fulfil the given definition ( $E_g \approx 5.5 \text{ eV}$ ), it is often considered a semiconductor as well. The wealth of research on these materials is a boon to the research on cuprous oxide as they have sufficiently similar crystal structures that many results derived by symmetry considerations are readily extensible to  $\text{Cu}_2\text{O}$ . Other important semiconductors are formed from combinations of elements from the groups III-V (e.g. GaAs) and II-VI (e.g. ZnSe). Oxide semiconductors such as  $\text{Cu}_2\text{O}$  are generally not as important for industrial applications and their fabrication is not as well understood. In the case of  $\text{Cu}_2\text{O}$ , for example, the purest crystals in circulation today are still natural crystals from the Tsumeb mine in Namibia [18].

### 2.2.1. Semiconductor solid-state theory

The most general nonrelativistic Hamiltonian for a solid-state system can be written as

$$H = \sum_i \frac{\mathbf{P}_i^2}{2M_i} + \sum_j \frac{\mathbf{p}_j^2}{2m_0} + \frac{e^2}{8\pi\epsilon_0} \sum_{\substack{i,i' \\ i \neq i'}} \frac{Z_i Z_{i'}}{|\mathbf{R}_i - \mathbf{R}_{i'}|} + \frac{e^2}{8\pi\epsilon_0} \sum_{\substack{j,j' \\ j \neq j'}} \frac{1}{|\mathbf{r}_j - \mathbf{r}_{j'}|} - \frac{e^2}{4\pi\epsilon_0} \sum_{i,j} \frac{Z_i}{|\mathbf{R}_i - \mathbf{r}_j|} \quad (2.11)$$

where  $i$  sums over the atomic nuclei with charge  $eZ_i$  and mass  $M_i$  and  $j$  sums over the electrons. As a typical condensed matter system contains roughly  $10^{23}$  particles per cubic centimeter, the full treatment of the corresponding Schrödinger equation is impossible. Another major shortcoming of this description is the fact that it contains no a-priori knowledge about the phase or structure of the quantum system of interest. In order to remedy this shortcoming, the **Born-Oppenheimer approximation** is almost universally employed in solid-state physics. It enables one to decouple the motion of the electrons and the atomic nuclei and is based on the assumption that due to their much lower mass, the electrons follow the movement of the nuclei adiabatically. This results in an electronic Hamiltonian that depends only parametrically on the positions of the atoms  $\{\mathbf{R}\}$

$$H_{\text{el}}(\{\mathbf{R}\}) = \sum_j \frac{\mathbf{p}_j^2}{2m_0} + \frac{e^2}{8\pi\epsilon_0} \sum_{\substack{j,j' \\ j \neq j'}} \frac{1}{|\mathbf{r}_j - \mathbf{r}_{j'}|} - \frac{e^2}{4\pi\epsilon_0} \sum_{i,j} \frac{Z_i}{|\mathbf{R}_i - \mathbf{r}_j|} \quad (2.12)$$

and an ionic Hamiltonian describing the motion of the atomic nuclei in the potential surface defined by the electronic ground-state energy  $E_{\text{el}}^0(\{\mathbf{R}\})$

$$H_{\text{ion}} = \sum_i \frac{\mathbf{P}_i^2}{2M_i} + \frac{e^2}{8\pi\epsilon_0} \sum_{\substack{i,i' \\ i \neq i'}} \frac{Z_i Z_{i'}}{|\mathbf{R}_i - \mathbf{R}_{i'}|} + E_{\text{el}}^0(\{\mathbf{R}\}). \quad (2.13)$$

The Hamiltonian  $H_{\text{ion}}$  leads to the concept of **phonons**, the quantised lattice vibrations. A short discussion of the phononic modes of  $\text{Cu}_2\text{O}$  can be found in Sec. 2.3.

In order to make the electronic Schrödinger equation tractable, the Hamiltonian is often reduced to a single-electron one

$$\mathcal{H} = \frac{\mathbf{p}^2}{2m_0} + V_{\text{eff}}(\mathbf{r}) \quad (2.14)$$

with some effective potential  $V_{\text{eff}}(\mathbf{r})$  containing the interaction of the electron with the crystal ions as well as the mean-field interaction with all other electrons. While it is in principle possible to derive effective potentials [61] called pseudo-potentials, this is highly nontrivial. Often, the one-

electron approximation is used instead to derive effective Hamiltonians describing the electronic properties which can be fitted to experimental results or more sophisticated calculations.

To a physicist, the defining characteristic of a crystal is the discrete translational symmetry  $V_{\text{eff}}(\mathbf{r}) = V_{\text{eff}}(\mathbf{r} - \mathbf{R}_n)$ . This implies that the corresponding Hamiltonian commutes with a group of translation operators  $T_{\mathbf{R}_n}$  which translate every function according to  $T_{\mathbf{R}_n} f(\mathbf{r}) = f(\mathbf{r} - \mathbf{R}_n)$ . The lattice vectors

$$\mathbf{R}_n = n_1 \mathbf{a}_1 + n_2 \mathbf{a}_2 + n_3 \mathbf{a}_3 \quad n_1, n_2, n_3 \in \mathbb{Z} \quad (2.15)$$

can be build up from the primitive lattice vectors  $\mathbf{a}_i$ . The lattice formed by all lattice vectors is called the **Bravais lattice** of the crystal and the lengths of the primitive lattice vectors  $|\mathbf{a}_i|$  are called the **lattice constants**. There are 14 different Bravais lattices, the ones with the highest overall symmetry being the three cubic ones: the simple cubic (sc), the face centered cubic (fcc) and the body centered cubic (bcc) [48]. Any crystal can be build up from the repetition of a fundamental building block with a volume  $\mathcal{V} = \mathbf{a}_1 \cdot (\mathbf{a}_2 \times \mathbf{a}_3)$ , called the **primitive unit cell**. One particular choice of primitive unit cell is the **Wigner-Seitz cell**, which has a lattice point of the Bravais lattice at its center and consists of all points which are closer to this lattice point than to any other. An important concept in solid-state physics is the so called **reciprocal lattice**

$$\mathbf{G}_n = n_1 \mathbf{b}_1 + n_2 \mathbf{b}_2 + n_3 \mathbf{b}_3 \quad n_1, n_2, n_3 \in \mathbb{Z} \quad (2.16)$$

whose primitive lattice vectors can be derived via

$$\mathbf{b}_i = \frac{2\pi}{\mathcal{V}} \mathbf{a}_j \times \mathbf{a}_k \quad \Rightarrow \quad \mathbf{a}_i \cdot \mathbf{b}_j = 2\pi \delta_{i,j} \quad (2.17)$$

where  $\{i, j, k\}$  denotes a cyclic permutation of  $\{1, 2, 3\}$ . Every normalisable, lattice periodic function  $F(\mathbf{r})$  can be decomposed into the Fourier components corresponding to the reciprocal lattice vectors

$$F(\mathbf{r}) = \sum_n F_n e^{i\mathbf{G}_n \cdot \mathbf{r}}. \quad (2.18)$$

The reciprocal lattice is of course a Bravais lattice as well, which must belong to the same crystal system but is not necessarily equivalent. The reciprocal lattice of the fcc lattice, for example, is a bcc lattice and vice versa [48]. The Wigner-Seitz cell of the reciprocal lattice is called the **first Brillouin zone** of the crystal.

The translational invariance of the Hamiltonian (2.14) implies that its eigenstates can be chosen to be simultaneous eigenstates of the translation operators<sup>6</sup>  $T_{\mathbf{R}_n}$ , which take the general form

$$\phi_{n,\mathbf{k}}(\mathbf{r}) = e^{i\mathbf{k}\cdot\mathbf{r}} u_{n,\mathbf{k}}(\mathbf{r}) \quad (2.19)$$

with the lattice periodic function  $u_{n,\mathbf{k}}(\mathbf{r}) = u_{n,\mathbf{k}}(\mathbf{r} + \mathbf{R}_n)$  and the quantum numbers  $n$  (called the band index) as well as  $\mathbf{k}$  (called the quasi momentum). This observation is called the **Bloch theorem** and the quasi-continuous bands  $E_n(\mathbf{k})$  formed by the eigenenergies are called the **band structure**. From the fact that every  $e^{i\mathbf{G}_n\cdot\mathbf{r}}$  is lattice periodic as well, follows that the Bloch states  $\phi_{n,\mathbf{k}}(\mathbf{r})$  and  $\phi_{n,\mathbf{k}+\mathbf{G}_n}(\mathbf{r})$  span the same Hilbert space. The band structure is therefore lattice periodic with respect to the reciprocal lattice  $E_n(\mathbf{k}) = E_n(\mathbf{k} + \mathbf{G}_n)$  and its discussion can be restricted to the first Brillouin zone. This is called the reduced zone scheme and is schematically shown in Fig. 2.2.

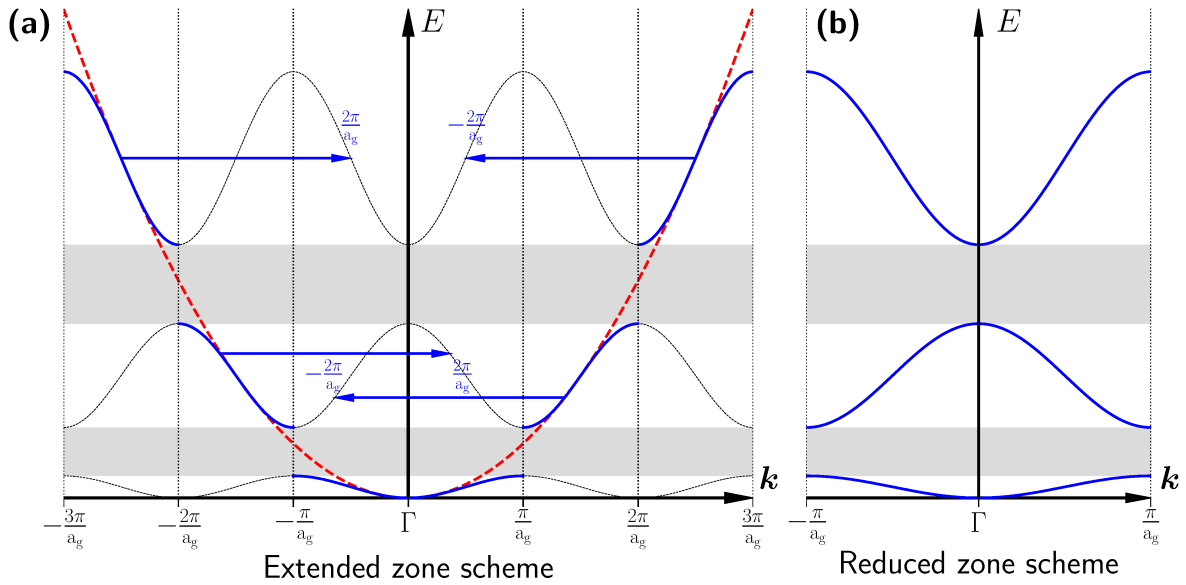


**Figure 2.2.:** Schematic representation of the transition from the extended zone scheme (a) to the reduced zone scheme (b). The red dotted line symbolises the free electron dispersion, the grey areas highlight the band gaps and  $a_g$  denotes the lattice constant. The dashed lines indicate the lattice periodicity of the band structure. Adapted from [64, 62].

Under the space-group symmetries  $\{\alpha, \tau\}$  the Bloch states transform like

$$\begin{aligned} \{\alpha, \tau\} \phi_{n,\mathbf{k}}(\mathbf{r}) &= e^{i\mathbf{k}\cdot\alpha^{-1}\cdot(\mathbf{r}-\tau)} u_{n,\mathbf{k}}\left(\alpha^{-1}\cdot(\mathbf{r}-\tau)\right) \\ &= e^{i(\alpha\mathbf{k})\cdot\mathbf{r}} \left[ e^{-i(\alpha\mathbf{k})\cdot\tau} u_{n,\mathbf{k}}\left(\alpha^{-1}\cdot(\mathbf{r}-\tau)\right) \right] \end{aligned} \quad (2.20)$$

<sup>6</sup>They can be chosen as simultaneous eigenstates of all translation operators due to the abelian nature of the translation group.

which has to be a degenerate eigenstate of the crystal Hamiltonian corresponding to  $\phi_{n,\alpha\cdot\mathbf{k}}(\mathbf{r})$ . The implication that the band structure is symmetric with respect to all symmetries in the point group of the crystal  $E_n(\mathbf{k}) = E_n(\alpha\mathbf{k})$  will be called **star<sup>7</sup> degeneracy<sup>8</sup>**. At points of high symmetry in the first Brillouin zone, there might be a subgroup of the point group called the **small group** which maps  $\mathbf{k}$  onto itself<sup>9</sup>  $\alpha\mathbf{k} = \mathbf{k}$ . In this case, the Bloch states can be classified according to the irreducible representations of the small group. In particular, at the  $\Gamma$ -point (i.e.  $\mathbf{k} = \mathbf{0}$ ) they can be classified according to the irreducible representations of the whole point group.

One of the most important sets of parameters of the band structure, besides the band gaps, are the curvatures of the bands around their extrema  $\mathbf{k}_0$ . These are often expressed as **effective mass tensors**  $\mathbf{m}_n^*$ ,

$$(\mathbf{m}_n^*)_{i,j}^{-1} = \frac{1}{\hbar^2} \frac{\partial^2}{\partial k_i \partial k_j} E_n(\mathbf{k}) \Big|_{\mathbf{k}=\mathbf{k}_0} \quad (2.21)$$

which can be interpreted as the inertial mass of a quasiparticle. If the effective mass tensor is proportional to the identity matrix, as is the case for the highest valence band and lowest conduction band of  $\text{Cu}_2\text{O}$ , the proportionality constant is simply called the **effective mass**  $m_n^*$ .

The effective mass of the highest valence band is negative in most semiconductors. In order to arrive at a more intuitive description, the problem can then be reformulated in terms of positively charged quasiparticles, the **holes**. In this way, the dynamics can be described in terms of a few particles with a positive effective mass in an otherwise empty band instead of a few electron-vacancies with negative mass in otherwise completely filled band. The change of the quasiparticle properties under this transformation are laid out in Tab. 2.1 and Fig. 2.3.

The description in terms of quasiparticles with effective masses introduces some ambiguity into the language of solid-state physics. There are two concepts of importance to solid-state physics called an “electron”, the elementary particle as well as a quasiparticle describing a many-body state of an elementary electron excited to the conduction band. Table 2.2 compares the properties of these two. For the remainder of this thesis, we will take the route of most text on solid-state physics and not explicitly distinguish between the two.

The boundaries of the crystal break its translational symmetry, complicating the treatment by the introduction of surface effects. If one is only interested in the bulk properties of the crystal, the

<sup>7</sup>The star of a point  $\mathbf{k}$  consists of the set of all distinct points that can be constructed by  $\alpha\mathbf{k}$ , where  $\alpha$  is any element of the crystal’s point group. In general, the number of distinct points will equal the order of the point group, it will only be lower at points of high symmetry (e.g.  $\mathbf{k} = \mathbf{0}$ ).

<sup>8</sup>The term “star degeneracy” is lent from the German word “Sternentartung” [65] and is not generally used in English texts [49]. The author does, however, deem it convenient to have a concise expression to refer to this phenomenon.

<sup>9</sup>This includes a possible translation by a reciprocal lattice vector  $\alpha\mathbf{k} = \mathbf{k} + \mathbf{G}_n$ , which is only relevant for points on the very boundary of or outside the first Brillouin zone.

	vacant electron	hole
mass	$m_e^* < 0$	$m_h^* = -m_e^*$
momentum	$\mathbf{k}_e$	$\mathbf{k}_h = -\mathbf{k}_e$
dispersion	$E_n(\mathbf{k}_e)$	$-E_n(\mathbf{k}_h)$
spin	$\sigma_e$	$\sigma_h = -\sigma_e$
charge	$-e$	$e$

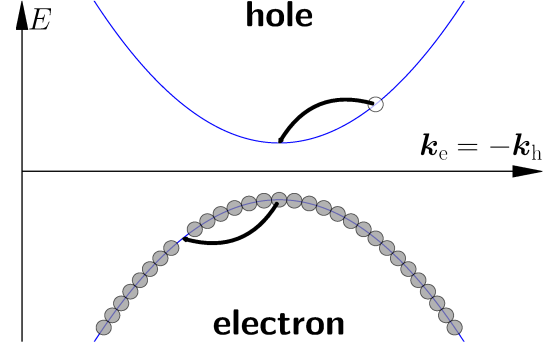


**Table 2.1:** Comparison of the properties of a vacant electron and the corresponding hole.

**Figure 2.3:** Schematic representation of equivalent scattering processes for a valence-band electron and hole.

	elementary particle	quasiparticle
mass	$m_0$	$m_e^*$
momentum	$\mathbf{p}$	$\mathbf{k}$
dispersion	$\mathbf{p}^2/(2m_0)$	$E_n(\mathbf{k})$
potential	$V_{\text{eff}}(\mathbf{r})$	0
wave function	$e^{i\mathbf{k}\cdot\mathbf{r}} u_{n,\mathbf{k}}(\mathbf{r})$	$e^{i\mathbf{k}\cdot\mathbf{r}}$

**Table 2.2.:** Comparison of the properties of the elementary particle and quasiparticle electron.

treatment can be simplified by the introduction of **periodic boundary-conditions**

$$\phi_{n,\mathbf{k}}(\mathbf{r}) = \phi_{n,\mathbf{k}}(\mathbf{r} + N\mathbf{a}_i) \quad N \in \mathbb{N}, \quad N \gg 1 \quad (2.22)$$

where  $\Omega = N^3 \mathcal{V}$  is the crystal volume and  $N^3$  the number of unit cells inside the crystal. The periodic boundary conditions effectively eliminate the crystal surface while keeping the crystal volume finite and the Bloch states normalisable. The relation  $e^{iN\mathbf{k}\cdot\mathbf{a}_i} = 1$  implied by Eq. (2.19) restricts the allowed  $\mathbf{k}$  to a discrete set of  $N^3$  equidistant values inside the first Brillouin zone. In general, the crystal is assumed to be of macroscopic size, leading to a quasi-continuous distribution of allowed quasi momenta with a separation of  $\Delta k = 2\pi/(N a_g)$  in a sc lattice. The quasi-continuity can then be exploited via

$$\sum_{\mathbf{k}} = \frac{1}{(\Delta k)^3} \sum_{\mathbf{k}} (\Delta k)^3 \approx \frac{\Omega}{(2\pi)^3} \int d^3\mathbf{k}. \quad (2.23)$$



Once the single-electron problem is solved, the electronic many-body state is assumed to be of Slater-determinant type

$$|\Phi\rangle = \mathcal{A} \prod_i |\phi_{n_i, \mathbf{k}_i}(\mathbf{r}_i)\rangle = \left[ \prod_i a_{n_i, \mathbf{k}_i}^\dagger \right] |\Phi_0\rangle, \quad (2.24)$$

expressed via the Slater antisymmetrisation operator  $\mathcal{A}$  [61] or the fermionic electron creation operators  $a_{n, \mathbf{k}}^\dagger$  creating an electron in the state  $|\phi_{n, \mathbf{k}}\rangle$ . The ket  $|\Phi_0\rangle$  denotes the empty-crystal state. The crystal ground-state (often called **crystal vacuum**) is then given by

$$|\Phi_{\text{vac}}\rangle = \left[ \prod_i a_{n_i, \mathbf{k}_i}^\dagger \right] |\Phi_0\rangle \quad (2.25)$$

where  $i$  enumerates all the valence bands and all allowed  $\mathbf{k}$  in the first Brillouin zone.

### 2.2.2. The $\mathbf{k} \cdot \mathbf{p}$ method

The starting point for the discussion of  $\mathbf{k} \cdot \mathbf{p}$  theory shall be the one-electron Hamiltonian (2.14) including spin-orbit coupling

$$\mathcal{H} = \frac{\mathbf{p}^2}{2m_0} + V(\mathbf{r}) + \frac{\hbar}{4m_0^2 c^2} [\boldsymbol{\sigma} \times \nabla V(\mathbf{r})] \cdot \mathbf{p}, \quad (2.26)$$

with the vector of the Pauli matrices  $\boldsymbol{\sigma}$

$$\sigma_x = \begin{pmatrix} 0 & 1 \\ 1 & 0 \end{pmatrix}, \quad \sigma_y = \begin{pmatrix} 0 & -i \\ i & 0 \end{pmatrix}, \quad \sigma_z = \begin{pmatrix} 1 & 0 \\ 0 & -1 \end{pmatrix}. \quad (2.27)$$

The spin-orbit term is inherited from the Pauli equation [47], an approximation to the relativistic Dirac equation for kinetic energies far lower than the rest energy  $m_0 c^2$ . Using the Bloch theorem  $\phi_{n, \sigma, \mathbf{k}}(\mathbf{r}) = e^{i\mathbf{k} \cdot \mathbf{r}} u_{n, \sigma, \mathbf{k}}(\mathbf{r})$ , where  $\sigma$  denotes the spin state, a Schrödinger equation

$$\mathcal{H}_{\mathbf{k} \cdot \mathbf{p}} u_{n, \sigma, \mathbf{k}}(\mathbf{r}) = E_{n, \sigma}(\mathbf{k}) u_{n, \sigma, \mathbf{k}}(\mathbf{r}) \quad (2.28)$$

describing only the lattice periodic part can be derived via

$$\mathcal{H}_{\mathbf{k} \cdot \mathbf{p}} = \mathcal{H} + e^{-i\mathbf{k} \cdot \mathbf{r}} [\mathcal{H}, e^{i\mathbf{k} \cdot \mathbf{r}}] = \mathcal{H} + \frac{\hbar}{m_0} \mathbf{k} \cdot \boldsymbol{\pi} + \frac{\hbar^2 \mathbf{k}^2}{2m_0}, \quad (2.29)$$

$$\boldsymbol{\pi} = \mathbf{p} + \frac{\hbar}{4m_0 c^2} [\boldsymbol{\sigma} \times \nabla V(\mathbf{r})]. \quad (2.30)$$

The Hamiltonian (2.29) describes the bands as a set of free-electron dispersions which are displaced by their respective  $E_{n,\sigma}(\mathbf{0})$  and coupled by the term  $\hbar \mathbf{k} \cdot \boldsymbol{\pi}/m_0$ . The coupling to bands with higher energy  $E_{n',\sigma'}(\mathbf{0}) > E_{n,\sigma}(\mathbf{0})$  does generally lead to a larger or even negative effective mass while the coupling to bands with  $E_{n',\sigma'}(\mathbf{0}) < E_{n,\sigma}(\mathbf{0})$  reduces the effective mass.

For every  $\mathbf{k}$  in the Brillouin zone, the eigenstates of  $\mathcal{H}_{\mathbf{k},p}$  span the complete Hilbert space of all normalisable, lattice periodic functions. We may therefore take the solution at one point  $\mathbf{k}_0$  in reciprocal space and expand the Hamiltonian at any other point in the corresponding eigenstates. Many physical properties of semiconductors are governed by a few of the lowest conduction bands and highest valence bands in the vicinity of their respective minima and maxima. A common approach is therefore to expand the bands around these extrema perturbation theoretically. This will be the approach which will be discussed in this Section. The discussion will be restricted to the case of  $\text{Cu}_2\text{O}$ , i.e. an expansion around the  $\Gamma$ -point in a crystal with point group  $O_h$ . The derivation of the Suzuki-Hensel Hamiltonian [66] describing the  $\Gamma_5^+ \otimes \Gamma_6^+ = \Gamma_7^+ \oplus \Gamma_8^+$  valence bands as well as a Hamiltonian for the  $\Gamma_6^+ \oplus \Gamma_8^-$  conduction bands [67] of  $\text{Cu}_2\text{O}$  will be laid out in the following. Although the application of perturbation theory to strain is not as straightforward [68], the influence of strain on the band structure can be described by effective Hamiltonians derived in the same manner as the  $\mathbf{k} \cdot \mathbf{p}$  Hamiltonians. Strain and its influence on the valence band of  $\text{Cu}_2\text{O}$  will be discussed in detail in Chapter 4.

The expansion of  $\mathcal{H}_{\mathbf{k},p}$  around  $\mathbf{k} = \mathbf{0}$  in second-order degenerate perturbation theory results in

$$\begin{aligned} \mathcal{H}_{n,n'}(\mathbf{k}) &= E_n(\mathbf{0}) \delta_{n,n'} + \frac{\hbar}{m_0} \langle u_{n,0} | \mathbf{k} \cdot \boldsymbol{\pi} | u_{n',0} \rangle \\ &+ \frac{\hbar^2}{m_0^2} \sum_{n'' \neq n,n'} \Delta_{n''}^{-1} \langle u_{n,0} | \mathbf{k} \cdot \boldsymbol{\pi} | u_{n'',0} \rangle \langle u_{n'',0} | \mathbf{k} \cdot \boldsymbol{\pi} | u_{n',0} \rangle, \end{aligned} \quad (2.31)$$

where  $n$  and  $n'$  denote eigenstates of  $\mathcal{H}$  with energies  $E_n(\mathbf{0}) \approx E_{n'}(\mathbf{0})$  and

$$\Delta_{n''}^{-1} = \frac{1}{2} \left[ \frac{1}{E_n(\mathbf{0}) - E_{n''}(\mathbf{0})} + \frac{1}{E_{n'}(\mathbf{0}) - E_{n''}(\mathbf{0})} \right]. \quad (2.32)$$

For the conciseness of the notation, the spin state has been omitted. In crystals with inversion symmetry, only terms with either even or odd order in  $\mathbf{k}$  may be nonzero simultaneously, based on the parity of the states  $|u_{n,0}\rangle$  and  $|u_{n',0}\rangle$ . The intermediate states  $|u_{n'',0}\rangle$  include the states from all other eigenspaces, but based on the irreducible representations of the  $|u_{n,0}\rangle$  and  $|u_{n',0}\rangle$  only the states of certain irreducible representations can contribute nonzero terms. In the case of  $\text{Cu}_2\text{O}$ , for example, if  $|u_{n,0}\rangle$  and  $|u_{n',0}\rangle$  are understood to be  $\Gamma_7^+$  and  $\Gamma_8^+$  valence-band states respectively, the irreducible representations of the intermediate states must be contained in both  $\Gamma_4^- \otimes \Gamma_7^+ = \Gamma_7^- \oplus \Gamma_8^-$  and  $\Gamma_4^- \otimes \Gamma_8^+ = \Gamma_6^- \oplus \Gamma_7^- \oplus 2\Gamma_8^-$ , limiting the intermediate states to  $\Gamma_7^- \oplus \Gamma_8^-$ . The irreducible representation  $\Gamma_4^-$  describes all polar vector operators, in this case  $\boldsymbol{\pi}$ .

The simplest approach to derive an effective Hamiltonian from Eq. (2.31) would be the application of the Wigner-Eckart theorem (2.10). We will, however, discuss another approach here, called the **method of invariants** [58, 59]. It requires that the effective Hamiltonian is symmetric with respect to the point group symmetries<sup>10</sup>  $\alpha$ , i.e.

$$\mathcal{H}(\mathcal{K}) = \mathcal{D}(\alpha) \cdot \mathcal{H}(\alpha^{-1}\mathcal{K}) \cdot \mathcal{D}^{-1}(\alpha), \quad (2.33)$$

where the  $\mathcal{D}(\alpha)$  are the unitary representation matrices transforming the basis and  $\mathcal{K}$  is some set of parameters the Hamiltonian depends on (e.g.  $\mathbf{k}$  or the strain tensor  $\epsilon$ ) transforming like the representation  $\Lambda_{\mathcal{K}}$ . If the representation of the basis is reducible  $\Lambda_b = \Gamma_i \oplus \Gamma_j$ , Eq. (2.33) can be broken down into the subspaces corresponding to the irreducible representations via

$$\mathcal{H}(\mathcal{K}) = \begin{pmatrix} \mathcal{H}_{\Gamma_i, \Gamma_i}(\mathcal{K}) & \mathcal{H}_{\Gamma_i, \Gamma_j}(\mathcal{K}) \\ \mathcal{H}_{\Gamma_j, \Gamma_i}(\mathcal{K}) & \mathcal{H}_{\Gamma_j, \Gamma_j}(\mathcal{K}) \end{pmatrix} \quad \text{and} \quad \mathcal{D}(\alpha) = \begin{pmatrix} \mathcal{D}_{\Gamma_i}(\alpha) & \mathbf{0} \\ \mathbf{0} & \mathcal{D}_{\Gamma_j}(\alpha) \end{pmatrix}. \quad (2.34)$$

For a Hamiltonian in an  $N$ -dimensional Hilbert space with a basis transforming like the (reducible) representation  $\Lambda_b$ , there are  $N^2$  linearly independent basis matrices  $\mathbf{X}_i$  transforming like  $\Lambda_b \otimes \Lambda_b$

$$\mathcal{D}_{\Lambda_b}(\alpha) \cdot \mathbf{X}_i \cdot \mathcal{D}_{\Lambda_b}^{-1}(\alpha) = \sum_j [\mathcal{D}_{\Lambda_b \otimes \Lambda_b}(\alpha)]_{i,j} \mathbf{X}_j. \quad (2.35)$$

The linearly independent components of both the basis matrices and  $\mathcal{K}$  can be chosen to transform according to the rows of the irreducible representations, written as  $\mathbf{X}_i^\Gamma$  and  $\mathcal{K}_i^\Gamma$ , respectively. An effective Hamiltonian  $\mathcal{H}(\mathcal{K})$  fulfilling Eq. (2.33) can then be constructed via

$$\mathcal{H}(\mathcal{K}) = \sum_{\Gamma} a_{\Gamma} \sum_i \mathbf{X}_i^{\Gamma} \mathcal{K}_i^{\Gamma}, \quad (2.36)$$

where  $\Gamma$  is any irreducible representation appearing in both  $\Lambda_b \otimes \Lambda_b$  and  $\Lambda_{\mathcal{K}}$ ,  $i$  sums over the rows of  $\Gamma$  and the  $a_{\Gamma}$  are free parameters which are assumed to be real. The Hamiltonian has to satisfy two additional constraints namely hermiticity and time-inversion symmetry

$$\mathcal{H}(\mathcal{K}) = \mathcal{H}^{\dagger}(\mathcal{K}), \quad (2.37)$$

$$\mathbf{T}^{-1} \cdot \mathcal{H}(f\mathcal{K}) \cdot \mathbf{T} = \mathcal{H}^*(\mathcal{K}), \quad (2.38)$$

where  $\mathbf{T}$  denotes the matrix applying the antiunitary<sup>11</sup> time-inversion operator  $\mathcal{T}$  to the basis and  $f = \pm 1$  depending on whether  $\mathcal{K}$  is symmetric or antisymmetric under time inversion. The angular

<sup>10</sup>This must be true for all elements  $\alpha$  of the point group. It does, however, suffice to enforce it for a set of generators of the group as the symmetry with respect to all other elements follows automatically.

<sup>11</sup>The antiunitarity of the operator  $\mathcal{T}$  implies  $\langle \mathcal{T}\phi | \mathcal{T}\psi \rangle = \langle \phi | \psi \rangle^* = \langle \psi | \phi \rangle$  for all  $|\phi\rangle$  and  $|\psi\rangle$ .

momenta as well as the linear momenta are odd with respect to time inversion  $\mathcal{T}(\mathbf{I}, \boldsymbol{\sigma}, \mathbf{p}, \mathbf{k}) = -(\mathbf{I}, \boldsymbol{\sigma}, \mathbf{p}, \mathbf{k})\mathcal{T}$ , the position operator as well as the crystal Hamiltonian are even  $\mathcal{T}(\mathcal{H}, \mathbf{r}) = (\mathcal{H}, \mathbf{r})\mathcal{T}$ . Hermiticity can be enforced by the choice of hermitian basis matrices and Eq. (2.38) may exclude certain terms in Eq. (2.36) if the basis matrices behave differently than  $\mathcal{K}$  under time inversion, i.e. if they do not fulfil

$$\mathbf{T}^{-1} \cdot \mathbf{X}_i^\Gamma \cdot \mathbf{T} = f \mathbf{X}_i^{\Gamma*}. \quad (2.39)$$

### Suzuki-Hensel Hamiltonian

The Suzuki-Hensel Hamiltonian [66] describes the valence bands of germanium, which crystallises in the diamond structure belonging to the same point group as the space group of  $\text{Cu}_2\text{O}$ . As is the case for germanium, the uppermost valence bands of  $\text{Cu}_2\text{O}$  are formed from a threefold degenerate set of atomic orbitals transforming like  $\Gamma_5^+$  at the  $\Gamma$ -point. This manifold is split up into six bands transforming like  $\Gamma_5^+ \otimes \Gamma_6^+ = \Gamma_7^+ \oplus \Gamma_8^+$  by spin-orbit interaction when the spin degrees of freedom ( $\Gamma_6^+$ ) are taken into account. As all basis states have the same parity, only terms of even order in  $\mathbf{k}$  may contribute to the Hamiltonian. This Section will investigate the terms of zeroth order and second order in  $\mathbf{k}$ .

The 36 linearly independent basis matrices can be constructed from the outer products of the 9 matrices  $\{I_x, I_y, I_z, I_x^2, I_y^2, I_z^2, \{I_y, I_z\}, \{I_z, I_x\}, \{I_x, I_y\}\}$  for the  $\Gamma_5^+$  Hilbert space and the 4 matrices  $\{\mathbf{1}_\sigma, \sigma_x, \sigma_y, \sigma_z\}$  for  $\Gamma_6^+$ . The bracketed terms denote the symmetrised product

$$\{I_x, I_y\} = \frac{1}{2} (I_x I_y + I_y I_x) \quad (2.40)$$

and the angular momentum matrices  $\mathbf{I}$  for spin  $\ell = 1$  are hermitian matrices fulfilling the commutation relation of angular momentum operators  $\mathbf{I} \times \mathbf{I} = i\mathbf{I}$  as well as  $\mathbf{I}^2 = \ell(\ell + 1)\mathbf{1}_I$ . They can be defined by [69]

$$I_x = \begin{pmatrix} 0 & 0 & 0 \\ 0 & 0 & -i \\ 0 & i & 0 \end{pmatrix}, \quad I_y = \begin{pmatrix} 0 & 0 & i \\ 0 & 0 & 0 \\ -i & 0 & 0 \end{pmatrix}, \quad I_z = \begin{pmatrix} 0 & -i & 0 \\ i & 0 & 0 \\ 0 & 0 & 0 \end{pmatrix}. \quad (2.41)$$

These matrices were chosen with respect to a time inversion symmetric (i.e. real) basis guaranteeing that the time-inversion operation consists only of a complex conjugation  $I_i^* = -I_i$  due to  $\mathbf{T} = \mathbf{1}$ .

The three spin matrices  $\{I_x, I_y, I_z\}$  transform like an axial vector (i.e.  $\Gamma_4^+$ ), irrespectively of whether their basis is understood to transform like any of the irreducible representations  $\Gamma_{4/5}^\pm$ . This is guaranteed by the fact that all four representations are mutually connected by the multiplication

with a one-dimensional representation (e.g.  $\Gamma_5^+ = \Gamma_2^- \otimes \Gamma_4^-$ )

$$\begin{aligned} \mathcal{D}_{\Gamma_5^+}(\alpha) \cdot I_i \cdot \mathcal{D}_{\Gamma_5^+}^{-1}(\alpha) &= \left[ \mathcal{D}_{\Gamma_2^-}(\alpha) \otimes \mathcal{D}_{\Gamma_4^-}(\alpha) \right] \cdot I_i \cdot \left[ \mathcal{D}_{\Gamma_2^-}^{-1}(\alpha) \otimes \mathcal{D}_{\Gamma_4^-}^{-1}(\alpha) \right] \\ &= \mathcal{D}_{\Gamma_4^-}(\alpha) \cdot I_i \cdot \mathcal{D}_{\Gamma_4^-}^{-1}(\alpha) = \sum_j \left[ \mathcal{D}_{\Gamma_4^-}(\alpha) \right]_{i,j} I_j. \end{aligned} \quad (2.42)$$

The intermediate step made use of the fact that  $\Gamma_2^-$  is one-dimensional and  $\mathcal{D}_{\Gamma_2^-}(\alpha)$  thus just a complex scalar. The Hamiltonian we will derive will therefore be applicable to all sets of bands transforming like  $\Gamma_{6/7}^\pm \oplus \Gamma_8^\pm$ .

Table 2.3 gives all symmetrised basis matrices up to second order in the angular momentum matrices as well as all terms of second order in  $\mathbf{k}$ . We will start by constructing a Hamiltonian for a scalar  $\mathcal{K}$  (transforming like  $\Gamma_1^+$ )

$$\mathcal{H}_{\text{so}} = E_0 - \frac{1}{3} \Delta_{\text{so}} \mathbf{I} \cdot \boldsymbol{\sigma}. \quad (2.43)$$

The free parameter  $E_0$  is an offset to the complete Hamiltonian, not explicitly given in Ref. [66], while  $\Delta_{\text{so}}$  is called the **spin-orbit splitting** and defines the splitting between the  $\Gamma_7^+$  and  $\Gamma_8^+$  valence bands at the  $\Gamma$ -point. The spin-orbit term can be rewritten via

$$\mathbf{I} \cdot \boldsymbol{\sigma} = \mathbf{J}^2 - \mathbf{I}^2 - \frac{\boldsymbol{\sigma}^2}{4} = \mathbf{J}^2 - \frac{11}{4} \quad (2.44)$$

where  $\mathbf{J} = \mathbf{I} + \boldsymbol{\sigma}/2$  denotes the total angular momentum.  $\mathbf{J}^2$  has two eigenspaces corresponding to spins of  $J = 1/2$  ( $\hat{=}\Gamma_7^+$ ) and  $J = 3/2$  ( $\hat{=}\Gamma_8^+$ ) with eigenvalues  $J(J+1)$ , i.e.  $3/4$  and  $15/4$  respectively. Hence, the eigenvalues of  $\mathcal{H}_{\text{so}}$  are  $E_0 + 2\Delta_{\text{so}}/3$  and  $E_0 - \Delta_{\text{so}}/3$ .

		$k^{(2)}$	$I^{(2)}$	$I\sigma$	$\sigma$
$\Gamma_1^+$	1	$\mathbf{k}^2$	$\mathbf{1}_I \propto \mathbf{I}^2$	$\mathbf{I} \cdot \boldsymbol{\sigma}$	$\mathbf{1}_\sigma \propto \boldsymbol{\sigma}^2$
$\Gamma_3^+$	$z^2$	$3k_z^2 - \mathbf{k}^2$	$3I_z^2 - \mathbf{I}^2$	$3I_z\sigma_z - \mathbf{I} \cdot \boldsymbol{\sigma}$	
	$x^2 - y^2$	$\sqrt{3}(k_x^2 - k_y^2)$	$\sqrt{3}(I_x^2 - I_y^2)$	$\sqrt{3}(I_x\sigma_x - I_y\sigma_y)$	
$\Gamma_4^+$	$x$	$[k_y, k_z] \propto B_x$	$I_x \propto [I_y, I_z]$	$I_y\sigma_z - I_z\sigma_y$	$\sigma_x$
	$y$	$[k_z, k_x] \propto B_y$	$I_y \propto [I_z, I_x]$	$I_z\sigma_x - I_x\sigma_z$	$\sigma_y$
	$z$	$[k_x, k_y] \propto B_z$	$I_z \propto [I_x, I_y]$	$I_x\sigma_y - I_y\sigma_x$	$\sigma_z$
$\Gamma_5^+$	$yz$	$\{k_y, k_z\}$	$\{I_y, I_z\}$	$I_y\sigma_z + I_z\sigma_y$	
	$zx$	$\{k_z, k_x\}$	$\{I_z, I_x\}$	$I_z\sigma_x + I_x\sigma_z$	
	$xy$	$\{k_x, k_y\}$	$\{I_x, I_y\}$	$I_x\sigma_y + I_y\sigma_x$	

**Table 2.3.:** Symmetrised components of the basis matrices and terms of second order in  $\mathbf{k}$ . Note, that there are also linearly independent basis matrices of order  $I^{(2)}\sigma$ , not given here.

The terms of second order in  $\mathbf{k}$  transform like  $\Gamma_4^- \otimes \Gamma_4^- = \Gamma_1^+ \oplus \Gamma_3^+ \oplus \Gamma_4^+ \oplus \Gamma_5^+$  where  $\Gamma_4^+$  corresponds to the commutator  $\mathbf{k} \times \mathbf{k}$  which vanishes in the absence of a magnetic field. As all the other terms are even under time inversion only those basis matrices which are themselves even under time inversion can contribute, i.e. all terms of even order in the angular momentum matrices. The resulting  $\mathbf{k}$ -dependent Hamiltonian is therefore

$$\begin{aligned} \mathcal{H}(\mathbf{k}) = & \frac{\hbar^2}{2m_0} \left\{ [A_1 + B_1 (\mathbf{I} \cdot \boldsymbol{\sigma})] \mathbf{k}^2 \right. \left. \left| \Gamma_1^+ \right. \right. \\ & + \left[ A_2 \left( I_x^2 - \frac{1}{3} \mathbf{I}^2 \right) + B_2 \left( I_x \sigma_x - \frac{1}{3} \mathbf{I} \cdot \boldsymbol{\sigma} \right) \right] k_x^2 + \text{c.p.} \left. \left| \Gamma_3^+ \right. \right. \\ & + \left. \left. [A_3 (I_y I_z + I_z I_y) + B_3 (I_y \sigma_z + I_z \sigma_y)] \{k_y, k_z\} + \text{c.p.} \right\} \left| \Gamma_5^+ \right. \right. \end{aligned} \quad (2.45)$$

where c.p. denotes the cyclically permuted terms and the  $A_i$  and  $B_i$  are free parameters. In most materials, the  $A_i$  are dominant and the  $B_i$  yield only minor corrections. The Hamiltonian describes a set of six bands consisting of three sets of two bands which are degenerate over the whole Brillouin zone. This degeneracy is a consequence of the combination of inversion symmetry  $\mathcal{I}$  inherent in  $O_h$  and the time-inversion symmetry, whose combination implies that there are two degenerate states  $\mathcal{I}|u_{n,\sigma,\mathbf{k}}\rangle = |u_{n,\sigma,-\mathbf{k}}\rangle$  and  $\mathcal{T}|u_{n,\sigma,\mathbf{k}}\rangle = |u_{n,-\sigma,-\mathbf{k}}\rangle$  for every state  $|u_{n,\sigma,\mathbf{k}}\rangle$ . The degeneracy due to time inversion is called **Kramers degeneracy** [70, 71].

In the presence of a magnetic field  $\mathbf{B}$  the commutator of the quasi-momentum takes the form

$$\mathbf{k} \times \mathbf{k} = \frac{e\mathbf{B}}{i\hbar} \quad (2.46)$$

which follows from the minimal coupling substitution  $\hbar\mathbf{k} \mapsto \hbar\mathbf{k} + e\mathbf{A}$ . As time inversion flips the angular as well as the magnetic momenta, the interaction with an external magnetic field is antisymmetric with respect to time inversion and breaks the time-inversion symmetry of the Hamiltonian. Therefore, only odd orders of the angular momentum operators may contribute to Eq. (2.36) and the resulting magnetic Hamiltonian is

$$\begin{aligned} \mathcal{H}(\mathbf{B}) = & \frac{e\hbar}{m_0} \left\{ A_4 I_x + B_4 \sigma_x + B'_4 \left( I_x^2 - \frac{1}{3} \mathbf{I}^2 \right) \sigma_x \right. \\ & \left. + B''_4 (\{I_x, I_y\} \sigma_y + \{I_x, I_z\} \sigma_z) \right\} B_x + \text{c.p.} . \end{aligned} \quad (2.47)$$

The two terms of order  $I^{(2)}\sigma$  are not listed in Tab. 2.3 and are only given here for completeness as they yield only minor corrections and are not relevant to the remainder of this thesis.

### Conduction bands

The lowermost conduction bands of Cu<sub>2</sub>O transform according to the representations  $\Gamma_6^+$  and  $\Gamma_8^-$ . As these two bands have opposing parity, they cannot be treated in a pseudo-spin formalism as we used for the valence bands. We will therefore derive the Hamiltonian in the two sub spaces as well as the cross space separately

$$\mathcal{H}(\mathbf{k}) = \begin{pmatrix} \mathcal{H}_6(\mathbf{k}) & \mathcal{H}_{6,8}^\dagger(\mathbf{k}) \\ \mathcal{H}_{6,8}(\mathbf{k}) & \mathcal{H}_8(\mathbf{k}) \end{pmatrix}. \quad (2.48)$$

The 16 linearly independent matrices for the  $\Gamma_8^-$  Hilbert space can be expressed via the powers

$$\begin{aligned} & \mathbf{1}_J, \quad J_x, \quad J_y, \quad J_z, \quad J_x^2, \quad J_y^2, \quad \{J_x, J_y\}, \quad \{J_y, J_z\}, \quad \{J_z, J_x\}, \quad \{J_y^2 - J_z^2, J_x\}, \\ & \{J_z^2 - J_x^2, J_y\}, \quad \{J_x^2 - J_y^2, J_z\}, \quad J_x^3, \quad J_y^3, \quad J_z^3, \quad J_x J_y J_z + J_z J_y J_x, \end{aligned} \quad (2.49)$$

of the spin-3/2 angular momentum matrices [69]

$$J_x = \begin{pmatrix} 0 & \frac{\sqrt{3}}{2} & 0 & 0 \\ \frac{\sqrt{3}}{2} & 0 & 1 & 0 \\ 0 & 1 & 0 & \frac{\sqrt{3}}{2} \\ 0 & 0 & \frac{\sqrt{3}}{2} & 0 \end{pmatrix}, \quad J_y = \begin{pmatrix} 0 & \frac{\sqrt{3}i}{2} & 0 & 0 \\ -\frac{\sqrt{3}i}{2} & 0 & i & 0 \\ 0 & -i & 0 & \frac{\sqrt{3}i}{2} \\ 0 & 0 & -\frac{\sqrt{3}i}{2} & 0 \end{pmatrix}, \quad J_z = \begin{pmatrix} -\frac{3}{2} & 0 & 0 & 0 \\ 0 & -\frac{1}{2} & 0 & 0 \\ 0 & 0 & \frac{1}{2} & 0 \\ 0 & 0 & 0 & \frac{3}{2} \end{pmatrix}. \quad (2.50)$$

The terms up to second order in these matrices transform just like the equivalent components of  $\mathbf{I}$  in Tab. 2.3. The resulting Hamiltonian thus takes the form

$$\begin{aligned} \mathcal{H}_8(\mathbf{k}) = E_8 + \frac{\hbar^2}{2m_0} & \left\{ A_8 \mathbf{k}^2 + A'_8 \left( \left[ J_x^2 - \frac{1}{3} \mathbf{J}^2 \right] k_x^2 + \text{c.p.} \right) \right. \\ & \left. + A''_8 (\{J_x, J_y\} \{k_x, k_y\} + \text{c.p.}) \right\}. \end{aligned} \quad (2.51)$$

This is equivalent to the well-known Luttinger Hamiltonian [69] or the projection of the Suzuki-Hensel Hamiltonian onto the  $\Gamma_8^+$  subspace.

The four linearly independent matrices in the  $\Gamma_6^+$  Hilbert-space transforming like  $\Gamma_6^+ \otimes \Gamma_6^+ = \Gamma_1^+ \oplus \Gamma_4^+$  can again be chosen as  $\{\mathbf{1}_\sigma, \sigma_x, \sigma_y, \sigma_z\}$ . In the absence of a magnetic field, the quadratic terms in  $\mathbf{k}$  contain no terms transforming like  $\Gamma_4^+$  and the Hamiltonian may only consist of basis matrices transforming like  $\Gamma_1^+$  yielding

$$\mathcal{H}_6(\mathbf{k}) = E_6 + \frac{\hbar^2 \mathbf{k}^2}{2m_0} A_6. \quad (2.52)$$

It is sufficient for most applications to treat the  $\Gamma_6^+$  conduction band by itself as the isotropic, parabolic band described by  $\mathcal{H}_6(\mathbf{k})$ .

For the cross space, only odd orders of  $\mathbf{k}$  may contribute as the two eigenspaces have opposing parity, and we will restrict the discussion to terms linear in  $\mathbf{k}$ . The wave vector transforms according to  $\Gamma_4^-$ , therefore only the one corresponding set of three basis matrices appearing in  $\Gamma_8^- \otimes \Gamma_6^+ = \Gamma_3^- \oplus \Gamma_4^- \oplus \Gamma_5^-$  may contribute to the Hamiltonian. These matrices can be expressed as [50]

$$U_x = i \begin{pmatrix} -\sqrt{\frac{1}{2}} & 0 \\ 0 & -\sqrt{\frac{1}{6}} \\ \sqrt{\frac{1}{6}} & 0 \\ 0 & \sqrt{\frac{1}{2}} \end{pmatrix}, \quad U_y = \begin{pmatrix} \sqrt{\frac{1}{2}} & 0 \\ 0 & \sqrt{\frac{1}{6}} \\ \sqrt{\frac{1}{6}} & 0 \\ 0 & \sqrt{\frac{1}{2}} \end{pmatrix}, \quad U_z = -i \begin{pmatrix} 0 & 0 \\ \sqrt{\frac{2}{3}} & 0 \\ 0 & \sqrt{\frac{2}{3}} \\ 0 & 0 \end{pmatrix}, \quad (2.53)$$

where the two columns correspond to  $\{|\Gamma_7^+, -1/2\rangle, |\Gamma_7^+, 1/2\rangle\}$  from left to right and the four rows correspond to  $\{|\Gamma_8^-, -3/2\rangle, |\Gamma_8^-, -1/2\rangle, |\Gamma_8^-, 1/2\rangle, |\Gamma_8^-, 3/2\rangle\}$  from top to bottom. Finally, the cross-space Hamiltonian can be expressed as

$$\mathcal{H}_{6,8}(\mathbf{k}) = \frac{\hbar}{m_0} B_{6,8} \mathbf{U} \cdot \mathbf{k}. \quad (2.54)$$

### 2.2.3. Excitons

The fundamental electronic absorption process in a semiconductor elevates one electron from a valence band to a conduction band, creating a hole and a (quasiparticle) electron. For a complete description of this process, the mutual interaction of these two quasiparticles due to their opposing charge has to be included. For large separations  $|\mathbf{r}_e - \mathbf{r}_h| \gg a_g$ , the interaction can be modelled by an effective Coulomb potential

$$V_c(|\mathbf{r}_e - \mathbf{r}_h|) = -\frac{e^2}{4\pi\epsilon} \frac{1}{|\mathbf{r}_e - \mathbf{r}_h|}, \quad (2.55)$$

with the crystal permittivity  $\epsilon = \epsilon_0 \epsilon_r$ . In the simplest model, called the **effective mass approximation**, only one set of valence and conduction band is taken into account and the bands are approximated by parabolas  $\mathbf{p}^2/(2m^*)$  around their respective extrema. The dynamics of the electron-hole pair are then described by the Schrödinger equation

$$\left[ E_g + \frac{\mathbf{p}_e^2}{2m_e^*} + \frac{\mathbf{p}_h^2}{2m_h^*} + V_c(|\mathbf{r}_e - \mathbf{r}_h|) \right] \Psi(\mathbf{r}_e, \mathbf{r}_h) = E \Psi(\mathbf{r}_e, \mathbf{r}_h), \quad (2.56)$$



whose bound states are called **Wannier excitons** [12]. It can be decoupled into

$$\frac{\mathbf{P}^2}{2M} \psi(\mathbf{R}) = E_{\text{COM}} \psi(\mathbf{R}), \quad (2.57)$$

$$\left[ \frac{\mathbf{p}^2}{2\mu} + V_c(r) \right] \phi(\mathbf{r}) = E_b \phi(\mathbf{r}), \quad (2.58)$$

via a transformation to the center-of-mass (COM) coordinates  $(\mathbf{P}, \mathbf{R})$  and the relative coordinates  $(\mathbf{p}, \mathbf{r})$

$$\begin{pmatrix} \mathbf{P} \\ \mathbf{R} \end{pmatrix} = \begin{pmatrix} \mathbf{p}_e + \mathbf{p}_h \\ \alpha \mathbf{r}_e + \beta \mathbf{r}_h \end{pmatrix}, \quad \begin{pmatrix} \mathbf{p} \\ \mathbf{r} \end{pmatrix} = \begin{pmatrix} \beta \mathbf{p}_e - \alpha \mathbf{p}_h \\ \mathbf{r}_e - \mathbf{r}_h \end{pmatrix}. \quad (2.59)$$

Here,  $\alpha = m_e^*/M$  and  $\beta = m_h^*/M$  denote the relative effective masses,  $M = m_e^* + m_h^*$  the excitonic mass and  $\mu = m_e^* m_h^*/M$  the reduced effective mass.

Equation (2.57) models the dynamics of the excitonic COM as a free particle of mass  $M$ . Equation (2.58), called the **Wannier equation**, describes the dynamics of the relative degrees of freedom and is structurally equivalent to the Schrödinger equation of the hydrogen atom. Its bound states do hence form a Rydberg series with binding energies  $E_b = -Ry^* n^{-2}$  depending on the principal quantum number  $n$  and the effective Rydberg ( $Ry = 13.6 \text{ eV}$  being the hydrogenic Rydberg)

$$Ry^* = \frac{\mu e^4}{8 \varepsilon^2 \hbar^2} = \frac{\mu}{m_0} \frac{Ry}{\varepsilon_r^2}. \quad (2.60)$$

These bound states appear in the absorption spectra as a series of resonances below the band gap and can be labelled by the same quantum numbers as the states of the hydrogen atom, namely the **principal quantum number**  $n$ , the **orbital quantum number**  $\ell$ , the **magnetic quantum number**  $m$  and the COM wave vector  $\mathbf{K}$ . The eigenenergies of Eq. (2.56) are then given by

$$E_{n,\ell,m}(\mathbf{K}) = E_g + \frac{\hbar^2 \mathbf{K}^2}{2M} - \frac{Ry^*}{n^2}. \quad (2.61)$$

Corrections to the effective mass approximation arise, for example, due to polaronic corrections to the interaction potential [72], the nonparabolic and anisotropic bands [25, 73], the electron-hole exchange interaction [74, 75] and possibly the coupling between excitonic series [28, 73]. Collectively, these corrections are often referred to as the **central-cell corrections** as they tend to be most relevant for small electron-hole separations  $|\mathbf{r}_e - \mathbf{r}_h| \sim a_g$ .

The wave functions derived from Eqs. (2.57-2.58) are the quasiparticle wave-functions. In the many-body picture the corresponding states take the form

$$|\Psi_{n,\ell,m}(\mathbf{K})\rangle = \sum_{\mathbf{k}} \tilde{\phi}_{n,\ell,m}(\mathbf{k}) b_{v,\beta}^{\dagger} \mathbf{K}-\mathbf{k} a_{c,\alpha}^{\dagger} \mathbf{K}+\mathbf{k} |\Phi_{\text{vac}}\rangle, \quad (2.62)$$

where v and c denote the valence and conduction band,  $b_{v,q}^{\dagger} = a_{v,-q}$  is the hole creation operator<sup>12</sup> and

$$\tilde{\phi}_{n,\ell,m}(\mathbf{k}) = \sqrt{\frac{1}{\Omega}} \int_{\Omega} d^3\mathbf{r} e^{-i\mathbf{k}\cdot\mathbf{r}} \phi_{n,\ell,m}(\mathbf{r}) \quad (2.63)$$

denotes the **envelope function**, i.e. the momentum-space wave function<sup>13</sup> corresponding to the solution  $\phi_{n,\ell,m}(\mathbf{r})$  of Eq. (2.58). In more sophisticated models such as those discussed in Chapter 3, the relative and COM coordinates do not decouple and the envelope functions will depend on  $\mathbf{K}$  as well. At  $\mathbf{K} = \mathbf{0}$ , the excitonic states do nonetheless transform according to irreducible representations of the point group, namely those contained in  $\Lambda_X = \Gamma_v \otimes \Gamma_c \otimes \Gamma_{\text{env}}$ . Here,  $\Gamma_{c/v}$  denote the irreducible representations of the band states at the  $\Gamma$ -point and  $\Gamma_{\text{env}}$  the one of the envelope function.

### Excitonic absorption

The light-matter interaction operator in the two-band picture, dipole approximation and ignoring the diamagnetic term can be written as

$$\frac{e}{m_0} \mathbf{A} \cdot \boldsymbol{\pi} = \frac{e}{m_0} \mathbf{A} \cdot \sum_{\mathbf{q}} \langle v, \mathbf{q} | \boldsymbol{\pi} | c, \mathbf{q} \rangle b_{v,-\mathbf{q}} a_{c,\mathbf{q}} + \text{h.c.} \quad (2.65)$$

where h.c. denotes the hermitian conjugate,  $\mathbf{A}$  the spatially homogeneous vector potential and  $\langle v, \mathbf{q} | \boldsymbol{\pi} | c, \mathbf{q} \rangle$  the matrix element of the pure Bloch states. The transition matrix element from the crystal vacuum to the excitonic state (2.62) does then take the form [76]

$$\langle \Phi_{\text{vac}} | \boldsymbol{\pi} | \Psi_{n,\ell,m}(\mathbf{K}) \rangle = -\delta_{\mathbf{K},\mathbf{0}} \sum_{\mathbf{k}} \tilde{\phi}_{n,\ell,m}(\mathbf{k}) \langle v, \mathbf{k} | \boldsymbol{\pi} | c, \mathbf{k} \rangle. \quad (2.66)$$

<sup>12</sup>The spin degrees of freedom have been omitted for conciseness. In order to include them, see the transformations in Tab. 2.1.

<sup>13</sup>The inverse transformation is given by

$$\phi_{n,\ell,m}(\mathbf{r}) = \sqrt{\frac{1}{\Omega}} \sum_{\mathbf{k}} e^{i\mathbf{k}\cdot\mathbf{r}} \tilde{\phi}_{n,\ell,m}(\mathbf{k}). \quad (2.64)$$

Depending on the properties of the inter-band matrix element  $\langle v, \mathbf{k} | \pi | c, \mathbf{k} \rangle$  around  $\mathbf{k} = \mathbf{0}$ , there are two different cases to distinguish. If the transition is **allowed** it can be approximated by a constant  $\langle v, \mathbf{k} | \pi | c, \mathbf{k} \rangle \approx C$ , in which case the transition matrix element takes the form

$$\langle \Phi_{\text{vac}} | \pi | \Psi_{n,\ell,m}(\mathbf{0}) \rangle = -C \sum_{\mathbf{k}} \tilde{\phi}_{n,\ell,m}(\mathbf{k}) = -\sqrt{\Omega} C \phi_{n,\ell,m}(\mathbf{0}). \quad (2.67)$$

As only the  $S$ -excitons (i.e.  $\ell = 0$ ) have a nonzero  $\phi_{n,\ell,m}(\mathbf{0})$ , only these may contribute to the one-photon dipole absorption and the transition is said to be of **first kind**.

If the transition is forbidden, one can approximate  $\langle v, \mathbf{k} | \pi | c, \mathbf{k} \rangle \approx \hbar \mathbf{M} \cdot \mathbf{k}$ , with some state-dependent  $\mathbf{M} \in \mathbb{C}^{3 \times 3}$ , resulting in

$$\langle \Phi_{\text{vac}} | \pi | \Psi_{n,\ell,m}(\mathbf{0}) \rangle = -\hbar \mathbf{M} \cdot \sum_{\mathbf{k}} \mathbf{k} \tilde{\phi}_{n,\ell,m}(\mathbf{k}) = i\sqrt{\Omega} \hbar \mathbf{M} \cdot [\nabla \phi_{n,\ell,m}(\mathbf{r})|_{\mathbf{r}=\mathbf{0}}]. \quad (2.68)$$

This matrix element can only be nonzero for  $P$ -excitons (i.e.  $\ell = 1$ ) and the transition is said to be of **second kind**. Both  $C$  and  $\mathbf{M}$  can be derived up to a few free parameters (in many cases only one) by the application of the Wigner-Eckart theorem (2.10). In materials with inversion symmetry, the transition is of first kind if the two relevant bands have opposing parity and of second kind if they have the same parity (as is the case for the main series of  $\text{Cu}_2\text{O}$ ).

One might be tempted to think that the dipole approximation breaks down for Rydberg excitons with spatial extensions on the order of the wavelength. The analysis does, however, show that substantial corrections do only arise when the wavelength becomes comparable to the lattice constant. Note also that the matrix elements (2.67) and (2.68) depend on the crystal volume  $\Omega$  which reflects the fact that the delocalised exciton can be created anywhere in the crystal and the rate of exciton creation is proportional to  $\Omega$ .

### 2.3. Cuprous oxide

Cuprous oxide crystallises in a simple cubic Bravais lattice with a lattice constant  $a_g = 0.427 \text{ nm}$  [77] and is built up from a fcc copper sublattice and a bcc oxygen sublattice (see. Fig. 2.4 (b) and (c)). The stoichiometry of the basis is  $\text{Cu}_4\text{O}_2$  and one particular choice for it is shown in Fig. 2.4 (a). The corresponding space group is  $O_h^4$ , which is nonsymmorphic and can be understood to consist of the product of all translations in the cubic Bravais lattice and the 48 symmetry elements  $\{\alpha, \tau\}$  given in App. B.1.

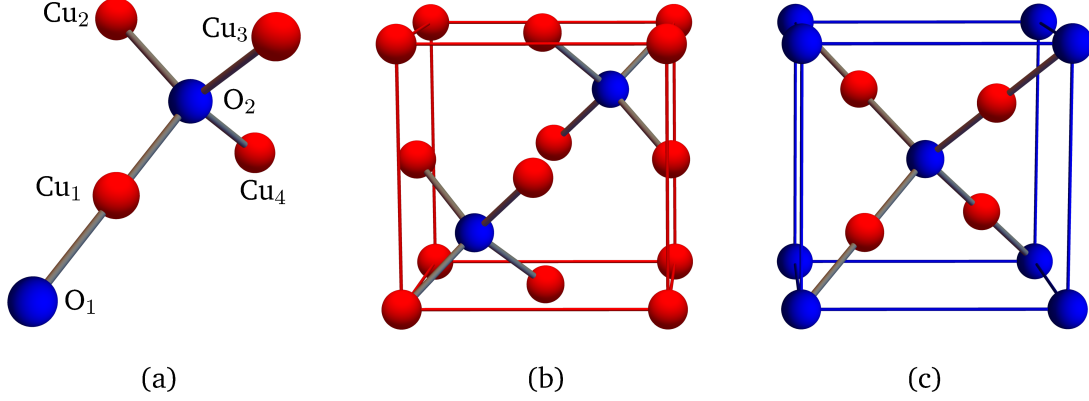


**Figure 2.4.:** (a): Possible choice for the basis of  $\text{Cu}_2\text{O}$ . Red spheres denote copper atoms, blue spheres oxygen atoms and grey lines bonds.  
 (b) and (c): Two valid choices for the primitive unit cell, showing the copper fcc lattice and the oxygen bcc lattice, respectively. The cubic frames are only guides to the eye.

### 2.3.1. Band structure

The oxygen and copper atoms contain 8 and 29 electrons in the configurations  $[\text{He}] 2s^2 2p^4$  and  $[\text{Ar}] 3d^{10} 4s^1$ , respectively. This implies that there are 132 electrons per primitive unit cell, 56 of which are valence electrons. One might expect that the uppermost valence bands and lowermost conduction bands are built up from the atomic orbitals of the valence electrons and indeed, the  $\Gamma_7^+ \oplus \Gamma_8^+$  valence bands are mostly built up from the copper  $3d$  levels [78, 79] and the  $\Gamma_6^+$  conduction band from the copper  $4s$  orbitals.

Figure 2.5 shows the two uppermost valence bands and the lowermost two conduction bands of  $\text{Cu}_2\text{O}$ , calculated via spin density-functional theory (sDFT) in generalised gradient approximation (GGA) [80]. As is often the case, the GGA underestimates the main band gap, resulting in 0.45 eV instead of 2.17208 eV. This shortcoming might be remedied by the use of better, more computationally intensive approximations, such as the GW approximation [81], which does reproduce the band gap of cuprous oxide. As the GGA reproduces the general structure of the bands quite well, we have opted to simply shift the conduction bands manually to give the correct experimental band gap. Note also that the gap between the two conduction bands is significantly overestimated with  $\sim 730$  meV compared to 450 meV [82].

The red dashed lines show the fits of the Hamiltonians derived in Sec. 2.2.2. The Suzuki-Hensel Hamiltonian for the valence bands uses the same parameters as given in Ref. [25] and Tab. A.1. As the gap between the conduction bands is not well reproduced by the sDFT calculations, the parameters given in Ref. [67] and Tab. A.1 do not fit the conduction bands shown here. The fit in Fig. 2.5 does therefore only serve illustrative purposes, the actual values used in the rest of this thesis were derived from fits over only a small part of Brillouin zone with a shifted  $\Gamma_8^-$  conduction band.

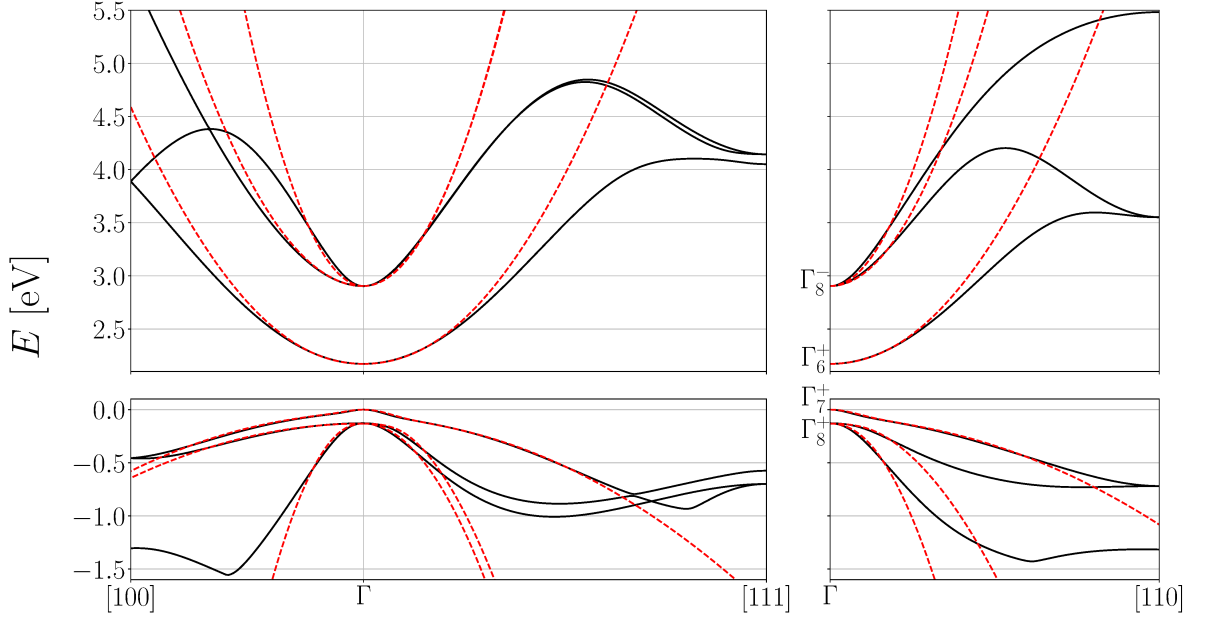


**Figure 2.5.:** Band structure of  $\text{Cu}_2\text{O}$  in the vicinity of the main band gap along the  $X \hat{=} [100]$ , the  $R \hat{=} [111]$  and the  $M \hat{=} [110]$  direction. The solid black lines show sDFT calculations [80] and the dashed red lines fits of the Hamiltonians from Sec. 2.2.2.

The effective masses of the  $\Gamma_7^+$  valence band and the  $\Gamma_6^+$  conduction band are  $m_h^*(\Gamma_7^+) = 0.556 m_0$  and  $m_e^*(\Gamma_6^+) = 0.99 m_0$ , respectively. The effective mass of the  $\Gamma_8$  bands is anisotropic and cannot even be expressed in terms of a second rank effective mass tensor. The averaged masses (both angularly and over the four sub bands) are well-defined and yield  $m_h^*(\Gamma_8^+) = 0.574 m_0$  and  $m_e^*(\Gamma_8^-) = 0.213 m_0$ .

### 2.3.2. Excitons

The sets of two conduction and valence bands form four excitonic series, the yellow ( $\Gamma_7^+ \otimes \Gamma_6^+$ ), the green ( $\Gamma_8^+ \otimes \Gamma_6^+$ ), the blue ( $\Gamma_7^+ \otimes \Gamma_8^-$ ) and the violet ( $\Gamma_8^+ \otimes \Gamma_8^-$ ). The main series is the yellow series, which was the first exciton series observed in any semiconductor [7, 8, 9] and the one in which the Rydberg excitons up to principal quantum numbers of  $n = 25$  [18] and orbital quantum numbers of  $\ell = 5$  [20] have been observed. Although the  $O(3)$  symmetry is broken in the cubic crystal environment of cuprous oxide, it is still a good approximation to label the yellow excitons by the orbital quantum number  $\ell$ . This is primarily owed to the fact that both bands contributing to this series have an isotropic effective mass, guaranteeing that for states with a momentum-space extension that is small compared to  $\pi/a_g$  (i.e.  $n \gtrsim 2$ ), the states with different  $\ell$  are only weakly coupled.

The records for the green, blue and violet series are still held by E. F. Gross and coworkers, who in their seminal works [8, 9] observed the green series up to  $n = 5$  and the blue and violet series

up to  $n = 2$ . S. Nikitine has claimed to have seen an additional red series with a limit below the main band gap at 2.038 eV [83] which is incongruent with the current understanding of the band structure of  $\text{Cu}_2\text{O}$ . Figure 2.6 shows a schematic of the exciton series and the bands they arise from.

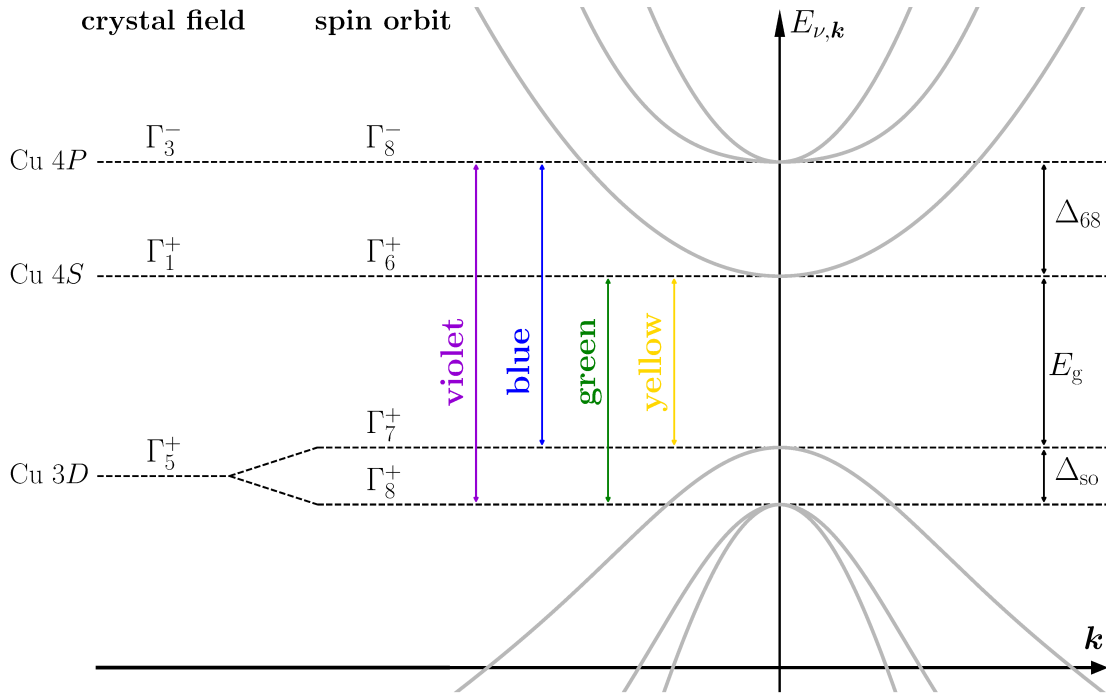


**Figure 2.6.:** Schematic of the four main exciton series in  $\text{Cu}_2\text{O}$  and the bands they arise from. Adapted from Refs. [84, 67].

One can easily derive selection rules based on the representations of the excitonic states given by  $\Gamma_v \otimes \Gamma_c \otimes \Gamma_{\text{env}}$ . The electric dipole operator is a polar vector operator transforming like  $\Gamma_4^-$ . The next higher order terms are the electric quadrupole ( $\Gamma_3^+ \oplus \Gamma_5^+$ ) and magnetic dipole ( $\Gamma_4^+$ ) terms which are suppressed by a factor on the order of  $|a_g/\lambda|^2 \approx 10^{-6}$  compared to the electric dipole. Table 2.4 contains the irreducible representations of the excitonic states and indicates the selection rules for the transitions from the crystal vacuum via electric or magnetic dipole transitions as well as electric quadrupole transitions. The breaking of the rotational symmetry due to the cubic crystal environment leads to a mixing of angular momenta. Therefore, even the yellow and green  $F$ -excitons as well as the blue and violet  $D$ -excitons have dipole allowed components, contrary to the discussion in Sec. 2.2.3.

	$S (\Gamma_1^+)$	$P (\Gamma_4^-)$
<b>yellow</b> ( $\Gamma_7^+ \otimes \Gamma_6^+$ )	$\Gamma_2^+ \oplus \Gamma_5^+$	$\Gamma_2^- \oplus \Gamma_3^- \oplus \Gamma_4^- \oplus 2\Gamma_5^-$
<b>green</b> ( $\Gamma_8^+ \otimes \Gamma_6^+$ )	$\Gamma_3^+ \oplus \Gamma_4^+ \oplus \Gamma_5^+$	$\Gamma_1^- \oplus \Gamma_2^- \oplus 2\Gamma_3^- \oplus 3\Gamma_4^- \oplus 3\Gamma_5^-$
<b>blue</b> ( $\Gamma_7^+ \otimes \Gamma_8^-$ )	$\Gamma_3^- \oplus \Gamma_4^- \oplus \Gamma_5^-$	$\Gamma_1^+ \oplus \Gamma_2^+ \oplus 2\Gamma_3^+ \oplus 3\Gamma_4^+ \oplus 3\Gamma_5^+$
<b>violet</b> ( $\Gamma_8^+ \otimes \Gamma_8^-$ )	$\Gamma_1^- \oplus \Gamma_2^- \oplus \Gamma_3^-$ $\oplus 2\Gamma_4^- \oplus 2\Gamma_5^-$	$2\Gamma_1^+ \oplus 2\Gamma_2^+ \oplus 4\Gamma_3^+$ $\oplus 6\Gamma_4^+ \oplus 6\Gamma_5^+$

	$D (\Gamma_3^+ \oplus \Gamma_5^+)$	$F (\Gamma_2^- \oplus \Gamma_4^- \oplus \Gamma_5^-)$
<b>yellow</b>	$\Gamma_1^+ \oplus 2\Gamma_3^+ \oplus 3\Gamma_4^+ \oplus 2\Gamma_5^+$	$2\Gamma_1^- \oplus \Gamma_2^- \oplus 2\Gamma_3^- \oplus 4\Gamma_4^- \oplus 3\Gamma_5^-$
<b>green</b>	$2\Gamma_1^+ \oplus 2\Gamma_2^+ \oplus 3\Gamma_3^+$ $\oplus 5\Gamma_4^+ \oplus 5\Gamma_5^+$	$2\Gamma_1^- \oplus 2\Gamma_2^- \oplus 5\Gamma_3^-$ $\oplus 7\Gamma_4^- \oplus 7\Gamma_5^-$

**Table 2.4.:** Irreducible representations  $\Gamma_v \otimes \Gamma_c \otimes \Gamma_{env}$  of the excitonic states in  $\text{Cu}_2\text{O}$ . The rows correspond to  $\Gamma_v \otimes \Gamma_c$  and the columns to  $\Gamma_{env}$ . The highlighted states correspond to states that may be accessible from the crystal vacuum via electric dipole transitions (green,  $\Gamma_4^-$ ), magnetic dipole transitions (orange,  $\Gamma_4^+$ ) and electric quadrupole transitions (red,  $\Gamma_3^+ \oplus \Gamma_5^+$ ). Some of these transitions may, however, be suppressed due to required spin flips.

### The yellow series

The main series of interest to this thesis is the yellow series. Its Rydberg energy derived from Eq. (2.60) is 86.07 meV and the excitonic mass  $M = 1.55 m_0$  which both agree very well with the experimental observations [25]. Nonetheless, there is a small but systematic deviation from the ideal Rydberg series which can be expressed as quantum defects  $\delta_{n,\ell}$  via

$$E_{n,\ell,m} = E_g - \frac{Ry^*}{(n - \delta_{n,\ell})^2}. \quad (2.69)$$

These behave very similarly to the quantum defects used to describe the states of alkali Rydberg atoms, in that they are positive, largest for low orbital quantum numbers and only dependent on  $\ell$  for large  $n$  [21, 25, 26]. For the excitons, they arise due to the nonparabolicity of the valence band which is most strongly felt by states with large momentum-space extensions, i.e. low  $n$  [25, 26, 27]. In the atomic case, they arise due to the deviation of the potential felt by the valence electron from an ideal Coulomb potential. Far from the core, the potential of the nucleus screened by all the core electrons is well described by the potential of an elementary point charge. Close to the core, however, the valence electron sees the inner structure of the core resulting in a shift which mostly affects states with small real-space extension, i.e. low  $n$ . A comparison of the excitonic quantum defects from theory and experiment can be found in Chapter 3.

Due to the nonparabolicity of the  $\Gamma_7^+$  valence band and the other central cell corrections, the binding energy of the  $1S$  excitons of the yellow series deviates quite strongly from the ideal Rydberg

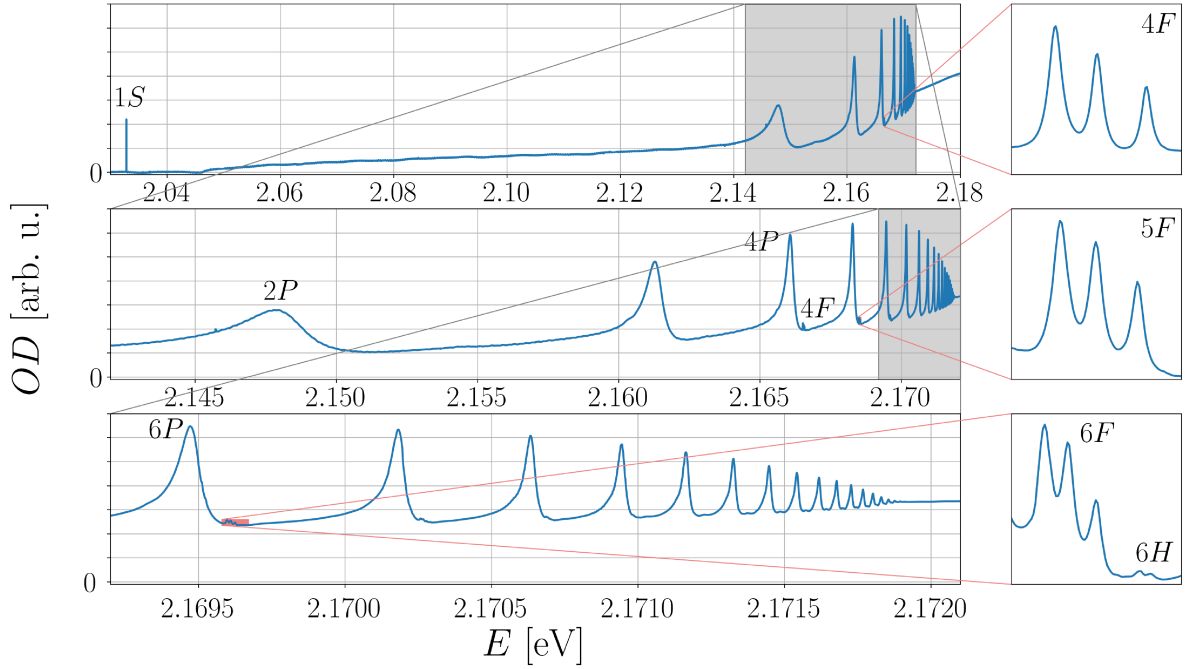


**Figure 2.7.:** Exemplary absorption spectrum of the yellow series, provided by the group of Prof. Manfred Bayer at the TU Dortmund. In addition to the dipole absorption of the  $P$ ,  $F$  and  $H$  excitons, the quadrupole absorption into the  $1S$  orthoexciton can be seen in the uppermost panel.

series [25, 26]. The binding energy of the  $\Gamma_2^+$  paraexciton is 151 meV and that of the  $\Gamma_5^+$  orthoexciton 139 meV compared to the 86 meV that would be expected [85]. As the  $1S$  states have the largest momentum space extensions, they feel the valence-band's decreasing curvature (i.e. increasing effective mass) for finite  $k$  the strongest, resulting in an increased binding energy. The splitting of 12 meV between the paraexciton and the orthoexciton is due to the electron-hole exchange interaction, which shifts the orthoexciton to higher energies but does not affect the paraexciton [74]. Figure 2.7 shows one exemplary absorption spectrum of the yellow series containing the  $P$  and  $F$  Rydberg-series as well as the quadrupole line of the  $1S$  orthoexciton. The line shapes can be fitted by an asymmetric Lorentzian profile

$$g_n(E) = \frac{f_n}{\pi} \frac{\frac{\Gamma_n}{2} + 2q_n(E - E_n)}{(E - E_n)^2 + \left(\frac{\Gamma_n}{2}\right)^2} \quad (2.70)$$

where  $f_n$  denotes the oscillator strength,  $\Gamma_n$  the full width half maximum (FWHM) linewidth,  $E_n$  the resonance energy and  $q_n$  the asymmetry parameter of the  $n$ th line. The asymmetry arises due to the energy dependence of the exciton-phonon scattering processes [86]. Although the group-theoretical analysis in Tab. 2.4 predicts four dipole-allowed  $F$ -excitons, only three are observed. This is due to the fact that the fourth one is very close to the middle one of the other three and that it arises from the paraexciton component  $\Gamma_2^+$  of  $\Gamma_7^+ \otimes \Gamma_6^+ = \Gamma_2^+ \oplus \Gamma_5^+$ , and is therefore spin-flip suppressed [20].



The oscillator strengths of the  $P$ -excitons are proportional to the areas below the absorption lines and agree with the scaling  $(n^2 - 1)n^{-5}$  expected from Eq. (2.68) [18, 76] for  $n \lesssim 10$ . The linewidths of the  $P$ -excitons exhibit the same scaling but are limited not by the optical decay path but by phonon scattering into the  $1S$  and  $2S$  excitons [33]. The linewidths and oscillator strength for the spectrum in Fig. 2.7 are shown in Fig. 2.8. For large  $n$  both quantities show a clear deviation from the expected  $(n^2 - 1)n^{-5}$  scaling, which is not well understood and discussed in more detail in Chapter 6.

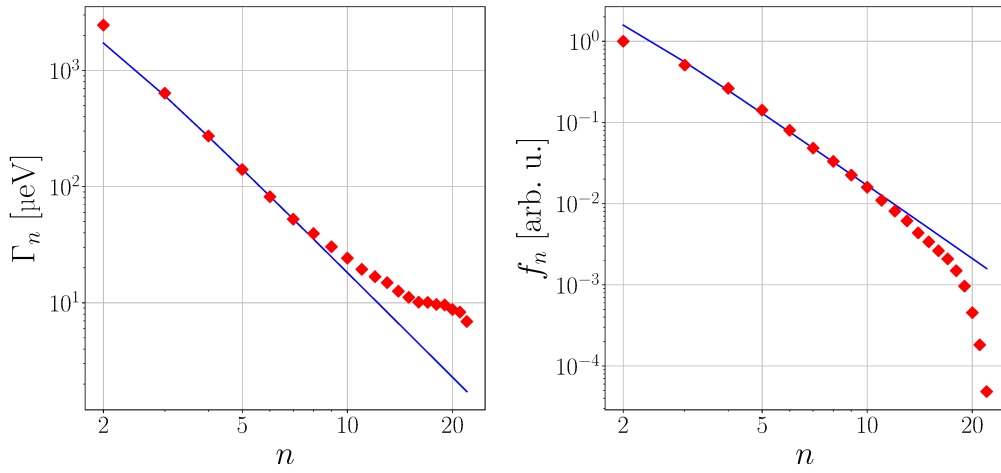


**Figure 2.8.:** The FWHM linewidths  $\Gamma_n$  and oscillator strengths  $f_n$  of the yellow  $P$  excitons derived by fits to the spectrum in Fig. 2.7. The blue lines show the expected scaling of  $(n^2 - 1)n^{-5}$  for both quantities, normalised to  $n = 7$ .

In addition to these deviations, an intensity dependent bleaching of the resonances has been observed [18] which can be fitted by a Rydberg blockade model. It has therefore been interpreted as a Rydberg blockade, motivating the nomenclature "Rydberg excitons" for the yellow excitons with a principal quantum numbers  $n \gtrsim 15$ . Nonetheless, there are other effects that might lead to an intensity dependent bleaching, first and foremost the creation of an electron-hole plasma screening the interaction of the constituents of the exciton [30, 31]. This leads to a **Mott transition**, a reduction of the band gap resulting in the ionisation of the excitonic states once the band gap crosses them. The two effects are hard to distinguish in the cw experiments performed thus far and no definitive conclusion regarding the nature of the bleaching has been reached.

### 2.3.3. Phonons

Phonons are the quasiparticles of the quantised lattice vibrations arising from the Hamiltonian (2.13). Cuprous oxide has 6 basis atoms per primitive unit cell which have a total of  $18N^3$  degrees of freedom resulting in 18 phonon branches for each allowed  $\mathbf{k}$  in the first Brillouin zone. As the vibrations correspond to a displacement of the nuclei from their rest positions, the representations

of phononic branches at the  $\Gamma$ -point are given by  $\Gamma_{\text{equiv}} \otimes \Gamma_4^-$  [49], where  $\Gamma_{\text{equiv}}$  denotes the equivalent representations of the copper atoms ( $\Gamma_1^+ \oplus \Gamma_5^+$ ) and the oxygen atoms ( $\Gamma_1^+ \oplus \Gamma_2^-$ ) and  $\Gamma_4^-$  is the irreducible representation of the displacement vector (see also App. B.1). This results in the phononic branches  $\Gamma_2^- \oplus \Gamma_3^- \oplus 2\Gamma_4^- \oplus \Gamma_5^-$  for the copper atoms and  $\Gamma_4^- \oplus \Gamma_5^+$  for the oxygen atoms. The  $\Gamma_4^-$  branches arising from the oxygen and the copper atoms may of course be mixed. The energies and descriptions of the phononic branches at the zone center are given in Tab. 2.5.

branch	energy	description
$\Gamma_4^-$	0.0 meV	acoustic modes
$\Gamma_5^-$	10.7 meV	rigid rotation of the $\text{Cu}_4\text{O}$ tetrahedron, bending the O-Cu-O bonds
$\Gamma_3^-$	13.6 meV	all four Cu atoms move towards the equator (or the poles) along constant lines of latitude
$\Gamma_4^-$	18.8 meV (TO) 19.1 meV (LO)	Cu and O atoms move in contrarious directions along [100], to keep the center of mass fixed
$\Gamma_2^-$	43.4 meV	breathing mode of the Cu tetrahedron
$\Gamma_5^+$	63.8 meV	relative motion of the two simple cubic O lattices
$\Gamma_4^-$	78.5 meV (TO) 82.1 meV (LO)	Cu and O move along the bonds, keeping the center of mass fixed

**Table 2.5.:** Phononic branches of  $\text{Cu}_2\text{O}$  at the zone center. TO denotes the transverse optical component and LO the longitudinal optical component. Copied from Refs. [87, 84].

Besides the direct absorption by the excitons, the phonons play an important role for the absorption of  $\text{Cu}_2\text{O}$  near the band gap as the dipole forbidden  $1S$  and  $2S$  excitons can be excited by an indirect, phonon-assisted process. At the low temperatures of  $\sim 1$  K all the experiments referenced in this thesis were performed at, all phononic states are virtually unoccupied and the phonon-assisted transitions may only proceed via the emission of a phonon. In particular, the  $\Gamma_3^-$  phonon leads to a strong background below the excitonic resonances setting in at 13.6 meV above the  $1S$  orthoexciton [32] (see the uppermost panel of Fig. 2.7 starting at  $\sim 2.045$  eV).

## Chapter 3.

### Yellow series quantum defects

The experimental observations of the yellow series' Rydberg excitons by Prof. Bayer's group at the TU Dortmund [18, 20] have provided a unique opportunity to investigate the fine structure of the Rydberg series in detail. While the effective mass approximation yields an astonishingly good fit [18], the experiments show a small but systematic deviation for all principal quantum numbers  $n$  that can be cast into quantum defects [25, 26]

$$\delta_{n,\ell} = n - \sqrt{-\frac{Ry^*}{E_{n,\ell}}} \quad (3.1)$$

known from alkali Rydberg atoms [21]. The quantum defects in  $\text{Cu}_2\text{O}$  arise due to the central cell corrections, first and foremost due to the nonparabolicity and anisotropy of the  $\Gamma_7^+$  valence band. In this Section, we will lay out an approach to include these features in the two-band Wannier equation, solve it numerically based on the solution of the hydrogen-atom Schrödinger equation in momentum space [88] and compare the results to the experiments. Thereby, we will be able to gauge the influence of the inclusion of the full band-structure on the excitonic fine-structure. Finally, we will discuss the derivation of the excitonic Van der Waals potentials based on the excitonic resonance energies and wave function derived from the two-band model. These Van der Waals potentials are crucial information for the assessment of the role of the Rydberg blockade in the intensity-dependent bleaching observed by Kazimierczuk *et al.* [18].

#### 3.1. Numerical approach

The starting point for the discussion of our numerical approach will be the multi-band exciton problem derived in Refs. [89, 90] and used by the authors of Refs. [73, 28], which is the most general model in the quasiparticle picture. A short discussion of the connection between the multi-band and the two-band problem, used in Refs. [25, 26] and the remainder of this Chapter, is provided in Sec. 3.1.1. Subsequently, the numerical solution of the two-band problem in momentum space

and the derivation of both the eigenenergies and the corresponding eigenfunctions is discussed in detail in Secs. 3.1.2 and 3.1.3.

### 3.1.1. Multi-band picture

In the multi-band picture, the exciton problem takes the form [89, 90]

$$[\mathcal{H}_c(-i\nabla_e) - \mathcal{H}_v(-i\nabla_h) + V(\mathbf{r}_e - \mathbf{r}_h)] \psi(\mathbf{r}_e, \mathbf{r}_h) = E \psi(\mathbf{r}_e, \mathbf{r}_h). \quad (3.2)$$

Here,  $\mathcal{H}_v(\mathbf{k}_h)$  and  $\mathcal{H}_c(\mathbf{k}_e)$  denote the effective band-structure Hamiltonians of Sec. 2.2.2 in the 36-dimensional Hilbert space of the electron-hole product states. This Schrödinger equation describes all four main series of  $\text{Cu}_2\text{O}$ , including their mutual coupling. The interaction potential  $V(\mathbf{r})$  is in the simplest case just the effective Coulomb potential  $V_c(r)$  but might include corrections, e.g. due to the electron-phonon interaction [72] or the dielectric function  $\varepsilon(\omega, \mathbf{k})$  [74, 28]. Further corrections may arise due to the electron-hole exchange interaction, which can be modelled by [91, 28]

$$\mathcal{H}_{\text{exch}} = \frac{J_0}{4} (1 - \boldsymbol{\sigma}_e \cdot \boldsymbol{\sigma}_h) \delta(\mathbf{r}_e - \mathbf{r}_h) = J_0 \left( 1 - \frac{1}{2} \mathbf{S}^2 \right) \delta(\mathbf{r}_e - \mathbf{r}_h), \quad (3.3)$$

with the electron and hole-spin Pauli matrices  $\boldsymbol{\sigma}_{e/h}$ , the coupled electron-hole spin  $\mathbf{S} = (\boldsymbol{\sigma}_e + \boldsymbol{\sigma}_h)/2$  and some constant  $J_0$ . The matrix  $\mathbf{S}^2$  has two eigenspaces with eigenvalues  $S(S+1) = 0, 2$  corresponding to the spin singlet and triplet, respectively. The definition of  $\mathcal{H}_{\text{exch}}$  indicates that the exchange interaction may only affect states that have an admixture of  $S$ -type (due to the  $\delta(\mathbf{r}_e - \mathbf{r}_h)$ ) as well as the spin-singlet state. In the case of the yellow  $S$ -excitons, the paraexciton consists only of spin triplet states [75] and is thus not affected by the exchange interaction. The exchange interaction is therefore only relevant to the  $S$ -orthoexcitons.

Transforming Eq. (3.2) to COM and relative coordinates results in<sup>1</sup>

$$[\mathcal{H}_c(-i(\alpha\nabla_{\mathbf{R}} + \nabla_{\mathbf{r}})) - \mathcal{H}_v(-i(\beta\nabla_{\mathbf{R}} - \nabla_{\mathbf{r}})) + V(\mathbf{r})] \psi(\mathbf{R}, \mathbf{r}) = E \psi(\mathbf{R}, \mathbf{r}), \quad (3.4)$$

with a Hamiltonian that is invariant under a translation in  $\mathbf{R}$ . The eigenstates can therefore be expressed in terms of the eigenstates  $\psi(\mathbf{R}, \mathbf{r}) = e^{i\mathbf{K}\cdot\mathbf{R}} \phi_{\mathbf{K}}(\mathbf{r})$  of the corresponding translation operators [89, 90] resulting in

$$[\mathcal{H}_c(\alpha\mathbf{K} - i\nabla_{\mathbf{r}}) - \mathcal{H}_v(\beta\mathbf{K} + i\nabla_{\mathbf{r}}) + V(\mathbf{r})] \phi_{\mathbf{K}}(\mathbf{r}) = E \phi_{\mathbf{K}}(\mathbf{r}). \quad (3.5)$$

<sup>1</sup>As the quasiparticles described by the band Hamiltonians have different effective masses, the relative masses  $\alpha$  and  $\beta$  do not have a self-evident definition anymore. They can be chosen freely as long as they fulfil  $\alpha + \beta = 1$ . One could in principle even define them to be  $\mathbb{R}^{3 \times 3}$  tensors fulfilling  $|\det(\alpha + \beta)| = 1$  [90]. It is nonetheless not possible to completely decouple the COM and relative degrees of freedom.

As the quasi-momentum is a conserved quantity in the crystal environment, the photon momentum  $\hbar\kappa$  is imprinted onto the exciton during the absorption process. In the dipole approximation,  $\kappa$  is set to zero. Note that even without this approximation, the  $\kappa$  corresponding to  $\sim 2$  eV is small compared to the extension of the first Brillouin zone  $|\kappa| \approx 0.004 \pi/a_g$ . We will therefore assume  $\kappa = \mathbf{K} = \mathbf{0}$  for the remainder of this Section, yielding

$$[\mathcal{H}_c(-i\nabla_{\mathbf{r}}) - \mathcal{H}_v(i\nabla_{\mathbf{r}}) + V(\mathbf{r})] \phi(\mathbf{r}) = E \phi(\mathbf{r}). \quad (3.6)$$

The kinetic terms  $\mathcal{H}_c(-i\nabla_{\mathbf{r}}) - \mathcal{H}_v(i\nabla_{\mathbf{r}})$  can be diagonalised by a unitary transformation  $\mathcal{U}(-i\nabla_{\mathbf{r}})$ , which does not commute with the potential due to its dependence on the momentum. It is therefore not strictly possible to decouple the exciton series by diagonalising only the kinetic part. The nonparabolic, anisotropic two-band Wannier equation which is derived this way does nonetheless describe the yellow series substantially better than the effective mass approximation [25, 26] and will be the model discussed in the remainder of this Chapter. As will be shown, the quantum defects observed by Kazimierczuk *et al.* [18] can be mostly attributed to the complex valence-band structure included in this model. The full problem including the coupling to the green exciton series as well as the other central-cell corrections has successfully been treated by F. Schweiner *et al.* in Refs. [73, 28].

### 3.1.2. Two-band picture

For a general valence-band structure, the two-band Wannier equation (2.56) takes the form

$$\left[ E_g + \frac{\mathbf{p}_e^2}{2m_e^*} + \frac{\mathbf{p}_h^2}{2m_h^*} + \Delta T(\mathbf{p}_h) + V_c(|\mathbf{r}_e - \mathbf{r}_h|) \right] \Psi(\mathbf{r}_e, \mathbf{r}_h) = E \Psi(\mathbf{r}_e, \mathbf{r}_h), \quad (3.7)$$

where the term  $\Delta T(\mathbf{p}_h)$  containing the valence-band nonparabolicity and the anisotropy has been added, while  $\Gamma_6^+$  conduction-band is approximated by an isotropic parabola. The transformation to relative and COM coordinates results in

$$\left[ \frac{\mathbf{P}^2}{2M} + \frac{\mathbf{p}^2}{2\mu} + \Delta T(\beta\mathbf{P} - \mathbf{p}) + V_c(r) \right] \Psi(\mathbf{R}, \mathbf{r}) = E' \Psi(\mathbf{R}, \mathbf{r}), \quad (3.8)$$

where we introduced  $E' = E - E_g$ . Contrary to the effective mass approximation, the COM and relative degrees of freedom do not decouple anymore. The Hamiltonian is invariant with respect to a translation in  $\mathbf{R}$  and we can again insert  $\Psi(\mathbf{R}, \mathbf{r}) = e^{i\mathbf{K}\cdot\mathbf{R}} \phi_{\mathbf{K}}(\mathbf{r})$  and set  $\mathbf{K} = \mathbf{0}$ , yielding the anisotropic Wannier equation

$$\left[ \frac{\mathbf{p}^2}{2\mu} + \Delta T(\mathbf{p}) + V_c(r) \right] \phi(\mathbf{r}) = E' \phi(\mathbf{r}). \quad (3.9)$$

In the derivation, we also made use of the fact that due to the inversion symmetry of  $\text{Cu}_2\text{O}$ ,  $\Delta T(\mathbf{p})$  has to be inversion-symmetric as well.  $\Delta T(\mathbf{p})$  may in general have a complicated dependency on the components of the momentum operator. It does therefore seem advantageous to treat the problem in momentum space where the momentum operator turns into a coordinate vector  $\mathbf{p} = \hbar \mathbf{k}$ . The Fourier transform yields an integral equation

$$\left[ \frac{\hbar^2 \mathbf{k}^2}{2\mu} + \Delta T(\hbar \mathbf{k}) + V_c(k) \star \right] \psi(\mathbf{k}) = E' \psi(\mathbf{k}), \quad (3.10)$$

where

$$V_c(k) \star \psi(\mathbf{k}) = (2\pi)^{-\frac{3}{2}} \int d^3 \mathbf{k}' V_c(|\mathbf{k} - \mathbf{k}'|) \psi(\mathbf{k}'), \quad (3.11)$$

denotes the convolution of the momentum-space wave-function  $\psi(\mathbf{k})$  with the Fourier transformed Coulomb potential

$$V_c(k) = -\frac{e^2}{(2\pi)^{\frac{3}{2}} \varepsilon k^2}. \quad (3.12)$$

Combining the Eqs. (3.9-3.12) and introducing the renormalised energy<sup>2</sup>  $q = \sqrt{-2\mu E'}/\hbar$  as well as  $\tau(\mathbf{k}) = 2\mu \Delta T(\hbar \mathbf{k})/\hbar^2$ , the problem can be rewritten as a Sturmian eigenvalue problem which depends only parametrically on  $q$

$$\left[ k^2 + \tau(\mathbf{k}) + q^2 \right] \psi(\mathbf{k}) = \frac{\lambda(q)}{a_B^* \pi^2} \int d^3 \mathbf{k}' \frac{\psi(\mathbf{k}')}{|\mathbf{k} - \mathbf{k}'|^2}. \quad (3.13)$$

The parameter  $\lambda(q)$  is the Sturmian eigenvalue and  $a_B^* = 4\pi\varepsilon\hbar^2/(\mu e^2)$  the excitonic Bohr radius. The eigenenergies of Eq. (3.9) can then be retrieved by solving for the eigenvalue branches  $\lambda_i(q)$  and locating all energies  $q_n$  for which at least one of these branches fulfils  $\lambda_i(q_n) = 1$ .

$\tau(\mathbf{k})$  is symmetric with respect to all symmetry operations of  $O_h$  due to the star degeneracy. This implies that it transforms according to the irreducible representation  $\Gamma_1^+$  and can be expanded into the corresponding cubic harmonics  $Y_{\ell\alpha}^{\Gamma_1^+}(\mathbf{n}_k)$  (see App. B.4)

$$\tau(\mathbf{k}) = \sum_{\ell\alpha} \tau_{\ell\alpha}(k) Y_{\ell\alpha}^{\Gamma_1^+}(\mathbf{n}_k). \quad (3.14)$$

The subscript  $\alpha$  indicates that more than one cubic harmonic of order  $\ell$  may transform like  $\Gamma_1^+$  (which does only happen for  $\ell \geq 12$ ). As the operators on both sides of Eq. (3.13) transform like  $\Gamma_1^+$ , only basis functions transforming like the same row of the same irreducible representation can

<sup>2</sup>Keep in mind that we are interested in the bound states for whom  $E' < 0$ .

be coupled. We can therefore choose an ansatz

$$\psi^{\Gamma,i}(\mathbf{k}) = \sum_{\ell_\alpha} F_{\ell_\alpha}(k) Y_{\ell_\alpha}^{\Gamma,i}(\mathbf{n}_\mathbf{k}), \quad (3.15)$$

transforming like the row  $i$  of the irreducible representation  $\Gamma$  with some radial wave functions  $F_{\ell_\alpha}(k)$ . The substitution of this ansatz into the right-hand side of Eq. (3.13) results in

$$\frac{1}{2k} \frac{\lambda(q)}{a_B^* \pi^2} \sum_{\ell_\alpha} \int_0^\infty dk' k' F_{\ell_\alpha}(k') \oint d^2 \mathbf{n}_{\mathbf{k}'} \frac{Y_{\ell_\alpha}^{\Gamma,i}(\mathbf{n}_{\mathbf{k}'})}{\frac{k^2+k'^2}{2kk'} - \mathbf{n}_\mathbf{k} \cdot \mathbf{n}_{\mathbf{k}'}}. \quad (3.16)$$

The integral over the angular degrees of freedom can then be evaluated analytically using the Funk-Hecke formula [92]

$$\oint d^2 \mathbf{n}_{\mathbf{k}'} S(\mathbf{n}_\mathbf{k} \cdot \mathbf{n}_{\mathbf{k}'}) Y_\ell(\mathbf{n}_{\mathbf{k}'}) = 2\pi Y_\ell(\mathbf{n}_\mathbf{k}) \int_{-1}^1 dt S(t) P_\ell(t) \quad (3.17)$$

$\forall S \in L^1(-1, 1).$

Here,  $Y_\ell(\mathbf{n}_\mathbf{k})$  denotes any linear combination of spherical harmonics of order  $\ell$  (such as the cubic harmonics) and  $P_\ell(t)$  the Legendre polynomials. Together with the relation between the  $P_\ell(t)$  and the Legendre functions of second kind  $Q_\ell(z)$  [93]

$$Q_\ell(z) = \frac{1}{2} \int_{-1}^1 dt \frac{P_\ell(t)}{z-t} \quad \forall z \in \mathbb{C} \setminus [-\infty, -1], \quad (3.18)$$

we obtain

$$\frac{\lambda(q)}{a_B^* \pi} \frac{2}{k} \sum_{\ell_\alpha} Y_{\ell_\alpha}^{\Gamma,i}(\mathbf{n}_\mathbf{k}) \int_0^\infty dk' k' F_{\ell_\alpha}(k') Q_\ell\left(\frac{k^2+k'^2}{2kk'}\right). \quad (3.19)$$

Multiplying from the left with  $Y_{\ell'_\alpha}^{\Gamma,i\dagger}(\mathbf{n}_\mathbf{k})$  and integrating over the angles yields

$$\sum_{\ell_\alpha} \left[ \left( k^2 + q^2 \right) \delta_{\ell'_\alpha, \ell_\alpha} + \sum_{\ell''_\alpha} \tau_{\ell''_\alpha}(k) C_{\ell_\alpha, \ell'_\alpha, \ell''_\alpha}^\Gamma \right] k F_{\ell_\alpha}(k) = \frac{2\lambda(q)}{a_B^* \pi} \int_0^\infty dk' k' F_{\ell'_\alpha}(k') Q_{\ell'}\left(\frac{k^2+k'^2}{2kk'}\right), \quad (3.20)$$

with the cubic Gaunt coefficients

$$C_{\ell_\alpha, \ell'_\alpha, \ell''_\alpha}^\Gamma = \oint d^2 \mathbf{n}_\mathbf{k} Y_{\ell'_\alpha}^{\Gamma,i\dagger}(\mathbf{n}_\mathbf{k}) Y_{\ell''_\alpha}^{\Gamma_1^+}(\mathbf{n}_\mathbf{k}) Y_{\ell_\alpha}^{\Gamma,i}(\mathbf{n}_\mathbf{k}). \quad (3.21)$$

These coefficients can be evaluated in terms of the **spherical Gaunt coefficients** (B.34) (see Apps. B.4 and B.5). Due to  $Y_{\ell''_\alpha}^{\Gamma_1^+}$  transforming like  $\Gamma_1^+$ , the cubic Gaunt coefficients are independent

of the row  $i$  of  $\Gamma$ . This guarantees that Eq. (3.20) takes the same form for all rows and the degeneracy which is required by symmetry is indeed observed. Substituting  $f_{\ell_\alpha}(k, q) = \sqrt{k^2 + q^2} k F_{\ell_\alpha}(k)$  yields

$$\sum_{\ell_\alpha} \left[ \delta_{\ell'_\alpha, \ell_\alpha} + \sum_{\ell''_\alpha} \frac{\tau_{\ell''_\alpha}(k)}{k^2 + q^2} C_{\ell'_\alpha, \ell''_\alpha, \ell_\alpha}^\Gamma \right] f_{\ell_\alpha}(k, q) = \frac{2\lambda(q)}{a_B^* \pi} \int_0^\infty dk' \frac{Q_{\ell'} \left( \frac{k^2 + k'^2}{2kk'} \right)}{\sqrt{k^2 + q^2} \sqrt{k'^2 + q^2}} f_{\ell'_\alpha}(k', q). \quad (3.22)$$

The integral kernel can be decomposed [88]

$$M_\ell(k, k', q) = \frac{2}{a_B^* \pi} \frac{Q_\ell \left( \frac{k^2 + k'^2}{2kk'} \right)}{\sqrt{k^2 + q^2} \sqrt{k'^2 + q^2}} = \sum_{j=0}^\infty g_{j,\ell}(k, q) g_{j,\ell}(k', q), \quad (3.23)$$

with expansion functions containing the Gegenbauer polynomials  $C_j^{(\ell+1)}(x)$

$$g_{j,\ell}(k, q) = \ell! \sqrt{\frac{j!}{a_B^* \pi (j + 2\ell + 1)!}} \frac{(4qk)^{\ell+1}}{(k^2 + q^2)^{\ell+3/2}} C_j^{(\ell+1)} \left( \frac{q^2 - k^2}{q^2 + k^2} \right). \quad (3.24)$$

These expansion functions are orthogonal with respect to  $j$

$$\int_0^\infty dk g_{j,\ell}(k, q) g_{j',\ell}(k, q) = \frac{1}{(j + \ell + 1) q a_B^*} \delta_{j,j'} \quad (3.25)$$

ensuring that they are eigenfunctions of the integral operator. Furthermore, the corresponding momentum-space **Coulomb-Sturmian functions**

$$G_{j,\ell_\alpha}^{\Gamma,i}(\mathbf{k}, q) = \frac{\sqrt{(j + \ell + 1) q a_B^*}}{k \sqrt{k^2 + q^2}} g_{j,\ell}(k, q) Y_{\ell_\alpha}^{\Gamma,i}(\mathbf{n}_k), \quad (3.26)$$

are known to form a complete orthonormal basis of the Hilbert space  $L_{k^2+q^2}^2$  [88]. We are therefore free to use them as the basis for the expansion of the wave functions  $\psi^{\Gamma,i}(\mathbf{k})$  which is equivalent to expanding the  $f_{\ell_\alpha}(k, q)$  in terms of the rescaled kernel expansion functions  $h_{j,\ell}(k, q) = q a_B^* (j + \ell + 1) g_{j,\ell}(k, q)$ ,

$$f_{\ell_\alpha}(k, q) = \sum_{j=0}^\infty c_j^{\ell_\alpha} h_{j,\ell}(k, q). \quad (3.27)$$

Inserting these expansions into Eq. (3.22), multiplying by  $h_{j',\ell'}(k, q)$  and integrating over  $k$  results in the algebraic eigenvalue problem

$$\mathbf{T}(q) \cdot \mathbf{c}(q) = \lambda(q) \mathbf{c}(q), \quad (3.28)$$



where  $c(q)$  denotes the vector of the expansion coefficient  $c_j^{\ell_\alpha}$  and the symmetric matrix  $T(q)$  is given by

$$T_{\{j', \ell'_\alpha\}, \{j, \ell_\alpha\}}(q) = q a_B^* (j' + \ell' + 1) \delta_{j', j} \delta_{\ell'_\alpha, \ell_\alpha} + \sum_{\ell''_\alpha} C_{\ell'_\alpha, \ell''_\alpha, \ell_\alpha}^\Gamma \int_0^\infty dk h_{j', \ell'}(k, q) \frac{\tau_{\ell''_\alpha}(k)}{k^2 + q^2} h_{j, \ell}(k, q). \quad (3.29)$$

For vanishing nonparabolicity  $\tau(\mathbf{k})$ , the effective-mass approximation is obtained and the Sturmian eigenvalues are given by  $\lambda_{j, \ell}(q) = q a_B^* (j + \ell + 1)$ . The corresponding eigenenergies can be retrieved by inserting  $q = \sqrt{-2\mu E'/\hbar}$ , requiring  $\lambda_{j, \ell}(q) = 1$  and solving for  $E'$ . This results in the analytically known solutions

$$E' = -\frac{\hbar^2}{2\mu a_B^{*2}} \frac{1}{(j + \ell + 1)^2} = -\frac{Ry^*}{(j + \ell + 1)^2} = -\frac{Ry^*}{n^2}, \quad (3.30)$$

as well as  $q_n = 1/(n a_B^*)$ . For a numerical implementation, the basis as well as the expansion of the band structure have to be cut off at some point. The algorithm with the band structure expansion, the basis of choice and an energy range  $I_q$  of interest as input parameters does thus take the form:

1. Divide  $I_q$  into a suitable grid  $G_q$ .
2. For each energy  $q_i \in G_q$ :
  - a) Calculate the  $T(q_i)$  in the given basis by numerical integration of Eq. (3.29).
  - b) Calculate the eigenvalues  $\lambda_j(q_i)$  of  $T(q_i)$ .
3. Interpolate the  $\lambda_j(q_i)$  onto the whole interval  $I_q$ .
4. Determine all  $q_n$  with  $\lambda_j(q_n) = 1$  for each eigenvalue branch.

### 3.1.3. Wave functions

The expansion coefficients of the wave functions are given by the eigenvector  $c_n(q_n)$  corresponding to the eigenvalue branch which fulfils  $\lambda_n(q_n) = 1$ . The unnormalised wave functions in momentum space do then take the form

$$\psi_{n, \ell_\alpha}^{\Gamma, i}(\mathbf{k}) = \sqrt{q_n a_B^*} \sum_{j=0}^{j_{\max}} c_{n, j}(q_n) \sqrt{j + \ell + 1} G_{j, \ell_\alpha}^{\Gamma, i}(\mathbf{k}, q_n), \quad (3.31)$$

where  $j_{\max}$  denotes the cutoff of the basis. The corresponding real-space wave functions are given by

$$\phi_{n,\ell_\alpha}^{\Gamma,i}(\mathbf{r}) = \sqrt{q_n a_B^*} \sum_{j=0}^{j_{\max}} c_{n,j}(q_n) (-1)^j \sqrt{j+\ell+1} R_{j,\ell_\alpha}^{\Gamma,i}(\mathbf{r}, q_n), \quad (3.32)$$

with the real-space Coulomb Sturmians

$$R_{j,\ell_\alpha}^{\Gamma,i}(\mathbf{r}, q_n) = \sqrt{\frac{(2q_n)^3 j!}{2(j+\ell+1)(j+2\ell+1)!}} e^{-q_n r} (2q_n r)^\ell L_j^{2\ell+1}(2q_n r) Y_{\ell_\alpha}^{\Gamma,i}(\mathbf{n}_r), \quad (3.33)$$

and the associated Laguerre polynomials  $L_j^{2\ell+1}(x)$ .

### 3.2. Band structure

As the expectation value of the radial momentum  $k_r$  vanishes for a hydrogenic atom [94] it cannot be used as a measure for the momentum-space extension of the states. The uncertainty, however, does not vanish and is given by

$$\Delta k_r = \frac{1}{n a_B^*} \sqrt{1 - \frac{\ell(\ell+1)}{n(\ell + \frac{1}{2})}}. \quad (3.34)$$

By inserting the effective Bohr radii of 0.505 nm for the  $1S$  states [84] and 1.1 nm for all other states<sup>3</sup>, we arrive at  $\Delta k_r(1S) = 0.27 \pi/a_g$  and  $\Delta k_r(2P) = 0.036 \pi/a_g$ . As can be seen in Fig 2.5, the Suzuki-Hensel Hamiltonian provides a good fit to the  $\Gamma_7^+$  valence band over more than half of the first Brillouin zone and should therefore suffice for the description of all yellow excitons. The Rydberg excitons of interest in this Section are those with an orbital quantum number  $\ell \leq 3$  which can only couple directly to one another via cubic harmonics of order  $\ell'' \leq 6$ , due to the triangle condition  $|\ell - \ell'| \leq \ell'' \leq \ell + \ell'$  for nonvanishing Gaunt coefficients. In general, including all states with  $\ell \leq 5$  and the expansion of  $\tau(\mathbf{k})$  up to order  $\ell'' = 10$  provided good convergence for these states.

Figure 3.1 shows the radial expansion functions  $\tau_{\ell''_\alpha}(k)$  up to order  $\ell'' = 10$ . It is apparent that the isotropic component  $\tau_0(k)$  is the dominant one over the whole Brillouin zone. Furthermore, all components vanish faster than  $k^2$  for  $k \rightarrow 0$ , which implies that the effective mass of the  $\Gamma_7^+$  valence-band is indeed isotropic and explains why the isotropic model used in Refs. [25, 26] describes the yellow series so remarkably well.

<sup>3</sup>The deviation of Bohr radius of the  $1S$  states arises due to the central cell corrections, first and foremost the non-parabolicity of the valence band [84].

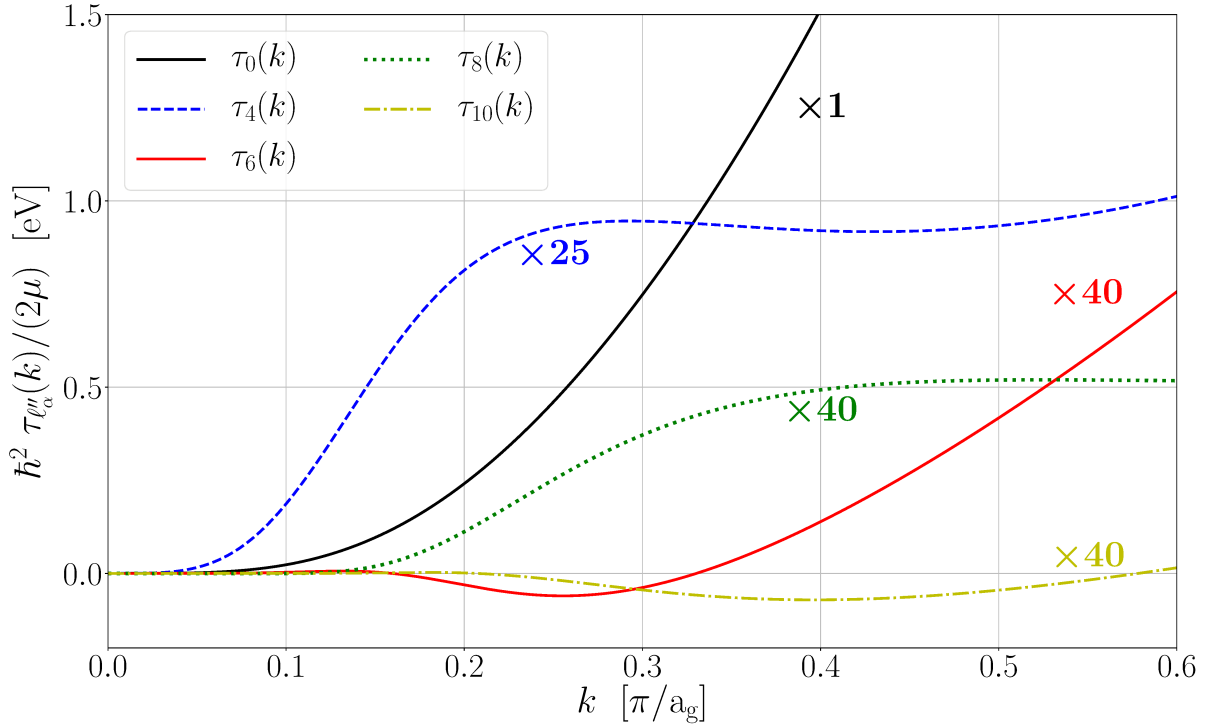


**Figure 3.1.:** Expansion of  $\tau(k)$  into cubic harmonics. The components have been rescaled by the factors shown in the plot for better visibility. Note that there is no cubic harmonic of order  $\ell'' = 2$  transforming like  $\Gamma_1^+$  (see Tab. B.4 and Fig. B.1).

### 3.3. Results

The quantum defects are very sensitive to small deviations from an ideal Rydberg series. This implies that if one wants to cast the experimental binding energies of the Rydberg excitons into quantum defects, one needs to know the band gap  $E_g$  to a high degree of precision. Applying the linear error propagation to Eq. (3.1) yields

$$|\Delta\delta_{n,\ell}| = \left| \frac{(n - \delta_{n,\ell})^3}{2 Ry^*} \Delta E_{n,\ell} \right| \quad (3.35)$$

which implies that the band gap must be known with an accuracy of  $\Delta E_g \leq 0.1 \mu\text{eV}$  in order to achieve  $|\Delta\delta_{25P}| \leq 0.01$ . A fit of the experimental  $P$ -exciton resonances to the results of this Section results in  $E_g = 2.1720733 \text{ eV}$  which agrees with the value used in the literature ( $E_g = 2.17208 \text{ eV}$  [18]) to within one least significant digit. The observation of the Rydberg series does therefore provide an opportunity to determine the main band gap of  $\text{Cu}_2\text{O}$  with unprecedented accuracy.

As the two-band model used in this Section neglects the spin degrees of freedom, it cannot model the electron-hole exchange interaction. This is relevant to the  $S$ -excitons as the species observed in the experiments are the orthoexcitons, i.e. the species affected by the exchange interaction. The resulting offset can be corrected phenomenologically by shifting the numerical  $S$ -exciton

binding energies by  $12.1 \text{ meV } n^{-3}$ . The exchange splitting  $\Delta_0 = 12.1 \text{ meV}$  for  $n = 1$  is known from experiment [91] and the  $n^{-3}$  scaling is typical for the exchange interaction at the zone center which scales with [74, 95]

$$|\phi_{n,\ell}(\mathbf{0})|^2 \propto \begin{cases} 0 & \text{for } \ell > 0 \\ n^{-3} & \text{for } \ell = 0. \end{cases} \quad (3.36)$$

The splitting due to the breaking of the rotational symmetry can be read from the compatibility table of  $O_h$  with respect to  $O(3)$  (see Tab. B.4). The representations of the lowermost angular momenta as well as the notation used in the following are given in Tab. 3.1.

$\ell$	notation	irreducible representation
$S$	$^1S_1$	$\Gamma_1^+$
$P$	$^3P_4$	$\Gamma_4^-$
$D$	$^2D_3$	$\Gamma_3^+$
	$^3D_5$	$\Gamma_5^+$
$F$	$^1F_2$	$\Gamma_2^-$
	$^3F_4$	$\Gamma_4^-$
	$^3F_5$	$\Gamma_5^-$

**Table 3.1.:** Splitting of the angular momenta under  $O_h$  symmetry. The left superscript in the notation column denotes the degeneracy of the corresponding states. The  $S$  and  $P$ -states do not split while the  $D$ -states split into one doublet and one triplet and the  $F$ -states into one singlet and two triplets.

Figure 3.2 shows the quantum defects calculated from the anisotropic, nonparabolic two-band model and compares them to the experiment<sup>4</sup>. The results for the  $S$  and  $P$ -excitons agree very well, not only with experimental results, but also with the results from the isotropic calculation [25, 26]. In fact, the degeneracy-weighted averages coincide with the isotropic results for all angular momenta. Thus, the main effect of the anisotropy is just the splitting of  $D$  and  $F$ -states. There is a deviation between experimental and numerical results at small  $n$  for all angular momenta which arises due to the neglect of the other central-cell corrections such as the polaronic corrections to the interaction potential.

In the effective mass approximation, all quantum defects would be zero, as the binding energies follow an ideal Rydberg series. It is therefore obvious that the two-band model including the complete valence band yields a substantial improvement. In fact, it can be seen that the nonparabolicity is the leading cause for the excitonic quantum defect.

<sup>4</sup>The resonance energies of the  $P$  and  $F$  excitons shown in the figure were retrieved from one-photon dipole-absorption spectra [18, 20] while the  $S$  and  $D$  resonance-energies were extrapolated from spectra obtained under the influence of an electric field. The electric field breaks the cubic symmetry, mixes the excitonic states and makes  $S$  and  $D$  states dipole allowed [25, 26].

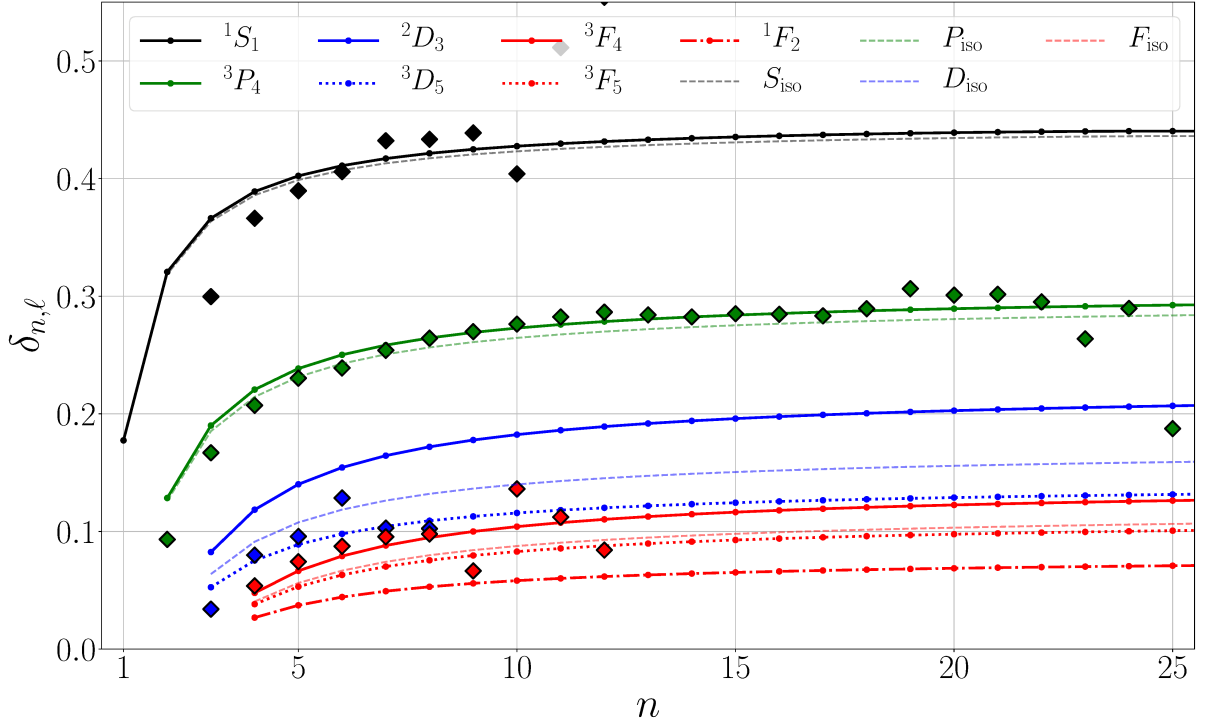


**Figure 3.2.:** Comparison of experimental and numerical quantum defects. The lines denote the numerical results and the diamonds the experimental ones. The experimental values for the  $F$  excitons shown here comprise an average of the three visible lines. The dashed lines show the results of the isotropic calculation, taking only  $\tau_0(k)$  into account. Both the numerical and experimental resonance energies can be found in App. A.2.

The three  $F$ -multiplets correspond to the three lines observed in Fig. 2.7 as each of the multiplets contributes one dipole-allowed  $\Gamma_4^-$  when multiplied with the ortho component  $\Gamma_5^+$  of the product of the band states  $\Gamma_7^+ \otimes \Gamma_6^+ = \Gamma_2^+ \oplus \Gamma_5^+$ . The fourth  $\Gamma_4^-$  in Tab. 2.4 stems from the product  $\Gamma_2^+ \otimes \Gamma_5^-$  which is spin-flip suppressed as it arises from the para component [20]. It does furthermore lie below the middle one of the three observed lines according to Ref. [20], which agrees very well with our calculation in which the  ${}^3F_5$  component is indeed in the middle.

While the splitting of the  $F$ -exciton shown in Fig. 3.3 (b) is well reproduced, an offset  $\Delta_{n-e}$  between the experimental and numerical results is apparent that is almost as large as the  ${}^3F_4$ - ${}^1F_2$ -splitting  $\Delta_{13}$ . At first glance, this offset scales with  $\sim n^{-2}$  which seems rather unlikely as it would imply that the  $F$  excitons have a different Rydberg energy. There are only four reliable data points ( $4 \leq n \leq 7$ ) which is not enough to make a definitive statement and the scaling of the offset as well as its origin are unclear. The fact that all  $F$ -multiplets are affected in the same manner could suggest that this offset arises from an isotropic correction. Such a correction should, however, influence all angular momenta, which it does not seem to do.

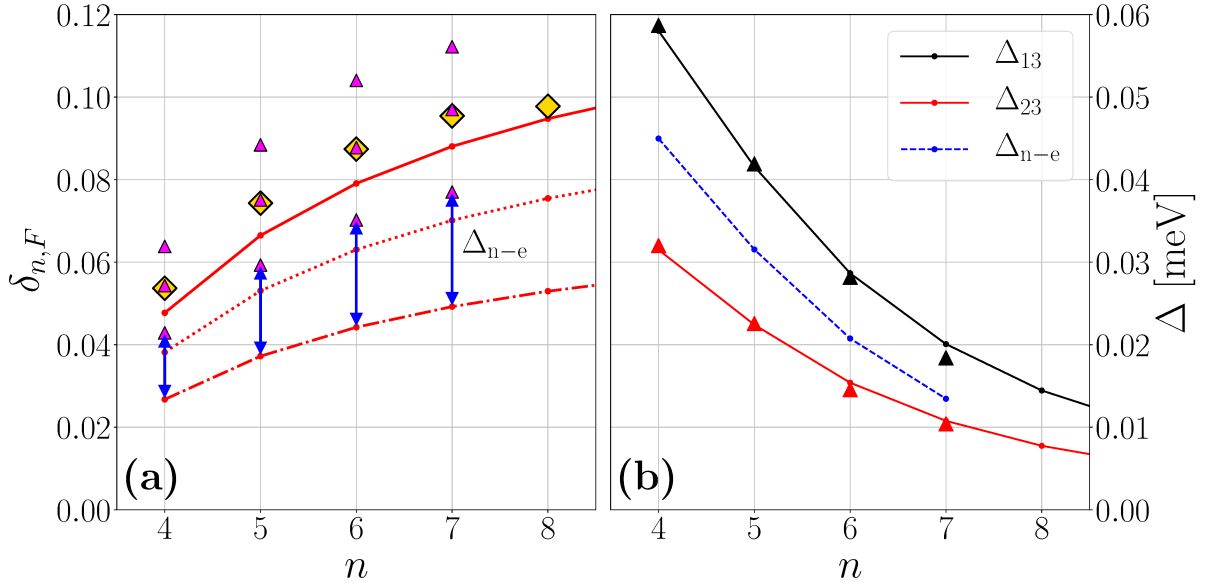


**Figure 3.3.:** Splitting between the three  $F$ -multiplets due to the anisotropy of the valence band. (a): Comparison of the quantum defects for the three  $F$ -resonances. The magenta triangles symbolise the three visible  $F$ -lines and the golden diamonds their average used in Fig. 3.2. The other line styles are the same as in Fig. 3.2. (b): Splitting between the multiplets.  $\Delta_{13}$  denotes the  ${}^3F_4$ - ${}^1F_2$  splitting and  $\Delta_{23}$  the  ${}^3F_5$ - ${}^1F_2$  splitting. The triangles show the experimental data and  $\Delta_{n-e}$  is the offset between the experimental and numerical data.

### 3.3.1. Conclusion

We have shown that the inclusion of the valence-band nonparabolicity and anisotropy into the two-band Wannier equation yields a substantial improvement for the yellow Rydberg excitons of  $\text{Cu}_2\text{O}$ . The improvements can be quantified by the parameter

$$\beta_{n,\ell} = \left| \frac{E_{n,\ell}^{\text{exp}} - E_{n,\ell}^{\text{num}}}{E_{n,\ell}^{\text{exp}} - \left(-\frac{Ry^*}{n^2}\right)} \right|, \quad (3.37)$$

where  $E_{n,\ell}^{\text{exp}}$  and  $E_{n,\ell}^{\text{num}}$  denote the experimental and numerical binding energies, respectively. This parameter can be interpreted as the relative improvement over the effective mass approximation and is shown in Fig. 3.4. The relative improvements range between a factor of 2 and 1000 for almost all states shown there.

The calculations presented here are a precursor to the calculations for Rydberg excitons in inhomogeneous strain traps laid out in the next Chapter. In order to go beyond the two-band model presented here, one would have to treat the multi-band problem lined out in Sec. 3.1.1. The calculations over a wide range of strains  $\epsilon$  in a system with reduced symmetry, however, would not be feasible in the multi-band picture.

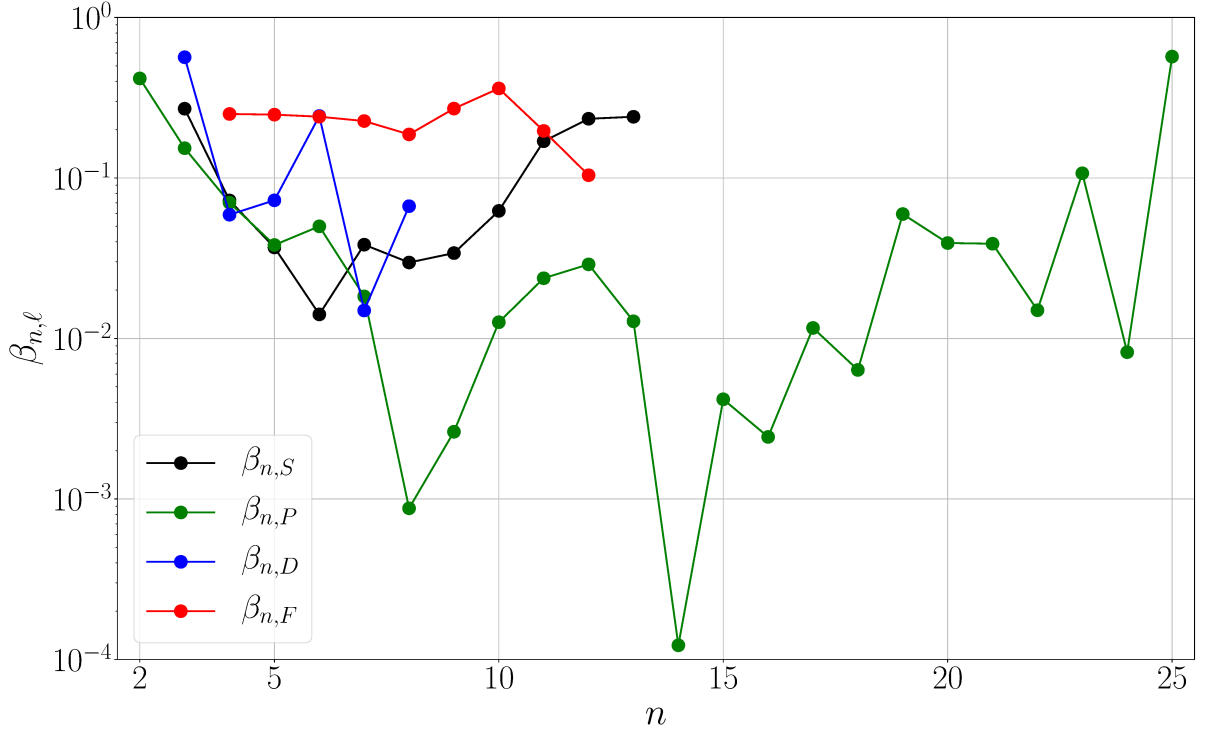


**Figure 3.4.:** Improvement of the nonparabolic model over the effective mass approximation. For the  $D$ -states, the experimental results are compared to the  $^3D_5$ -component and for the  $F$ -states, the (degeneracy-weighted) averages are compared.

### 3.4. Excitonic Van der Waals potentials

One particular application for these results is the calculation of excitonic dipole-dipole potentials. The fine structure of the Rydberg states plays an important role in their mutual dipole-dipole interaction which has been put forward as a possible explanation for the intensity dependent bleaching observed by T. Kazimierczuk *et al.* [18]. The most prominent feature of the excitonic fine structure is the quantum defect induced by the valence-band nonparabolicity. It is therefore necessary to include the quantum defect in the calculation of the two-exciton Van der Waals potentials. The corresponding calculations have been performed by V. Walther and Prof. T. Pohl at the University of Aarhus [37], using the wave function and quantum defects derived from the isotropic band-structure model laid out in this Chapter as well as the software pairinteraction [96].

The Van der Waals potential of two neutral atoms (or excitons) arises from the mutual interaction of their polarisations induced by fluctuations of the electric field. It has a characteristic dependency on the spatial separation  $R_{ij}$ , scaling with  $R_{ij}^{-6}$  for large separations, and does strongly depend on the principal quantum number  $n$  due to the swift increase in the polarisability of the Rydberg states which scales with  $\sim n^7$  for both alkali Rydberg atoms and Rydberg excitons [21, 22]. The actual interaction potentials increase even faster with  $\sim n^{11}$ . Figure 3.5 (a) shows a schematic of the two-exciton problem and the different coordinate systems used. In addition to the two intra-

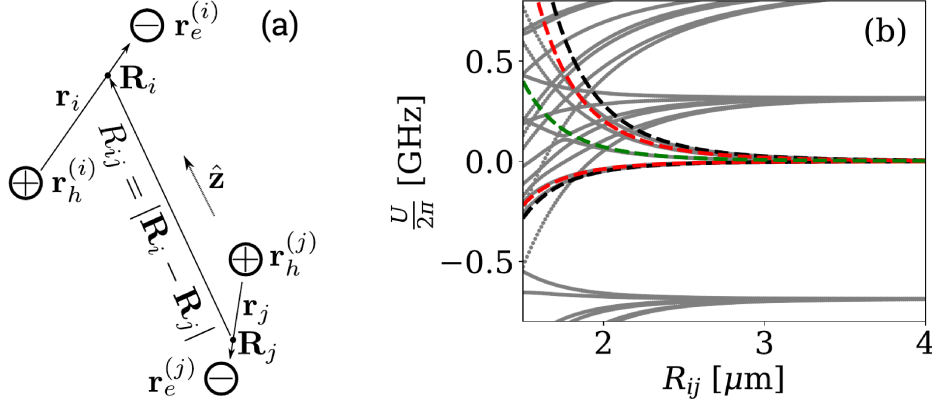


**Figure 3.5.:** (a): Schematic representation of the two-exciton problem with the center-of-mass coordinates  $\mathbf{R}_{i/j}$ , their separation  $R_{ij}$  and the internal coordinates  $\mathbf{r}_{i/j}$ . (b): Inter-excitonic Van der Waals potentials around the  $15P - 15P$  asymptote. The grey lines are derived from a complete diagonalisation while the coloured lines stem from the perturbation-theoretical ansatz in Eq. (3.43). The colours denote the absolute value of the total magnetic quantum number  $M = m_i + m_j$ ,  $|M| = 0$  (black),  $|M| = 1$  (red) and  $|M| = 2$  (green). Created by V. Walther [37].

excitonic Coulomb potentials, the two-exciton problem contains four inter-excitonic potentials

$$V^{ij} = \frac{e^2}{4\pi\epsilon} \left( \frac{1}{|\mathbf{r}_e^i - \mathbf{r}_e^j|} + \frac{1}{|\mathbf{r}_h^i - \mathbf{r}_h^j|} - \frac{1}{|\mathbf{r}_h^i - \mathbf{r}_e^j|} - \frac{1}{|\mathbf{r}_e^i - \mathbf{r}_h^j|} \right), \quad (3.38)$$

where  $i, j$  label the two excitons and e, h the electrons and holes. This potential can be rewritten by a multipole expansion which in the lowest nonvanishing order gives [37, 97]

$$V^{ij} \approx \mathcal{V}^{ij} = \frac{e^2}{4\pi\epsilon} \left( \frac{r_i r_j}{R_{ij}^3} - \frac{3 (\mathbf{r}_i \cdot \mathbf{R}_{ij}) (\mathbf{r}_j \cdot \mathbf{R}_{ij})}{R_{ij}^5} \right), \quad (3.39)$$

where  $\mathbf{r}_i, \mathbf{r}_j$  are the internal excitonic coordinates and  $\mathbf{R}_{ij} = \mathbf{R}_i - \mathbf{R}_j$  is the distance of the excitonic centers of mass. The full Van der Waals Hamiltonian in the Hilbert space of the two-exciton product-states  $|n_i, \ell_i, m_i; n_j, \ell_j, m_j\rangle$  does then take the form

$$\mathcal{H} = \mathcal{H}_i + \mathcal{H}_j + \mathcal{V}^{ij}, \quad (3.40)$$

with  $\mathcal{H}_i$  and  $\mathcal{H}_j$  denoting the Hamiltonians of the unperturbed excitons. The reduction to the lowest order in the multipole expansion and the neglect of exchange effects are only valid for sufficiently large separations of the two excitons [98]

$$R_{ij} \gg 2 \left( \sqrt{\langle r_i^2 \rangle} + \sqrt{\langle r_j^2 \rangle} \right). \quad (3.41)$$

For general separations that fulfil Eq. (3.41), the approach to calculate the two-exciton potentials is to expand the Hamiltonian  $\mathcal{H}$  in the unperturbed two-exciton states around the manifold of



interest and diagonalise it numerically. If the shifts due to the interaction are much smaller than the energetic separation of the unperturbed manifolds

$$\left| \langle n_i, \ell_i, m_i; n_j, \ell_j, m_j | \mathcal{V}^{ij} | n'_i, \ell'_i, m'_i; n'_j, \ell'_j, m'_j \rangle \right| \ll \left| E_{n_i, \ell_i} + E_{n_j, \ell_j} - E_{n'_i, \ell'_i} - E_{n'_j, \ell'_j} \right|, \quad (3.42)$$

however, the shifts are well approximated by second-order degenerate perturbation theory

$$\mathcal{H}_{\text{vdW}} = \sum_{\substack{\nu \in \mathcal{M} \\ \nu' \in \mathcal{M}}} \sum_{\alpha \notin \mathcal{M}} \frac{|\nu\rangle \langle \nu| \mathcal{V}^{ij} |\alpha\rangle \langle \alpha| \mathcal{V}^{ij} |\nu'\rangle \langle \nu'|}{E_{\mathcal{M}} - E_{\alpha}} = \sum_{\mu \in \mathcal{M}} \frac{C_6^{\mu}}{R_{ij}^6} |\mu\rangle \langle \mu|. \quad (3.43)$$

Here,  $\mathcal{M}$  denotes the degenerate manifold of interest,  $|\mu\rangle$  the eigenstates of  $\mathcal{H}_{\text{vdW}}$  and  $C_6^{\mu}$  the corresponding Van der Waals coefficients. For  $n = 15$ , this description, which yields the characteristic  $R_{ij}^{-6}$  scaling of the Van der Waals potential, agrees with the full numerical calculations already for  $R_{ij} \gtrsim 2.5 \mu\text{m}$  (see Fig. 3.5 (b)).

For rotationally symmetric excitons, the two-exciton problem retains a 2D rotational symmetry about the inter-excitonic axis, which guarantees that the total magnetic quantum number  $M = m_i + m_j$  stays a good quantum number. Due to time-inversion symmetry, two states that are connected by a flip of all magnetic quantum numbers are degenerate. Every state with  $M \neq 0$  does therefore have a degenerate partner state with  $M' = -M$  and the asymptotes can be labelled by  $|M|$ . Figure 3.6 shows the  $C_6$  coefficients for the  $S-S$  asymptotes and the  $P-P$  asymptotes. They do follow the expected  $n^{11}$  scaling rather smoothly with the small irregularity at  $n = 11$  in Fig. (b) arising from a near Förster-resonance between the manifolds  $|11P, 11P\rangle$  and  $|10D, 12D\rangle$  (and of course  $|12D, 10D\rangle$ ).

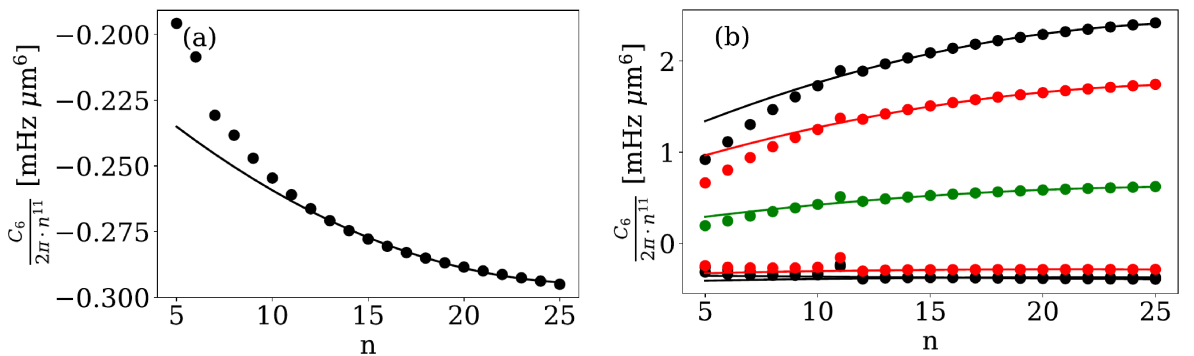


**Figure 3.6.:**  $C_6$  coefficients for the  $S-S$ -asymptotes (a) and  $P-P$ -asymptotes (b). The colour encodes  $|M|$  with black referring to  $|M| = 0$ , red to  $|M| = 1$  and green to  $|M| = 2$ . The dotted lines show the  $C_6$ -coefficients derived from a complete diagonalisation of  $\mathcal{H}$  given in Eq. (3.40) and the solid lines show fits of  $C_6(n) = n^{11}(c_0 + c_1 n + c_2 n^2)$  for  $n \geq 12$ . Created by V. Walther [37].

Even for the  $15P-15P$  asymptote, shifts on the order of  $2\pi 0.5 \text{ GHz}$  are achievable at distances of  $R_{ij} \sim 2 \mu\text{m}$  (see Fig. 3.5 (b)). This corresponds to  $\sim 2 \mu\text{eV}$  and thereby roughly one fifth of the linewidth of the  $15P$  state. As a shift of about one linewidth is necessary in order to achieve

complete blockade and the potentials depend so strongly on both  $R_{ij}$  and  $n$ , the blockade may be a factor in the observed intensity-dependent bleaching. For a more in-depth analysis, a detailed investigation of the exciton densities is necessary.

## Chapter 4.

### Strain traps for Rydberg excitons

In order to tune the interaction of Rydberg systems, precise control over their relative positions is vital, ideally below the length scale of the blockade radius. In atomic Rydberg physics, different trapping schemes are routinely employed, among the most ubiquitous of which are the so-called **optical dipole traps** [99]. These exploit the AC Stark shift of a neutral atom in an intense light field which, for a two-level atom, shifts the ground state downwards if the light is red-detuned relative to the main transition and upwards if it is blue-detuned, resulting in high-field seeking and low-field seeking ground-state atoms, respectively. It is therefore possible to trap atoms in the waist of a Gaussian beam, at the singularity in the center of a Laguerre-Gaussian beam, create optical lattices by interference of multiple beams or create even more sophisticated trap geometries by the use of spatial light modulators. This versatility is one reason why optical dipole traps are often the trapping mechanism of choice in experiments on cold atoms. They are, however, only applicable to cold atoms as typical trap depths are only on the order of  $\Delta E \lesssim 100 \mu\text{K } k_B$  [99]. The application of optical dipole traps to excitons is under investigation, but the lowest experimental temperatures achieved thus far are only  $\sim 50 \text{ mK}$  [19], almost three orders of magnitude higher than the typical atomic trap depths. Furthermore, suitable excitonic transitions for the realisation of excitonic dipole traps have to be identified. The separation of adjacent Rydberg states of the yellow series is on the order of  $100 \mu\text{eV}$  corresponding to wavelengths of a couple mm, far longer than the natural localisation of these states due to the crystal dimension and the diameter of the exciting beam. Possible candidates might be the transitions to Rydberg excitons of other series, which will be discussed in Chapter 5.

In the pursuit of excitonic BEC of the  $1S$  paraexciton in  $\text{Cu}_2\text{O}$ , another trapping mechanism has been thoroughly tested [100, 101, 102, 103, 104, 105, 106, 107, 108], namely the potentials arising from an inhomogeneous straining of the crystal. Strain distorts the crystal structure and alters the band structure of the material. The local energy shifts emanating from these changes in the band structure can be interpreted as effective potentials for the excitons which can reach trap depths of  $10 \text{ meV} \approx 100 \text{ K } k_B$ . In this Chapter, the application of such strain potentials to the Rydberg excitons will be investigated, using the example of waveguide potentials induced by a cylindrical stressor pressed onto the crystal surface [109] (see Fig. 4.1). This geometry does only

serve as an example of what is possible, inspired by one particular trap geometry of optical dipole traps often employed in atomic physics. It will be assumed that the strain is homogeneous over the extension of the exciton which allows us to derive a local band structure which governs the excitonic dynamics. If the length scale on which the strain field varies becomes comparable to the extension of the excitonic states of interest, the description becomes significantly more involved as this would result in separate potentials for both electron and hole, preventing the separation of the coordinates, and a spatially varying effective mass.

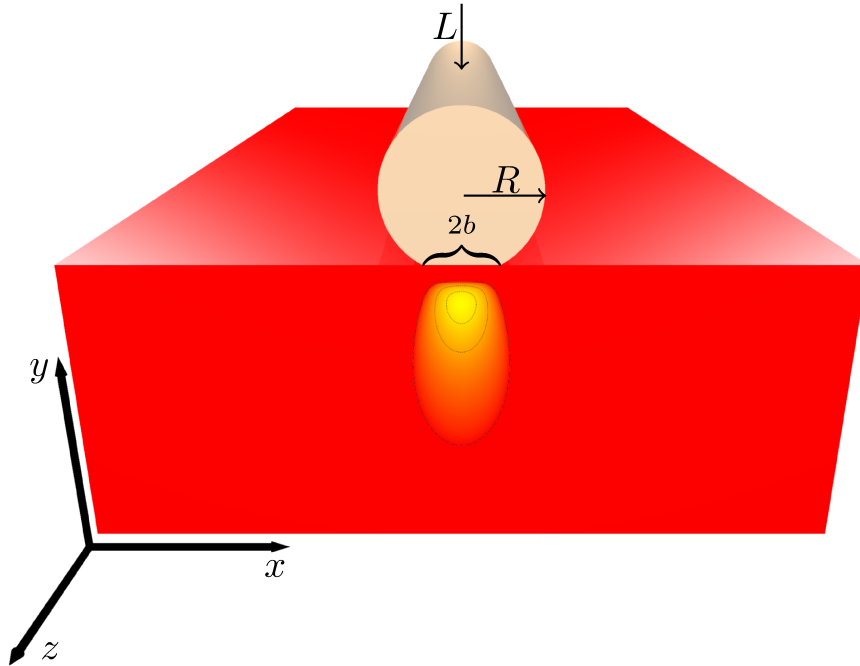


**Figure 4.1.:** Schematic of the setup with a cylindrical stressor pressed onto a  $\text{Cu}_2\text{O}$  crystal and the strain potential induced by it.  $R$  denotes the radius of the stressor,  $L$  the line load (force per unit length) and  $2b$  the width of the contact area.

#### 4.1. Continuum mechanics

Crystals deform under the influence of stress which is usually described in terms of the second-rank tensor defined by [110]

$$\sigma_{x_i x_j} = \frac{d^2 F_{x_j}}{dx_j dx_k}. \quad (4.1)$$

Here,  $dF_{x_i}$  denotes the normal force acting along the  $x_i$ -axis on some infinitesimal cubic volume and  $\{x_i, x_j, x_k\}$  denotes some cyclic permutation of  $\{x, y, z\}$ . The diagonal elements of  $\sigma$ , which has to be symmetric in mechanical equilibrium, describe the normal pressure acting on the faces of the infinitesimal cube while the off-diagonal elements describe the shear stresses. The deformation

induced by the stress can be described by the displacement vector  $\mathbf{u}(\mathbf{r})$  or, in the linear elastic regime, by the strain tensor  $\epsilon$  which is defined as the symmetric tensor

$$\epsilon_{x_i x_j} = \frac{1}{2} \left( \frac{\partial u_{x_i}(\mathbf{r})}{\partial x_j} + \frac{\partial u_{x_j}(\mathbf{r})}{\partial x_i} \right). \quad (4.2)$$

The coordinate transformation under strain is then given by  $\mathbf{r}' = \mathbf{r} + \mathbf{u}(\mathbf{r}) \approx (\mathbf{1} + \epsilon) \mathbf{r}$ . The antisymmetric equivalent to  $\epsilon$ , ignored here, corresponds to a rotation of the coordinate system. The strain tensor does therefore have six independent components, which in the elastic regime are connected to the six components of the stress tensor  $\sigma$  by **Hooke's law**

$$\begin{pmatrix} \epsilon_{xx} \\ \epsilon_{yy} \\ \epsilon_{zz} \\ \epsilon_{yz} \\ \epsilon_{zx} \\ \epsilon_{xy} \end{pmatrix} = \begin{pmatrix} S_{11} & S_{12} & S_{12} & 0 & 0 & 0 \\ S_{12} & S_{11} & S_{12} & 0 & 0 & 0 \\ S_{12} & S_{12} & S_{11} & 0 & 0 & 0 \\ 0 & 0 & 0 & S_{44}/2 & 0 & 0 \\ 0 & 0 & 0 & 0 & S_{44}/2 & 0 \\ 0 & 0 & 0 & 0 & 0 & S_{44}/2 \end{pmatrix} \cdot \begin{pmatrix} \sigma_{xx} \\ \sigma_{yy} \\ \sigma_{zz} \\ \sigma_{yz} \\ \sigma_{zx} \\ \sigma_{xy} \end{pmatrix}. \quad (4.3)$$

The material constants  $S_{11}$ ,  $S_{12}$  and  $S_{44}$  are the **compliance constants** for a material with cubic symmetry, assuming that the Cartesian axes relative to which the tensors are defined coincide with the cubic symmetry axes of the crystal. In an elastically isotropic material<sup>1</sup>, only two of these parameters are independent and one may set  $S_{44} = 2(S_{11} - S_{12})$ . The parameter  $A = 2(S_{11} - S_{12})/S_{44}$  can therefore be interpreted as a measure for the elastic anisotropy and takes the value  $A = 1.48$  in cuprous oxide. Many other conventions for the choice of the two isotropic compliance constants exist, for example using **Young's modulus**  $Y = 1/S_{11}$  and the **Poisson ratio**  $\nu = -S_{12}/S_{11}$ . The transformation in Eq. (4.3) can of course be inverted  $\sigma = C \cdot \epsilon$  with three independent **elastic constants**  $C_{11}$ ,  $C_{12}$  and  $C_{44}$  for a material with cubic symmetry [111].

In the mechanical equilibrium and the absence of any body forces acting on the solid, the components of the stress tensor have to fulfil [110]

$$\nabla^T \sigma(\mathbf{r}) = \mathbf{0}^T. \quad (4.4)$$

At the same time, the components of the strain tensor have to fulfil the compatibility relations

$$2 \frac{\partial^2 \epsilon_{xy}(\mathbf{r})}{\partial x \partial y} = \frac{\partial^2 \epsilon_{xx}(\mathbf{r})}{\partial y^2} + \frac{\partial^2 \epsilon_{yy}(\mathbf{r})}{\partial x^2}, \quad (4.5)$$

$$2 \frac{\partial^2 \epsilon_{yz}(\mathbf{r})}{\partial y \partial z} = \frac{\partial^2 \epsilon_{yy}(\mathbf{r})}{\partial z^2} + \frac{\partial^2 \epsilon_{zz}(\mathbf{r})}{\partial y^2}, \quad (4.6)$$

<sup>1</sup>For example an amorphous solid such as glass or a crystal with grain sizes that are small compared to the characteristic length scale of the strain distribution.

$$2 \frac{\partial^2 \epsilon_{zx}(\mathbf{r})}{\partial z \partial x} = \frac{\partial^2 \epsilon_{zz}(\mathbf{r})}{\partial x^2} + \frac{\partial^2 \epsilon_{xx}(\mathbf{r})}{\partial z^2}, \quad (4.7)$$

$$\frac{\partial^2 \epsilon_{xx}(\mathbf{r})}{\partial y \partial z} = \frac{\partial}{\partial x} \left[ -\frac{\partial \epsilon_{yz}(\mathbf{r})}{\partial x} + \frac{\partial \epsilon_{zx}(\mathbf{r})}{\partial y} + \frac{\partial \epsilon_{xy}(\mathbf{r})}{\partial z} \right], \quad (4.8)$$

$$\frac{\partial^2 \epsilon_{yy}(\mathbf{r})}{\partial z \partial x} = \frac{\partial}{\partial y} \left[ \frac{\partial \epsilon_{yz}(\mathbf{r})}{\partial x} - \frac{\partial \epsilon_{zx}(\mathbf{r})}{\partial y} + \frac{\partial \epsilon_{xy}(\mathbf{r})}{\partial z} \right], \quad (4.9)$$

$$\frac{\partial^2 \epsilon_{zz}(\mathbf{r})}{\partial x \partial y} = \frac{\partial}{\partial z} \left[ \frac{\partial \epsilon_{yz}(\mathbf{r})}{\partial x} + \frac{\partial \epsilon_{zx}(\mathbf{r})}{\partial y} - \frac{\partial \epsilon_{xy}(\mathbf{r})}{\partial z} \right], \quad (4.10)$$

which guarantee that the strain tensor does indeed correspond to a displacement field  $\mathbf{u}(\mathbf{r})$ . With the relations given above, the problem can be formulated both in terms of the components of the strain tensor or those of the displacement vector.

One can show from Eqs. (4.4 – 4.7) that for an elastically isotropic material, the traces of both the stress and the strain tensor have to fulfil the Laplace equation  $\nabla^2 \text{Tr}[\boldsymbol{\sigma}(\mathbf{r})] = \nabla^2 \text{Tr}[\boldsymbol{\epsilon}(\mathbf{r})] = 0$ . This implies that they, like all harmonic functions, must assume their global extrema in any bounded domain on the boundary of that domain and that they may not have a local extremum inside the domain<sup>2</sup> [112]. In the case of an elastically isotropic, strained crystal,  $\text{Tr}[\boldsymbol{\epsilon}]$  may only have any extrema on the crystal surface. This observation has implications for the achievable potential geometries in the low-strain regime as will be shown later in this Chapter.

#### 4.1.1. Hertzian contact theory

The treatment of contact problems is often complicated by the fact that the objects under stress tend to deform. In this way not only the geometry of the bodies but also their contact area changes depending on the applied stress. In the limit of two bodies whose radius of curvature is large compared to the size of the contact area, the problem can be treated as that of two half spaces loaded over their mutual contact area. This description, pioneered by H. Hertz and M. T. Huber at the turn of twentieth century [113, 114], yields analytical solutions for some geometries with elastically isotropic materials and is called **Hertzian contact theory**. The special case of two cylinders in contact along a generatrix, which contains a cylinder pressed onto a half space as a limiting case, has been treated by E. McEwen [115]. With the orientation of the coordinate system<sup>3</sup> as indicated in Fig. 4.1, the stress tensor does then take the form<sup>4</sup>

$$\sigma_{xx} = -\hat{\sigma} \left[ m - 2\tilde{y} + m \frac{\tilde{y}^2 + n^2}{n^2 + m^2} \right], \quad (4.11)$$

<sup>2</sup>Except for the trivial case, in which the harmonic function is constant.

<sup>3</sup>Contrary to Fig. 4.1, however, the origin of the coordinate system is placed at the center of the contact zone.

<sup>4</sup>Note that the definitions of the components  $\sigma_{zz}$  and  $\sigma_{xy}$  contain a sign error in the original article [115, 116] (given there as  $\hat{x}\hat{x} = \sigma_{xx}$  and  $\hat{y}\hat{z} = \sigma_{yz}$  due to a different orientation of the coordinate system). As given there, the strain-tensor component  $\epsilon_{zz}$  does not vanish as required for a plane strain, and the stress tensor does not fulfil the equations of mechanical equilibrium (4.4).

$$\sigma_{yy} = -\hat{\sigma} \left[ m - m \frac{\tilde{y}^2 + n^2}{m^2 - n^2} \right], \quad (4.12)$$

$$\sigma_{zz} = -2\hat{\sigma} \nu [m - \tilde{y}], \quad (4.13)$$

$$\sigma_{xy} = -\hat{\sigma} \left[ n \frac{m^2 - \tilde{y}^2}{m^2 + n^2} \right], \quad (4.14)$$

$$\sigma_{yz} = \sigma_{zx} = 0. \quad (4.15)$$

Here,  $(\tilde{x}, \tilde{y}, \tilde{z})^T = b^{-1}(x, y, z)^T$  denotes the dimensionless coordinates,  $\hat{\sigma}$  the maximum stress at the center of the contact zone and the quantities  $m$  and  $n$  are defined by

$$m = \frac{\tilde{y}}{\sqrt{2}|\tilde{y}|} \sqrt{(1 - \tilde{x}^2 + \tilde{y}^2) + \sqrt{(1 - \tilde{x}^2 + \tilde{y}^2)^2 + 4\tilde{x}^2\tilde{y}^2}}, \quad (4.16)$$

$$n = \frac{\tilde{x}}{\sqrt{2}|\tilde{x}|} \sqrt{(\tilde{x}^2 - 1 - \tilde{y}^2) + \sqrt{(1 - \tilde{x}^2 + \tilde{y}^2)^2 + 4\tilde{x}^2\tilde{y}^2}}. \quad (4.17)$$

Note, that the strain field is scale invariant. For a fixed  $\hat{\sigma}$  but variable stressor properties, the strain field is simply stretched according to the characteristic length scale  $b$  and does not change otherwise. The characteristic length scale, which is the half-width of the contact area, is given by

$$b = 2|\hat{\sigma}| R (\Theta_{\text{Cu}_2\text{O}} + \Theta_{\text{stressor}}) \quad (4.18)$$

with  $\Theta = (1 - \nu^2)/Y$ , the Poisson ratio  $\nu$ , Young's modulus  $Y$  and the radius  $R$  of the stressor. The line load shown in Fig. 4.1 is connected to the maximum stress via  $L = \hat{\sigma}\pi b/2$ . As required by symmetry, the stress tensor is one of plane strain, i.e. one resulting in  $\epsilon_{zz} = \epsilon_{yz} = \epsilon_{zx} = 0$ .

The relevant components of both the stress and strain tensor are shown in Fig. 4.2. Numerical calculations employing the finite element method (FEM) are shown for comparison in the panels (c) – (e). They were performed on a domain  $x \in [-20b, 20b]$  and  $y \in [-40b, 0]$  with the Neumann boundary conditions at  $y = 0$ , implied by the Hertzian results. At all other boundaries, the Dirichlet boundary condition  $\mathbf{u}(\mathbf{r}) = \mathbf{0}$  was used. The isotropic case reproduces the Hertzian results as expected, except for the component  $\epsilon_{xy}$ . The FEM result deviates from the Hertzian result by a factor of  $A = 1.48$  due to the fact that elastic isotropy implies a different conversion for the off-diagonal elements with  $\epsilon_{xy} = (S_{11} - S_{12}) \sigma_{xy}$ . The panels (d) and (e) compare the strain tensor for different orientations of the main crystal axes of  $\text{Cu}_2\text{O}$  relative to the crystal surface and stressor.

It can be seen that the assumption of elastic isotropy does not significantly alter the general structure of the strain field but may introduce relative deviations on the order of 20%. This means that the overall potential geometries do not depend on the assumption of elastic isotropy but the maximum stress  $\hat{\sigma}$  needed to achieve a certain trap depth might. Similar conclusions have been

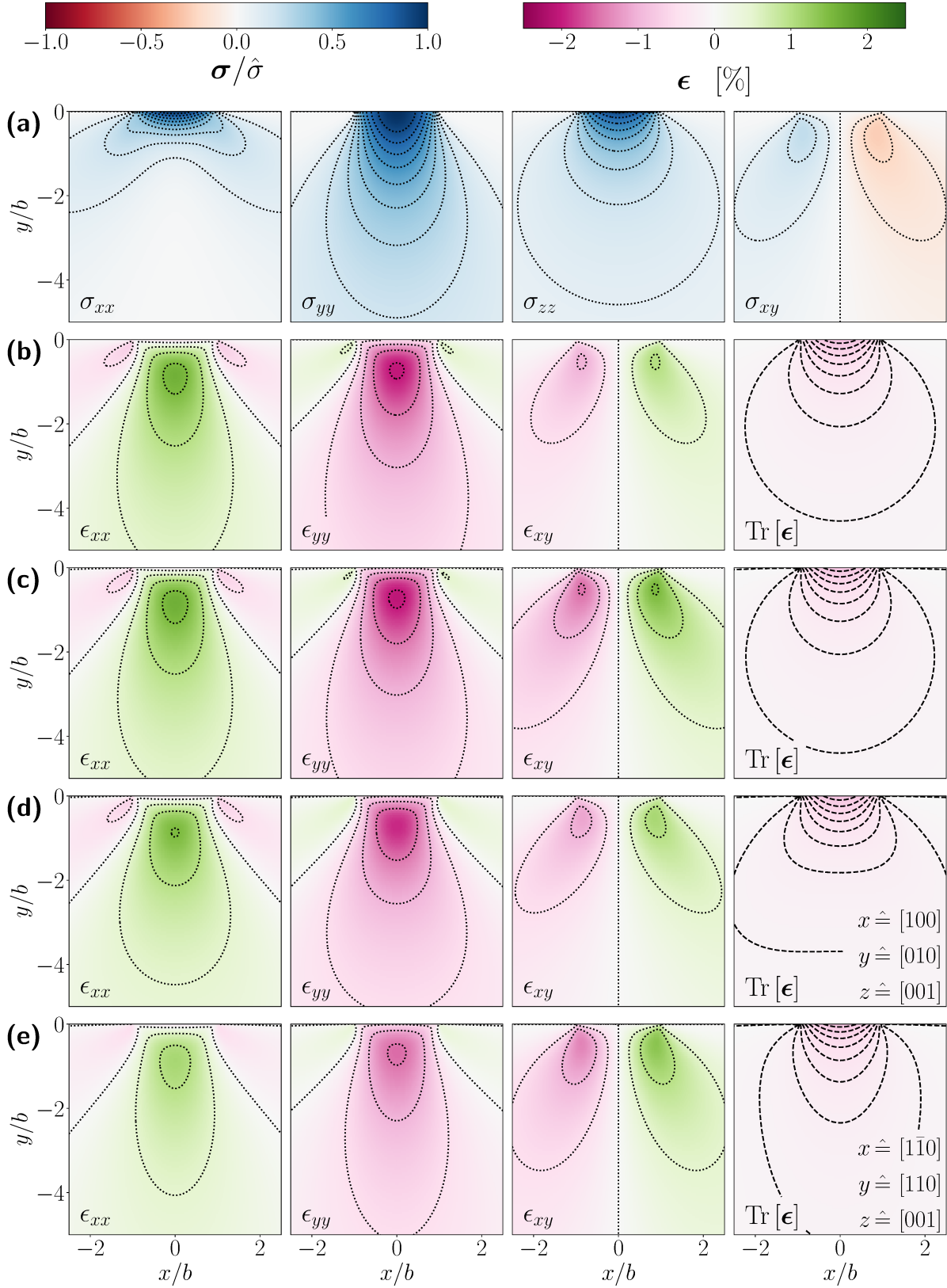


**Figure 4.2.:** (a) and (b): Stress and strain tensor according to Eqs. (4.3, 4.11–4.15) for the Poisson ratio  $\nu = -S_{12}/S_{11} = 0.464$  and Young's modulus  $Y = 1/S_{11} = 23.99$  GPa.

(a): Stress tensor in units of the maximum stress  $\hat{\sigma}$ . The contour lines denote multiples of  $0.1 \hat{\sigma}$ .  
 (b): Corresponding strain tensor for a compressive stress of  $\hat{\sigma} = -1$  GPa. The contour lines denote multiples of  $0.5\%$  (dotted) or multiples of  $0.1\%$  (dashed).

(c – e): Strain tensor from FEM calculations for the elastically isotropic case (c) and the anisotropic case (d, e) with two different orientations of the crystal axes relative to the stressor.



reached for germanium [117]. We will thus take the approach often employed in the literature [102, 103, 105, 106, 107, 109] and proceed using the results from Hertzian contact theory.

## 4.2. Band structures of strained crystals

As stated before, the influence of strain cannot readily be interpreted as a small perturbation of the crystal Hamiltonian. Strain changes the periodicity of the crystal potential which may lead to very large local changes in both the potential and the wave functions, even at low strain. Starting from the  $\mathbf{k} \cdot \mathbf{p}$ -Hamiltonian of the strained crystal [68, 58, 59]

$$\begin{aligned} \mathcal{H}_{\mathbf{k}\mathbf{p}}^{(\epsilon)} = & \frac{\mathbf{p}^2}{2m_0} + V_\epsilon(\mathbf{r}) + \frac{\hbar}{m_0} \mathbf{k} \cdot \left( \mathbf{p} + \frac{\hbar}{4m_0c^2} [\boldsymbol{\sigma} \times \nabla V_\epsilon(\mathbf{r})] \right) \\ & + \frac{\hbar^2 \mathbf{k}^2}{2m_0} + \frac{\hbar}{4m_0^2c^2} [\boldsymbol{\sigma} \times \nabla V_\epsilon(\mathbf{r})] \cdot \mathbf{p} \end{aligned} \quad (4.19)$$

with the crystal potential  $V_\epsilon(\mathbf{r})$ , one can however retrieve the periodicity of the unstrained crystal via the inverse strain transformation  $\mathbf{r} \approx (\mathbf{1} + \epsilon) \cdot \mathbf{r}'$ . This transformation implies<sup>5</sup> both  $\mathbf{p} \approx (\mathbf{1} - \epsilon) \cdot \mathbf{p}'$  as well as  $\mathbf{p}^2 \approx \mathbf{p}'^2 - 2\mathbf{p}' \cdot \epsilon \cdot \mathbf{p}'$  and the rewritten Hamiltonian takes the form

$$\begin{aligned} \mathcal{H}_{\mathbf{k}\mathbf{p}'}^{(\epsilon)} = & \frac{\mathbf{p}'^2}{2m_0} - \frac{\mathbf{p}' \cdot \epsilon \cdot \mathbf{p}'}{m_0} + V_\epsilon((\mathbf{1} + \epsilon) \cdot \mathbf{r}') \\ & + \frac{\hbar}{m_0} \mathbf{k} \cdot \left( (\mathbf{1} - \epsilon) \cdot \mathbf{p}' + \frac{\hbar}{4m_0c^2} [\boldsymbol{\sigma} \times [(\mathbf{1} - \epsilon) \cdot \nabla' V_\epsilon((\mathbf{1} + \epsilon) \cdot \mathbf{r}')] ] \right) \\ & + \frac{\hbar^2 \mathbf{k}^2}{2m_0} + \frac{\hbar}{4m_0^2c^2} [\boldsymbol{\sigma} \times [(\mathbf{1} - \epsilon) \cdot \nabla' V_\epsilon((\mathbf{1} + \epsilon) \cdot \mathbf{r}')] ] \cdot (\mathbf{1} - \epsilon) \cdot \mathbf{p}'. \end{aligned} \quad (4.20)$$

The transformed crystal potential can be approximated by a Taylor series up to first order in the components of  $\epsilon$

$$\begin{aligned} V_\epsilon((\mathbf{1} + \epsilon) \cdot \mathbf{r}') & \approx V(\mathbf{r}') + \sum_{i,j} \frac{\epsilon_{ij}}{2 - \delta_{i,j}} \left[ \frac{\partial}{\partial \epsilon_{ij}} V_\epsilon((\mathbf{1} + \epsilon) \cdot \mathbf{r}') \right]_{\epsilon=0} \\ & = V(\mathbf{r}') + \sum_{i,j} \frac{\epsilon_{ij}}{2 - \delta_{i,j}} V^{ij}(\mathbf{r}'), \end{aligned} \quad (4.21)$$

<sup>5</sup>These transformations assume that the strain is small and all terms of higher than first order in the strain tensor can be neglected. The geometric series does therefore yield  $(\mathbf{1} + \epsilon)^{-1} \approx \mathbf{1} - \epsilon$ .

where  $V(\mathbf{r}')$  is the potential of the unstrained crystal and the factor  $1/(2 - \delta_{i,j})$  corrects the double counting of the off-diagonal elements [58]. Inserting all this into Eq. (4.20) yields

$$\begin{aligned} \mathcal{H}_{\mathbf{k},\mathbf{p}'}^{(\epsilon)} = & \mathcal{H}_{\mathbf{k},\mathbf{p}'} - \frac{\mathbf{p}' \cdot \boldsymbol{\epsilon} \cdot \mathbf{p}'}{m_0} + \sum_{i,j} \frac{\epsilon_{ij}}{2 - \delta_{i,j}} V^{ij}(\mathbf{r}') - \frac{\hbar}{m_0} \mathbf{k} \cdot \boldsymbol{\epsilon} \cdot \mathbf{p}' \\ & + \frac{\hbar}{4m_0^2 c^2} \left[ \boldsymbol{\sigma} \times \left[ \nabla' \sum_{i,j} \frac{\epsilon_{ij}}{2 - \delta_{i,j}} V^{ij}(\mathbf{r}') - \boldsymbol{\epsilon} \cdot \nabla' V(\mathbf{r}') \right] \right] \cdot (\hbar \mathbf{k} + \mathbf{p}') \\ & - \frac{\hbar}{4m_0^2 c^2} [\boldsymbol{\sigma} \times \nabla' V(\mathbf{r}')] \cdot \boldsymbol{\epsilon} \cdot \mathbf{p}', \end{aligned} \quad (4.22)$$

where terms of second or higher order in  $\epsilon$  have again been ignored. The physical wave functions  $\psi_{n,\mathbf{k}}^\epsilon(\mathbf{r})$  of the strained crystal Hamiltonian (4.19) can be retrieved from the eigenfunctions  $\phi_{n,\mathbf{k}}^\epsilon(\mathbf{r}')$  of the Hamiltonian (4.22) via the transformation  $\psi_{n,\mathbf{k}}^\epsilon(\mathbf{r}) = \phi_{n,\mathbf{k}}^\epsilon((\mathbf{1} - \boldsymbol{\epsilon}) \cdot \mathbf{r})$ .

In the low-strain regime, the result can indeed be interpreted as a small perturbation to the Hamiltonian of the unstrained crystal  $\mathcal{H}_{\mathbf{k},\mathbf{p}'}$ . We can therefore construct an effective strain Hamiltonian by the same approach as laid out in Sec. 2.2.2. The strain tensor is a symmetric second rank tensor that is even under both spatial inversion and time inversion. It does therefore transform in the same way as the symmetric terms of second order in the components of  $\mathbf{k}$ , namely according to the representation  $\Gamma_1^+ \oplus \Gamma_3^+ \oplus \Gamma_5^+$ . The valence-band strain-Hamiltonian<sup>6</sup> does therefore take a form analogous to Eq. (2.45) [66]

$$\begin{aligned} \mathcal{H}(\boldsymbol{\epsilon}) = & [D_1 + E_1 (\mathbf{I} \cdot \boldsymbol{\sigma})] \text{Tr}[\boldsymbol{\epsilon}] \quad | \Gamma_1^+ \\ & + \left[ D_2 \left( I_x^2 - \frac{1}{3} \mathbf{I}^2 \right) + E_2 \left( I_x \sigma_x - \frac{1}{3} \mathbf{I} \cdot \boldsymbol{\sigma} \right) \right] \epsilon_{xx} + \text{c.p.} \quad | \Gamma_3^+ \\ & + [D_3 (I_y I_z + I_z I_y) + E_3 (I_y \sigma_z + I_z \sigma_y)] \epsilon_{yz} + \text{c.p.} \quad | \Gamma_5^+ \end{aligned} \quad (4.23)$$

with the free parameters  $D_i, E_i$ , called **deformation potentials**. The parameters  $E_i$ , related to the strain-dependent change of the spin-orbit interaction, yield only minor corrections and are not precisely known. They will be neglected for the rest of this thesis, as is usually done in the literature [103, 105]. Analogously, the Hamiltonian for the  $\Gamma_6^+$  conduction band takes the form

$$\mathcal{H}_6(\boldsymbol{\epsilon}) = C_1 \text{Tr}[\boldsymbol{\epsilon}]. \quad (4.24)$$

The translational symmetries of a crystal will be altered by a homogeneous straining while the rotational symmetries may be completely broken. In the unstrained crystal, the position of every

<sup>6</sup>Note, that the indices of the strain tensor used here refer to the main symmetry axes of the crystal and not necessarily to the coordinate system used in Fig. 4.1.

atom can be written as

$$\mathbf{r}_{i,j}^\nu = \mathbf{R}_i + \mathbf{s}_{\nu_j} \quad (4.25)$$

where  $i$  denotes the unit cell,  $\mathbf{R}_i$  a lattice vector and  $\mathbf{s}_{\nu_j}$  the position of the  $j$ th atom of species  $\nu$  within the unit cell. The invariance of the crystal structure with respect to the application of a space-group element  $\{\alpha, \tau\}$  guarantees that for all atoms in the crystal  $\alpha \mathbf{r}_{i,j}^\nu + \tau = \mathbf{r}_{i',j'}^\nu$  is the position of an atom of the same species. In the low-strain regime, every atom is displaced according to  $\tilde{\mathbf{r}}_{i,j}^\nu = (\mathbf{1} + \epsilon) \mathbf{r}_{i,j}^\nu$ . It does therefore follow that for every space-group element  $\{\alpha, \tau\}$  whose pure rotation  $\alpha$  commutes with the strain tensor

$$(\mathbf{1} + \epsilon) (\alpha \mathbf{r}_{i,j}^\nu + \tau) = \alpha \tilde{\mathbf{r}}_{i,j}^\nu + (\mathbf{1} + \epsilon) \tau = (\mathbf{1} + \epsilon) \mathbf{r}_{i',j'}^\nu = \tilde{\mathbf{r}}_{i',j'}^\nu. \quad (4.26)$$

This suggests that if  $\{\alpha, \tau\}$  is a space-group element of the unstrained crystal and  $[\alpha, \epsilon] = 0$ , then  $\{\alpha, (\mathbf{1} + \epsilon) \tau\}$  is space-group element of the strained crystal. The point group of the strained crystal does thus consist of all elements of the unstrained crystal's point group that commute with the strain tensor.

The effect of these strain Hamiltonians on the band structure can be split into two effects which can be treated independently of one another. The first effect is a modification of the band gap  $\Delta E_g(\epsilon)$  due to the relative shift of the valence and conduction band at the zone center. The second effect is a distortion of the valence band which reduces the symmetry of the anisotropic Wannier equation, mixes the excitonic states and induces a binding energy shift  $\Delta E_b(\epsilon)$  for every state. As a homogeneous strain cannot break inversion symmetry, parity stays a good quantum number, and we may restrict our analysis to the odd-parity states which include the  $P$ -excitons and thereby the optically active Rydberg states. While  $\Delta E_g(\epsilon)$  depends only on the series but not on the excitonic state,  $\Delta E_b(\epsilon)$  depends strongly on the state. It is roughly proportional to the unperturbed binding energy and therefore generally much smaller for the Rydberg states. There is, in principle, a third contribution induced by a modification of the electron-hole exchange interaction [103] arising from the mixed terms of the exchange Hamiltonian in Eq. (3.3) and the strain Hamiltonian. The exchange interaction may, however, only affect even-parity states and will therefore be ignored in the remainder of this Section.

### 4.3. Band-gap shift

The band-gap shift is just the modification of the main band gap at the zone center and enters the Wannier equation as a constant offset which can be normalised away. It can be modelled by the Hamiltonian  $\mathcal{H}_6(\epsilon) - \mathcal{H}_{\text{so}} - \mathcal{H}(\epsilon)$  in the 12-dimensional basis of electron-hole product states. The shift can be retrieved either by complete diagonalisation or via perturbation theory, which yields in

third order

$$\begin{aligned} \Delta E_g(\epsilon) = & -D'_1 \text{Tr}[\epsilon] \\ & - \frac{2D_3^2 [\epsilon_{xy}^2 + \epsilon_{yz}^2 + \epsilon_{zx}^2]}{3\Delta_{\text{so}}} - \frac{D_2^2 [(\epsilon_{xx} - \epsilon_{yy})^2 + (\epsilon_{yy} - \epsilon_{zz})^2 + (\epsilon_{zz} - \epsilon_{xx})^2]}{9\Delta_{\text{so}}} \\ & - \frac{D_2^3 (\epsilon_{xx} + \epsilon_{yy} - 2\epsilon_{zz})(\epsilon_{xx} - 2\epsilon_{yy} + \epsilon_{zz})(-2\epsilon_{xx} + \epsilon_{yy} + \epsilon_{zz})}{27\Delta_{\text{so}}^2} + \frac{2D_3^3 \epsilon_{xy}\epsilon_{yz}\epsilon_{zx}}{\Delta_{\text{so}}^2} \\ & + \frac{D_2 D_3^2 [\epsilon_{xx}(\epsilon_{xy}^2 + \epsilon_{zx}^2 - 2\epsilon_{yz}^2) + \epsilon_{yy}(\epsilon_{xy}^2 + \epsilon_{yz}^2 - 2\epsilon_{zx}^2) + \epsilon_{zz}(\epsilon_{zx}^2 + \epsilon_{yz}^2 - 2\epsilon_{xy}^2)]}{3\Delta_{\text{so}}^2}. \end{aligned} \quad (4.27)$$

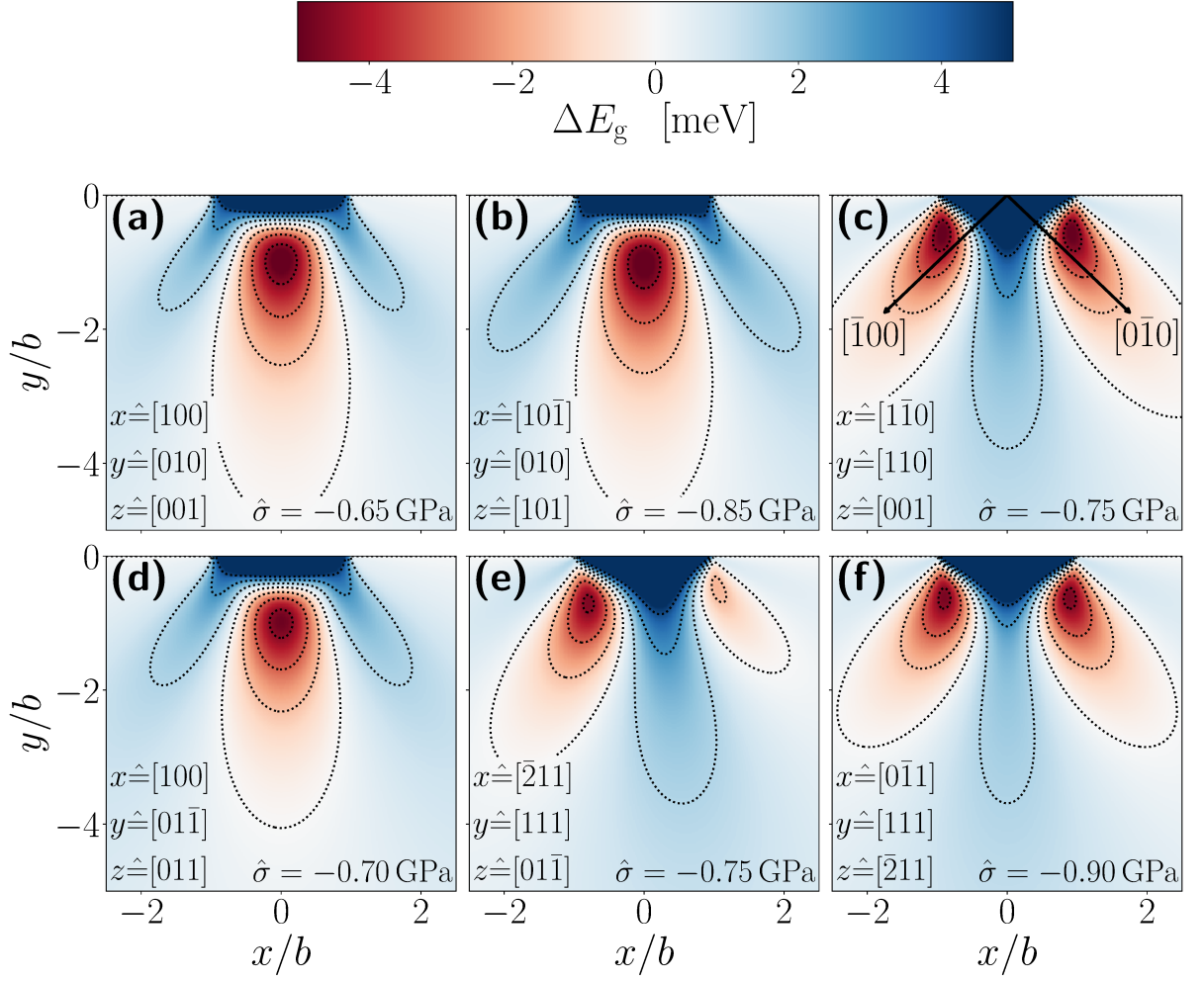
Here,  $D'_1 = D_1 - C_1$  is the relative deformation potential of conduction and valence band. One immediate observation regarding Eq. (4.27) is that the linear term, which dominates in the low-strain regime, is proportional to  $\text{Tr}[\epsilon]$ . The band-gap shift is therefore barred from developing any local extrema within the crystal if the approximations of low strain and elastic isotropy are applied simultaneously. The effect of the elastic anisotropy on  $\text{Tr}[\epsilon]$  is small as can be seen in Fig. 4.2 (c) – (e). It is therefore unclear whether local minima in  $\Delta E_g(\mathbf{r})$  are achievable at all in the regime where the linear term dominates. With the geometry discussed here, it is definitely not possible.

Figure 4.3 shows the potential contributions  $\Delta E_g(\mathbf{r})$  for a variety of different orientations of the stressor relative to the crystal axes. As can be seen, the orientation strongly influences the geometry and strength of the potential. At stresses used in typical experiments  $|\hat{\sigma}| < 1 \text{ GPa}$  [100, 103, 107], band-gap shifts on the order of a few meV are achievable. These experiments were, however, performed on macroscopic crystals, not the thin slabs (thickness  $\sim 30 \mu\text{m}$ ) used for the experiments on Rydberg excitons which might be significantly more prone to destruction under such conditions.

In the following, we will restrict the discussion to the situation shown in Fig. 4.3 (a), as we do not expect significant changes in the properties of the traps beyond the change in geometry. Figure 4.4 shows the derivatives of the strain potentials in  $y$  and  $x$ -direction. For low strain, the linear term yields a purely repulsive potential in  $y$ -direction (see Fig. (a)), repelling the excitons from the contact surface. A potential minimum may only form for a compressive stress  $|\hat{\sigma}| > 0.25 \text{ GPa}$ . For a reasonable definition of “trapped excitons”, an exciton has to be able to traverse the whole potential during its lifetime. This implies that the inverses of the trap frequencies

$$\omega_{x_i} = \sqrt{\frac{1}{M} \left. \frac{\partial^2 \Delta E(\mathbf{r})}{\partial x_i^2} \right|_{\mathbf{r}=\mathbf{r}_{\min}}} \quad (4.28)$$

have to be smaller than the excitonic lifetime  $\tau_{n,\ell}$ . The estimate of the excitonic lifetimes from the linewidths [18] results in estimates on the order of 100 ps for the 15P-states, which are of course only lower bounds. The Rydberg resonances in particular are subject to an additional broadening



**Figure 4.3.:** Band-gap shift  $\Delta E_g$  for different orientations of the stressor relative to the crystal axes and compressive stresses  $\hat{\sigma}$  such that the trap depths reach approximately  $-5$  meV. The contour lines denote multiples of 2 meV.

(see Fig. 2.8 or Chapter 6), whose influence on the lifetime is just as unknown as the influence of the strain. Figure 4.5 shows the trap frequencies and the characteristic length scale  $b$  for one particular stressor. At  $\hat{\sigma} = -0.65$  GPa, the half-width of the contact area is  $b \approx 30 \mu\text{m}$  compared to an exciton diameter of  $\langle 2r \rangle_{15P} \approx 0.75 \mu\text{m}$  for the  $15P$ -exciton. The approximation of a homogeneous strain over the exciton volume is therefore justified. The corresponding trap frequencies do, however, only reach  $\omega_x \approx 2 \text{ GHz} = (500 \text{ ps})^{-1}$  and the excitons cannot traverse the trap during their short lifetime. If  $\hat{\sigma}$  is kept fixed, the trap frequencies scale with  $\omega \propto b^{-1} \propto R^{-1}$ . Larger trap frequencies should therefore be attainable by the use of a stressor with a smaller radius  $R$ , just not in the confines of this theoretical description.

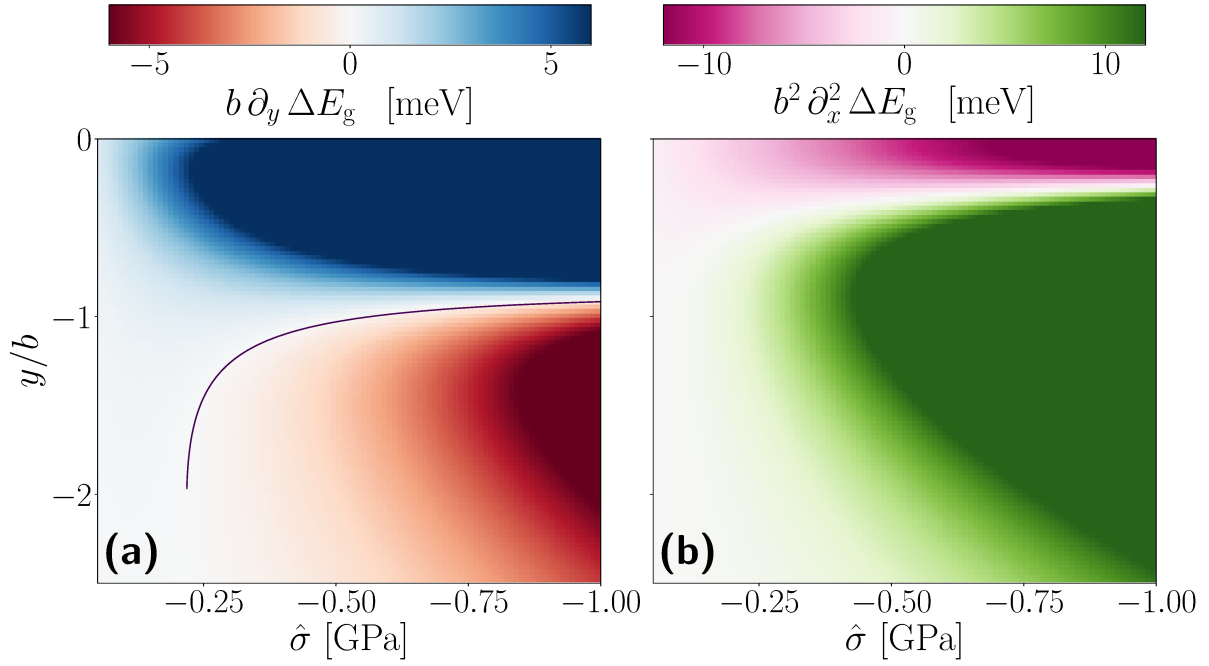


**Figure 4.4.:** Derivatives of the band-gap shift at  $x = 0$  for the geometry of Fig. 4.3 (a) in dependence of  $\hat{\sigma}$ . (a): First derivative in  $y$ -direction. The potential minimum is marked by the solid line. (b): Second derivative in  $x$ -direction. As the first derivative does always vanish at  $x = 0$ , a minimum in  $x$  direction exists wherever the second derivative is positive.

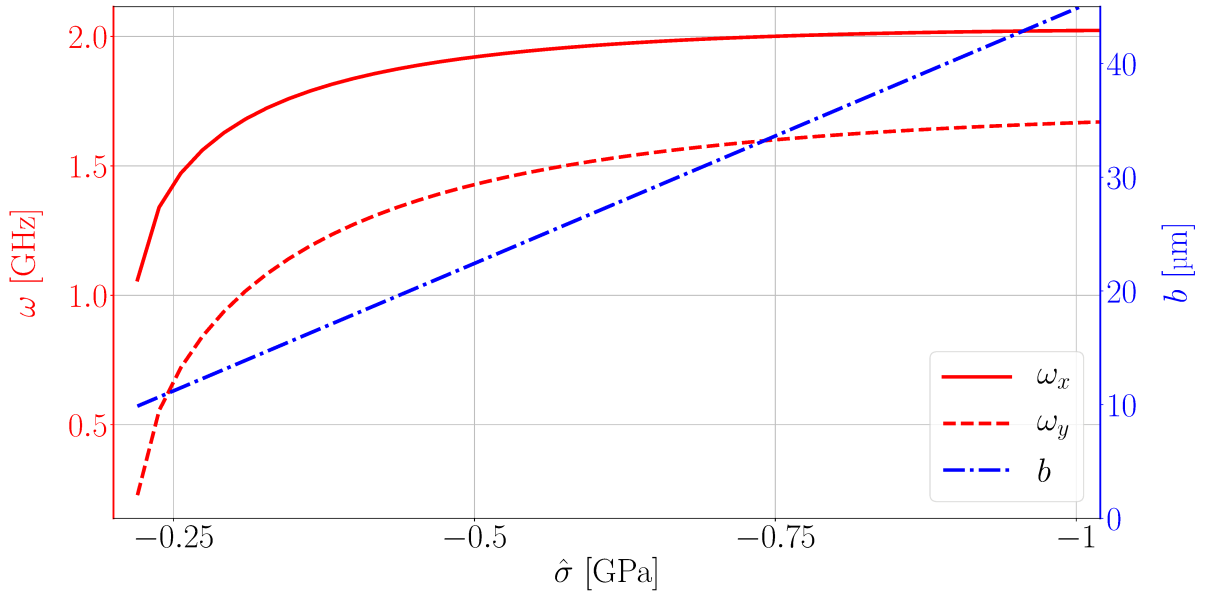


**Figure 4.5.:** Trap frequencies  $\omega_{x_i}$  and half-width of the contact zone  $b$  for different  $\hat{\sigma}$  and a glass stressor with  $Y = 75$  GPa,  $\nu = 0.3$  and a radius  $R = 0.5$  mm.

#### 4.4. Binding energy shift

In addition to the modification of the band gap, a state-dependent shift of the binding energy  $\Delta E_b$  is induced by the deformation of the valence band which can be modelled by a two-band model as presented in Chapter 3. The main differences are that due to the reduced symmetry of the strained crystal, different lattice harmonics have to be used in both the expansion of the band structure and the wave functions. Furthermore, the anisotropic mass leads to significantly slower convergence and much larger basis sets needed for the calculations to converge.

We will again restrict the analysis to the case in which the main crystal axes coincide with the axes of the macroscopic coordinate system (see Fig. 4.1). The strain tensor does then take the general form

$$\epsilon = \begin{pmatrix} \epsilon_{xx} & \epsilon_{xy} & 0 \\ \epsilon_{xy} & \epsilon_{yy} & 0 \\ 0 & 0 & 0 \end{pmatrix} \quad (4.29)$$

with the component  $\epsilon_{xy}$  vanishing at  $x = 0$  as well. The (local) point group of the strained crystal is thus  $D_{2h}$  at  $x = 0$  and  $C_{2h}$  everywhere else. The corresponding lattice harmonics are discussed in App. B.4. The single groups of both  $C_{2h}$  and  $D_{2h}$  contain only one-dimensional representations which implies that all degeneracies may potentially be lifted. For the  $P$ -states, for example, the splitting is given by  $\Gamma_1^- \oplus 2\Gamma_2^-$  in the case of  $C_{2h}$  and  $\Gamma_2^- \oplus \Gamma_3^- \oplus \Gamma_4^-$  in the case of  $D_{2h}$ .

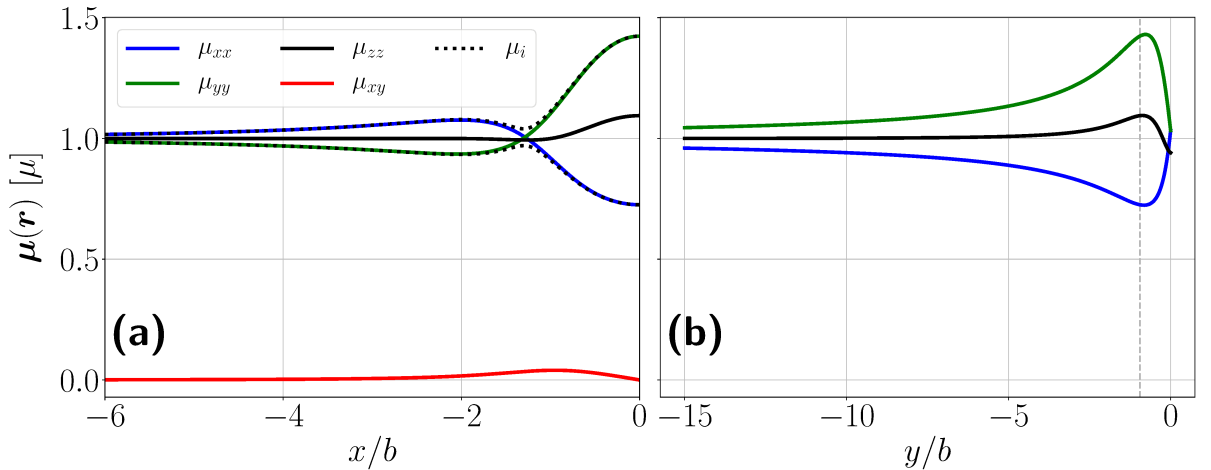


**Figure 4.6.:** Mass tensor  $\mu(r)$  of the reduced effective mass in units of the unperturbed exciton's reduced mass  $\mu = 0.356 m_0$ . All components not shown explicitly are zero by symmetry.

(a): In  $x$ -direction at  $y = -0.95b$ . The dotted lines indicate the eigenvalues  $\mu_i$ . (b): In  $y$ -direction at  $x = 0$  with the dashed vertical line marking  $y = -0.95b$ .  $\mu$  is already diagonal.

In the vicinity of the  $\Gamma$ -point, the most important effect of the distortion of the valence band is the introduction of an anisotropic effective mass which results in a strong coupling of the angular

momenta. The effective-mass Wannier equation including this anisotropy can be written as

$$\left[ \frac{\mathbf{p} \cdot \boldsymbol{\mu}^{-1} \cdot \mathbf{p}}{2} + V(r) \right] \phi(\mathbf{r}) = E_b \phi(\mathbf{r}). \quad (4.30)$$

The reduced effective-mass tensor  $\boldsymbol{\mu}$  can be assumed to be diagonal without loss of generality. If it is not, it can be chosen to be symmetric and then be diagonalised by an orthogonal transformation, i.e. a rotation of the coordinate system. The anisotropic Kepler problem described by Eq. (4.30) has ellipsoidal symmetry ( $D_{2h}$ ) and can be treated numerically by a straightforward extension of the elegant scheme put forward by D. Wintgen *et al.* [118]. Figure 4.6 shows the spatial variation of the components of  $\boldsymbol{\mu}$ . The reduced mass becomes asymptotically isotropic far away from the contact zone. In the region of the minimum of  $\Delta E_g$  around  $(x, y) \approx (0, -0.95)b$ , however, it becomes significantly anisotropic with the eigenvalues of  $\boldsymbol{\mu}$  being spread out over almost a factor of two.

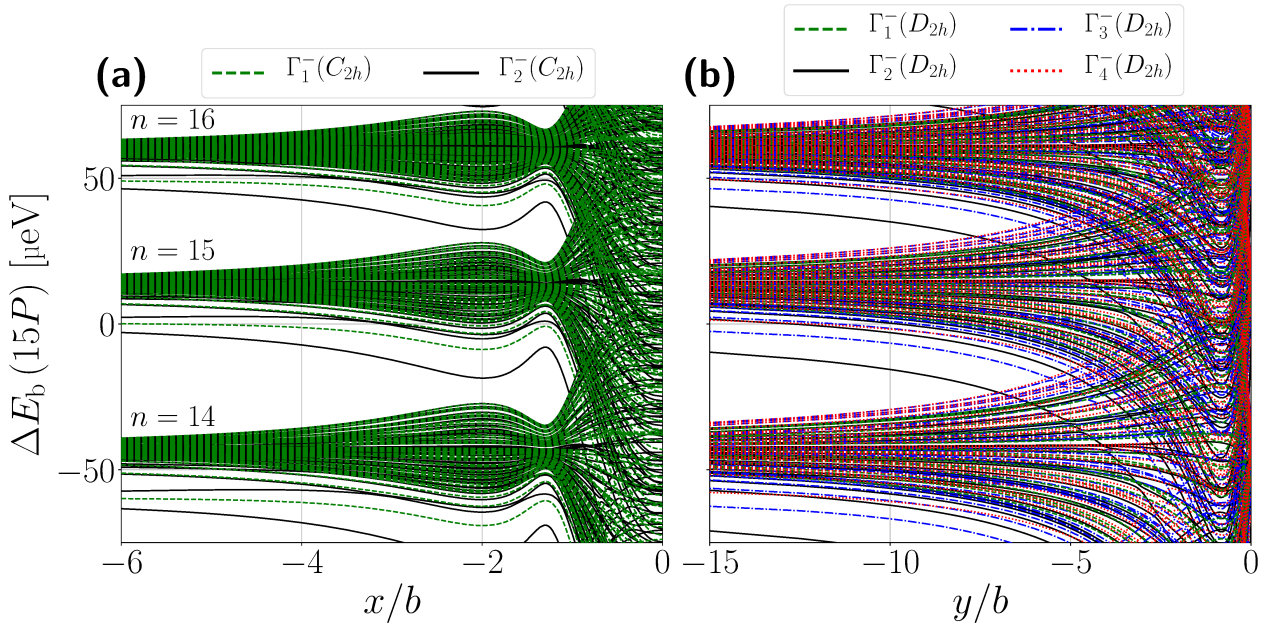


**Figure 4.7.:** Binding energies in the vicinity of the  $15P$  exciton relative to the unperturbed  $15P$  state at  $E_b(15P) = -397.4\mu\text{eV}$  on lines through the minimum of  $\Delta E_g$ . (a): in  $x$ -direction at  $y = -0.95b$ . (b): in  $y$ -direction at  $x = 0$ .

The binding energies in the vicinity of the unperturbed  $15P$  excitons derived from the non-parabolic, anisotropic Wannier equation are shown in Fig. 4.7. In these calculations, all states with a radial quantum number  $n_r = n - \ell - 1 \leq 29$  and  $\ell \leq 25$  had to be included in order to achieve convergence over the whole region. Outside the central region, the shifts seem to mirror the behaviour of the inverse mass tensor  $\boldsymbol{\mu}^{-1}$  which indicates that the main effect of the strain is indeed the introduction of an anisotropic effective mass.



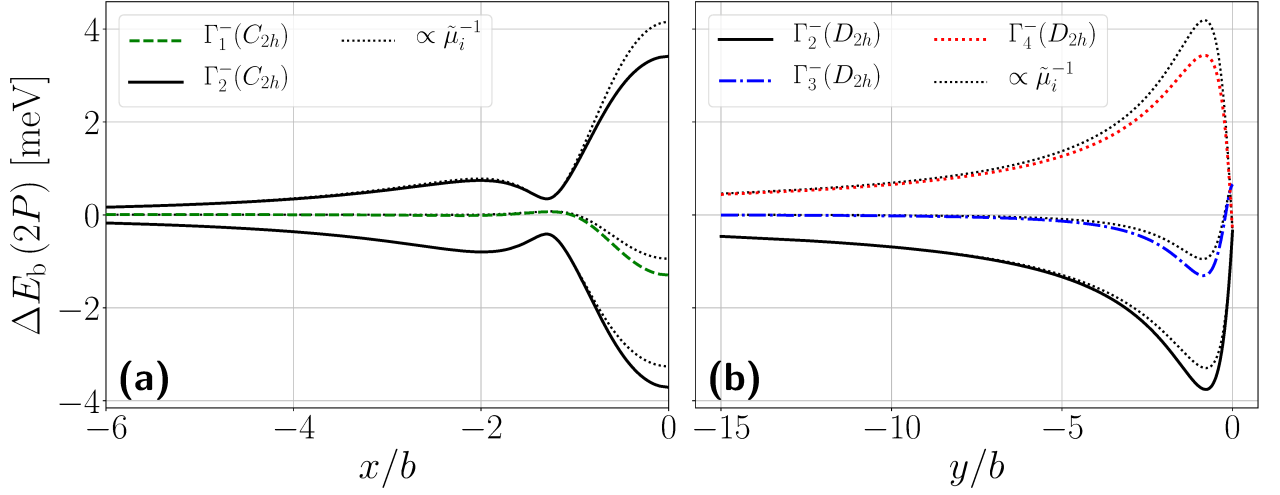


**Figure 4.8.:** Binding-energy shift  $\Delta E_b$  for the  $2P$ -excitons along the same lines as in Fig. 4.7. The black dotted lines are proportional to the eigenvalues  $\tilde{\mu}_i^{-1}$  of  $\tilde{\mu}^{-1}$  and are plotted for comparison.

Figure 4.8 shows the binding-energy shifts for the  $2P$ -excitons which are significantly larger due to the fact that the binding energy of the unperturbed manifold is larger as well. A comparison with Fig. 4.6 reveals that over most of the region shown there, the band-gap shifts are almost proportional to the eigenvalues of  $\tilde{\mu}^{-1} = \mu^{-1} - 1/\mu$ . This is not surprising as the Hamiltonian of Eq. (4.30) can be written as

$$\mathcal{H}_0 + \frac{\mathbf{p} \cdot \tilde{\mu}^{-1} \cdot \mathbf{p}}{2} \quad (4.31)$$

where  $\mathcal{H}_0$  is the Hamiltonian of the isotropic Wannier equation in effective-mass approximation. If  $\tilde{\mu}^{-1}$  is assumed to be diagonal and its trace vanishes (as is the case), the projection of the anisotropic term onto the  $2P$ -manifold will be proportional to  $\tilde{\mu}^{-1}$ , if the Cartesian basis

$$\{Y_x, Y_y, Y_z\} = \left\{ \sqrt{\frac{1}{2}} (Y_1^{-1} - Y_1^1), i\sqrt{\frac{1}{2}} (Y_1^{-1} + Y_1^1), Y_1^0 \right\} \quad (4.32)$$

is used. The binding-energy shift of the  $2P$ -states can therefore be expected to show the observed proportionality as long as the coupling to other manifolds as well as the change in the nonparabolicity can be neglected. Comparing Figs. 4.7 and 4.8, it can be seen that  $\Delta E_b$  is roughly proportional to the binding energies of the unperturbed states  $E_b(2P) = -24.57 \text{ meV}$  and  $E_b(15P) = -397.4 \mu\text{eV}$ . At  $x = -2b$ , for example, the lowest states are shifted downwards by  $\Delta E_b(2P) = -0.80 \text{ meV} = 3.25\% E_b(2P)$  and  $\Delta E_b(15P) = -18.6 \mu\text{eV} = 4.7\% E_b(15P)$ . While the magnitudes of  $\Delta E_b$  are comparable to  $\Delta E_g$  for the  $2P$ -states, they are considerably smaller for the  $15P$ -manifold. In fact, as a contribution to the potential, they are negligible for the Rydberg states. The strong mixing of the states near the center of the trap, however, must be taken into account.

## 4.5. Conclusion

We have shown in this Chapter that the main contribution to the strain potential for the Rydberg excitons is the band-gap shift  $\Delta E_g$  which is independent of the particular state and can reach trap depths of several meV in the range of strains that Cu<sub>2</sub>O crystals have been subjected to in experiments. Multiple observations do, however, imply that it might be advantageous to look for alternatives in the low-strain regime. Due to the small energetic separation of the Rydberg states, the anisotropic mass introduced by the strain mixes these states particularly strongly. The introduction of potentials far larger than the typical separation in combination with the strong mixing due to the anisotropic mass makes it challenging to address a single state of interest optically, as experimental spectra are superpositions of the local spectra of all points within the beam path. Furthermore, the thin crystals might be more prone to destruction under large strain.

Challenges in the search of low-strain alternatives might arise from the observation that it might not even be possible to achieve potential minima in the static low strain regime. Alternatives might be the use of dynamical phenomena such as surface acoustic waves [119] which should allow for the creation of potential minima at arbitrarily low strain. It might furthermore not even be necessary to trap the excitons. Without external potentials, a typical free Rydberg exciton travels less than its own radius during its short lifetime [33]. It might therefore suffice to locally tune the resonance condition of an exciton and thereby localise its excitation. One should, however, keep in mind that due to their low mass, excitons react strongly to any external potentials.

## Chapter 5.

# Excitonic transitions beyond the dipole approximation

While Wannier-excitons share remarkable similarities with atomic quantum systems, they do also possess features that put them apart from atoms. Perhaps, the most striking one is the fact that the ground state of an exciton is the crystal vacuum  $|\Phi_{\text{vac}}\rangle$ , containing no excitons at all. Another notable difference is the potential existence of multiple excitonic series. The corresponding states constitute partners for additional optical transitions which may have very different characteristics to the intra-series transitions mimicking atomic transitions.

In atomic systems, the transition wavelength between adjacent Rydberg states, i.e. states with considerable overlap, increases with  $n^3$  while the spatial extension of the states scales only with  $n^2$ . This implies that for large enough  $n$ , the transition wavelengths will always be much larger than the extension of the states. In this case, the electromagnetic field can be assumed to be spatially homogeneous over the volume of the atom, resulting in the well-known **electric dipole approximation** (or simply **dipole approximation**). As the ground-state wave function of a typical atom has a diameter of roughly 1 Å, while the transition wavelengths connecting the ground state to the next higher states are on the order of hundreds of nanometers, the assumptions of the dipole-approximation are fulfilled for even the lowest principal quantum numbers. Only in x-ray transitions from the inner shells, nondipolar corrections may contribute significantly [120, 121]. The transition wavelengths for both excitonic inter-series transitions<sup>1</sup> and the excitation of excitons from the crystal vacuum, in contrast, approach constant values. At first glance, it does therefore seem possible to reach a regime in which the transition wavelength becomes comparable to the spatial extension of the states and the dipole approximation breaks down. This is a necessary precondition for the quantum system to “see” the full spatial mode structure and open up an additional degree of freedom to tailor the light-matter interaction. The first step to this end is deriving the corresponding transition matrix elements to assess if and how the breakdown of the dipole approximation manifests itself.

---

<sup>1</sup>The term “inter-series transition” refers to a transition between excitonic states of different series, e.g. the yellow and the green series.

Section 5.1 contains a detailed discussion of the excitonic transitions from the Rydberg states of the yellow series to those of the green and blue series in dipole approximation and beyond. As will be shown, these matrix elements depend on a few material parameters which are closely related to the band structure parameters and can be derived quantitatively from fits to the band structure. Additionally, a brief, purely group-theoretical discussion of the use of orbital angular momentum (OAM) in excitonic transitions will be provided in Sec. 5.2.

### 5.1. Excitonic inter-series transitions

Some proposals for the implementation of quantum-information protocols based on the yellow Rydberg excitons have been put forward which require the existence of experimentally accessible, optical transitions. The observation of signs of coherent excitation in the single-photon absorption spectra [29], for example, raises the question whether the Rydberg excitons can be exploited for coherent-manipulation schemes such as single-photon generation based on electromagnetically induced transparency [122] or the generation of giant optical nonlinearities [123]. Furthermore, the application of optical dipole potentials to Rydberg excitons discussed in Chapter 4 is currently under investigation. The first step to the realisation of these proposals is the identification of suitable, allowed transitions.

Rydberg-Rydberg transitions within the yellow series, while convenient in the respect that they closely resemble atomic transitions and follow the same selection rules and scaling laws, are located in an experimentally inconvenient range of wavelengths, between 1 cm and 10 cm. For the optical dipole traps, for example, the smallest localisation lengths achievable would be on the order of a few mm, much longer than the natural localisation due to the crystal dimension and the beam diameter, on the order of  $30\mu\text{m}$  to  $100\mu\text{m}$ . A few of these excitonic intra-series transitions have been studied experimentally, e.g., the transitions between the  $1S$  and  $2P$  states of the yellow series [124]. They have furthermore been put forward as possible platform for the implementation of excitonic masers [44, 45].

The inconvenient energy range of the intra-series transitions motivates the investigation of the inter-series transitions as alternatives with transition wavelengths on the order of  $1\mu\text{m}$  to  $10\mu\text{m}$ . The physics of these transitions, however, can be distinctly different from those seen in atomic physics, not least due to the fact that the transition wavelengths approach constant values for large principal quantum numbers  $n$ . Experimental observations of these transitions are scarce, but signatures of the optical coupling of the yellow  $1S$  exciton to that of the blue series have been observed in polariton propagation [82]. Under the assumption that angular momentum is a good quantum number and that the dipole approximation captures the relevant physics, one can derive the dipole selection-rules group-theoretically. As the two valence bands do both have positive parity, the parity change inherent in dipole transitions has to be carried by the hydrogen-like envelope

functions and the atomic selection rule  $\Delta\ell = \pm 1$  does hold for the yellow-green dipole transitions as well. In the case of the yellow-blue transitions, on the other hand, the two conduction bands have opposing parity and the dipole selection rule is  $\Delta\ell = 0$ . Figure 5.1 shows a schematic term diagram of the yellow, blue and green series in  $\text{Cu}_2\text{O}$  with the dipole-allowed transitions indicated by the red arrows. As will be shown later in this Section, the dipole approximation should be used with care in excitonic inter-series transition and will generally break down for large principal quantum numbers.

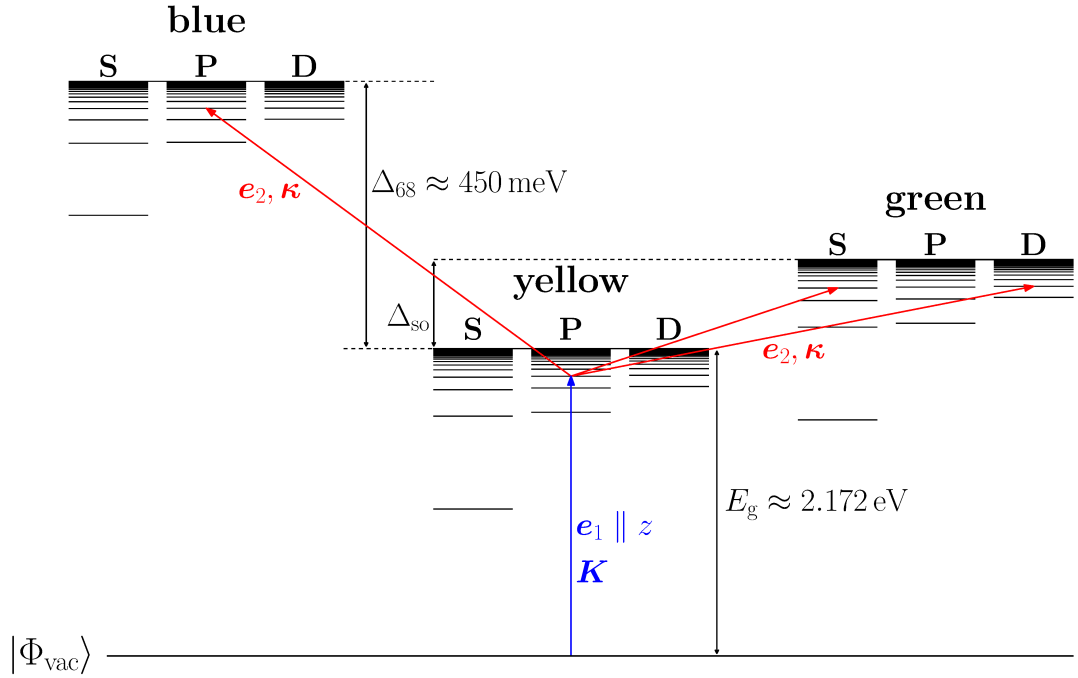


**Figure 5.1.:** Schematic term diagram of the excitonic states of the yellow, green and blue series. The red and blue arrows indicate the dipole-allowed transitions for a pump-beam with polarisation  $\mathbf{e}_1 \parallel z$  and a wave vector  $\mathbf{K}$  as well as a probe beam with  $\mathbf{e}_2$  and  $\mathbf{\kappa}$ .

Table 5.1 contains the excitonic properties used in this Section. Recent calculations of the green resonance energies from the multi-band problem discussed in Sec. 3.1.1 suggest that a green exciton series exists, that does roughly follow a Rydberg series with a Rydberg energy of 150 meV [125]. This agrees quite well with both the experiments<sup>2</sup> and the Rydberg energy derived from the effective mass of the heavy hole [26]. The implication that separate heavy and light-hole series exist, however, appears to be at odds with a simple, group-theoretical analysis [127, 67] and a thorough investigation of the properties of these states seems warranted.

All green excitons but the  $1S$  state sit on top of the yellow continuum and couple to it via the band-structure Hamiltonian. Thus, the green Rydberg states have to be interpreted as resonances,

<sup>2</sup>The actual resonance energies presented in Ref. [125] agree quite well with the experiments [9, 83]. The difference in the Rydberg energies given in Tab. 5.1 and Ref. [126] versus the numerical estimate given in Ref. [125] is mostly due to the different number of resonances considered. The experimental estimate is only based on states with  $n_g \leq 4$  and therefore sensitive to the central-cell corrections.

not bound states. The coupling to the yellow continuum has been included in Ref. [125] and the results suggest that the coupling correlates with the momentum-space extension of the green states, i.e. that it is small for states with large principal quantum numbers. The bare green Rydberg resonances do therefore resemble bound states which is important as it implies that Rydberg states of the higher series may indeed exist. Their radiative and nonradiative decay rates, however, are as of now unknown. Recently published photoluminescence spectra [128] suggest that the nonradiative lifetimes of the green states are rather short as these states do not appear in the spectra, contrary to those of the yellow, blue and violet series.

We will start the analysis by deriving the transition matrix elements for the excitonic states introduced in Eq. (2.62)

$$\left| \Psi_{n,\ell,m}^{v,\sigma_h;c,\sigma_e}(\mathbf{K}) \right\rangle = \sum_{\mathbf{k}} \tilde{\phi}_{n,\ell,m}^{c,v}(\mathbf{k}) b_{v,\sigma_h,\beta}^\dagger \mathbf{K}-\mathbf{k} a_{c,\sigma_e,\alpha}^\dagger \mathbf{K}+\mathbf{k} \left| \Phi_{\text{vac}} \right\rangle \quad (5.1)$$

with hydrogen-like envelope functions  $\tilde{\phi}_{n,\ell,m}^{c,v}(\mathbf{k})$  and the excitonic properties given in Tab. 5.1. In order to derive meaningful transition matrix-elements and reproduce the cubic selection rules, the cubic symmetry of the crystal environment has to be taken into account. We will subsequently achieve this by using a symmetrised basis

$$\left| S; \gamma, \Gamma_\xi, i; n, \ell; \mathbf{K} \right\rangle = \sum_{\sigma_h, \sigma_e} \sum_{m=-\ell}^{\ell} (S, \sigma_h, \sigma_e; \ell, m | \Gamma_\xi, i)_\gamma \left| \Psi_{n,\ell,m}^{v,\sigma_h;c,\sigma_e}(\mathbf{K}) \right\rangle, \quad (5.2)$$

which is connected to the basis (5.1) by a unitary transformation and can be understood to be an extension of the basis derived by R. G. Waters *et al.* [127]. Here,  $i$  denotes the row of the representation  $\Gamma_\xi$  according to which the state transforms and the index  $\gamma$  indicates that multiple states may exist for whom all other quantum numbers coincide if  $\Gamma_\xi$  appears more than once in  $\Gamma_{\text{env}} \otimes \Gamma_c \otimes \Gamma_v$ . If a state is uniquely labelled without it, the index  $\gamma$  will be omitted. The coefficients  $(S, \sigma_h, \sigma_e; \ell, m | \Gamma_\xi, i)_\gamma$  follow from the coupling coefficients of the point group  $O_h$  [50] and are given in App. C.2. As a shorthand, the band indices are combined into series indices  $S = \{c, v\}$  taking the values Y (yellow), G (green) and B (blue). In this Section, we will only look at the transitions from the  $z$  component of the dipole-allowed yellow  $nP$ -excitons (i.e.  $|Y; \Gamma_4^-, z; nP; \mathbf{K}\rangle$ ) to the green  $S$  and  $D$ -states as well as the blue  $S$  and  $P$ -states.

While the use of the basis (5.1) implies the assumption that electron and hole-spin as well as all hydrogenic quantum numbers are good quantum numbers, the use of the Waters basis (5.2) assumes only that the quantum numbers  $n$  and  $\ell$  are good quantum numbers. As we have shown, this is a good approximation for the yellow series but it is unclear how well it approximates the green and blue series in which the angular momenta may be mixed due to the anisotropic effective masses of the  $\Gamma_8^+$  valence-band and the  $\Gamma_8^-$  conduction-band. This mixing may lead to a redistribution of oscillator strength to states that are dark in our analysis. Apart from this redistribution, we do not expect that a more sophisticated model for these states alters the general results of this

	$m_h^*$	$m_e^*$	$a_B^*/\text{nm}$	$Ry^*/\text{meV}$	$Ry_{\text{exp}}^*/\text{meV}$
yellow	$\frac{-m_0}{A_1-2B_1} = 0.56 m_0$	$\frac{m_0}{A_6 - \frac{4B_{6,8}^2}{3m_0\Delta_{68}}} = 0.99 m_0$	1.12	86.07	86.04 [26]
green	$\frac{-m_0}{A_1+B_1} = 0.57 m_0$	$\frac{m_0}{A_6 - \frac{4B_{6,8}^2}{3m_0\Delta_{68}}} = 0.99 m_0$	1.09	87.94	139 [126]
blue	$\frac{-m_0}{A_1-2B_1} = 0.56 m_0$	$\frac{m_0}{A_8 + \frac{2B_{6,8}^2}{3m_0\Delta_{68}}} = 0.21 m_0$	2.58	37.22	46 [9]

**Table 5.1.:** Estimates of the properties of the excitonic series used in this Section. The values for the  $\Gamma_8^+$  valence band and the  $\Gamma_8^-$  conduction band are based on averages over all angles and the two sub-bands. The right most column gives experimental estimates based on a few low- $n$  states.

Section regarding, e.g., the applicability of the dipole approximation, as it should not have a large effect on the electron-hole separation. In any case, the exact values of the excitonic parameters are to be considered estimates based on the band-structure parameters of  $\text{Cu}_2\text{O}$ .

### 5.1.1. Theory of excitonic inter-series transitions

We are interested in inter-series transitions, i.e. transitions that conserve the numbers of both holes and electrons. The relevant light-matter interaction operator for a vector potential in Coulomb gauge  $\mathbf{A}(\mathbf{r}) = \mathbf{A} e^{-i\mathbf{\kappa}\cdot\mathbf{r}}$  can then be written as

$$\begin{aligned}
\frac{e}{m_0} \mathbf{A}(\mathbf{r}) \cdot \boldsymbol{\pi} &= \frac{e}{m_0} \mathbf{A} \cdot \sum_{\mathbf{v}, \mathbf{v}'} \sum_{\mathbf{q}} \langle \mathbf{v}, \mathbf{q} - \boldsymbol{\kappa} | e^{-i\mathbf{\kappa}\cdot\mathbf{r}} \boldsymbol{\pi} | \mathbf{v}', \mathbf{q} \rangle b_{\mathbf{v}, \mathbf{q} - \boldsymbol{\kappa}}^\dagger b_{\mathbf{v}', \mathbf{q}} \\
&+ \frac{e}{m_0} \mathbf{A} \cdot \sum_{\mathbf{c}, \mathbf{c}'} \sum_{\mathbf{q}} \langle \mathbf{c}, \mathbf{q} - \boldsymbol{\kappa} | e^{-i\mathbf{\kappa}\cdot\mathbf{r}} \boldsymbol{\pi} | \mathbf{c}', \mathbf{q} \rangle a_{\mathbf{c}, \mathbf{q} - \boldsymbol{\kappa}}^\dagger a_{\mathbf{c}', \mathbf{q}}
\end{aligned} \tag{5.3}$$

where umklapp processes have been ignored due to the small magnitude of the wave vectors of interest,  $\mathbf{v}, \mathbf{v}'$  as well as  $\mathbf{c}, \mathbf{c}'$  denote the valence and conduction bands, respectively. The conservation of the pseudo momentum has already been used to eliminate one summation over the first Brillouin zone and the electron and hole spin are included in the band indices in order to keep the notation concise. Every light field can be decomposed into plane waves by a Fourier decomposition and the choice of the vector potential does not limit the applicability of the results. The fermionic creation and annihilation operators fulfil the anti-commutator relations

$$\left[ b_{\mathbf{v}, \mathbf{q}}^\dagger, b_{\mathbf{v}', \mathbf{q}'} \right]_+ = \left[ a_{\mathbf{v}, \mathbf{q}}^\dagger, a_{\mathbf{v}', \mathbf{q}'} \right]_+ = \delta_{\mathbf{v}, \mathbf{v}'} \delta_{\mathbf{q}, \mathbf{q}'}. \tag{5.4}$$

All other two-operator anti-commutators vanish. With the excitonic state according to Eq. (2.62), the transition matrix elements for a transition where the hole changes the valence band (e.g. be-

tween the yellow and green series) do thus take the form

$$\begin{aligned} \left\langle \Psi_{\tau}^{v,c}(\mathbf{K}) \left| \frac{e}{m_0} \mathbf{A}(\mathbf{r}) \cdot \boldsymbol{\pi} \right| \Psi_{\tau'}^{v',c}(\mathbf{K}') \right\rangle &= \frac{e}{m_0} \mathbf{A} \cdot \sum_{\mathbf{k}'} \sum_{\mathbf{k}} \sum_{\nu, \nu'} \sum_{\mathbf{q}} \langle \nu, \mathbf{q} - \boldsymbol{\kappa} | e^{-i\boldsymbol{\kappa} \cdot \mathbf{r}} \boldsymbol{\pi} | \nu', \mathbf{q} \rangle \\ &\times \tilde{\phi}_{\tau'}^{c,v'}(\mathbf{k}') \tilde{\phi}_{\tau}^{c,v\dagger}(\mathbf{k}) \left\langle \Phi_{\text{vac}} \left| b_{v,\beta} \mathbf{K} - \mathbf{k} \ a_{c,\alpha} \mathbf{K} + \mathbf{k} \ b_{\nu,q-\boldsymbol{\kappa}}^{\dagger} \ b_{\nu',q} \ b_{\nu',\beta'}^{\dagger} \mathbf{K}' - \mathbf{k}' \ a_{c,\alpha'}^{\dagger} \mathbf{K}' + \mathbf{k}' \right| \Phi_{\text{vac}} \right\rangle. \end{aligned} \quad (5.5)$$

The index  $\tau \hat{=} \{n, \ell, m\}$  denotes all quantum numbers not explicitly given. The relative masses  $\alpha, \beta$  will generally differ for the two series but must fulfil  $\alpha + \beta = \alpha' + \beta' = 1$ . The matrix element of the vacuum state can only be nonzero if the quasiparticles are annihilated from the same states they are created in, which implies  $\nu = v$  as well as  $\nu' = v'$  and thereby

$$\begin{aligned} \left\langle \Phi_{\text{vac}} \left| b_{v,\beta} \mathbf{K} - \mathbf{k} \ a_{c,\alpha} \mathbf{K} + \mathbf{k} \ b_{\nu,q-\boldsymbol{\kappa}}^{\dagger} \ b_{\nu',q} \ b_{\nu',\beta'}^{\dagger} \mathbf{K}' - \mathbf{k}' \ a_{c,\alpha'}^{\dagger} \mathbf{K}' + \mathbf{k}' \right| \Phi_{\text{vac}} \right\rangle \\ = -\delta_{\nu,v} \ \delta_{\nu',v'} \ \delta_{\beta} \mathbf{K} - \mathbf{k}, \mathbf{q} - \boldsymbol{\kappa} \ \delta_{\mathbf{q},\beta'} \mathbf{K}' - \mathbf{k}' \ \delta_{\alpha} \mathbf{K} + \mathbf{k}, \alpha' \mathbf{K}' + \mathbf{k}'. \end{aligned} \quad (5.6)$$

In this derivation, the anticommutator relations were used to rewrite the problem in terms of the number operators  $n_{\nu,q} = a_{\nu,q}^{\dagger} a_{\nu,q}$  and the fact was exploited that the crystal vacuum contains neither electrons nor holes. Reinserting this result into Eq. (5.5) all but one of the summations can be carried out and the resulting matrix element is

$$\begin{aligned} \left\langle \Psi_{\tau}^{v,c}(\mathbf{K}) \left| \frac{e}{m_0} \mathbf{A}(\mathbf{r}) \cdot \boldsymbol{\pi} \right| \Psi_{\tau'}^{v',c}(\mathbf{K}') \right\rangle &= -\delta_{\mathbf{K},\mathbf{K}'-\boldsymbol{\kappa}} \frac{e}{m_0} \mathbf{A} \cdot \sum_{\mathbf{k}} \tilde{\phi}_{\tau}^{v,c\dagger}(\mathbf{k} + \beta \mathbf{K} + \boldsymbol{\kappa}) \\ &\times \tilde{\phi}_{\tau'}^{v',c}(\mathbf{k} + \beta' \mathbf{K} + \beta' \boldsymbol{\kappa}) \langle v, -\mathbf{k} - \boldsymbol{\kappa} | e^{-i\boldsymbol{\kappa} \cdot \mathbf{r}} \boldsymbol{\pi} | v', -\mathbf{k} \rangle. \end{aligned} \quad (5.7)$$

The Kronecker delta guarantees the conservation of the quasi-momentum as would be expected. The corresponding matrix element for an electron changing the conduction band (e.g. yellow-blue transitions) takes the form

$$\begin{aligned} \left\langle \Psi_{\tau}^{v,c}(\mathbf{K}) \left| \frac{e}{m_0} \mathbf{A}(\mathbf{r}) \cdot \boldsymbol{\pi} \right| \Psi_{\tau'}^{v,c'}(\mathbf{K}') \right\rangle &= \delta_{\mathbf{K},\mathbf{K}'-\boldsymbol{\kappa}} \frac{e}{m_0} \mathbf{A} \cdot \sum_{\mathbf{k}} \tilde{\phi}_{\tau}^{v,c\dagger}(\mathbf{k} - \alpha \mathbf{K}) \\ &\times \tilde{\phi}_{\tau'}^{v,c'}(\mathbf{k} - \alpha' \mathbf{K} + \beta' \boldsymbol{\kappa}) \langle c, \mathbf{k} | e^{-i\boldsymbol{\kappa} \cdot \mathbf{r}} \boldsymbol{\pi} | c', \mathbf{k} + \boldsymbol{\kappa} \rangle. \end{aligned} \quad (5.8)$$

Single-photon transitions which entail a change of both valence and conduction band (say from the yellow to the violet series) are forbidden to all orders as these are two-particle transitions which require at least two photons.

In dipole approximation, the spatial mode-structure of the electromagnetic field is neglected, which corresponds to setting  $\mathbf{K} = \mathbf{K}' = \boldsymbol{\kappa} = \mathbf{0}$  in Eqs. (5.7, 5.8). In the dipole approximation,



Eq. (5.7) does therefore reduce to

$$\left\langle \Psi_{\tau}^{v,c} \left| \frac{e}{m_0} \mathbf{A} \cdot \boldsymbol{\pi} \right| \Psi_{\tau'}^{v',c} \right\rangle = -\frac{e}{m_0} \mathbf{A} \cdot \sum_{\mathbf{k}} \tilde{\phi}_{\tau}^{v,c\dagger}(\mathbf{k}) \tilde{\phi}_{\tau'}^{v',c}(\mathbf{k}) \langle v, -\mathbf{k} | \boldsymbol{\pi} | v', -\mathbf{k} \rangle. \quad (5.9)$$

The difference between Eqs. (5.7) and (5.9) can be separated into two distinct effects:

1. The offset  $\boldsymbol{\kappa}$  between the Bloch states and
2. the offset  $\mathbf{q} = (\beta' - \beta) \mathbf{K} - \alpha' \boldsymbol{\kappa}$  between the envelope functions.

The former also appears in the transition from the crystal vacuum to the excitonic states and is there related to the higher multipole orders allowing, for example, quadrupole transitions into the yellow  $nS$  orthoexcitons. It can be expected to result in contributions comparable to the dipole term only if the wavelengths of the exciting light fields are comparable to the lattice constant. As this regime is never reached, the corresponding corrections may be neglected in most cases. The corresponding approximation will be called the **inter-band dipole-approximation** in the following.

The offset in the envelope functions, to the contrary, can be expected to contribute significantly for transitions between excitonic Rydberg states based on a simple scaling argument. For large  $n$ , the offset  $\mathbf{q}$  will become constant as the energetic separation of Rydberg states from two different series is essentially given by the corresponding band gap. The momentum-space extensions of the envelope functions, on the other hand, scale roughly with  $n^{-1}$  (see Eq. (3.34)) and their overlap will vanish for large  $n$ .

The dipole approximation is therefore only valid as long as at least one of the states in question has a momentum-space extension much larger than the displacement  $|\mathbf{q}|$ . This statement is in fact equivalent to stating that the dipole approximation is valid as long as the real-space extension of at least one of the states is much smaller than the wavelength  $\lambda_q = 2\pi/|\mathbf{q}|$ . One peculiar difference to atomic systems arises from the fact that the mass of one of the constituent quasiparticles changes during the transition, leading to the dependence of  $\mathbf{q}$  on the COM momentum of the initial state  $|\mathbf{K}|$ . This dependency can be very relevant in  $\text{Cu}_2\text{O}$  as the main band-gap is much larger than the secondary band-gaps  $E_g \gg \Delta_{\text{so}}, \Delta_{68}$ , implying  $|\mathbf{K}| \gg |\boldsymbol{\kappa}|$ .

The momentum-space displacements for both co-propagating and counter-propagating pump and probe beams as well as the yellow-green and yellow-blue transitions are given in Tab. 5.2. The wave number for an electromagnetic wave with photon energy  $E$  is given by

$$|\mathbf{k}(E)| = \frac{E \sqrt{\varepsilon_{\infty}}}{\hbar c}, \quad (5.10)$$

where  $\sqrt{\varepsilon_{\infty}} \approx 2.55$  is the refractive index of  $\text{Cu}_2\text{O}$  and the energetic separations  $E$  of the states have been approximated by  $E_g$ ,  $\Delta_{\text{so}}$  and  $\Delta_{68}$ , respectively. The “wavelengths”  $\lambda_q$  are the relevant

	co-propagating		counter-propagating	
	displacement $q$	wavelength $\lambda_q = 2\pi/ q $	displacement $q$	wavelength $\lambda_q = 2\pi/ q $
yellow-green	$(\beta_y - \beta_g) \mathbf{K}  + \alpha_g \boldsymbol{\kappa} $ $\approx 0.12 \times 10^{-3}\pi/a_g$	$7.4\mu\text{m}$	$(\beta_y - \beta_g) \mathbf{K}  - \alpha_g \boldsymbol{\kappa} $ $\approx -0.17 \times 10^{-3}\pi/a_g$	$4.9\mu\text{m}$
yellow-blue	$(\alpha_b - \alpha_y) \mathbf{K}  - \beta_b \boldsymbol{\kappa} $ $\approx -1.96 \times 10^{-3}\pi/a_g$	$0.44\mu\text{m}$	$(\alpha_b - \alpha_y) \mathbf{K}  + \beta_b \boldsymbol{\kappa} $ $\approx -0.82 \times 10^{-3}\pi/a_g$	$1.0\mu\text{m}$

**Table 5.2.:** Estimates of the momentum-space displacements  $q$  and “wavelengths”  $\lambda_q$  for the yellow-green and yellow-blue transitions.

parameters to be compared to the real-space extension of the excitonic states in order to assess whether the dipole approximation holds. If they are much larger than the real-space extension of the smaller state, the dipole approximation can be assumed to hold. The diameter of the yellow  $10P$  state is roughly  $340\text{ nm}$ , less than one tenth of the  $\lambda_q$  for the yellow-green transitions. One can therefore expect that the dipole approximation will still be accurate for yellow-green transitions involving this state. This does, however, depend strongly on the excitonic parameters: The term proportional to  $|\mathbf{K}|$ , which is dominant for yellow-blue transitions, is strongly suppressed for the yellow-green ones due to  $|\beta_y - \beta_g| = 0.0078$  arising from the similar estimates for the hole masses of the two valence bands. In the case of the yellow-blue transitions on the other hand, the  $\lambda_q$  may be smaller than the diameter of the states already for  $n_y = 12$ , implying that the dipole approximation may be severely broken for transitions involving these states.

### Inter-band matrix elements

One necessary ingredient to evaluate the matrix elements (5.7) and (5.8) are the inter-band matrix elements  $\langle \nu, -\mathbf{k} - \boldsymbol{\kappa} | e^{-i\boldsymbol{\kappa} \cdot \mathbf{r}} \boldsymbol{\pi} | \nu', -\mathbf{k} \rangle$ . We will show in this Section that these matrix elements are related to the  $\mathbf{k}$ -dependent and the magnetic part of the band Hamiltonians. In fact, absolute values can be derived if the corresponding band parameters are known. We will start by rewriting the matrix element in terms of the lattice periodic parts  $|u_\nu, \mathbf{k}\rangle$  of the Bloch states which results in

$$\begin{aligned}
 \langle \nu, -\mathbf{k} - \boldsymbol{\kappa} | e^{-i\boldsymbol{\kappa} \cdot \mathbf{r}} \boldsymbol{\pi} | \nu', -\mathbf{k} \rangle &= \langle u_\nu, -\mathbf{k} - \boldsymbol{\kappa} | e^{i\mathbf{k} \cdot \mathbf{r}} \boldsymbol{\pi} e^{-i\mathbf{k} \cdot \mathbf{r}} | u_{\nu'}, -\mathbf{k} \rangle \\
 &= \langle u_\nu, -\mathbf{k} - \boldsymbol{\kappa} | \boldsymbol{\pi} | u_{\nu'}, -\mathbf{k} \rangle - \hbar \mathbf{k} \langle u_\nu, -\mathbf{k} - \boldsymbol{\kappa} | u_{\nu'}, -\mathbf{k} \rangle.
 \end{aligned}
 \tag{5.11}$$

Both  $|\mathbf{k}|$  and  $|\boldsymbol{\kappa}|$  tend to be small compared to the extension of the first Brillouin zone, and we will only consider terms of zeroth and first order in them. The term proportional to  $\hbar \mathbf{k}$  is of order  $\mathcal{O}(k\kappa)$  if the bands have opposing parity and of order  $\mathcal{O}(k^2\kappa)$  if they have the same parity and will thus be neglected. If the inter-band dipole-approximation is applied by setting  $\boldsymbol{\kappa} = \mathbf{0}$  the above

result simplifies to

$$\langle \nu, -\mathbf{k} - \boldsymbol{\kappa} | e^{-i\boldsymbol{\kappa} \cdot \mathbf{r}} \boldsymbol{\pi} | \nu', -\mathbf{k} \rangle \approx \langle u_\nu, -\mathbf{k} | \boldsymbol{\pi} | u_{\nu'}, -\mathbf{k} \rangle. \quad (5.12)$$

As stated previously, substantial corrections to this approximation are only expected once the wavelength becomes comparable to lattice constant, i.e.  $|\boldsymbol{\kappa}| \sim \pi/a_g$ . We will nonetheless evaluate the full matrix element  $\langle u_\nu, -\mathbf{k} - \boldsymbol{\kappa} | \boldsymbol{\pi} | u_{\nu'}, -\mathbf{k} \rangle$  in the following. In order to evaluate these elements, we will use the perturbative expansion

$$|u_\nu, \mathbf{k}\rangle \approx |u_\nu, \mathbf{0}\rangle + \frac{\hbar}{m_0} \sum_{\xi} \frac{|u_\xi, \mathbf{0}\rangle \langle u_\xi, \mathbf{0} | \mathbf{k} \cdot \boldsymbol{\pi} | u_\nu, \mathbf{0}\rangle}{E_\nu(\mathbf{0}) - E_\xi(\mathbf{0})} \quad (5.13)$$

where  $\xi$  sums over all states that are not degenerate with  $|u_\nu, \mathbf{0}\rangle$ .

### 5.1.2. Yellow-green transitions

For the yellow-green transitions, the inter-band matrix elements

$$\begin{aligned} \langle u_{\Gamma_7^+}, \sigma_h, -\mathbf{k} - \boldsymbol{\kappa} | \boldsymbol{\pi} | u_{\Gamma_8^+}, \sigma'_h, -\mathbf{k} \rangle = \\ \frac{\hbar}{m_0} \sum_{\xi} \frac{\langle u_{\Gamma_7^+}, \sigma_h, \mathbf{0} | -(\mathbf{k} + \boldsymbol{\kappa}) \cdot \boldsymbol{\pi} | u_\xi, \mathbf{0} \rangle \langle u_\xi, \mathbf{0} | \boldsymbol{\pi} | u_{\Gamma_8^+}, \sigma'_h, \mathbf{0} \rangle}{E_{\Gamma_7^+}(\mathbf{0}) - E_\xi(\mathbf{0})} \\ + \frac{\hbar}{m_0} \sum_{\xi} \frac{\langle u_{\Gamma_7^+}, \sigma_h, \mathbf{0} | \boldsymbol{\pi} | u_\xi, \mathbf{0} \rangle \langle u_\xi, \mathbf{0} | -\mathbf{k} \cdot \boldsymbol{\pi} | u_{\Gamma_8^+}, \sigma'_h, \mathbf{0} \rangle}{E_{\Gamma_8^+}(\mathbf{0}) - E_\xi(\mathbf{0})} \end{aligned} \quad (5.14)$$

have to be evaluated where  $\sigma_h \in \{\pm 1/2\}$  and  $\sigma'_h \in \{\pm 1/2, \pm 3/2\}$  denote the spin states and  $\xi$  is understood to contain the spins of the intermediate states. The intermediate states must be of symmetry  $\Gamma_7^-$  or  $\Gamma_8^-$  and the next band of this symmetry, the  $\Gamma_8^-$  conduction band, is separated by roughly  $20 \Delta_{so}$  from the valence bands [80]. One can therefore make the approximation  $\Delta_\xi^{-1} = (E_{\Gamma_7^+}(\mathbf{0}) - E_\xi(\mathbf{0}))^{-1} \approx (E_{\Gamma_8^+}(\mathbf{0}) - E_\xi(\mathbf{0}))^{-1}$  and rewrite Eq. (5.14) as

$$\langle u_{\Gamma_7^+}, \sigma_h, -\mathbf{k} - \boldsymbol{\kappa} | \boldsymbol{\pi} | u_{\Gamma_8^+}, \sigma'_h, -\mathbf{k} \rangle = -\hbar \mathbf{M}_{\sigma_h, \sigma'_h} \cdot \mathbf{k} - \hbar \mathbf{N}_{\sigma_h, \sigma'_h} \cdot \boldsymbol{\kappa} \quad (5.15)$$

where the symmetric matrix  $\mathbf{M}_{\sigma_h, \sigma'_h} \in \mathbb{C}^{3 \times 3}$  is given by

$$\begin{aligned} M_{\sigma_h, \sigma'_h}^{x_i, x_j} = \frac{1}{m_0} \sum_{\xi} \Delta_\xi^{-1} \left[ \langle u_{\Gamma_7^+}, \sigma_h, \mathbf{0} | \pi_{x_j} | u_\xi, \mathbf{0} \rangle \langle u_\xi, \mathbf{0} | \pi_{x_i} | u_{\Gamma_8^+}, \sigma'_h, \mathbf{0} \rangle \right. \\ \left. + \langle u_{\Gamma_7^+}, \sigma_h, \mathbf{0} | \pi_{x_i} | u_\xi, \mathbf{0} \rangle \langle u_\xi, \mathbf{0} | \pi_{x_j} | u_{\Gamma_8^+}, \sigma'_h, \mathbf{0} \rangle \right]. \end{aligned} \quad (5.16)$$

By comparing this result with Eq. (2.31), we see that the  $\mathbf{k}$ -dependent terms of the Suzuki-Hensel Hamiltonian given in Eq. (2.45) can be written as

$$\mathcal{H}_{\sigma_h, \sigma'_h}(\mathbf{k}) = \frac{\hbar^2}{2m_0} \mathbf{k} \cdot \mathbf{M}_{\sigma_h, \sigma'_h} \cdot \mathbf{k}. \quad (5.17)$$

It does therefore follow from the symmetry of the matrices  $\mathbf{M}_{\sigma_h, \sigma'_h}$  that

$$\frac{m_0}{\hbar} \nabla_{\mathbf{k}} \mathcal{H}_{\sigma_h, \sigma'_h}(\mathbf{k}) = \hbar \mathbf{M}_{\sigma_h, \sigma'_h} \cdot \mathbf{k}, \quad (5.18)$$

which is just the first term of Eq. (5.15) and thereby the inter-band matrix element in dipole approximation. This result has previously been derived in  $\mathbf{k} \cdot \mathbf{p}$ -theory [66, 59] and similar relations exist in tight-binding theory [129]. The matrices  $\mathbf{N}_{\sigma_h, \sigma'_h}$  are defined by

$$N_{\sigma_h, \sigma'_h}^{x_i, x_j} = \frac{1}{m_0} \sum_{\xi} \Delta_{\xi}^{-1} \langle u_{\Gamma_7^+}, \sigma_h, \mathbf{0} | \pi_{x_j} | u_{\xi}, \mathbf{0} \rangle \langle u_{\xi}, \mathbf{0} | \pi_{x_i} | u_{\Gamma_8^+}, \sigma'_h, \mathbf{0} \rangle, \quad (5.19)$$

the symmetric part of which is simply  $(\mathbf{N}_{\sigma_h, \sigma'_h} + \mathbf{N}_{\sigma_h, \sigma'_h}^T)/2 = \mathbf{M}_{\sigma_h, \sigma'_h}/2$ . For the antisymmetric part  $\tilde{\mathbf{N}}_{\sigma_h, \sigma'_h} = (\mathbf{N}_{\sigma_h, \sigma'_h} - \mathbf{N}_{\sigma_h, \sigma'_h}^T)/2$ , the product can be rewritten as [69, 67]

$$\frac{\hbar^2}{2m_0} \mathbf{k} \cdot \tilde{\mathbf{N}}_{\sigma_h, \sigma'_h} \cdot \mathbf{k} = \frac{\hbar^2}{2m_0} \tilde{\mathbf{v}}_{\sigma_h, \sigma'_h} \cdot (\mathbf{k} \times \mathbf{k}) = \frac{\hbar e}{2im_0} \tilde{\mathbf{v}}_{\sigma_h, \sigma'_h} \cdot \mathbf{B} = \frac{1}{2} [\mathcal{H}(\mathbf{B})]_{\sigma_h, \sigma'_h} \quad (5.20)$$

where the commutator of the components of the quasi momentum in Eq. (2.46) has been used,  $\mathcal{H}(\mathbf{B})$  denotes the magnetic part of the Suzuki-Hensel Hamiltonian given in Eq. (2.47) and the vectors  $\tilde{\mathbf{v}}_{\sigma_h, \sigma'_h}$  are defined as

$$\tilde{\mathbf{v}}_{\sigma_h, \sigma'_h} = \left( \tilde{N}_{\sigma_h, \sigma'_h}^{y,z}, \tilde{N}_{\sigma_h, \sigma'_h}^{z,x}, \tilde{N}_{\sigma_h, \sigma'_h}^{x,y} \right)^T. \quad (5.21)$$

Finally, the inter-band matrix element takes the form

$$\langle u_{\Gamma_7^+}, \sigma_h, -\mathbf{k} - \boldsymbol{\kappa} | \pi | u_{\Gamma_8^+}, \sigma'_h, -\mathbf{k} \rangle = -\hbar \mathbf{M}_{\sigma_h, \sigma'_h} \cdot \left( \mathbf{k} + \frac{\boldsymbol{\kappa}}{2} \right) - \hbar \tilde{\mathbf{N}}_{\sigma_h, \sigma'_h} \cdot \boldsymbol{\kappa}. \quad (5.22)$$

The first term can directly be retrieved from the Suzuki-Hensel Hamiltonian via Eq. (5.18). The second term can be evaluated up to a constant by the application of the Wigner-Eckart theorem to Eq. (5.19) and a subsequent antisymmetrisation. The unknown parameter appearing during this procedure is related to the parameters of the magnetic part of the Suzuki-Hensel Hamiltonian and can be derived by comparing the terms in Eq. (5.20). The matrices  $\mathbf{M}_{\sigma_h, \sigma'_h}$  and  $\tilde{\mathbf{N}}_{\sigma_h, \sigma'_h}$  and their derivation are given in the App. C.1.

Inserting Eq. (5.15) into Eq. (5.7) results in

$$\begin{aligned} \left\langle \Psi_{\tau}^{y, \sigma_h, \sigma_e}(\mathbf{K}) \left| e^{-i\mathbf{\kappa} \cdot \mathbf{r}} \boldsymbol{\pi} \right| \Psi_{\tau'}^{g, \sigma'_h, \sigma_e}(\mathbf{K} + \mathbf{\kappa}) \right\rangle &= \sum_{\mathbf{k}} \tilde{\phi}_{\tau}^{y\dagger}(\mathbf{k} + \beta_y \mathbf{K}) \\ &\times \tilde{\phi}_{\tau'}^g(\mathbf{k} + \beta_g \mathbf{K} - \alpha_g \mathbf{\kappa}) \left( \hbar \mathbf{M}_{\sigma_h, \sigma'_h} \cdot \mathbf{k} + \hbar \mathbf{N}_{\sigma_h, \sigma'_h} \cdot \mathbf{\kappa} \right) \end{aligned} \quad (5.23)$$

where the indices y, g indicate properties of the yellow and green series, respectively. This expression can be transformed to real space via the Fourier transformation as defined in Eq. (2.63) which yields

$$\begin{aligned} \left\langle \Psi_{\tau}^{y, \sigma_h, \sigma_e}(\mathbf{K}) \left| e^{-i\mathbf{\kappa} \cdot \mathbf{r}} \boldsymbol{\pi} \right| \Psi_{\tau'}^{g, \sigma'_h, \sigma_e}(\mathbf{K} + \mathbf{\kappa}) \right\rangle &= \mathbf{M}_{\sigma_h, \sigma'_h} \cdot \mathbf{O} [\phi_{\tau}^y, \phi_{\tau'}^g, (\beta_y - \beta_g) \mathbf{K} + \alpha_g \mathbf{\kappa}] \\ &- \hbar W [\phi_{\tau}^y, \phi_{\tau'}^g, (\beta_y - \beta_g) \mathbf{K} + \alpha_g \mathbf{\kappa}] \left( \mathbf{M}_{\sigma_h, \sigma'_h} \cdot (\beta_g \mathbf{K} - \alpha_g \mathbf{\kappa}) - \mathbf{N}_{\sigma_h, \sigma'_h} \cdot \mathbf{\kappa} \right) \end{aligned} \quad (5.24)$$

with the real-space integrals given by

$$\mathbf{O} [\phi, \psi, \mathbf{q}] = \frac{\hbar}{i} \int_{\Omega} d^3 \mathbf{r} e^{i\mathbf{q} \cdot \mathbf{r}} \phi^{\dagger}(\mathbf{r}) \nabla \psi(\mathbf{r}), \quad (5.25)$$

$$W [\phi, \psi, \mathbf{q}] = \int_{\Omega} d^3 \mathbf{r} e^{i\mathbf{q} \cdot \mathbf{r}} \phi^{\dagger}(\mathbf{r}) \psi(\mathbf{r}). \quad (5.26)$$

Information on the evaluation of these integrals can be found in App. C.3. In the dipole approximation, Eq. (5.24) simplifies to

$$\langle \Psi_{\tau}^y | \boldsymbol{\pi} | \Psi_{\tau'}^g \rangle = \mathbf{M}_{\sigma_h, \sigma'_h} \cdot \mathbf{O} [\phi_{\tau}^y, \phi_{\tau'}^g, \mathbf{0}], \quad (5.27)$$

which closely resembles an atomic transition matrix element and follows the corresponding selection rules.

Using the Waters-basis (5.2), the dipole matrix elements from the yellow  $P$ -states to the green  $S$  and  $D$ -states can be expressed as

$$\sum_{\gamma, i} \left| \left\langle Y; \Gamma_4^-, z; n_y, P; \mathbf{0} \left| \pi_{x_j} \right| G; \gamma, \Gamma_{\xi}^+, i; n_g, \ell; \mathbf{0} \right\rangle \right|^2 = C_{\ell, x_j}^{\Gamma_{\xi}^+} \left| p_r^{\ell}(n_y, n_g) \right|^2, \quad (5.28)$$

where  $C_{\ell, x_j}^{\Gamma_{\xi}^+}$  is a coefficient containing the band-structure parameters, the integral over angular coordinates and spin degrees of freedom as well as the polarisation  $x_j$ . The index  $i$  sums over the rows of the irreducible representation  $\Gamma_{\xi}^+$  and the radial parameter  $p_r^{\ell}(n_y, n_g)$  is given by the radial

integral

$$p_r^\ell(n_y, n_g) = \frac{\Omega}{(2\pi)^3} \int_0^\infty dk k^3 \phi_{n_y P}^{y\dagger}(k) \phi_{n_g \ell}^g(k), \quad (5.29)$$

where the  $\phi(k)$  denote the radial envelope functions and the quasi-continuity of  $k$  has been used (see Eq. (2.23)). The coefficients  $C_{\ell, x_j}^{\Gamma_\xi^+}$  adhere to the selection rules of  $O_h$  and are listed in Tab. 5.3. The green even-parity excitons split according to  $\Gamma_{\text{env}} \otimes (\Gamma_c \otimes \Gamma_v)$  into

$C_{\ell, x_j}^{\Gamma_\xi^+}$	polarisation $x_j$ ( $\mathbf{e}_2$ )			$C_{\ell, x_j}^{\Gamma_\xi^+}$	polarisation $x_j$ ( $\mathbf{e}_2$ )				
	$x$	$y$	$z$		$x$	$y$	$z$		
green $S$	$1\Gamma_3^+$	0	0	0.11	green $D$	$2\Gamma_1^+$	0	0	0.47
	$1\Gamma_4^+$	0.85	0.85	0		$2\Gamma_2^+$	0	0	0
	$1\Gamma_5^+$	0.52	0.52	0		$3\Gamma_3^+$	0	0	0.87
	$\Sigma$	1.37	1.37	0.11		$5\Gamma_4^+$	0.41	0.41	0
					$5\Gamma_5^+$	0.44	0.44	0	
					$\Sigma$	0.85	0.85	1.34	

**Table 5.3.:** Angular coefficients for dipole transitions into the green  $S$  and  $D$ -excitons.

$$\mathbf{S} : \quad \Gamma_1^+ \otimes (\Gamma_6^+ \otimes \Gamma_8^+) = \Gamma_3^+ \oplus \Gamma_4^+ \oplus \Gamma_5^+, \quad (5.30)$$

$$\mathbf{D} : \quad (\Gamma_3^+ \oplus \Gamma_5^+) \otimes (\Gamma_6^+ \otimes \Gamma_8^+) = 2\Gamma_1^+ \oplus 2\Gamma_2^+ \oplus 3\Gamma_3^+ \oplus 5\Gamma_4^+ \oplus 5\Gamma_5^+. \quad (5.31)$$

The purely group-theoretical analysis of the excitonic wave functions cannot make any statements about the mixing of the states belonging to the same irreducible representation. Therefore, only the accumulated matrix elements (summed over  $\gamma$  and  $i$ ) are given in Eq. (5.28) and Tab. 5.3. In reality, the corresponding states need not be degenerate.

Figure 5.2 shows the radial matrix elements  $|p_r(n_y, n_g)|^2$ . These tend to be largest close to the diagonal  $n_y = n_g$  as one would expect from a simple overlap argument assuming that they are largest when the real-space extensions are comparable, i.e. near  $n_y \approx n_g \sqrt{a_B^{g*}/a_B^{y*}} \approx 0.99 n_g$ . As stated before, the dipole approximation can be expected to yield a good description of the yellow-green transitions for the excitonic parameters used in this Section and  $n_y \lesssim 10$ , based on the comparison of the  $\lambda_q$  to the diameter of the states  $3a_B^{y*} n_y^2$ . In order to assess the accuracy of the dipole approximation, the relative deviation compared to the full matrix element in Eq. (5.24) is shown in Tab. 5.4 for a few representative transitions. The relative corrections reach about 25 % for  $n \approx 20$  and are larger for counter-propagating pump and probe beams, as expected from the discussion of Tab. 5.2. If one were to perform the inter-band dipole approximation which

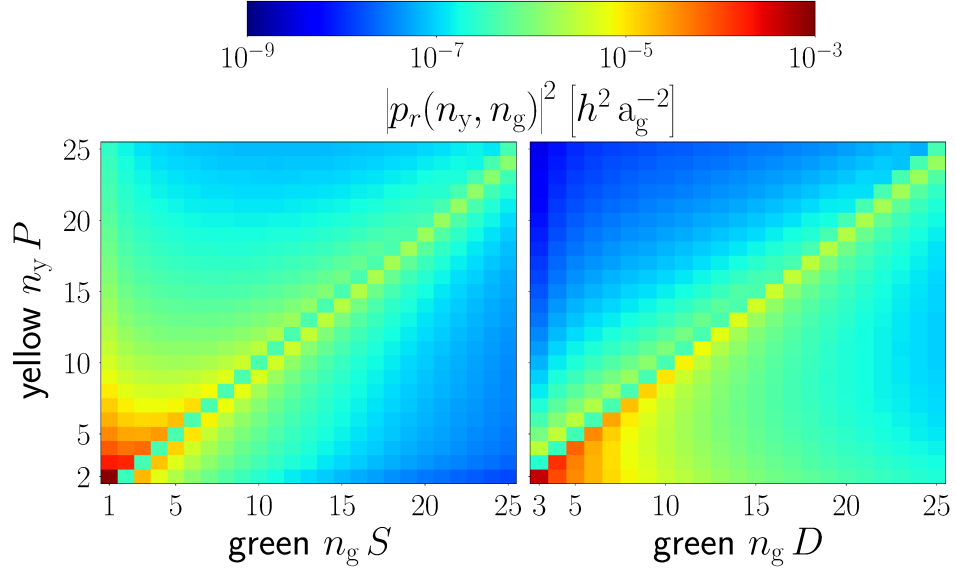


**Figure 5.2.:** Radial matrix elements  $|p_r(n_y, n_g)|^2$  for the transitions to the green  $S$  and  $D$ -states.

$n_y$	$n_g$	co-propagating		counter-propagating	
		$S \Gamma_3$	$D \Gamma_3$	$S \Gamma_3$	$D \Gamma_3$
19	20	1.02	0.96	0.75	0.83
14	15	1.01	0.99	0.89	0.94
8	9	1.00	1.00	0.99	0.99

**Table 5.4.:** Transition strengths from the yellow  $n_y$   $P$ -exciton to all green  $S$  and  $D$ -excitons transforming like  $\Gamma_3^+$ . The values given are the correction from Eq. (5.24) relative to the result from the dipole approximation. Both pump and probe beam are assumed to be  $z$ -polarised and propagating along the  $y$ -axis.

corresponds to setting  $\kappa = 0$  in Eq. (5.22) or ignoring the term  $\propto \mathbf{N}_{\sigma_h, \sigma'_h} \cdot \kappa$  in Eq. (5.24), the values given in Tab. 5.4 would change by less than one least significant digit.

### 5.1.3. Yellow-blue transitions

In order to evaluate the transition matrix-element of the yellow-blue transitions (5.8), the inter-band matrix-element

$$\begin{aligned}
 \langle \Gamma_6^+, \sigma_e, \mathbf{k} | e^{-i\kappa \cdot \mathbf{r}} \pi | \Gamma_8^-, \sigma'_e, \mathbf{k} + \kappa \rangle &= \langle u_{\Gamma_6^+}, \sigma_e, \mathbf{k} | \pi | u_{\Gamma_8^-}, \sigma'_e, \mathbf{k} + \kappa \rangle \\
 &+ \hbar(\mathbf{k} + \kappa) \langle u_{\Gamma_6^+}, \sigma_e, \mathbf{k} | u_{\Gamma_8^-}, \sigma'_e, \mathbf{k} + \kappa \rangle
 \end{aligned} \tag{5.32}$$

has to be evaluated. We will again ignore the term  $\propto \hbar(\mathbf{k} + \boldsymbol{\kappa})$  as its lowest order terms are of order  $\mathcal{O}(k\kappa)$  and  $\mathcal{O}(\kappa^2)$ . The transition between the two conduction bands is dipole allowed at the  $\Gamma$ -point and the lowest order term is constant

$$\langle \Gamma_6^+, \sigma_e, \mathbf{k} | e^{-i\boldsymbol{\kappa} \cdot \mathbf{r}} \boldsymbol{\pi} | \Gamma_8^-, \sigma'_e, \mathbf{k} + \boldsymbol{\kappa} \rangle \approx \langle u_{\Gamma_6^+}, \sigma_e, \mathbf{0} | \boldsymbol{\pi} | u_{\Gamma_8^-}, \sigma'_e, \mathbf{0} \rangle = B_{6,8} \mathbf{U}_{\sigma_e, \sigma'_e}^\dagger, \quad (5.33)$$

where  $B_{6,8}$  is the conduction band parameter and  $\mathbf{U}_{\sigma_e, \sigma'_e}^\dagger \in \mathbb{C}^3$  is the vector defined by the elements of the matrices given in Eq. (2.53). The next higher-order terms are of second order in  $\mathbf{k}$  and  $\boldsymbol{\kappa}$  and are therefore being ignored. As the parameter  $B_{6,8}$  is just a band-structure parameter, it can be

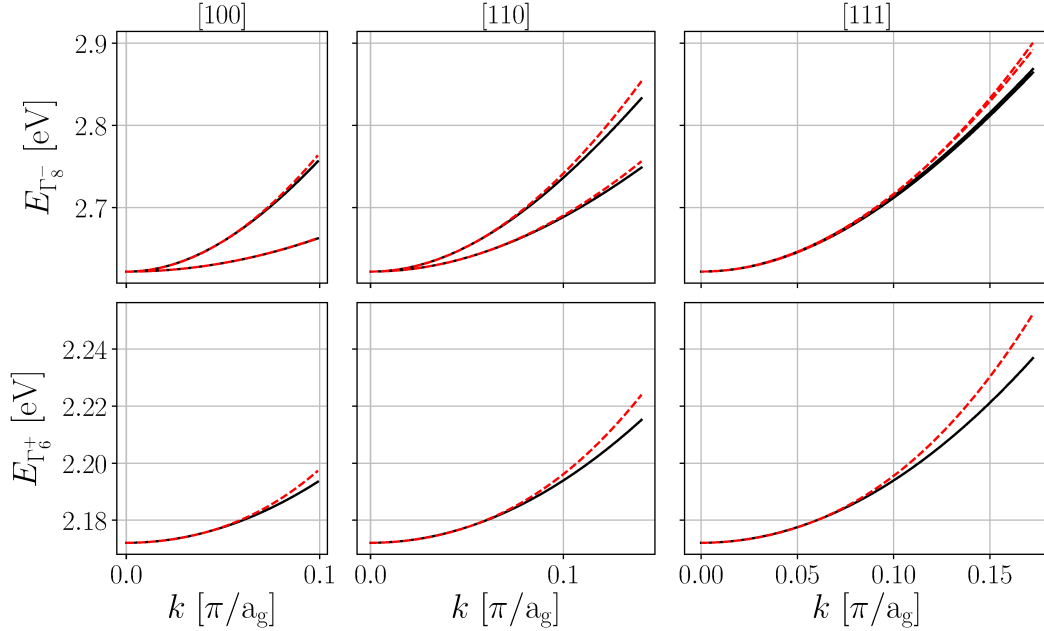


**Figure 5.3.:** Fit of the Hamiltonian (2.48) to the conduction bands of  $\text{Cu}_2\text{O}$ . Black solid lines show the (shifted) results of the sDFT calculations [80] and the red dashed lines show the fits.

retrieved from fits of the band Hamiltonian (2.48) to sDFT calculations [80] or experiments. The sDFT calculations we used for fitting do not reproduce the band gaps but do generally reproduce the shape of the bands rather well [80]. The fit was therefore restricted to a small region around the  $\Gamma$ -point and the band gaps were corrected manually. The result is shown in Fig. 5.3 and yields  $B_{6,8} = 0.342 \hbar\pi/a_g$ .

Inserting this into Eq. (5.8), we arrive at

$$\begin{aligned} \langle \Psi_\tau^{y, \sigma_h, \sigma_e}(\mathbf{K}) | e^{-i\boldsymbol{\kappa} \cdot \mathbf{r}} \boldsymbol{\pi} | \Psi_{\tau'}^{b, \sigma_h, \sigma'_e}(\mathbf{K} + \boldsymbol{\kappa}) \rangle &= B_{6,8} \mathbf{U}_{\sigma_e, \sigma'_e}^\dagger \sum_{\mathbf{k}} \tilde{\phi}_\tau^{y\dagger}(\mathbf{k} - \alpha_y \mathbf{K}) \tilde{\phi}_{\tau'}^b(\mathbf{k} - \alpha_b \mathbf{K} + \beta_b \boldsymbol{\kappa}) \\ &= B_{6,8} \mathbf{U}_{\sigma_e, \sigma'_e}^\dagger W \left[ \phi_\tau^y, \phi_{\tau'}^b, (\alpha_b - \alpha_y) \mathbf{K} - \beta_b \boldsymbol{\kappa} \right]. \end{aligned} \quad (5.34)$$



$D_{P,x_j}^{\Gamma^+}$		polarisation $x_j$ ( $\mathbf{e}_2$ )		
		$x$	$y$	$z$
blue P	$1 \Gamma_1^+$	0	0	1/3
	$1 \Gamma_2^+$	0	0	0
	$2 \Gamma_3^+$	0	0	1/3
	$3 \Gamma_4^+$	5/12	5/12	0
	$3 \Gamma_5^+$	1/4	1/4	0
	$\Sigma$	2/3	2/3	2/3

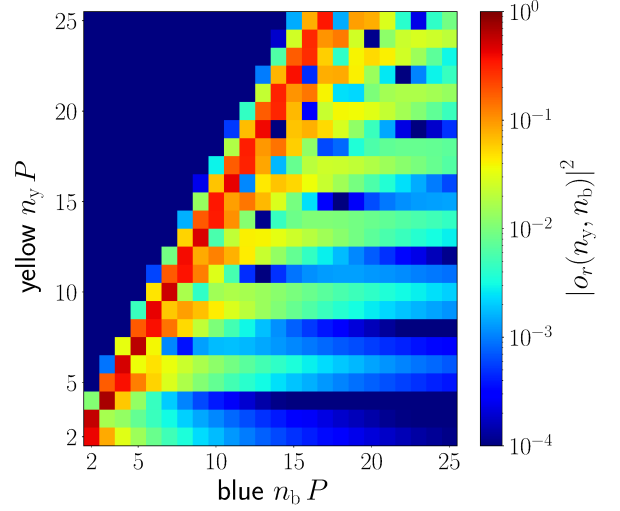


**Table 5.5:** Angular coefficients for dipole transitions into the blue  $P$ -excitons.

**Figure 5.4:** Radial overlap matrix elements  $|o_r(n_y, n_b)|^2$ .

In dipole approximation, this expression reduces to a simple overlap integral of the real-space envelope functions, implying the selection rule  $\Delta\ell = 0$ . The transition strength into the blue  $P$ -excitons corresponding to  $\Gamma_\xi^+$  can therefore be written as

$$\sum_{\gamma,i} \left| \left\langle Y; \Gamma_4^-, z; n_y, P; \mathbf{0} \left| \pi_{x_j} \right| B; \gamma, \Gamma_\xi^+, i; n_b, P; \mathbf{0} \right\rangle \right|^2 = |B_{6,8}|^2 D_{P,x_j}^{\Gamma_\xi^+} |o_r(n_y, n_b)|^2, \quad (5.35)$$

where the  $D_{P,x_j}^{\Gamma_\xi^+}$  are parameters derived from the integral over the angular and spin degrees of freedom. The irreducible representations of the blue  $P$ -states are given by

$$\Gamma_{\text{env}} \otimes \Gamma_v \otimes \Gamma_c = \Gamma_4^- \otimes \Gamma_7^+ \otimes \Gamma_8^- = \Gamma_1^+ \oplus \Gamma_2^+ \oplus 2\Gamma_3^+ \oplus 3\Gamma_4^+ \oplus 3\Gamma_5^+ \quad (5.36)$$

and the corresponding coefficients can be found in Tab. 5.3. The radial overlaps are given by

$$o_r(n_y, n_b) = \frac{\Omega}{(2\pi)^3} \int_0^\infty dk k^2 \phi_{n_y P}^{y\dagger}(k) \phi_{n_b P}^b(k) \quad (5.37)$$

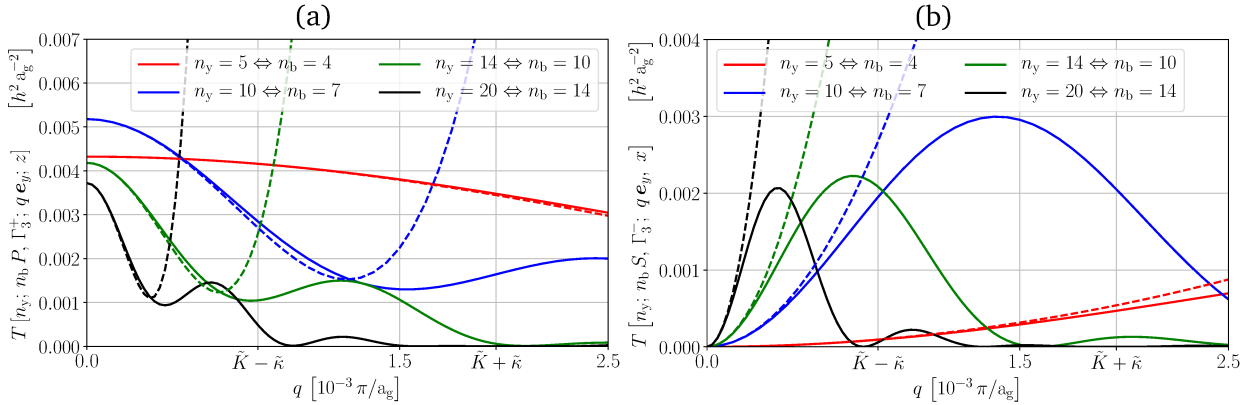
and depicted in Fig. 5.4. As expected from the simple overlap argument, the transition strengths reach their maximum for  $n_y \approx n_b \sqrt{a_B^{b*}/a_B^{y*}} = 1.52 n_b$ .

Figure 5.5 shows the transition strengths beyond the dipole approximation for a few transitions to the  $\Gamma_3^\pm$  components of the blue  $S$  and  $P$ -excitons. The quantity shown there is

$$T[n_y; n_b \ell, \Gamma_\xi; \mathbf{q}; x_j] = |B_{6,8}|^2 \sum_{\gamma,i} \left| \sum_{\sigma_h=-1/2}^{1/2} \sum_{\sigma_e=-1/2}^{1/2} \sum_{\sigma'_e=-3/2}^{3/2} \sum_{m=-1}^1 \sum_{m'=-\ell}^\ell \right. \\ \left. \times \left( Y, \sigma_h, \sigma_e; P, m \left| \Gamma_4^-, z \right. \right)^* (B, \sigma_h, \sigma'_e; \ell, m' \left| \Gamma_\xi, i \right. \right)_\gamma U_{\sigma_e, \sigma'_e}^{x_j \dagger} W \left( \phi_{n_y P m}^y; \phi_{n_b \ell m'}^b; \mathbf{q} \right) \right|^2, \quad (5.38)$$

which agrees with the exact result for counter-propagating beams at  $|\mathbf{k}| = \tilde{K} - \tilde{\kappa}$ , with the one for co-propagating beams at  $|\mathbf{k}| = \tilde{K} + \tilde{\kappa}$  and with the dipole approximation at  $|\mathbf{k}| = 0$ . The rescaled wave numbers for the parameters used in this Section are  $\tilde{K} = (\alpha_y - \alpha_b) |\mathbf{K}| = 1.39 \times 10^{-3} \pi/a_g$  and  $\tilde{\kappa} = \beta_b |\mathbf{\kappa}| = 0.57 \times 10^{-3} \pi/a_g$ .

Due to the large difference in the effective masses of the two conduction bands as well as the larger  $|\mathbf{\kappa}|$ , the dipole approximation breaks down much earlier in the yellow-blue transitions. While it does describe the transitions  $n_y = 5 \Leftrightarrow n_b = 4$  reasonably well, the relative error is on the order of 50% already for  $n_y = 10 \Leftrightarrow n_b = 7$ . For counter-propagating beams, this deviation can be corrected by including the octupole contribution. For all other cases, however, the inclusion of the octupole term does not suffice. In fact, already at  $n_y = 10$  the dipole-forbidden transition to the blue  $S$ -excitons have comparable transition-strengths to the dipole-allowed ones to the blue  $P$ -excitons. One can therefore state that for these transitions as well as those with higher principal quantum numbers, the dipole approximation is completely broken.



**Figure 5.5.:** Transition strengths to the blue  $n_b S \Gamma_3^-$  and  $n_b P \Gamma_3^+$  states including all multipole orders. (a): To the blue  $P$ -states using a  $z$ -polarised probe beam. The dashed lines show the sum of dipole and octupole contributions. (b): To the blue  $S$ -states using an  $x$ -polarised probe beam. The dashed lines show the quadrupole contribution.

#### 5.1.4. Conclusion

We have shown that the dipole approximation should be used with care in excitonic inter-series transitions as can be expected from simple overlap and scaling arguments. With the excitonic parameters used, the dipole approximation yields reasonably accurate results for the yellow-green transitions up to  $n \approx 20$ . This does, however, hinge crucially on the similar estimates of the hole masses for the two valence-bands. In the yellow-blue transitions, the dipole approximation clearly does not hold for principal quantum numbers as low as  $n_y = 10 \Leftrightarrow n_b = 7$  to the extent that even the inclusion of the next relevant multipole order does not reliably correct the deviations. In fact, even in this intermediate range of principal quantum numbers, dipole-forbidden transitions to the blue  $S$ -excitons may have comparable transition strengths to the dipole-allowed transitions

to the blue  $P$ -states. The breakdown of the dipole-approximation does of course imply that the excitons “see” the spatial mode structure which opens up an additional degree of freedom to tailor the light-matter interaction.

## 5.2. Transformational properties of Laguerre-Gaussian modes under $O_h$ symmetry

The question to which degree atomic selection rules can be tuned via the spatial mode structure is a pertinent one that has received much attention in the last years. One particular set of spatial modes that has aroused interest are the Laguerre-Gaussian modes [130]

$$\mathbf{A}_{lp}(r, \varphi, z) = \mathbf{A}_0 e^{ikz} \frac{w(0)}{w(z)} \exp \left[ -\frac{r^2}{w^2(z)} + \frac{ikr^2}{2R(z)} + i\phi_g(z) \right] \left( \frac{\sqrt{2}r}{w(z)} \right)^{|l|} L_p^{|l|} \left( \frac{2r^2}{w^2(z)} \right) e^{il\varphi} \quad (5.39)$$

where  $w(z)$ ,  $R(z)$  and  $\phi_g(z)$  denote the beam radius, curvature and Gouy phase, respectively, and  $L_p^{|l|}(x)$  denotes the generalised Laguerre polynomials. Each photon of these modes carries  $l$  units of orbital angular momentum, in addition to the one unit of spin angular momentum, due to the azimuthal phase dependence  $e^{il\varphi}$ . As angular momentum is a conserved quantity in our universe, an electron absorbing such a photon must take up the additional angular momentum, which should be reflected in the selection rules.

The intensity distribution and phase of the Laguerre-Gaussian modes with  $l, p \in \{0, 1, 2\}$  are shown in Fig. 5.6. The modes with  $|l| \geq 1$  possess a phase singularity at their center. The intensity has to vanish at such a singularity, implying that for an atom positioned there, dipole transitions are suppressed. The field gradient, which drives the quadrupole transitions, does not necessarily vanish allowing for the selective driving of quadrupole transitions [131, 132] or even higher multipole orders. Still, these schemes do rather correspond to a suppression of undesirable multipole orders than a real tuning of the selection rules, speaking to the fact that the atom only “sees” the local field and not the complete spatial mode structure.

In optical transitions from the crystal vacuum to the yellow Rydberg states, a regime can be reached where the spatial extension of both the initial and final state is comparable to or even larger than the photon’s in-crystal wavelength ( $\sim 300$  nm). One might be tempted to think that in this case, the dipole approximation breaks down and the selection rules become sensitive to the spatial mode of the photon. Experiment [18] as well as theory [76] do, however, show that this is not the case and the relevant quantity to be compared to the wavelength is not the spatial extension of the excitonic state, but the lattice constant  $a_g$ . As this is far smaller than the wavelength, the dipole approximation does hold even for the transition to the Rydberg excitons.

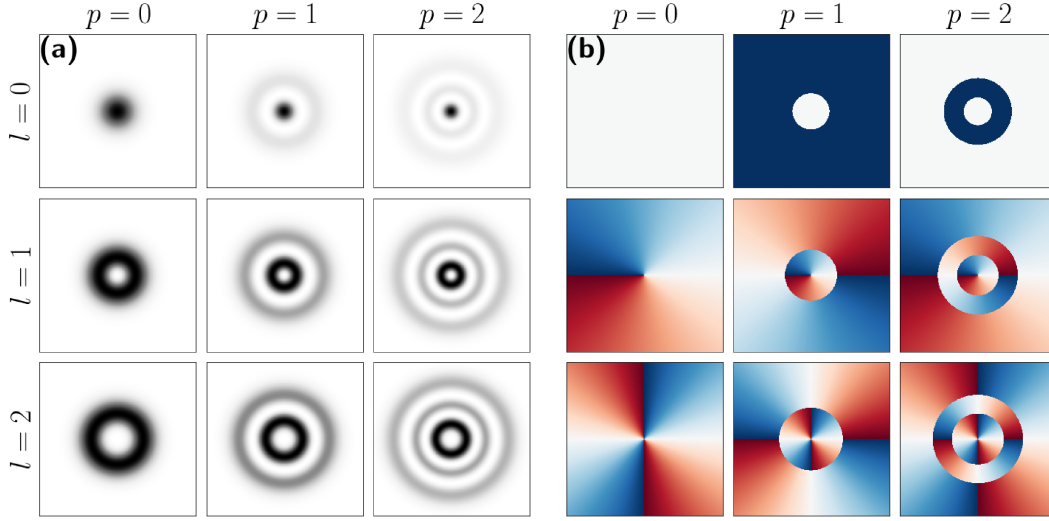


**Figure 5.6.:** Laguerre-Gaussian modes for  $l, p \in \{0, 1, 2\}$  in the  $x - y$  plane ( $z = 0$ ). (a): Intensity  $\propto |\mathbf{A}_{lp}(r, \varphi, 0)|^2$ . Individually normalised for each mode. (b): Phase  $\arg(\mathbf{A}_{lp}(r, \varphi, 0))$  from  $-\pi$  (red) to  $\pi$  (blue).

It might nonetheless be interesting to take a look at the transformational properties of these modes under the point group  $O_h$ , for example for the future application to excitonic inter-series transitions. In this Section, the corresponding group-theoretical calculations will be laid out which have been performed in cooperation by A. Konzelmann from the University of Stuttgart and the author of this thesis. The analysis will be restricted to the first terms of the multipole expansion around the beam waist [130]

$$\mathbf{A}_{lp}(r, \varphi, z) \approx L_p^{|l|}(0) \mathbf{A}_0 \left( \frac{\sqrt{2}r}{w(0)} \right)^{|l|} e^{il\varphi} (1 + ikz) \quad (5.40)$$

and beams orientated along one of the main crystal axes. The first two terms of the Taylor expansion  $e^{ikz} \approx 1 + ikz$  correspond to the longitudinal first-class (electric dipole) and second class (magnetic dipole and electric quadrupole) transitions<sup>3</sup>, respectively. The final interaction operator is proportional to  $\mathbf{A}_{lp}(r, \varphi, z) \cdot \boldsymbol{\pi}$  and the representation of the term in Eq. (5.40) has to be multiplied by  $\Gamma_4^-$  corresponding to the polar vector operator  $\boldsymbol{\pi}$ . If the beam is assumed to be orientated along the  $[001]$  axis, Eq. (5.40) can be rewritten via  $r^{|l|} e^{il\varphi} = (x \pm iy)^{|l|}$ , where the sign coincides with the sign of  $l$ .

Accordingly, there are six linearly independent basis functions for  $|l| \neq 0$ , which are mapped onto one another by the symmetry operations of the crystal's point group. For the first-class transition, these six basis functions can be expressed as

$$f_{x_k}^{\pm}(\mathbf{r}) = (x_i \pm ix_j)^{|l|}, \quad (5.41)$$

<sup>3</sup>Hereafter referred to as first and second-class transitions.

where  $\{x_i, x_j, x_k\}$  is a cyclic permutation of  $\{x, y, z\}$  and the prefactor in Eq. (5.40) has been ignored. For the second-class transitions, the six basis functions are

$$w_{x_k}^{\pm}(\mathbf{r}) = x_k (x_i \pm ix_j)^{|l|}. \quad (5.42)$$

For both transitions of first and second kind,  $l = 0$  is a special case. The first-kind basis functions (5.41) reduce to only one constant basis function transforming like  $\Gamma_1^+$  while the second-kind basis functions (5.42) reduce to three linearly independent basis functions transforming like  $\Gamma_4^-$ .

class	$E$	$8C_3$	$3C_2$	$6C_4$	$6C_2^1$	$I$	$8S_6$	$3\sigma_h$	$6S_4$	$6\sigma_d$
first	6	0	$2(-1)^{ l }$	$2 \cos\left(\frac{ l \pi}{2}\right)$	0	$6(-1)^{ l }$	0	2	$2 \cos\left(\frac{ l \pi}{2}\right)$	0
second	6	0	$2(-1)^{ l }$	$2 \cos\left(\frac{ l \pi}{2}\right)$	0	$-6(-1)^{ l }$	0	-2	$-2 \cos\left(\frac{ l \pi}{2}\right)$	0

**Table 5.6.:** Characters of the representations of the basis functions for first-class transitions (5.41) and second-class transitions (5.42).

In order to derive the representations of the vector spaces spanned by these basis functions, we need to derive their characters. To achieve this, we will first have to derive the transformation matrices  $\mathcal{D}(a)$  which transform the six basis functions according to Eq. (2.6). As the characters  $\chi(a) = \text{Tr}[\mathcal{D}(a)]$  do only depend on the diagonal elements of the transformation matrices  $\mathcal{D}(a)$ , it suffices to derive these (see also the discussion in App. B.2). Furthermore, the characters for symmetry elements belonging to the same conjugacy class have to coincide and we may pick one arbitrary symmetry element from each conjugacy class. This yields the characters in Tab. 5.6. It is directly apparent that these characters are periodic in  $|l|$  with periodicity 4. Furthermore, the characters for first and second-class transitions are almost identical, except that the signs for the improper rotations<sup>4</sup> are flipped. This implies that the representations of the operators for first and second-kind transitions are identical except for a flipped parity. The characters can be decomposed into those of the irreducible representations by the application of the orthogonality relation (B.4). The characters for the first class transitions are explicitly given in Tab. 5.7 together with the corresponding representations.

The representations of the complete first-class light-matter interaction operators  $\mathbf{A}_{lp} \cdot \boldsymbol{\pi}$  can be retrieved by multiplying the representations in Tab. 5.7 with  $\Gamma_4^-$  representing the vector operator  $\boldsymbol{\pi}$ . The representations for the first and second class operators are given in Tab. 5.8. As all these operators have a well-defined parity, one can formulate parity selection-rules, stating that the product of the parities of initial and final state have to coincide with  $(-1)^{|l|}$  for first-class transitions and with  $(-1)^{|l|+1}$  for second-class transitions. Apart from this selection rule, the takeaway from this simple group-theoretical treatment is that most transitions observing the parity selection rule will

<sup>4</sup>The improper rotations contained in  $O_h$  consist of the inversion  $I$ , the reflections  $3\sigma_h$  and  $6\sigma_d$  as well as the combinations of one reflection and a rotation  $8S_6$  and  $6S_4$  [50].

$n \in \mathbb{N}_0$	$E$	$8C_3$	$3C_2$	$6C_4$	$6C_2^1$	$I$	$8S_6$	$3\sigma_h$	$6S_4$	$6\sigma_d$	representation
$l = 0$	1	1	1	1	1	1	1	1	1	1	$\Gamma_1^+$
$ l  = 4n + 1$	6	0	-2	0	0	-6	0	2	0	0	$\Gamma_4^- \oplus \Gamma_5^-$
$ l  = 4n + 2$	6	0	2	-2	0	6	0	2	-2	0	$\Gamma_2^+ \oplus \Gamma_3^+ \oplus \Gamma_5^+$
$ l  = 4n + 3$	6	0	-2	0	0	-6	0	2	0	0	$\Gamma_4^- \oplus \Gamma_5^-$
$ l  = 4n + 4$	6	0	2	2	0	6	0	2	2	0	$\Gamma_1^+ \oplus \Gamma_3^+ \oplus \Gamma_4^+$

**Table 5.7.:** Characters and representations for the term in Eq. (5.40) corresponding to the first-class transitions. Except for  $l = 0$ , where the second-class representation is  $\Gamma_4^-$ , the second-class representations are simply connected to the first-class ones by a parity-flip.

be allowed due to the sheer number of irreducible representations appearing in the representation of the operators. In fact, the only irreducible representations that could be present but are not are  $\Gamma_1^\pm$  for  $|l| = 4n + 2$  and  $\Gamma_2^\pm$  for  $|l| = 4n + 4$ . Consequently, no further selection rules can be formulated. It should also be noted that the group theoretical approach laid out in this Section cannot make any statements about the strengths of the corresponding transitions. They might be strongly suppressed or in fact completely forbidden depending on the states under investigation. Another fact the reader should keep in mind, is that the transformational properties were derived for the case in which the center of inversion is placed at the center of the beam. They can only directly be applied to excitonic transition matrix elements if the exciton's center of inversion can be assumed to coincide with that of the beam. In order for this assumption to even be meaningful, the excitons must first be localised on a length scale much smaller than the beam diameter by, say, an external potential.

$n \in \mathbb{N}_0$	first class	second class
$l = 0$	$\Gamma_4^-$	$\Gamma_1^+ \oplus \Gamma_3^+ \oplus \Gamma_4^+ \oplus \Gamma_5^+$
$ l  = 4n + 1$	$\Gamma_1^+ \oplus \Gamma_2^+ \oplus 2\Gamma_3^+ \oplus 2\Gamma_4^+ \oplus 2\Gamma_5^+$	$\Gamma_1^- \oplus \Gamma_2^- \oplus 2\Gamma_3^- \oplus 2\Gamma_4^- \oplus 2\Gamma_5^-$
$ l  = 4n + 2$	$\Gamma_2^- \oplus \Gamma_3^- \oplus 2\Gamma_4^- \oplus 3\Gamma_5^-$	$\Gamma_2^+ \oplus \Gamma_3^+ \oplus 2\Gamma_4^+ \oplus 3\Gamma_5^+$
$ l  = 4n + 3$	$\Gamma_1^+ \oplus \Gamma_2^+ \oplus 2\Gamma_3^+ \oplus 2\Gamma_4^+ \oplus 2\Gamma_5^+$	$\Gamma_1^- \oplus \Gamma_2^- \oplus 2\Gamma_3^- \oplus 2\Gamma_4^- \oplus 2\Gamma_5^-$
$ l  = 4n + 4$	$\Gamma_1^- \oplus \Gamma_3^- \oplus 3\Gamma_4^- \oplus 2\Gamma_5^-$	$\Gamma_1^+ \oplus \Gamma_3^+ \oplus 3\Gamma_4^+ \oplus 2\Gamma_5^+$

**Table 5.8.:** Representations of the first-class operator  $\propto (x + iy)^{|l|} \pi$  and the second-class operator  $\propto z(x + iy)^{|l|} \pi$ .

## Chapter 6.

### Influence of charged impurities

The number of excitonic resonances that can be resolved in the experiments have been shown to depend strongly on the crystal sample. Often, a band-gap shift can be made out where the resonances above some energy, the effective band gap, vanish. Accordingly, the band-gap shift can be interpreted as a measure for the crystal “quality”. To this day, the “best” crystals are still naturally grown ones from the Tsumeb mine in Namibia [18]. Research into the fabrication of artificial crystals is ongoing [133, 134] and the observation of Rydberg excitons up to  $n = 14$  has been reported [133]. One effect deteriorating the crystal quality may be a persistent, inhomogeneous straining of the crystal. The spectrum is then convoluted with the distribution of strain shifts over the laser spot, obscuring the tightly spaced Rydberg resonances.

Another effect that can be expected to influence the crystal “quality” and thereby the visibility of the Rydberg excitons are crystal defects. For example, charged point defects and the disorder potential induced by them have been put forward as a possible explanation for the exponential decay of the band gap called the **Urbach tail** and the band-gap shift connected to it [34, 35, 36]. A population of charged impurities constitutes a plasma just like the electron-hole plasma which has already been shown to strongly influence the Rydberg excitons and result in a band gap shift [30, 31]. Contrary to the electrons and holes, however, the charged impurities have essentially infinite mass and an adiabatic approximation can be utilised to eliminate their dynamics. In that respect, the physics should resemble that of atoms in an ionic plasma where the dynamics of the ions can be adiabatically eliminated compared to the dynamics of the atom’s electrons. For exactly these situations, micro-field distributions have been derived which are the statistical distributions of local electric fields induced by an ionic background plasma. The simplest micro-field distribution derived for a static, homogeneous and uncorrelated distribution of charges has been derived by J. Holtmark in 1919 [135, 136, 137]. Micro-field distributions for more involved scenarios, including the presence of a screening electronic plasma and correlations between the charges, have been derived as well [138, 139]. For most of these cases, however, no analytical solutions exist and numerical approximations have to suffice. For charged point defects the assumptions of the Holtmark distribution should be well justified.

In a compensated crystal with both donor and acceptor impurities, it may be energetically favourable for donor-acceptor pairs to spontaneously ionise if the sum of their binding energies is lower than the band gap [57, Sec. 7.1.3]

$$E_g > E_A + E_D - \frac{e^2}{4\pi\epsilon |\mathbf{R}_A - \mathbf{R}_D|}. \quad (6.1)$$

The last term arises from the Coulomb interaction of the charged impurities and enhances the effect for small spatial separations. The process of the ionisation of a spatially separated pair is shown schematically in Fig. 6.1. For large impurity concentrations, the dynamics can be more

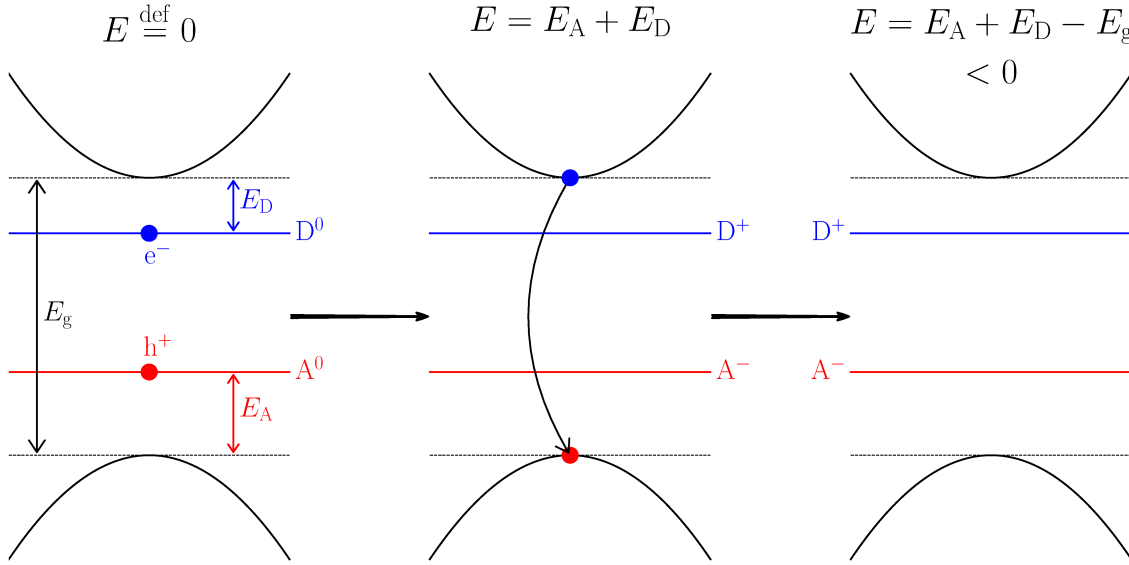


**Figure 6.1.:** Schematic of the spontaneous ionisation of a donor-acceptor pair.  $D^0$  and  $A^0$  denote the electrically neutral impurity states and  $D^+$  as well as  $A^-$  the charged states. If the impurities are close enough and the wavefunctions of electron and hole overlap, direct transitions may occur as well [140, 141].

complicated. The Coulomb attraction may lead to the formation of compound impurities formed from the combination of multiple simple impurities. In cuprous oxide the most common impurities are copper and oxygen vacancies which fulfil the condition (6.1) even for infinitely large separation. The most common type of compound impurity is a combination of these two impurities, which is positively charged in its ground state [142]. For the following discussion, the exact nature of the impurities will be of minor importance. In fact, the results will not even depend on the signs of the charges as long as every impurity carries exactly one (positive or negative) elemental charge. The macroscopic crystal will of course be electrically neutral and every charged impurity has to be compensated either by an impurity of opposite charge or by a free charge carrier, the concentration of which goes to zero at 0 K.

In this chapter, we will first derive the Hamiltonian for an exciton in a background of charged carriers, taking only the linear term of the potential into account. We will then derive the Holts-



mark micro-field distribution, calculate the Holtmark spectra and compare them to experimental absorption spectra.

## 6.1. Interaction of Rydberg excitons with charged impurities

The Hamiltonian of an exciton in a background of charged impurities takes the form

$$\mathcal{H} = \mathcal{H}_0 + \frac{e^2}{4\pi\epsilon} \sum_i s_i \left\{ \frac{1}{|\mathbf{r}_e - \mathbf{R}_i|} - \frac{1}{|\mathbf{r}_h - \mathbf{R}_i|} \right\} = \mathcal{H}_0 + \sum_i \mathcal{H}_i \quad (6.2)$$

where  $\mathcal{H}_0$  is the Hamiltonian of the unperturbed exciton,  $s_i = \pm 1$  denotes the sign of the impurity's charge,  $\mathbf{R}_i$  is its position and  $\mathbf{r}_{e/h}$  the positions of the constituent quasiparticles of the exciton. Transforming to the excitonic COM and relative coordinates  $\{\mathbf{R}, \mathbf{r}\}$  and defining  $\boldsymbol{\rho}_i = \mathbf{R} - \mathbf{R}_i$  yields

$$\mathcal{H}_i = s_i \frac{e^2}{4\pi\epsilon} \left\{ \frac{1}{|\boldsymbol{\rho}_i - \alpha\mathbf{r}|} - \frac{1}{|\boldsymbol{\rho}_i + \beta\mathbf{r}|} \right\} \quad (6.3)$$

with the relative electron and hole masses  $\alpha, \beta$ . The potential described by this result can be expanded by a Taylor series around  $\mathbf{r} = \mathbf{0}$ , whose first nonvanishing term is

$$\mathcal{H}_i \approx s_i \frac{e^2}{4\pi\epsilon} \frac{\boldsymbol{\rho}_i \cdot \mathbf{r}}{|\boldsymbol{\rho}_i|^3} = e\mathbf{F}_i \cdot \mathbf{r}. \quad (6.4)$$

Equation (6.2) can then be rewritten as

$$\mathcal{H} = \mathcal{H}_0 + e\mathbf{F} \cdot \mathbf{r} = \mathcal{H}_0 + e \sum_i \mathbf{F}_i \cdot \mathbf{r}. \quad (6.5)$$

If the unperturbed exciton's Hamiltonian permits the separation of COM and relative coordinate, Eq. (6.5) does so as well. This is a consequence of the linear approximation to the potential which is only applicable when the length scale on which the electric field  $\mathbf{F}$  varies is much larger than the spatial extension of the exciton. In order to test this hypothesis, we performed Monte-Carlo simulations calculating the median relative deviation between the exact potential induced by a distribution of charged impurities and the linear approximation. For an impurity density of  $1.2 \times 10^9 \text{ cm}^{-3}$ , the deviation reaches roughly 7% at a distance of  $1 \mu\text{m}$  which does roughly coincide with the radius of the  $25P$ -state. As will be shown later, the  $25P$ -state is the highest resolvable resonance at such an impurity density and for the other impurity densities of interest to this chapter, the relative deviation at the extension of the highest resolvable state is comparable. The linear approximation should therefore yield a reasonable approximation to the full potential in Eq. (6.3).

### 6.1.1. The Holtzmark distribution

The Holtzmark distribution [135, 136, 137] describes the statistical distribution of local electric fields induced by a static, homogeneous and uncorrelated distribution of point charges. The probability distribution  $P(\mathcal{F}) d^3\mathcal{F}$  can be interpreted as the probability that the components of the local field  $\mathbf{F}$  fulfil

$$\mathcal{F}_{x_i} \leq F_{x_i} \leq \mathcal{F}_{x_i} + d\mathcal{F}_{x_i}. \quad (6.6)$$

For  $N$  charges in a spherical volume  $\mathcal{B}$  of radius  $R$ , the micro-field distribution can formally be written as

$$P(\mathcal{F}) d^3\mathcal{F} = \int \int_{dV} d^3\rho_1 \cdots d^3\rho_N \left( \frac{3}{4\pi R^3} \right)^N \quad (6.7)$$

where  $dV$  denotes the domain for which the conditions (6.6) are fulfilled. The integration limits can be extended over the whole sphere by multiplication with the integral

$$H(\{\rho\}, \mathcal{F}) = \frac{d^3\mathcal{F}}{(2\pi)^3} \int d^3\omega e^{i\omega \cdot (\mathbf{F}[\{\rho\}] - \mathcal{F})} = \delta(\mathbf{F}[\{\rho\}] - \mathcal{F}) d^3\mathcal{F} \quad (6.8)$$

which is just the Fourier representation of the Dirac delta distribution and yields

$$\begin{aligned} P(\mathcal{F}) d^3\mathcal{F} &= \frac{d^3\mathcal{F}}{(2\pi)^3} \int \int_{\mathcal{B}} d^3\rho_1 \cdots d^3\rho_N \int d^3\omega e^{i\omega \cdot (\mathbf{F}[\{\rho\}] - \mathcal{F})} \left( \frac{3}{4\pi R^3} \right)^N \\ &= \frac{d^3\mathcal{F}}{(2\pi)^3} \int d^3\omega e^{-i\omega \cdot \mathcal{F}} [J(\omega)]^N = \frac{d^3\mathcal{F}}{2\pi^2 \mathcal{F}} \int_0^\infty d\omega \omega [J(\omega)]^N \sin(\omega \mathcal{F}). \end{aligned} \quad (6.9)$$

The integral  $J(\omega)$  is defined by

$$\begin{aligned} J(\omega) &= \frac{3}{4\pi R^3} \int_{\mathcal{B}} d^3\rho e^{i\omega \cdot \mathbf{F}_i(\rho)} = \frac{3}{4\pi R^3} \int_{\mathcal{B}} d^3\rho e^{i \frac{s_i e}{4\pi\epsilon} \frac{\omega \cdot \rho}{|\rho|^3}} \\ &= \frac{1}{5} \left[ 2 \cos(a\omega) + \left( 3(a\omega)^{-1} - 4a\omega \right) \sin(a\omega) + \sqrt{8\pi} (a\omega)^{3/2} \left( 2C \left[ \sqrt{\frac{2a\omega}{\pi}} \right] - 1 \right) \right], \end{aligned} \quad (6.10)$$

where  $C[x]$  denotes the cosine Fresnel-integral and  $a = e/(4\pi\epsilon R^2)$ . The result is independent of the charge's sign  $s$  due to the fact that only the linear term is taken into account and a positive charge at  $\rho$  gives exactly the same contribution as a negative charge at  $-\rho$ . The micro-field distribution is therefore independent of whether only positive impurities are present, only negative ones or a mixture of both.

The Holtsmark distribution is retrieved from Eq. (6.9) in the thermodynamic limit, i.e. in the limit  $N \rightarrow \infty$  and  $R \rightarrow \infty$  with a constant impurity density  $\rho_{\text{ci}} = 3N/(4\pi R^3)$ . Equation (6.10) fulfils  $|J(\omega)| \leq 1$  for all  $\omega$  with the only point at which equality is achieved being  $J(0) = 1$ . This implies that in the limit  $N \rightarrow \infty$ , only the vicinity of  $\omega = 0$  may be relevant and the exact solution can be retrieved by expanding  $J(\omega) \approx 1 - \sqrt{8\pi/25} (a\omega)^{3/2}$  and exploiting the relation

$$\lim_{N \rightarrow \infty} \left[ 1 - \frac{x}{N} \right]^N = e^{-x}. \quad (6.11)$$

The Holtsmark distribution is then given by [135, 136, 137]

$$P(\xi) d\xi = \frac{2}{\pi} \xi d\xi \int_0^\infty dx x e^{-x^{3/2}} \sin(\xi x), \quad (6.12)$$

which does only depend on the magnitude of the normalised electric field  $\xi = |\mathcal{F}|/\mathcal{F}_0$  but not on its direction, due to the isotropy of the impurity distribution. The normalisation constant is given by

$$\mathcal{F}_0 = \frac{e}{2\varepsilon} \left[ \frac{4\rho_{\text{ci}}}{15} \right]^{2/3} = \frac{e}{4\pi\varepsilon R_{\text{ci}}^2} \left( \frac{8\pi}{25} \right)^{1/3} \approx \frac{e}{4\pi\varepsilon R_{\text{ci}}^2}, \quad (6.13)$$

where the impurity radius  $R_{\text{ci}} = \sqrt[3]{3/(4\pi\rho_{\text{ci}})}$  coincides roughly with the average distance of the nearest-neighbour impurity and  $\mathcal{F}_0$  is in good approximation the electric field induced by a charge at a distance of  $R_{\text{ci}}$ . The Holtsmark distribution  $P(\xi)$  and the corresponding cumulative distri-

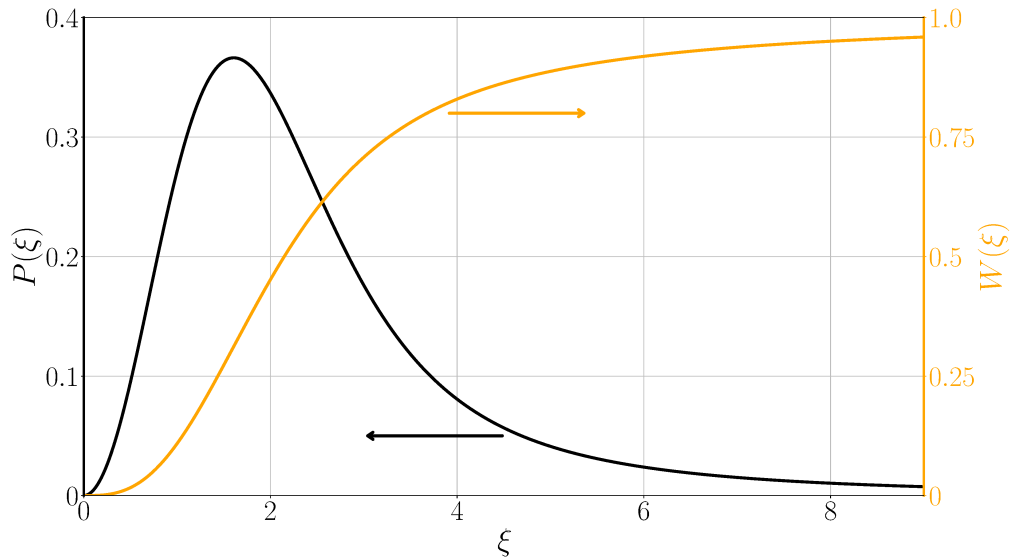


**Figure 6.2.:** Holtsmark distribution  $P(\xi)$  according to Eq. (6.12) and the cumulative distribution  $W(\xi)$ .

bution  $W(\xi)$  are shown in Fig. 6.2. The Holtsmark distribution has a first moment of  $\bar{\xi} \approx 3.41$ , a median of  $\tilde{\xi} \approx 2.15$  and reaches its maximum at  $\xi_{\text{max}} \approx 1.61$ .

### 6.1.2. Stark spectra

In order to calculate the excitonic spectra in a background of charged impurities, we first have to calculate the Stark spectra for particular electric fields  $\alpha_0(\omega, \mathbf{F})$  and average them over the Holtsmark distribution

$$\alpha(\omega, \rho_{\text{ci}}) = \frac{1}{\mathcal{F}_0(\rho_{\text{ci}})} \int_0^\infty dF P\left(\frac{F}{\mathcal{F}_0(\rho_{\text{ci}})}\right) \oint d^2\mathbf{n}_F \frac{\alpha_0(\omega, \mathbf{F})}{4\pi}. \quad (6.14)$$

The Hamiltonian  $\mathcal{H}_0$  whose eigenstates will be used as the basis in which to expand the full Stark-Hamiltonian (6.5) is the Hamiltonian of the isotropic, nonparabolic Wannier equation. Due to the isotropy of  $\mathcal{H}_0$ , the quantisation axis can always be chosen to be parallel to the electric field. The Stark spectrum  $\alpha_0(\omega, F)$  is then independent of the direction of the electric field if the ensuing statistical distribution of quantisation axes is taken into account by regarding the light as unpolarised with respect to the quantisation axis. Consequently, the Holtsmark spectrum simplifies to

$$\alpha(\omega, \rho_{\text{ci}}) = \frac{1}{\mathcal{F}_0(\rho_{\text{ci}})} \int_0^\infty dF P\left(\frac{F}{\mathcal{F}_0(\rho_{\text{ci}})}\right) \alpha_0(\omega, F). \quad (6.15)$$

From the eigenvalues and eigenfunctions of the Stark Hamiltonian, the resonance parameters such as the oscillator strength  $f_i$ , the FWHM linewidth  $\Gamma_i$  and the resonance frequency  $\omega_i$  can be determined. The spectrum can then be modelled by asymmetric Lorentzians

$$\alpha_0(\omega, F) = A\omega \sum_i \frac{f_i \frac{\Gamma_i}{2} + 2q_i g\left(\frac{\omega - \omega_i}{\Gamma_i/2}\right) (\omega - \omega_i)}{\pi (\omega - \omega_i)^2 + \left(\frac{\Gamma_i}{2}\right)^2} \quad (6.16)$$

where the dependency on the field strength  $F$  is mediated by the line parameters. The proportionality constant  $A$  is unknown,  $q_i$  is the line-asymmetry parameter and

$$g(x) = \begin{cases} 1 & \text{if } |x| \leq 4 \\ e^{-\left(\frac{|x|-4}{4}\right)^2} & \text{else} \end{cases} \quad (6.17)$$

denotes the asymmetry-modulation function. The exact choice of this function has little influence on the final spectra and the parameter 4 has been chosen somewhat arbitrarily. Without such a modulation, i.e. with  $g(x) = 1$ , the lines decay with  $(\omega - \omega_i)^{-1}$  far from the resonance which leads to a linearly decreasing absorption coefficient in the vicinity of the band gap. This is not observed in the experiments which agree very well with the Elliott's prediction [76], derived by modelling the lines as symmetric Lorentzians. Symmetric Lorentzians decay with  $(\omega - \omega_i)^{-2}$  and result in a linearly increasing absorption coefficient in the vicinity of the band gap. The modulation of the

asymmetry guarantees, that the line shape resembles an asymmetric Lorentzian in the vicinity of the resonance but a symmetric one far from it without impacting the normalisation.

The asymmetry parameter  $q_i$  cannot be derived from the Wannier equation and has to be fitted to the experiment. Fortunately, it is almost independent of the resonance and a fixed value of  $q_i = -0.24$  can be used for all resonances. The  $q_i$  are linked to the frequency dependence of the phonon-exciton scattering for isolated resonances [86]. The semblance of asymmetry can also arise from the superposition of multiple resonances, as will be the case in the discussion of the results of this Chapter. All line parameters derived from fits to the Holtmark spectra shall therefore be interpreted as empirical parameters facilitating the comparison of the line shapes, only.

The oscillator strengths of the Stark-shifted excitons can be derived from the transition matrix elements from the crystal vacuum to the basis states, which can be calculated from the radial real-space wave functions  $R_{n,\ell}(r)$  via

$$o_{n,\ell,m} \propto \begin{cases} \left. \frac{\partial R_{n,\ell}(r)}{\partial r} \right|_{r=0} & \text{for } \ell = 1 \\ 0 & \text{else.} \end{cases} \quad (6.18)$$

The relative oscillator strengths are then given by

$$f_i \propto |\mathbf{o} \cdot \mathbf{c}_i|^2, \quad (6.19)$$

where  $\mathbf{c}_i$  is an algebraic eigenvector of the Stark-Hamiltonian (6.5) and  $\mathbf{o}$  is the vector of the transition matrix elements, both expressed in the basis of the eigenstates of  $\mathcal{H}_0$ .

The excitonic linewidths are known from both experiment [18, 20, 25, 26, 143] and theory [33]. The theoretical linewidths are dominated by the phonic decay channels into the  $1S$  and  $2S$  states, mostly Fröhlich-scattering by the LO phonons and deformation-potential scattering by the  $\Gamma_{3/5}^-$  phonons. The results agree very well with the experimental linewidths for the odd-parity states (i.e.  $P$ ,  $F$ , etc.) but substantially underestimate the linewidths for the even-parity states. The linewidths of the  $P$  and  $F$ -excitons are therefore modelled by the theoretical values given in Tab. 6.1, while the  $S$  and  $D$ -states are modelled by the experimental linewidths derived from the second harmonic generation (SHG) spectra in Ref. [143]. These result in  $\Gamma_{nS} = 2 \text{ meV } n^{-3}$  and  $\Gamma_{nD} = 3 \text{ meV } n^{-3}$ . The  $n^{-3}$  scaling is also used to extrapolate the linewidths of the odd-parity states and follows from the theory laid out in Ref. [33].

If the linewidths were to follow the expected scaling with  $n^{-3}$  for large  $n$ , it should in principle be possible to observe arbitrarily large  $n$  as the separation of the Rydberg states decreases with  $n^{-3}$  as well. In practice, only a finite number of resonances are visible due to a variety of additional broadening mechanisms. One of these seems to result in a homogeneous broadening of all exciton resonances by roughly  $5 \mu\text{eV}$  (see Fig. 6.3). This observation is also congruent with the vanishing

$n$	$P$	$F$	$n$	$P$	$F$	$n$	$P$	$F$	$n$	$P$	$F$
2	1896		3	648.4		4	268.5	8.162	5	139.8	7.489
6	81.68	5.024	7	51.74	3.75	8	34.79	2.974	9	24.5	2.369
10	17.89	1.89	11	13.46	1.516	12	10.38	1.226	13	8.17	1.001
14	6.545	0.825	15	5.325	0.687	16	4.389	0.577	17	3.66	0.488
18	3.084	0.416	19	2.623	0.358	20	2.249	0.31	21	1.943	0.27
22	1.691	0.236	23	1.48	0.208	24	1.303	0.184			

**Table 6.1.:** Input linewidths  $\Gamma_{n,\ell}$  in  $\mu\text{eV}$ , calculated by Prof. H. Stolz [33].

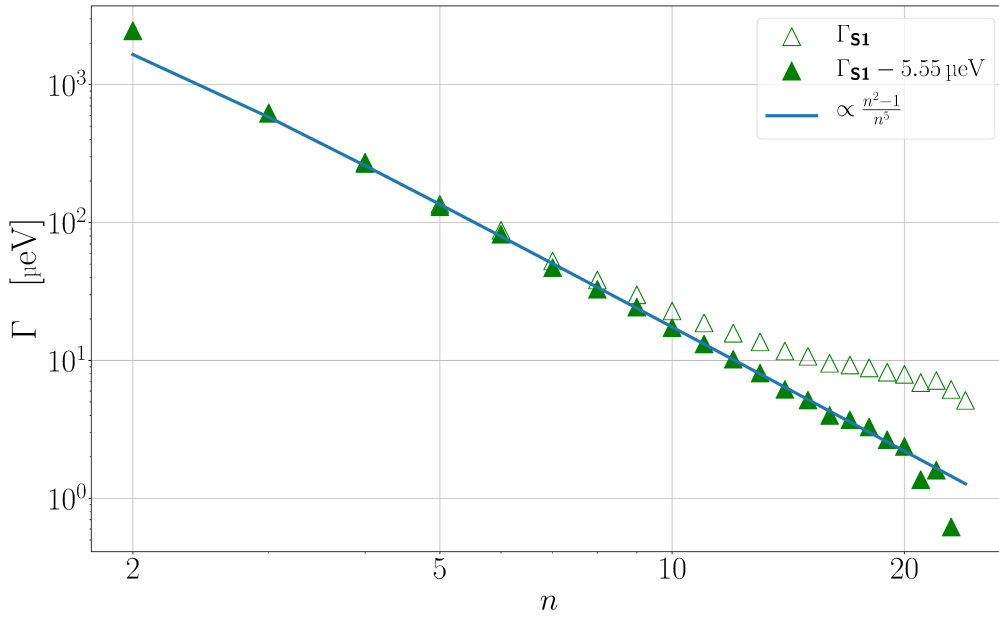


**Figure 6.3.:** Linewidth of the  $P$ -excitons and the additional broadening derived from fits to the experimental spectrum **S1**. The deviation from the expected  $(n^2 - 1)n^{-5}$  scaling can be explained by a homogeneous broadening of  $5.55\mu\text{eV}$ . For more information on the experimental spectra, see Sec. 6.2.

of the  $F$ -excitons, whose linewidths should also scale with  $n^{-3}$  for large  $n$ . They do, however, start to first overlap and then disappear when their separation is between  $5\mu\text{eV}$  and  $10\mu\text{eV}$  [20]. As we do not know the origin of this broadening, we chose to empirically model it by adding  $5.55\mu\text{eV}$  to all excitonic linewidths. In order to propagate the input linewidth to the Stark states, we decided to use a weighted average

$$\Gamma_i = \mathbf{c}_i \cdot \mathbf{\Gamma} \cdot \mathbf{c}_i, \quad (6.20)$$

where  $\Gamma$  is the diagonal matrix of the input linewidths. This is of course only an estimate of the actual scattering rates as it neglects the phase information of the scattering matrix-elements but is necessary as we do not know the underlying scattering matrix elements.

Clearly, expanding the excitonic Stark-Hamiltonian in a basis of bound exciton states is only a good approximation for Stark-states that are themselves bound. The ionisation due to the electric field could be modelled by the introduction of a complex absorbing potential [144] or a complex rotation scheme [41]. Fortunately, the states in the vicinity of the classical ionisation threshold [21]

$$E_{\text{ion}}(F) = -\sqrt{\frac{e^3 F}{\pi \varepsilon}} \quad (6.21)$$

tend to be very sensitive to variations of the electric field  $F$  and to be broadened by ionisation. They do not contribute any prominent features in the Holtmark-averaged spectra, only a quasi-continuous background.

Due to the rotational symmetry of the excitonic Hamiltonian  $\mathcal{H}_0$ , the Stark-Hamiltonian retains an  $O(2)$  symmetry about the field axis. The magnetic quantum number  $m$  does therefore remain a good quantum number, and we can restrict the calculation to  $m = 0, 1$ . This is possible, as the optically active  $P$ -states can only be mixed into states with  $m = 0, \pm 1$  and the states with  $m = \pm 1$  are degenerate<sup>1</sup>, due to time-inversion symmetry. The basis used for the results presented in this chapter, consists of all states with  $\ell \leq 25$  and  $n_r = n - \ell - 1 \leq 100$ . This yields a basis of dimension 2275 for  $m = 0$  and 2175 for  $m = 1$ .

## 6.2. Results

In this Section, two experimental absorption spectra will be compared to Holtmark spectra, with an impurity density  $\rho_{\text{ci}}$  chosen to reproduce the maximum observed principal quantum number  $n_{\text{max}}$ . The first spectrum **S1** is the spectrum published in Ref. [18], reaches a maximum principal quantum number  $n_{\text{max}} = 25$  and was recorded at a temperature of 1.2 K. The spectrum **S2**, on the other hand, was recorded at 1.3 K and the excitons are discernible up to  $n_{\text{max}} = 13$ . The quantity  $n_{\text{max}}$  is an important quantity for the comparison of different spectra but does not have an exact definition. In our analysis, a resonance was considered to have vanished as soon as its spectral range could not reliably be fitted by the asymmetric Lorentzian line shapes of Eq. (6.16). Both experimental spectra were provided by the group of Prof. M. Bayer at the TU Dortmund.

Figure 6.4 shows a comparison of the experimental and numerical spectra for impurity densities of  $\rho_{\text{ci}} = 1.2 \times 10^9 \text{ cm}^{-3}$  (**S1**) and  $\rho_{\text{ci}} = 1.0 \times 10^{11} \text{ cm}^{-3}$  (**S2**), respectively. For large  $n$ , the averaging over the Stark-shifted exciton lines leads to an apparent broadening shortly before the

<sup>1</sup>To be more precise, for every state with  $m = 1$  exists a degenerate state with  $m = -1$  whose wave function is just the complex conjugate.

resonances vanish into the background. A similar transition can be seen in the experimental spectra, it does however proceed over a considerably larger range of principal quantum numbers. In Fig. 6.4 (a), the loss of oscillator strength relative to the theoretical prediction is already apparent at  $n = 10$  in **S1**, but does only set in around  $n = 17$  in the numerical spectrum. Furthermore, additional lines corresponding first and foremost to the  $S$ ,  $D$  and  $F$ -excitons start to appear in the numerical spectrum shown in Fig. 6.4 (b). These lines are a consequence of the breaking of the rotational symmetry inherent in our model, which shifts oscillator strength to formerly dark states. The additional lines are not observed experiment, even though they should be resolvable if the impurities are indeed the limiting factor to the observation of the Rydberg excitons in this crystal. It should be noted here, that a set of yet unexplained intermediate peaks have been observed in experimental spectra [29] and are in fact also visible in **S1** and **S2**. The fact that they appear at lower  $n$  in **S2** might simply be a consequence of the relative height as compared to the  $P$ -excitons, but it might also be an indicator that they are related to the quality of the crystal. Nonetheless, neither the positions nor the oscillator strengths of these peaks match that of the additional lines in the numerical spectra nor in fact the positions where states with larger angular momenta would be expected. It does therefore seem unlikely that they are connected to the additional lines in the numerical spectrum of Fig. 6.4 (b).

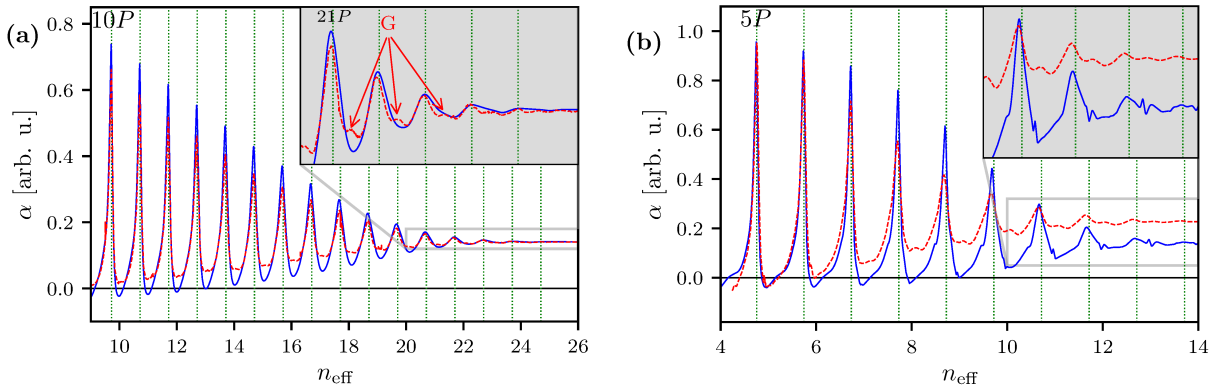


**Figure 6.4.:** Comparison of the experimental (red dashed lines) and numerical spectra (blue solid lines). The green vertical lines denote the numerical positions of the unperturbed  $P$ -excitons and the marker **G** a few of the intermediate peaks observed in the experimental spectra. The effective principal quantum number is given by  $n_{\text{eff}} = \sqrt{-Ry^*/(E - E_g)}$ . The deviations of the resonance positions  $\delta_n = n - n_{\text{eff}}$  are simply the quantum defects. (a): **S1** compared to numerical spectrum for  $\rho_{\text{ci}} = 1.2 \times 10^9 \text{ cm}^{-3}$ . (b): **S2** compared to Holtmark spectrum with  $\rho_{\text{ci}} = 1.0 \times 10^{11} \text{ cm}^{-3}$ . The background of phonon-assisted absorption into the  $1S$  and  $2S$ -states [32] has been removed from both **S1** and **S2** by the experimental group.

Figure 6.5 shows the parameters of the asymmetric Lorentzians derived from fits to the numerical and experimental spectra under the assumption that the underground below each line is constant over its width. In both the oscillator strength and the linewidth, the theoretically expected scaling has been normalised in order to increase the visibility of any deviations. The numerical oscillator strengths follow the expected scaling longer than is observed in the experiment and only



start to decrease significantly at  $n \approx 2n_{\max}(\rho_{\text{ci}})/3$ . They do, however, decrease much faster once the lines start to vanish. Nonetheless, to the best of our knowledge the charged impurities are the first investigated effect that does reproduce this decrease of oscillator strength at all. The observation could be explained neither by plasma nor by phonon interaction [33].

The linewidths  $\Gamma_n$  start to deviate from those of the unperturbed excitons at  $n \approx n_{\max}(\rho_{\text{ci}})/2$  and drop of shortly before the resonances vanish. For intermediate  $n$ , the numerical linewidths overestimate the experimental ones slightly for **S1** and underestimate them for **S2**. Nonetheless, the model reproduces the general behaviour of the linewidths, particularly the decrease shortly before the resonances vanish.

The asymmetry of the lines  $q_i$  are also reasonably well reproduced. In particular, the increase and the change in sign at  $n \approx 4n_{\max}(\rho_{\text{ci}})/5$  can be seen in both the numerical and experimental spectra. As stated before, this change in asymmetry is an effect of the superposition of multiple lines and not related to the cause of the asymmetry of the unperturbed excitons.

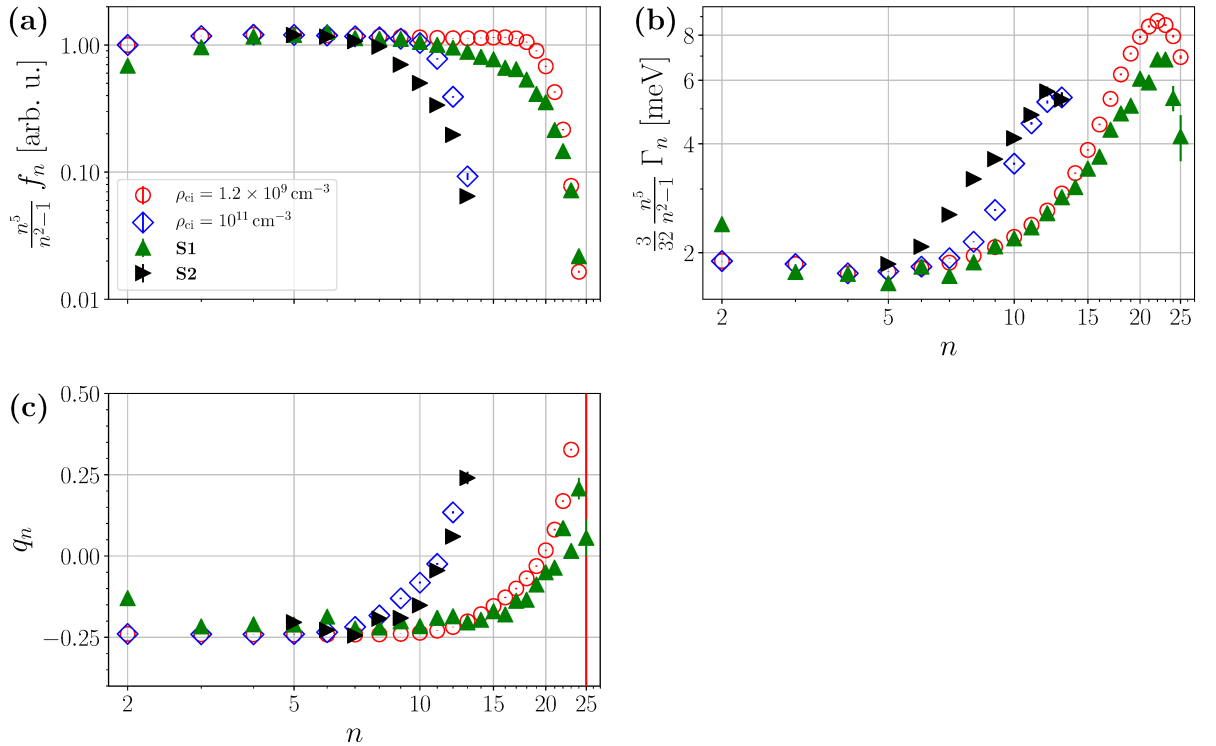


**Figure 6.5.:** Line parameters of the asymmetric Lorentzian according to fits to the numerical and experimental spectra.

Figure 6.6 shows the band gap shift derived from the maximum observable quantum number  $n_{\max}(\rho_{\text{ci}})$  for a range of impurity densities. The band gap shift can be fitted by a power law

$$\Delta E_{\text{g}}(\rho_{\text{ci}}) = -(0.71 \pm 0.17) \mu\text{eV} \left( \frac{\rho_{\text{ci}}}{\text{cm}^{-3}} \right)^{0.254 \pm 0.011} \propto \rho_{\text{ci}}^{1/4}. \quad (6.22)$$

The same scaling with  $\rho^{1/4}$  has been observed for the influence of a screening electron-hole plasma, both in experiment and theory [31]. In the case of the charged impurities, this is a purely empirical observation and no statements can be made on whether this behaviour extends beyond the range of densities investigated here.

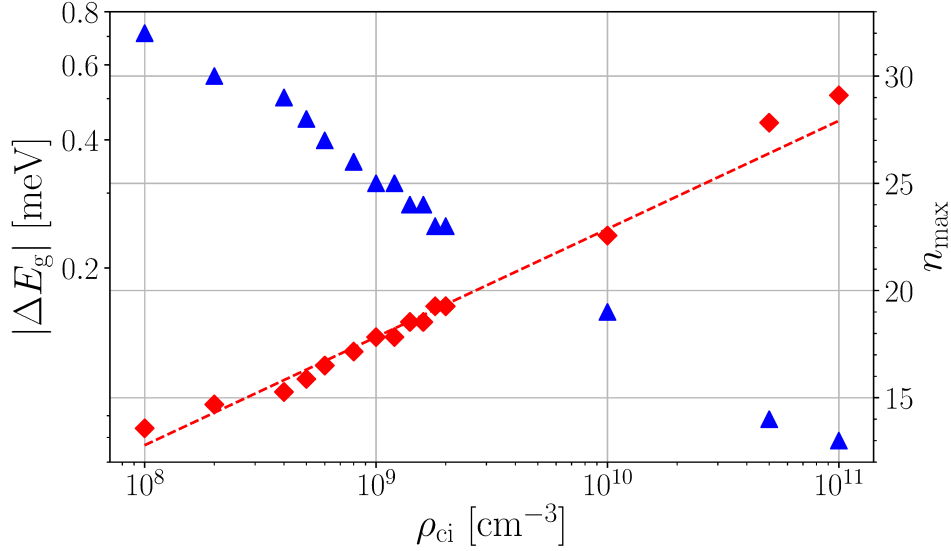


**Figure 6.6.:** Band gap shift  $\Delta E_g$  in dependence of the density of charged impurities derived from the maximum observable quantum number  $n_{max}(\rho_{ci})$ . The red dashed line shows the power-law fit.

### 6.3. Conclusion

The results of this Chapter have shown that some previously unexplained features of the excitonic spectra could be explained by the presence of charged impurities. This includes the loss of oscillator strengths of the Rydberg excitons as well as the change in the asymmetry of the lines. Both the linewidths and the asymmetries are reasonably well reproduced by the model. The oscillator strengths do however show a markedly different behaviour in the Holtmark spectra, following the theoretical predictions for the unperturbed excitons much longer and decreasing much faster compared to the experimental spectra.

The symmetry breaking inherent in the model leads to a redistribution of oscillator strengths to originally dark states which leads to a change of the perceived asymmetry of the lines as well as the appearance of additional lines. For low densities, these lines are masked by the additional broadening shown in Fig. 6.3. For large densities, on the other hand, these lines should be visible in the spectra if the charged impurities are indeed the limiting factor to the observation of the Rydberg excitons. If they are not visible, the calculations performed in this Chapter could be used to establish an upper limit on the impurity density in the crystal.

## Chapter 7.

### Summary & Outlook

In this thesis, we have investigated the influence of the complex valence-band structure on the Rydberg excitons in  $\text{Cu}_2\text{O}$  and assessed their reaction to multiple external perturbations. In the process, we have shown that the valence-band nonparabolicity is the leading cause of the excitonic quantum defects in  $\text{Cu}_2\text{O}$  which were observed by Kazimierczuk *et al.* [18]. In fact, the inclusion of the complex valence-band structure into the Wannier equation results in a reduction of the relative deviation between the experimental and theoretical Rydberg resonance-energies by factors between 30 and  $10^4$ , compared to the effective-mass approximation. Based on the excitonic wave functions derived from this treatment, we discussed the calculation of the excitonic Van der Waals potentials. These are relevant to the assessment of the role the excitonic Rydberg blockade plays in the intensity-dependent bleaching of the exciton resonances observed in the experiment [18]. Due to the uncertainty in the exciton density achieved in these experiments, the amount of blockade could not be quantified yet. Plans exist to investigate the contributions of the different blockade processes in pulsed excitation based on their characteristic time scales. In any case, the calculated interaction potentials will be a vital ingredient to any future investigation of the excitonic Van der Waals interaction in  $\text{Cu}_2\text{O}$ .

Another external perturbation discussed in this thesis is the effective potential induced by an inhomogeneous straining of the crystal. It constitutes one possible mechanism to gain control over the relative position of the excitons on length scales comparable to the estimated blockade radii (a few  $\mu\text{m}$ ). The influence of strain on the odd-parity excitons observed in single-photon dipole absorption can be separated into two distinct effects. The band-gap shift  $\Delta E_g$  shifts all states of one series equally and does not affect the internal degrees of freedom whatsoever. The distortion of the valence band induces a binding-energy shift  $\Delta E_b$  which strongly depends on the excitonic state and also encompasses a strong mixing of the Rydberg states. As it is roughly proportional to the binding energy of the unperturbed state it can be neglected as a potential contribution for the Rydberg states. In order to achieve a trapping potential, i.e. a minimum in  $\Delta E_g$ , large stresses on the order of 0.25 GPa are necessary. This might be too much for the thin crystals ( $\sim 30\mu\text{m}$ ) used for the experiments on Rydberg excitons. The fragility of the crystals as well as the strong mixing of the Rydberg states by the distortion of the valence band indicate that it might be worthwhile

to investigate low-strain alternatives. Viable routes to this end might be dynamical phenomena such as surface-acoustic waves or schemes which do not rely on a trapping potential at all. Due to the short lifetime, a free exciton does typically only travel distances less than the extension of its real-space wave function. This implies that it might be possible to localise the excitons by locally tuning the resonance condition but without explicitly trapping them.

The physics of excitonic transitions is one of the main features that put excitons apart from atomic systems. We have provided calculations of the transition strengths between the Rydberg states of the yellow, green and blue series and shown that the relevant material parameters can be related to the known band-structure parameters. The calculations show that the dipole approximation should be used with care in inter-series transitions and that regimes might be reachable in which the dipole approximation is completely broken, specifically for the yellow-blue transitions. One shortcoming of the theoretical treatment presented is the lack of detailed knowledge about the properties of the green and blue states. The states have been approximated by simple, hydrogen-like envelope functions which might not capture all the states' properties such as the mixing of angular momenta by the anisotropic effective mass or the coupling between the excitonic series. In order to remedy this shortcoming, the authors of Ref. [125] are performing calculations for the yellow-green transitions based on the eigenstates of the multi-band problem presented in Sec. 3.1.1.

Finally, we have shown that a population of charged impurities might explain the deviation of both the oscillator strengths and the line asymmetries from the expected scaling. The strongly inhomogeneous electric fields induced by these impurities result in an inhomogeneous broadening of the resonances as well as the possible ionisation of the Rydberg excitons producing similar spectral features to those observed in the experiments. The necessary densities are moderate and lie in the range between  $10^9 \text{ cm}^{-3}$  and  $10^{11} \text{ cm}^{-3}$ . Other effects might exist which could produce similar signatures, e.g. surface charges or electric fields induced by optical phonons, and the progression of the oscillator strengths cannot be reproduced exactly. The exact origin of the observed features does thus remain an open question, as no independent verification of the impurity density exists.

The community has now gathered a thorough understanding of the single-exciton spectra in  $\text{Cu}_2\text{O}$ , with and without external perturbation by, e.g., electric and magnetic fields as well as strain. Together with the exciton-exciton interaction potentials, it will serve as a starting point for the investigation of the dynamics of interacting excitonic Rydberg gases. Future applications of this research might include the implementation of quantum information protocols via the creation of giant optical nonlinearities [23, 123] or single-photon sources [122]. It may furthermore serve as groundwork for the design of sensitive field probes based on Rydberg excitons, similar to those that have been demonstrated based on alkali Rydberg atoms [145, 146, 147].

# Appendix A.

## Important tables

### A.1. Material properties of Cu<sub>2</sub>O

Table A.1 contains the material properties used in this thesis.

<b>Suzuki-Hensel parameters</b>	$A_1$	-1.76	$A_2$	4.519	[25]
	$A_3$	-2.201	$B_1$	0.02	
	$B_2$	-0.022	$B_3$	-0.202	
<b>magnetic valence-band parameter</b>	$F$	-0.43			[42, 67]
<b>inverse electron mass</b>	$A_4$	1.01			[148]
<b>parameters of the conduction-band Hamiltonian</b>	$B_{6,8}$	$0.342 \hbar\pi/a_g$	$A_6$	2.44	[67]
	$A_8$	3.99	$A'_8$	-1.94	
			$A''_8$	1.25	
<b>main band gap</b>	$E_g$	2.17208 eV			[18]
<b>spin-orbit splitting</b>	$\Delta_{so}$	131 meV			[9]
<b>conduction-band gap</b>	$\Delta_{68}$	450 meV			[82]
<b>deformation potentials</b>	$D'_1$	2.1 eV	$D_2$	-3.9 eV	[149]
			$D_3$	1.9 eV	
<b>compliance constants</b>	$S_{11}$	$41.69 \text{ TPa}^{-1}$	$S_{12}$	$-19.36 \text{ TPa}^{-1}$	[111]
			$S_{44}$	$82.64 \text{ TPa}^{-1}$	
<b>dielectric constant</b>	$\epsilon_r$	7.5			[150]
<b>dielectric constant</b>	$\epsilon_\infty$	6.46			[151]
<b>lattice constant</b>	$a_g$	0.427 nm			[77]

Table A.1.: Material properties of Cu<sub>2</sub>O used in this work.

## A.2. Excitonic binding energies

The experimental resonance energies are given in Tab. A.2 and the numerical ones in Tab. A.3.

<b>n</b>	<b><i>S</i></b>		<b><i>P</i></b>	<b><i>D</i></b>	<b><i>F</i></b>	
	[25]	[91]	[18]	[25]	[20]	[20]
1		2.0330				
2		2.1544	2.1484			
3	$2.160270 \pm 2.0 \cdot 10^{-5}$	2.1603	2.16135	$2.16229 \pm 2.0 \cdot 10^{-5}$		
4	2.165555		2.16609	$2.166472 \pm 2.0 \cdot 10^{-5}$	2.1665468	2.1665182 2.1665448 2.1665773
5	2.168024		2.16829	2.16849480	2.16852583	2.16850568 2.16852396 2.16854615
6	2.169323		2.16948	2.16957671	2.16961126	2.16959665 2.16960891 2.16962508
7	2.170078		2.170182	2.17026399	2.17026787	2.17025707 2.17026569 2.17027629
8	2.170570		2.170635	2.17069335	2.17069497	
9	2.170899		2.170944		2.17099485	
10	$2.171139 \pm 1.0 \cdot 10^{-5}$		2.171163		2.17118868	
11	$2.17129093 \pm 2.8 \cdot 10^{-7}$		2.171324		2.17134724	
12	$2.171416 \pm 2.0 \cdot 10^{-6}$		2.171446		2.17146712	
13	$2.1715170 \pm 1.7 \cdot 10^{-6}$		2.171541			
14			2.1716159			
15			2.1716758			
16			2.1717248			
17			2.1717653			
18			2.1717989			
19			2.171827			
20			2.1718515			
21			2.1718724			
22			2.1718906			
23			2.1719068			
24			2.1719202			
25			2.1719335			

**Table A.2.:** Experimental exciton binding energies used in this work. All energies in eV. The values in the right column for the F-exciton contain the peak energies of the three absorption lines, while the left column contains an average. The value for the band gap, we got from fitting the experimental P-excitons to the numerical results is  $E_g = 2.172\,073\,3$  eV.

$n$	$^1S_1$	$S_{\text{iso}}$	$^3P_4$	$P_{\text{iso}}$	$^2D_3$	$^3D_5$	$D_{\text{iso}}$	$^3F_4$	$^3F_5$	$^1F_2$	$F_{\text{iso}}$
1	-139.3061	-139.1199									
2	-32.0307	-31.9656	-24.5720	-24.5102							
3	-12.8563	-12.8329	-10.9011	-10.8638	-10.1117	-9.9077	-9.9834				
4	-6.78981	-6.77852	-6.02569	-6.00590	-5.71278	-5.58784	-5.63347	-5.51008	-5.48355	-5.45205	-5.48985
5	-4.16848	-4.16224	-3.79632	-3.78517	-3.64415	-3.56865	-3.59602	-3.53622	-3.51707	-3.49465	-3.52151
6	-2.81139	-2.80762	-2.60342	-2.59665	-2.51877	-2.47087	-2.48818	-2.45513	-2.44188	-2.42648	-2.44488
7	-2.02141	-2.01897	-1.89377	-1.88939	-1.84207	-1.81010	-1.82165	-1.80157	-1.79227	-1.78150	-1.79436
8	-1.52222	-1.52056	-1.43838	-1.43540	-1.40457	-1.38229	-1.39034	-1.37728	-1.37058	-1.36283	-1.37207
9	-1.18710	-1.18592	-1.12913	-1.12701	-1.10584	-1.08973	-1.09556	-1.08660	-1.08164	-1.07591	-1.08274
10	-0.95140	-0.95054	-0.90967	-0.90812	-0.89296	-0.88097	-0.88531	-0.87890	-0.87515	-0.87081	-0.87598
11	-0.77942	-0.77878	-0.74840	-0.74722	-0.73601	-0.72685	-0.73016	-0.72543	-0.72252	-0.71916	-0.72316
12	-0.65013	-0.64963	-0.62644	-0.62553	-0.61701	-0.60985	-0.61245	-0.60885	-0.60655	-0.60390	-0.60706
13	-0.55050	-0.55010	-0.53201	-0.53129	-0.52466	-0.51897	-0.52103	-0.51823	-0.51639	-0.51426	-0.51680
14	-0.47211	-0.47179	-0.45740	-0.45682	-0.45156	-0.44696	-0.44863	-0.44641	-0.44492	-0.44319	-0.44525
15	-0.40933	-0.40907	-0.39744	-0.39697	-0.39273	-0.38896	-0.39033	-0.38854	-0.38731	-0.38588	-0.38758
16	-0.35828	-0.35807	-0.34853	-0.34814	-0.34467	-0.34155	-0.34268	-0.34122	-0.34019	-0.33900	-0.34042
17	-0.31621	-0.31604	-0.30812	-0.30780	-0.30492	-0.30230	-0.30325	-0.30204	-0.30118	-0.30018	-0.30137
18	-0.28114	-0.28099	-0.27434	-0.27407	-0.27167	-0.26945	-0.27025	-0.26924	-0.26850	-0.26765	-0.26867
19	-0.25158	-0.25146	-0.24583	-0.24560	-0.24356	-0.24167	-0.24236	-0.24150	-0.24087	-0.24014	-0.24101
20	-0.22646	-0.22635	-0.22154	-0.22134	-0.21960	-0.21797	-0.21857	-0.21784	-0.21729	-0.21666	-0.21741
21	-0.20491	-0.20482	-0.20068	-0.20051	-0.19901	-0.19760	-0.19811	-0.19748	-0.19701	-0.19646	-0.19712
22	-0.18630	-0.18622	-0.18263	-0.18248	-0.18118	-0.17995	-0.18040	-0.17986	-0.17944	-0.17896	-0.17953
23	-0.17011	-0.17004	-0.16691	-0.16678	-0.16565	-0.16457	-0.16496	-0.16449	-0.16412	-0.16370	-0.16420
24	-0.15594	-0.15588	-0.15313	-0.15302	-0.15203	-0.15107	-0.15142	-0.15100	-0.15068	-0.15031	-0.15075
25	-0.14347	-0.14342	-0.14099	-0.14089	-0.14002	-0.13917	-0.13948	-0.13911	-0.13883	-0.13850	-0.13889

**Table A.3.:** Numerical binding energies from the two-band model discussed in Chapter 3. All values in meV.





## Appendix B.

### Group theoretical tables

This appendix contains group theoretical tables and other data for the point groups relevant to this work.

#### B.1. Point group symmetries of $\text{Cu}_2\text{O}$

Table B.1 contains the transformational properties of the atomic  $S$ ,  $P$  and  $D$  orbitals under the 48 symmetry operations contained in the cubic symmetry group  $O_h$ . In addition, the table also lists the nontrivial translations  $\tau$  needed in order to map the  $\text{Cu}_2\text{O}$  crystal onto itself<sup>1</sup> as well as the transformational properties of the Cu and O sublattices. From the latter, the equivalent representations of the two sublattices can be deduced, resulting in  $\Gamma_{\text{equiv}}(\text{Cu}) = \Gamma_1^+ \oplus \Gamma_5^+$  as well as  $\Gamma_{\text{equiv}}(\text{O}) = \Gamma_1^+ \oplus \Gamma_2^-$ .

The equivalent representations can be used to deduce both the phonon symmetries and the crystal-field splitting of the atomic orbitals at the  $\Gamma$ -point. Correspondingly, the phonon-symmetries are

$$\begin{aligned}\Gamma_{\text{equiv}}(\text{Cu}) \otimes \Gamma_4^- &= \Gamma_2^- \oplus \Gamma_3^- \oplus 2\Gamma_4^- \oplus \Gamma_5^-, \\ \Gamma_{\text{equiv}}(\text{O}) \otimes \Gamma_4^- &= \Gamma_4^- \oplus \Gamma_5^+, \end{aligned}\tag{B.1}$$

where  $\Gamma_4^-$  symbolises the displacement vector (see also Sec. 2.3.3). The crystal-field splitting of the atomic orbitals can be derived by multiplying  $\Gamma_{\text{equiv}}$  with the symmetries of the atomic orbitals. The 20 copper  $3d$  orbitals<sup>2</sup>, for example, split into

$$\Gamma_{\text{equiv}}(\text{Cu}) \otimes (\Gamma_3^+ \oplus \Gamma_5^+) = \Gamma_1^+ \oplus 2\Gamma_3^+ \oplus 2\Gamma_4^+ \oplus 3\Gamma_5^+, \tag{B.2}$$

where one of the three  $\Gamma_5^+$ -manifolds forms the valence-band.

<sup>1</sup>Note that the translations  $\tau$  depend on the particular choice for the center of inversion. In the following, the center of inversion will be assumed to lie at the center of the  $\text{O}_2$  atom (for the labelling of the basis atoms, see Fig. 2.4 (a)).

<sup>2</sup>Five orbitals on each of the four copper basis-atoms.

$\alpha$	$\tau$	$\Gamma_1^+$	$p_x$ $x$	$p_y$ $y$	$p_z$ $z$	$d_{yz}$	$d_{zx}$	$d_{xy}$	$d_{z^2} \propto 2z^2 - x^2 - y^2$	$d_{x^2-y^2} \propto x^2 - y^2$	$\Gamma_1^+ \oplus \Gamma_5^+$	$\Gamma_1^+ \oplus \Gamma_2^-$
$E$	$\mathbf{0}$	$s$	$x$	$y$	$z$	$d_{yz}$	$d_{zx}$	$d_{xy}$	$d_{z^2}$	$d_{x^2-y^2}$	$\text{Cu}_1 \text{ Cu}_2 \text{ Cu}_3 \text{ Cu}_4$	$\text{O}_1 \text{ O}_2$
$8C_3$	$\mathbf{0}$	$s$	$-z$	$-x$	$y$	$-d_{xy}$	$-d_{yz}$	$d_{zx}$	$-\frac{\sqrt{3}}{2}d_{x^2-y^2} - \frac{1}{2}d_{z^2}$	$-\frac{1}{2}d_{x^2-y^2} + \frac{\sqrt{3}}{2}d_{z^2}$	$\text{Cu}_3 \text{ Cu}_2 \text{ Cu}_4 \text{ Cu}_1$	$\text{O}_1 \text{ O}_2$
	$\mathbf{0}$	$s$	$-z$	$x$	$-y$	$-d_{xy}$	$d_{yz}$	$-d_{zx}$	$-\frac{\sqrt{3}}{2}d_{x^2-y^2} - \frac{1}{2}d_{z^2}$	$-\frac{1}{2}d_{x^2-y^2} + \frac{\sqrt{3}}{2}d_{z^2}$	$\text{Cu}_2 \text{ Cu}_3 \text{ Cu}_1 \text{ Cu}_4$	$\text{O}_1 \text{ O}_2$
	$\mathbf{0}$	$s$	$z$	$-x$	$-y$	$d_{xy}$	$-d_{yz}$	$-d_{zx}$	$-\frac{\sqrt{3}}{2}d_{x^2-y^2} - \frac{1}{2}d_{z^2}$	$-\frac{1}{2}d_{x^2-y^2} + \frac{\sqrt{3}}{2}d_{z^2}$	$\text{Cu}_4 \text{ Cu}_1 \text{ Cu}_3 \text{ Cu}_2$	$\text{O}_1 \text{ O}_2$
	$\mathbf{0}$	$s$	$z$	$x$	$y$	$d_{xy}$	$d_{yz}$	$d_{zx}$	$-\frac{\sqrt{3}}{2}d_{x^2-y^2} - \frac{1}{2}d_{z^2}$	$-\frac{1}{2}d_{x^2-y^2} + \frac{\sqrt{3}}{2}d_{z^2}$	$\text{Cu}_1 \text{ Cu}_4 \text{ Cu}_2 \text{ Cu}_3$	$\text{O}_1 \text{ O}_2$
	$\mathbf{0}$	$s$	$-y$	$-z$	$x$	$-d_{zx}$	$-d_{xy}$	$d_{yz}$	$\frac{\sqrt{3}}{2}d_{x^2-y^2} - \frac{1}{2}d_{z^2}$	$-\frac{1}{2}d_{x^2-y^2} - \frac{\sqrt{3}}{2}d_{z^2}$	$\text{Cu}_2 \text{ Cu}_4 \text{ Cu}_3 \text{ Cu}_1$	$\text{O}_1 \text{ O}_2$
	$\mathbf{0}$	$s$	$-y$	$z$	$-x$	$-d_{zx}$	$d_{xy}$	$-d_{yz}$	$\frac{\sqrt{3}}{2}d_{x^2-y^2} - \frac{1}{2}d_{z^2}$	$-\frac{1}{2}d_{x^2-y^2} - \frac{\sqrt{3}}{2}d_{z^2}$	$\text{Cu}_4 \text{ Cu}_2 \text{ Cu}_1 \text{ Cu}_3$	$\text{O}_1 \text{ O}_2$
	$\mathbf{0}$	$s$	$y$	$-z$	$-x$	$d_{zx}$	$-d_{xy}$	$-d_{yz}$	$\frac{\sqrt{3}}{2}d_{x^2-y^2} - \frac{1}{2}d_{z^2}$	$-\frac{1}{2}d_{x^2-y^2} - \frac{\sqrt{3}}{2}d_{z^2}$	$\text{Cu}_3 \text{ Cu}_1 \text{ Cu}_2 \text{ Cu}_4$	$\text{O}_1 \text{ O}_2$
	$\mathbf{0}$	$s$	$y$	$z$	$x$	$d_{zx}$	$d_{xy}$	$d_{yz}$	$\frac{\sqrt{3}}{2}d_{x^2-y^2} - \frac{1}{2}d_{z^2}$	$-\frac{1}{2}d_{x^2-y^2} - \frac{\sqrt{3}}{2}d_{z^2}$	$\text{Cu}_1 \text{ Cu}_3 \text{ Cu}_4 \text{ Cu}_2$	$\text{O}_1 \text{ O}_2$
$3C_2$	$\mathbf{0}$	$s$	$-x$	$-y$	$z$	$-d_{yz}$	$-d_{zx}$	$d_{xy}$	$d_{z^2}$	$d_{x^2-y^2}$	$\text{Cu}_4 \text{ Cu}_3 \text{ Cu}_2 \text{ Cu}_1$	$\text{O}_1 \text{ O}_2$
	$\mathbf{0}$	$s$	$-x$	$y$	$-z$	$-d_{yz}$	$d_{zx}$	$-d_{xy}$	$d_{z^2}$	$d_{x^2-y^2}$	$\text{Cu}_3 \text{ Cu}_4 \text{ Cu}_1 \text{ Cu}_2$	$\text{O}_1 \text{ O}_2$
	$\mathbf{0}$	$s$	$x$	$-y$	$-z$	$d_{yz}$	$-d_{zx}$	$-d_{xy}$	$d_{z^2}$	$d_{x^2-y^2}$	$\text{Cu}_2 \text{ Cu}_1 \text{ Cu}_4 \text{ Cu}_3$	$\text{O}_1 \text{ O}_2$
$6C_4$	$\mathbf{O}_1$	$s$	$x$	$-z$	$y$	$-d_{yz}$	$d_{xy}$	$-d_{zx}$	$-\frac{\sqrt{3}}{2}d_{x^2-y^2} - \frac{1}{2}d_{z^2}$	$\frac{1}{2}d_{x^2-y^2} - \frac{\sqrt{3}}{2}d_{z^2}$	$\text{Cu}_4 \text{ Cu}_3 \text{ Cu}_1 \text{ Cu}_2$	$\text{O}_2 \text{ O}_1$
	$\mathbf{O}_1$	$s$	$x$	$z$	$-y$	$-d_{yz}$	$-d_{xy}$	$d_{zx}$	$-\frac{\sqrt{3}}{2}d_{x^2-y^2} - \frac{1}{2}d_{z^2}$	$\frac{1}{2}d_{x^2-y^2} - \frac{\sqrt{3}}{2}d_{z^2}$	$\text{Cu}_3 \text{ Cu}_4 \text{ Cu}_2 \text{ Cu}_1$	$\text{O}_2 \text{ O}_1$
	$\mathbf{O}_1$	$s$	$-z$	$y$	$x$	$d_{xy}$	$-d_{zx}$	$-d_{yz}$	$\frac{\sqrt{3}}{2}d_{x^2-y^2} - \frac{1}{2}d_{z^2}$	$\frac{1}{2}d_{x^2-y^2} + \frac{\sqrt{3}}{2}d_{z^2}$	$\text{Cu}_4 \text{ Cu}_1 \text{ Cu}_2 \text{ Cu}_3$	$\text{O}_2 \text{ O}_1$
	$\mathbf{O}_1$	$s$	$z$	$y$	$-x$	$-d_{xy}$	$-d_{zx}$	$d_{yz}$	$\frac{\sqrt{3}}{2}d_{x^2-y^2} - \frac{1}{2}d_{z^2}$	$\frac{1}{2}d_{x^2-y^2} + \frac{\sqrt{3}}{2}d_{z^2}$	$\text{Cu}_2 \text{ Cu}_3 \text{ Cu}_4 \text{ Cu}_1$	$\text{O}_2 \text{ O}_1$
	$\mathbf{O}_1$	$s$	$-y$	$x$	$z$	$d_{zx}$	$-d_{yz}$	$-d_{xy}$	$d_{z^2}$	$-d_{x^2-y^2}$	$\text{Cu}_3 \text{ Cu}_1 \text{ Cu}_4 \text{ Cu}_2$	$\text{O}_2 \text{ O}_1$
	$\mathbf{O}_1$	$s$	$y$	$-x$	$z$	$-d_{zx}$	$d_{yz}$	$-d_{xy}$	$d_{z^2}$	$-d_{x^2-y^2}$	$\text{Cu}_2 \text{ Cu}_4 \text{ Cu}_1 \text{ Cu}_3$	$\text{O}_2 \text{ O}_1$
$6C_2^1$	$\mathbf{O}_1$	$s$	$-x$	$-z$	$-y$	$d_{yz}$	$d_{xy}$	$d_{zx}$	$-\frac{\sqrt{3}}{2}d_{x^2-y^2} - \frac{1}{2}d_{z^2}$	$\frac{1}{2}d_{x^2-y^2} - \frac{\sqrt{3}}{2}d_{z^2}$	$\text{Cu}_1 \text{ Cu}_2 \text{ Cu}_4 \text{ Cu}_3$	$\text{O}_2 \text{ O}_1$
	$\mathbf{O}_1$	$s$	$-x$	$z$	$y$	$d_{yz}$	$-d_{xy}$	$-d_{zx}$	$-\frac{\sqrt{3}}{2}d_{x^2-y^2} - \frac{1}{2}d_{z^2}$	$\frac{1}{2}d_{x^2-y^2} - \frac{\sqrt{3}}{2}d_{z^2}$	$\text{Cu}_2 \text{ Cu}_1 \text{ Cu}_3 \text{ Cu}_4$	$\text{O}_2 \text{ O}_1$
	$\mathbf{O}_1$	$s$	$-z$	$-y$	$-x$	$d_{xy}$	$d_{zx}$	$d_{yz}$	$\frac{\sqrt{3}}{2}d_{x^2-y^2} - \frac{1}{2}d_{z^2}$	$\frac{1}{2}d_{x^2-y^2} + \frac{\sqrt{3}}{2}d_{z^2}$	$\text{Cu}_1 \text{ Cu}_4 \text{ Cu}_3 \text{ Cu}_2$	$\text{O}_2 \text{ O}_1$
	$\mathbf{O}_1$	$s$	$z$	$-y$	$x$	$-d_{xy}$	$d_{zx}$	$-d_{yz}$	$\frac{\sqrt{3}}{2}d_{x^2-y^2} - \frac{1}{2}d_{z^2}$	$\frac{1}{2}d_{x^2-y^2} + \frac{\sqrt{3}}{2}d_{z^2}$	$\text{Cu}_3 \text{ Cu}_2 \text{ Cu}_1 \text{ Cu}_4$	$\text{O}_2 \text{ O}_1$
	$\mathbf{O}_1$	$s$	$-y$	$-x$	$-z$	$d_{zx}$	$d_{yz}$	$d_{xy}$	$d_{z^2}$	$-d_{x^2-y^2}$	$\text{Cu}_1 \text{ Cu}_3 \text{ Cu}_2 \text{ Cu}_4$	$\text{O}_2 \text{ O}_1$
	$\mathbf{O}_1$	$s$	$y$	$x$	$-z$	$-d_{zx}$	$-d_{yz}$	$d_{xy}$	$d_{z^2}$	$-d_{x^2-y^2}$	$\text{Cu}_4 \text{ Cu}_2 \text{ Cu}_3 \text{ Cu}_1$	$\text{O}_2 \text{ O}_1$
$I$	$\mathbf{O}_1$	$s$	$-x$	$-y$	$-z$	$d_{yz}$	$d_{zx}$	$d_{xy}$	$d_{z^2}$	$d_{x^2-y^2}$	$\text{Cu}_1 \text{ Cu}_2 \text{ Cu}_3 \text{ Cu}_4$	$\text{O}_2 \text{ O}_1$
$8S_6$	$\mathbf{O}_1$	$s$	$-z$	$-x$	$-y$	$d_{xy}$	$d_{yz}$	$d_{zx}$	$-\frac{\sqrt{3}}{2}d_{x^2-y^2} - \frac{1}{2}d_{z^2}$	$-\frac{1}{2}d_{x^2-y^2} + \frac{\sqrt{3}}{2}d_{z^2}$	$\text{Cu}_1 \text{ Cu}_4 \text{ Cu}_2 \text{ Cu}_3$	$\text{O}_2 \text{ O}_1$
	$\mathbf{O}_1$	$s$	$-z$	$x$	$y$	$d_{xy}$	$-d_{yz}$	$-d_{zx}$	$-\frac{\sqrt{3}}{2}d_{x^2-y^2} - \frac{1}{2}d_{z^2}$	$-\frac{1}{2}d_{x^2-y^2} + \frac{\sqrt{3}}{2}d_{z^2}$	$\text{Cu}_4 \text{ Cu}_1 \text{ Cu}_3 \text{ Cu}_2$	$\text{O}_2 \text{ O}_1$
	$\mathbf{O}_1$	$s$	$z$	$-x$	$y$	$-d_{xy}$	$d_{yz}$	$-d_{zx}$	$-\frac{\sqrt{3}}{2}d_{x^2-y^2} - \frac{1}{2}d_{z^2}$	$-\frac{1}{2}d_{x^2-y^2} + \frac{\sqrt{3}}{2}d_{z^2}$	$\text{Cu}_2 \text{ Cu}_3 \text{ Cu}_1 \text{ Cu}_4$	$\text{O}_2 \text{ O}_1$
	$\mathbf{O}_1$	$s$	$z$	$x$	$-y$	$-d_{xy}$	$-d_{yz}$	$d_{zx}$	$-\frac{\sqrt{3}}{2}d_{x^2-y^2} - \frac{1}{2}d_{z^2}$	$-\frac{1}{2}d_{x^2-y^2} + \frac{\sqrt{3}}{2}d_{z^2}$	$\text{Cu}_3 \text{ Cu}_2 \text{ Cu}_4 \text{ Cu}_1$	$\text{O}_2 \text{ O}_1$
	$\mathbf{O}_1$	$s$	$-y$	$-z$	$-x$	$d_{zx}$	$d_{xy}$	$d_{yz}$	$\frac{\sqrt{3}}{2}d_{x^2-y^2} - \frac{1}{2}d_{z^2}$	$-\frac{1}{2}d_{x^2-y^2} - \frac{\sqrt{3}}{2}d_{z^2}$	$\text{Cu}_1 \text{ Cu}_3 \text{ Cu}_4 \text{ Cu}_2$	$\text{O}_2 \text{ O}_1$
	$\mathbf{O}_1$	$s$	$-y$	$z$	$x$	$d_{zx}$	$-d_{xy}$	$-d_{yz}$	$\frac{\sqrt{3}}{2}d_{x^2-y^2} - \frac{1}{2}d_{z^2}$	$-\frac{1}{2}d_{x^2-y^2} - \frac{\sqrt{3}}{2}d_{z^2}$	$\text{Cu}_3 \text{ Cu}_1 \text{ Cu}_2 \text{ Cu}_4$	$\text{O}_2 \text{ O}_1$
	$\mathbf{O}_1$	$s$	$y$	$-z$	$x$	$-d_{zx}$	$d_{xy}$	$-d_{yz}$	$\frac{\sqrt{3}}{2}d_{x^2-y^2} - \frac{1}{2}d_{z^2}$	$-\frac{1}{2}d_{x^2-y^2} - \frac{\sqrt{3}}{2}d_{z^2}$	$\text{Cu}_4 \text{ Cu}_2 \text{ Cu}_1 \text{ Cu}_3$	$\text{O}_2 \text{ O}_1$
	$\mathbf{O}_1$	$s$	$y$	$z$	$-x$	$-d_{zx}$	$-d_{xy}$	$d_{yz}$	$\frac{\sqrt{3}}{2}d_{x^2-y^2} - \frac{1}{2}d_{z^2}$	$-\frac{1}{2}d_{x^2-y^2} - \frac{\sqrt{3}}{2}d_{z^2}$	$\text{Cu}_2 \text{ Cu}_4 \text{ Cu}_3 \text{ Cu}_1$	$\text{O}_2 \text{ O}_1$
$3\sigma_h$	$\mathbf{O}_1$	$s$	$-x$	$y$	$z$	$d_{yz}$	$-d_{zx}$	$-d_{xy}$	$d_{z^2}$	$d_{x^2-y^2}$	$\text{Cu}_2 \text{ Cu}_1 \text{ Cu}_4 \text{ Cu}_3$	$\text{O}_2 \text{ O}_1$
	$\mathbf{O}_1$	$s$	$x$	$-y$	$z$	$-d_{yz}$	$d_{zx}$	$-d_{xy}$	$d_{z^2}$	$d_{x^2-y^2}$	$\text{Cu}_3 \text{ Cu}_4 \text{ Cu}_1 \text{ Cu}_2$	$\text{O}_2 \text{ O}_1$
	$\mathbf{O}_1$	$s$	$x$	$y$	$-z$	$-d_{yz}$	$-d_{zx}$	$d_{xy}$	$d_{z^2}$	$d_{x^2-y^2}$	$\text{Cu}_4 \text{ Cu}_3 \text{ Cu}_2 \text{ Cu}_1$	$\text{O}_2 \text{ O}_1$
$6S_4$	$\mathbf{0}$	$s$	$-x$	$-z$	$y$	$-d_{yz}$	$-d_{xy}$	$d_{zx}$	$-\frac{\sqrt{3}}{2}d_{x^2-y^2} - \frac{1}{2}d_{z^2}$	$\frac{1}{2}d_{x^2-y^2} - \frac{\sqrt{3}}{2}d_{z^2}$	$\text{Cu}_3 \text{ Cu}_4 \text{ Cu}_2 \text{ Cu}_1$	$\text{O}_1 \text{ O}_2$
	$\mathbf{0}$	$s$	$-x$	$z$	$-y$	$-d_{yz}$	$d_{xy}$	$-d_{zx}$	$-\frac{\sqrt{3}}{2}d_{x^2-y^2} - \frac{1}{2}d_{z^2}$	$\frac{1}{2}d_{x^2-y^2} - \frac{\sqrt{3}}{2}d_{z^2}$	$\text{Cu}_4 \text{ Cu}_3 \text{ Cu}_1 \text{ Cu}_2$	$\text{O}_1 \text{ O}_2$
	$\mathbf{0}$	$s$	$-z$	$-y$	$x$	$-d_{xy}$	$-d_{zx}$	$d_{yz}$	$\frac{\sqrt{3}}{2}d_{x^2-y^2} - \frac{1}{2}d_{z^2}$	$\frac{1}{2}d_{x^2-y^2} + \frac{\sqrt{3}}{2}d_{z^2}$	$\text{Cu}_2 \text{ Cu}_3 \text{ Cu}_4 \text{ Cu}_1$	$\text{O}_1 \text{ O}_2$
	$\mathbf{0}$	$s$	$z$	$-y$	$-x$	$d_{xy}$	$-d_{zx}$	$-d_{yz}$	$\frac{\sqrt{3}}{2}d_{x^2-y^2} - \frac{1}{2}d_{z^2}$	$\frac{1}{2}d_{x^2-y^2} + \frac{\sqrt{3}}{2}d_{z^2}$	$\text{Cu}_4 \text{ Cu}_1 \text{ Cu}_2 \text{ Cu}_3$	$\text{O}_1 \text{ O}_2$
	$\mathbf{0}$	$s$	$-y$	$x$	$-z$	$-d_{zx}$	$d_{yz}$	$-d_{xy}$	$d_{z^2}$	$-d_{x^2-y^2}$	$\text{Cu}_2 \text{ Cu}_4 \text{ Cu}_1 \text{ Cu}_3$	$\text{O}_1 \text{ O}_2$
	$\mathbf{0}$	$s$	$y$	$-x$	$-z$	$d_{zx}$	$-d_{yz}$	$-d_{xy}$	$d_{z^2}$	$-d_{x^2-y^2}$	$\text{Cu}_3 \text{ Cu}_1 \text{ Cu}_4 \text{ Cu}_2$	$\text{O}_1 \text{ O}_2$
$6\sigma_d$	$\mathbf{0}$	$s$	$x$	$-z$	$-y$	$d_{yz}$	$-d_{xy}$	$-d_{zx}$	$-\frac{\sqrt{3}}{2}d_{x^2-y^2} - \frac{1}{2}d_{z^2}$	$\frac{1}{2}d_{x^2-y^2} - \frac{\sqrt{3}}{2}d_{z^2}$	$\text{Cu}_2 \text{ Cu}_1 \text{ Cu}_3 \text{ Cu}_4$	$\text{O}_1 \text{ O}_2$
	$\mathbf{0}$	$s$	$x$	$z$	$y$	$d_{yz}$	$d_{xy}$	$d_{zx}$	$-\frac{\sqrt{3}}{2}d_{x^2-y^2} - \frac{1}{2}d_{z^2}$	$\frac{1}{2}d_{x^2-y^2} - \frac{\sqrt{3}}{2}d_{z^2}$	$\text{Cu}_1 \text{ Cu}_2 \text{ Cu}_4 \text{ Cu}_3$	$\text{O}_1 \text{ O}_2$
	$\mathbf{0}$	$s$	$-z$	$y$	$-x$	$-d_{xy}$	$d_{zx}$	$-d_{yz}$	$\frac{\sqrt{3}}{2}d_{x^2-y^2} - \frac{1}{2}d_{z^2}$	$\frac{1}{2}d_{x^2-y^2} + \frac{\sqrt{3}}{2}d_{z^2}$	$\text{Cu}_3 \text{ Cu}_2 \text{ Cu}_1 \text{ Cu}_4$	$\text{O}_1 \text{ O}_2$
	$\mathbf{0}$	$s$	$z$	$y$	$x$	$d_{xy}$	$d_{zx}$	$d_{yz}$	$\frac{\sqrt{3}}{2}d_{x^2-y^2} - \frac{1}{2}d_{z^2}$	$\frac{1}{2}d_{x^2-y^2} + \frac{\sqrt{3}}{2}d_{z^2}$	$\text{Cu}_1 \text{ Cu}_4 \text{ Cu}_3 \text{ Cu}_2$	$\text{O}_1 \text{ O}_2$
	$\mathbf{0}$	$s$	$-y$	$-x$	$z$	$-d_{zx}$	$-d_{yz}$	$d_{xy}$	$d_{z^2}$	$-d_{x^2-y^2}$	$\text{Cu}_4 \text{ Cu}_2 \text{ Cu}_3 \text{ Cu}_1$	$\text{O}_1 \text{ O}_2$
	$\mathbf{0}$	$s$	$y$	$x$	$z$	$d_{zx}$	$d_{yz}$	$d_{xy}$	$d_{z^2}$	$-d_{x^2-y^2}$	$\text{Cu}_1 \text{ Cu}_3 \text{ Cu}_2 \text{ Cu}_4$	$\text{O}_1 \text{ O}_2$

**Table B.1.:** The 48 point-group symmetries of Cu<sub>2</sub>O and transformation properties of  $S$ ,  $P$  and  $D$  orbitals as well as the Cu and O sublattices. The names of the basis atoms Cu<sub>*i*</sub> and O<sub>*j*</sub> refer to the nomenclature introduced in Fig. 2.4 (a).

## B.2. Character table of $O_h$

The characters of a representation  $\Lambda$  are defined as

$$\chi_\Lambda(a) = \text{Tr} [\mathbf{D}_\Lambda(a)]. \quad (\text{B.3})$$

As the trace is invariant under similarity transformations, the characters of two equivalent representations have to coincide, as well as the characters of two elements  $a, b$  belonging to the same conjugacy class. The irreducible representations of a group can therefore uniquely be identified by their characters.

It can be shown that the characters of the irreducible representations have to fulfil the orthogonality relations [48, 49]

$$\sum_{i=1}^r r_i \chi_\Gamma^*(i) \chi_{\Gamma'}(i) = g \delta_{\Gamma, \Gamma'}, \quad (\text{B.4})$$

$$\sum_{\Gamma=1}^r \chi_\Gamma^*(i) \chi_\Gamma(j) = \frac{g}{r_i} \delta_{i,j} \quad (\text{B.5})$$

where  $i$  and  $j$  label the conjugacy classes,  $\Gamma$  and  $\Gamma'$  denote the irreducible representations and  $r_i$  is the number of elements in the  $i$ th conjugacy class. Two important relations for the characters are

$$\chi_{\Lambda_\alpha \otimes \Lambda_\beta}(i) = \chi_{\Lambda_\alpha}(i) \chi_{\Lambda_\beta}(i), \quad (\text{B.6})$$

$$\chi_{\Lambda_\alpha \oplus \Lambda_\beta}(i) = \chi_{\Lambda_\alpha}(i) + \chi_{\Lambda_\beta}(i). \quad (\text{B.7})$$

The Eqs. (B.4, B.6, B.7) allow for the decomposition of every product of two irreducible representations into a sum of irreducible representations. These decompositions are given as so called multiplication tables (e. g. Tab. B.3), not to be confused with multiplication tables of the group elements. The character table of the group  $O_h$  with the basis functions used in this thesis is given in Tab. B.2. The rows are labelled by the irreducible representations and the columns by the conjugacy classes. The corresponding multiplication table is given in Tab. B.3.

	$O_h$		$E$	$\bar{E}$	$8C_3$	$8\bar{C}_3$	$3C_2$	$6C_4$	$6\bar{C}_4$	$6C_{2'}$	$I$	$\bar{I}$	$8S_6$	$8\bar{S}_6$	$3\sigma_h$	$6S_4$	$6\bar{S}_4$	$6\sigma_d$	Basis functions
M	BSW	K					$3\bar{C}_2$			$6\bar{C}_{2'}$					$3\bar{\sigma}_h$			$6\bar{\sigma}_d$	
$A_{1g}$	$\Gamma_1$	$\Gamma_1^+$	1	1	1	1	1	1	1	1	1	1	1	1	1	1	1	1	$R$
$A_{2g}$	$\Gamma_2$	$\Gamma_2^+$	1	1	1	1	-1	-1	-1	1	1	1	1	1	1	-1	-1	-1	$(x^2 - y^2)(y^2 - z^2)(z^2 - x^2)$
$E_g$	$\Gamma_{12}$	$\Gamma_3^+$	2	2	-1	-1	2	0	0	0	2	2	-1	-1	2	0	0	0	$(2z^2 - x^2 - y^2), \sqrt{3}(x^2 - y^2)$
$F_{1g}$	$\Gamma'_{15}$	$\Gamma_4^+$	3	3	0	0	-1	1	1	-1	3	3	0	0	-1	1	1	-1	$S_x, S_y, S_z$
$F_{2g}$	$\Gamma'_{25}$	$\Gamma_5^+$	3	3	0	0	-1	-1	-1	1	3	3	0	0	-1	-1	-1	1	$yx, xz, xy$
$A_{1u}$	$\Gamma'_1$	$\Gamma_1^-$	1	1	1	1	1	1	1	1	-1	-1	-1	-1	-1	-1	-1	-1	$\Gamma_2^- \times \Gamma_2^+$
$A_{2u}$	$\Gamma'_2$	$\Gamma_2^-$	1	1	1	1	1	-1	-1	-1	-1	-1	-1	-1	-1	1	1	1	$xyz$
$E_u$	$\Gamma'_{12}$	$\Gamma_3^-$	2	2	-1	-1	2	0	0	0	-2	-2	1	1	-2	0	0	0	$\Gamma_3^+ \times \Gamma_2^-$
$F_{1u}$	$\Gamma_{15}$	$\Gamma_4^-$	3	3	0	0	-1	1	1	-1	-3	-3	0	0	1	-1	-1	1	$x, y, z$
$F_{2u}$	$\Gamma_{25}$	$\Gamma_5^-$	3	3	0	0	-1	-1	-1	1	-3	-3	0	0	1	1	1	-1	$\Gamma_5^+ \times \Gamma_1^-$
		$\Gamma_6^+$	2	-2	1	-1	0	$\sqrt{2}$	$-\sqrt{2}$	0	2	-2	1	-1	0	$\sqrt{2}$	$-\sqrt{2}$	0	$\phi\left(\frac{1}{2}, -\frac{1}{2}\right), \phi\left(\frac{1}{2}, \frac{1}{2}\right)$
		$\Gamma_7^+$	2	-2	1	-1	0	$-\sqrt{2}$	$\sqrt{2}$	0	2	-2	1	-1	0	$-\sqrt{2}$	$\sqrt{2}$	0	$\Gamma_6^+ \times \Gamma_2^+$
		$\Gamma_8^+$	4	-4	-1	1	0	0	0	0	4	-4	-1	1	0	0	0	0	$\phi\left(\frac{3}{2}, -\frac{3}{2}\right), \phi\left(\frac{3}{2}, -\frac{1}{2}\right)$ $\phi\left(\frac{3}{2}, \frac{1}{2}\right), \phi\left(\frac{3}{2}, \frac{3}{2}\right)$
		$\Gamma_6^-$	2	-2	1	-1	0	$\sqrt{2}$	$-\sqrt{2}$	0	-2	2	-1	1	0	$-\sqrt{2}$	$\sqrt{2}$	0	$\Gamma_6^+ \times \Gamma_1^-$
		$\Gamma_7^-$	2	-2	1	-1	0	$-\sqrt{2}$	$\sqrt{2}$	0	-2	2	-1	1	0	$\sqrt{2}$	$-\sqrt{2}$	0	$\Gamma_6^+ \times \Gamma_2^-$
		$\Gamma_8^-$	4	-4	-1	1	0	0	0	0	-4	4	1	-1	0	0	0	0	$\Gamma_8^+ \times \Gamma_1^-$

**Table B.2.:** Character Table of the double group of  $O_h$ . Copied from Refs. [50, 62]. The three notations refer to one often used in molecular physics (M), the Bouckaert-Smoluchowski-Wigner (BSW) notation [51] and the Koster notation (K) [50].  $R$  denotes a scalar,  $S_{x_i}$  refers to angular momentum operators and  $\phi(S, m_s)$  to the half-integer spin states.

### B.3. Multiplication table of $O_h$

$\Gamma_1$	$\Gamma_2$	$\Gamma_3$	$\Gamma_4$	$\Gamma_5$	$\Gamma_6$	$\Gamma_7$	$\Gamma_8$	
$\Gamma_1$	$\Gamma_2$	$\Gamma_3$	$\Gamma_4$	$\Gamma_5$	$\Gamma_6$	$\Gamma_7$	$\Gamma_8$	$\Gamma_1$
	$\Gamma_1$	$\Gamma_3$	$\Gamma_5$	$\Gamma_4$	$\Gamma_7$	$\Gamma_6$	$\Gamma_8$	$\Gamma_2$
		$\Gamma_1 \oplus \Gamma_2 \oplus \Gamma_3$	$\Gamma_4 \oplus \Gamma_5$	$\Gamma_4 \oplus \Gamma_5$	$\Gamma_8$	$\Gamma_8$	$\Gamma_6 \oplus \Gamma_7 \oplus \Gamma_8$	$\Gamma_3$
			$\Gamma_1 \oplus \Gamma_3 \oplus \Gamma_4 \oplus \Gamma_5$	$\Gamma_2 \oplus \Gamma_3 \oplus \Gamma_4 \oplus \Gamma_5$	$\Gamma_6 \oplus \Gamma_8$	$\Gamma_7 \oplus \Gamma_8$	$\Gamma_6 \oplus \Gamma_7 \oplus 2\Gamma_8$	$\Gamma_4$
				$\Gamma_1 \oplus \Gamma_3 \oplus \Gamma_4 \oplus \Gamma_5$	$\Gamma_7 \oplus \Gamma_8$	$\Gamma_6 \oplus \Gamma_8$	$\Gamma_6 \oplus \Gamma_7 \oplus 2\Gamma_8$	$\Gamma_5$
					$\Gamma_1 \oplus \Gamma_4$	$\Gamma_2 \oplus \Gamma_5$	$\Gamma_3 \oplus \Gamma_4 \oplus \Gamma_5$	$\Gamma_6$
						$\Gamma_1 \oplus \Gamma_4$	$\Gamma_3 \oplus \Gamma_4 \oplus \Gamma_5$	$\Gamma_7$
							$\Gamma_1 \oplus \Gamma_2 \oplus \Gamma_3 \oplus 2\Gamma_4 \oplus 2\Gamma_5$	$\Gamma_8$

**Table B.3.:** Multiplication table of the double group of  $O_h$  copied from Ref. [50]. For the sake of brevity (and avoiding triviality), parity as well as the lower left half have been omitted.

## B.4. Compatibility and lattice harmonics

In this Section, the compatibility tables for  $O(3) \mapsto O_h$ ,  $O(3) \mapsto C_{2h}$  and  $O(3) \mapsto D_{2h}$  will be given as well as the corresponding symmetrised bases.

### B.4.1. Compatibility of $O_h$ with respect to $O(3)$

As  $O_h$  is a subgroup of the continuous rotation group  $O(3)$ , linear combinations of its basis functions, the spherical harmonics  $Y_\ell^m(\mathbf{n})$ , can be constructed which transform according to the rows of the irreducible representations of  $O_h$  [55, 48, 152]. As the derivation hinges solely on the transformational properties, the corresponding symmetrisation is applicable to the spherical tensor operators [153] just as well as it is applicable to the spherical harmonics. We will therefore use the generic basis  $P_\ell^m$  which may be either a function or an operator transforming according to the row  $m$  of the irreducible representation  $\Gamma_\ell$  of  $O(3)$ . Parity will not be given explicitly as its inclusion is trivial.

The compatibility table B.4 lists the irreducible representations of  $O_h$  into which the irreducible representations of  $O(3)$  split under the corresponding reduction of symmetry. In Tabs. B.5 to B.9,

single group		double group	
$O(3)$	$O_h$	$O(3)$	$O_h$
$\Gamma_0$	$\Gamma_1$	$\Gamma_{1/2}$	$\Gamma_6$
$\Gamma_1$	$\Gamma_4$	$\Gamma_{3/2}$	$\Gamma_8$
$\Gamma_2$	$\Gamma_3 \oplus \Gamma_5$	$\Gamma_{5/2}$	$\Gamma_7 \oplus \Gamma_8$
$\Gamma_3$	$\Gamma_2 \oplus \Gamma_4 \oplus \Gamma_5$	$\Gamma_{7/2}$	$\Gamma_6 \oplus \Gamma_7 \oplus \Gamma_8$
$\Gamma_4$	$\Gamma_1 \oplus \Gamma_3 \oplus \Gamma_4 \oplus \Gamma_5$	$\Gamma_{9/2}$	$\Gamma_6 \oplus 2\Gamma_8$
$\Gamma_5$	$\Gamma_3 \oplus 2\Gamma_4 \oplus \Gamma_5$	$\Gamma_{11/2}$	$\Gamma_6 \oplus \Gamma_7 \oplus 2\Gamma_8$
$\Gamma_6$	$\Gamma_1 \oplus \Gamma_2 \oplus \Gamma_3 \oplus \Gamma_4 \oplus 2\Gamma_5$	$\Gamma_{13/2}$	$\Gamma_6 \oplus 2\Gamma_7 \oplus 2\Gamma_8$
$\Gamma_7$	$\Gamma_2 \oplus \Gamma_3 \oplus 2\Gamma_4 \oplus 2\Gamma_5$	$\Gamma_{15/2}$	$\Gamma_6 \oplus \Gamma_7 \oplus 3\Gamma_8$
$\Gamma_8$	$\Gamma_1 \oplus 2\Gamma_3 \oplus 2\Gamma_4 \oplus 2\Gamma_5$	$\Gamma_{17/2}$	$2\Gamma_6 \oplus \Gamma_7 \oplus 3\Gamma_8$
$\Gamma_9$	$\Gamma_1 \oplus \Gamma_2 \oplus \Gamma_3 \oplus 3\Gamma_4 \oplus 2\Gamma_5$	$\Gamma_{19/2}$	$2\Gamma_6 \oplus 2\Gamma_7 \oplus 3\Gamma_8$
$\Gamma_{10}$	$\Gamma_1 \oplus \Gamma_2 \oplus 2\Gamma_3 \oplus 2\Gamma_4 \oplus 3\Gamma_5$	$\Gamma_{21/2}$	$\Gamma_6 \oplus 2\Gamma_7 \oplus 4\Gamma_8$
$\Gamma_{11}$	$\Gamma_2 \oplus 2\Gamma_3 \oplus 3\Gamma_4 \oplus 3\Gamma_5$	$\Gamma_{23/2}$	$2\Gamma_6 \oplus 2\Gamma_7 \oplus 4\Gamma_8$
$\Gamma_{12}$	$2\Gamma_1 \oplus \Gamma_2 \oplus 2\Gamma_3 \oplus 3\Gamma_4 \oplus 3\Gamma_5$	$\Gamma_{25/2}$	$3\Gamma_6 \oplus 2\Gamma_7 \oplus 4\Gamma_8$

**Table B.4.:** Compatibility table of  $O_h$  with respect to  $O(3)$  [50]. Parity has been omitted in order to keep the notation concise but it can trivially be included as it is a good quantum number for both  $O(3)$  and  $O_h$ . The irreducible representations of the single and double group of  $O(3)$  are labelled by the angular momentum quantum number  $\ell$  as  $\Gamma_\ell$ .

the symmetrised bases up to  $\ell = 6$  are listed (those transforming like  $\Gamma_1(O_h)$  up to  $\ell = 10$ ). The index  $\alpha$  indicates that multiple bases of order  $\ell$  may exist which transform according to the same irreducible representation. For example, there are two bases of order  $\ell = 5$  transforming like  $\Gamma_4$  (see Tab. B.4). The coefficients for even more cubic harmonics can be found in Refs. [56, 152].

$\Gamma_\ell(O(3))$	$\Gamma_1(O_h)$
$\ell_\alpha = 0$	$P_0^0$
$\ell_\alpha = 4$	$\sqrt{\frac{5}{24}} (P_4^4 + P_4^{-4}) + \sqrt{\frac{7}{12}} P_4^0$
$\ell_\alpha = 6$	$\sqrt{\frac{7}{16}} (P_6^4 + P_6^{-4}) - \sqrt{\frac{1}{8}} P_6^0$
$\ell_\alpha = 8$	$\sqrt{\frac{65}{384}} (P_8^8 + P_8^{-8}) + \sqrt{\frac{7}{96}} (P_8^4 + P_8^{-4}) + \sqrt{\frac{33}{64}} P_8^0$
$\ell_\alpha = 9$	$i\sqrt{\frac{21}{144}} (P_9^8 - P_9^{-8}) - i\sqrt{\frac{51}{144}} (P_9^4 - P_9^{-4})$
$\ell_\alpha = 10$	$\sqrt{\frac{187}{768}} (P_{10}^8 + P_{10}^{-8}) + \sqrt{\frac{11}{64}} (P_{10}^4 + P_{10}^{-4}) - \sqrt{\frac{65}{384}} P_{10}^0$

**Table B.5.:** Cubic bases transforming like  $\Gamma_1(O_h)$  up to  $\ell = 10$ .

$\Gamma_\ell(O(3))$	$\Gamma_2(O_h)$
$\ell_\alpha = 3$	$-\frac{i}{\sqrt{2}} (P_2^2 - P_3^{-2})$
$\ell_\alpha = 6$	$-\sqrt{\frac{5}{32}} (P_6^6 + P_6^{-6}) + \sqrt{\frac{11}{32}} (P_6^2 + P_6^{-2})$

**Table B.6.:** Cubic bases transforming like  $\Gamma_2(O_h)$  up to  $\ell = 6$ .

Further cubic harmonics can be generated from the known ones, the coefficients do however tend to become very convoluted for large  $\ell$  such that generally only numerical values are given [56, 152]. We will give an example how to generate the cubic harmonics transforming like  $\Gamma_1(O_h)$  for  $\ell = 12$  that is readily extensible to other irreducible representations and higher orders. First, we acknowledge that according to Tab. B.4, there are two linearly independent components. Subsequently, we use the fact both  $P_6^{\Gamma_1} P_6^{\Gamma_1}$  and  $P_6^{\Gamma_1} P_8^{\Gamma_1}$  have to transform like  $\Gamma_1 \otimes \Gamma_1 = \Gamma_1$ . Here,  $P_6^{\Gamma_1}$  and  $P_8^{\Gamma_1}$  label the terms of order  $\ell_\alpha = 6$  and  $\ell_\alpha = 8$  in Tab. B.5. The terms can be written as

$\Gamma_\ell(\mathbf{O}(3))$	$\Gamma_3(\mathbf{O}_h)$
$\ell_\alpha = 2$	$P_2^0$
$u_1^3$	$\sqrt{\frac{1}{2}} (P_2^2 + P_2^{-2})$
$u_2^3$	
$\ell_\alpha = 4$	$\sqrt{\frac{7}{24}} (P_4^{-4} + P_4^4) - \sqrt{\frac{5}{12}} P_4^0$
$u_1^3$	$\sqrt{\frac{1}{2}} (P_4^{-2} + P_4^2)$
$u_2^3$	
$\ell_\alpha = 5$	$\sqrt{\frac{1}{2}} (P_5^{-4} - P_5^4)$
$u_1^3$	$\sqrt{\frac{1}{2}} (P_5^2 - P_5^{-2})$
$u_2^3$	
$\ell_\alpha = 6$	$\frac{1}{4} (P_6^4 + P_6^{-4}) + \sqrt{\frac{7}{8}} P_6^0$
$u_1^3$	$\sqrt{\frac{11}{32}} (P_6^6 + P_6^{-6}) + \sqrt{\frac{5}{32}} (P_6^2 + P_6^{-2})$
$u_2^3$	

**Table B.7.:** Cubic bases transforming like  $\Gamma_3(\mathbf{O}_h)$  up to  $\ell = 6$ . The labelling of the rows agrees with the one used in Ref. [50] and Tab. B.2, i.e. for  $\Gamma_3^+$  the rows transform like  $u_1^3 \hat{=} (2z^2 - x^2 - y^2)$  and  $u_2^3 \hat{=} \sqrt{3}(x^2 - y^2)$ .

[153]

$$\begin{aligned}
 P_6^{\Gamma_1} P_6^{\Gamma_1} &= \sum_{m=-6}^6 \sum_{m'=-6}^6 C_6^m C_6^{m'} P_6^m P_6^{m'} \\
 &= \sum_{L=0}^{12} \sum_{m=-6}^6 \sum_{m'=-6}^6 C_6^m C_6^{m'} \langle 6, m; 6, m' | L, m+m' \rangle P_L^{m+m'},
 \end{aligned} \tag{B.8}$$

$$\begin{aligned}
 P_6^{\Gamma_1} P_8^{\Gamma_1} &= \sum_{m=-6}^6 \sum_{m'=-8}^8 C_6^m C_8^{m'} P_6^m P_8^{m'} \\
 &= \sum_{L=2}^{14} \sum_{m=-6}^6 \sum_{m'=-8}^8 C_6^m C_8^{m'} \langle 6, m; 8, m' | L, m+m' \rangle P_L^{m+m'},
 \end{aligned} \tag{B.9}$$

where the  $\langle \ell, m; \ell', m' | L, m+m' \rangle$  denote the Clebsch-Gordan coefficients and  $C_\ell^m$  the coefficients given in Tab. B.5. The components for different  $L$  transform independently of one another under both  $\mathbf{O}_h$  and  $\mathbf{O}(3)$ . Accordingly, the summand for each  $L$  has to transform according to  $\Gamma_1$  and, as we are only interested in  $L = 12$ , we can restrict our analysis to this component, yielding

$$\begin{aligned}
 P_{12a}^{\Gamma_1} &= \sum_{m=-6}^6 \sum_{m'=-6}^6 C_6^m C_6^{m'} \langle 6, m; 6, m' | 12, m+m' \rangle P_{12}^{m+m'} \\
 &= \sqrt{\frac{231}{2944}} (P_{12}^{-8} + P_{12}^8) - \sqrt{\frac{154}{29716}} (P_{12}^{-4} + P_{12}^4) + \sqrt{\frac{68607}{6180928}} P_{12}^0,
 \end{aligned} \tag{B.10}$$



$\Gamma_\ell(\mathbf{O}(3))$	$\Gamma_4(\mathbf{O}_h)$
$\ell_\alpha = 1$	$u_x^4$ $-\sqrt{\frac{1}{2}} (P_1^1 - P_1^{-1})$ $u_y^4$ $i\sqrt{\frac{1}{2}} (P_1^1 + P_1^{-1})$ $u_z^4$ $P_1^0$
$\ell_\alpha = 3$	$u_x^4$ $-\sqrt{\frac{5}{16}} (P_3^3 - P_3^{-3}) + \sqrt{\frac{3}{16}} (P_3^1 - P_3^{-1})$ $u_y^4$ $-i\sqrt{\frac{5}{16}} (P_3^3 + P_3^{-3}) - i\sqrt{\frac{3}{16}} (P_3^{-1} + P_3^1)$ $u_z^4$ $P_3^0$
$\ell_\alpha = 4$	$u_x^4$ $i\sqrt{\frac{1}{16}} (P_4^3 + P_4^{-3}) + i\sqrt{\frac{7}{16}} (P_4^{-1} + P_4^1)$ $u_y^4$ $\sqrt{\frac{1}{16}} (P_4^3 - P_4^{-3}) + \sqrt{\frac{7}{16}} (P_4^{-1} - P_4^1)$ $u_z^4$ $i\sqrt{\frac{1}{2}} (P_4^4 - P_4^{-4})$
$\ell_\alpha = 5_1$	$u_x^4$ $-\sqrt{\frac{5}{256}} (P_5^5 - P_5^{-5}) - \sqrt{\frac{81}{256}} (P_5^3 - P_5^{-3}) - \sqrt{\frac{42}{256}} (P_5^1 - P_5^{-1})$ $u_y^4$ $-i\sqrt{\frac{5}{256}} (P_5^5 + P_5^{-5}) + i\sqrt{\frac{81}{256}} (P_5^3 + P_5^{-3}) - i\sqrt{\frac{42}{256}} (P_5^1 + P_5^{-1})$ $u_z^4$ $\sqrt{\frac{1}{2}} (P_5^4 + P_5^{-4})$
$\ell_\alpha = 5_2$	$u_x^4$ $-\sqrt{\frac{63}{256}} (P_5^5 - P_5^{-5}) + \sqrt{\frac{35}{256}} (P_5^3 - P_5^{-3}) - \sqrt{\frac{30}{256}} (P_5^1 - P_5^{-1})$ $u_y^4$ $-i\sqrt{\frac{63}{256}} (P_5^5 + P_5^{-5}) - i\sqrt{\frac{35}{256}} (P_5^3 + P_5^{-3}) - i\sqrt{\frac{30}{256}} (P_5^1 + P_5^{-1})$ $u_z^4$ $P_5^0$
$\ell_\alpha = 6$	$u_x^4$ $i\sqrt{\frac{11}{64}} (P_6^5 + P_6^{-5}) + i\sqrt{\frac{15}{64}} (P_6^3 + P_6^{-3}) - i\sqrt{\frac{6}{64}} (P_6^1 + P_6^{-1})$ $u_y^4$ $\sqrt{\frac{11}{64}} (P_6^{-5} - P_6^5) + \sqrt{\frac{15}{64}} (P_6^3 - P_6^{-3}) + \sqrt{\frac{6}{64}} (P_6^1 - P_6^{-1})$ $u_z^4$ $i\sqrt{\frac{1}{2}} (P_6^4 - P_6^{-4})$

**Table B.8.:** Cubic bases transforming like  $\Gamma_4(\mathbf{O}_h)$  up to  $\ell = 6$ . The labelling of the rows agrees with the one used in Ref. [50].

$\Gamma_\ell(\mathbf{O}(3))$	$\Gamma_5(\mathbf{O}_h)$
$\ell_\alpha = 2$	$u_{yz}^5$ $\sqrt{\frac{1}{2}} (P_2^{-1} + P_2^1)$ $u_{zx}^5$ $i\sqrt{\frac{1}{2}} (P_2^{-1} - P_2^1)$ $u_{xy}^5$ $\sqrt{\frac{1}{2}} (P_2^{-2} - P_2^2)$
$\ell_\alpha = 3$	$u_{yz}^5$ $\sqrt{\frac{3}{16}} (P_3^3 - P_3^{-3}) + \sqrt{\frac{5}{16}} (P_3^1 - P_3^{-1})$ $u_{zx}^5$ $-i\sqrt{\frac{3}{16}} (P_3^3 + P_3^{-3}) + i\sqrt{\frac{5}{16}} (P_3^1 + P_3^{-1})$ $u_{xy}^5$ $\sqrt{\frac{1}{2}} (P_3^2 + P_3^{-2})$
$\ell_\alpha = 4$	$u_{yz}^5$ $-\sqrt{\frac{7}{16}} (P_4^3 + P_4^{-3}) + \sqrt{\frac{1}{16}} (P_4^{-1} + P_4^1)$ $u_{zx}^5$ $-i\sqrt{\frac{7}{16}} (P_4^3 - P_4^{-3}) - i\sqrt{\frac{1}{16}} (P_4^1 - P_4^{-1})$ $u_{xy}^5$ $\sqrt{\frac{1}{2}} (P_4^2 - P_4^{-2})$
$\ell_\alpha = 5$	$u_{yz}^5$ $i\sqrt{\frac{15}{64}} (P_5^5 - P_5^{-5}) + i\sqrt{\frac{3}{64}} (P_5^3 - P_5^{-3}) + i\sqrt{\frac{14}{64}} (P_5^{-1} - P_5^1)$ $u_{zx}^5$ $\sqrt{\frac{15}{64}} (P_5^5 + P_5^{-5}) - \sqrt{\frac{3}{64}} (P_5^3 + P_5^{-3}) - \sqrt{\frac{14}{64}} (P_5^1 + P_5^{-1})$ $u_{xy}^5$ $i\sqrt{\frac{1}{2}} (P_5^2 + P_5^{-2})$
$\ell_\alpha = 6_1$	$u_{yz}^5$ $-\sqrt{\frac{165}{512}} (P_6^5 + P_6^{-5}) + \sqrt{\frac{81}{512}} (P_6^3 + P_6^{-3}) - \sqrt{\frac{5}{256}} (P_6^1 + P_6^{-1})$ $u_{zx}^5$ $i\sqrt{\frac{165}{512}} (P_6^5 - P_6^{-5}) + i\sqrt{\frac{81}{512}} (P_6^3 - P_6^{-3}) + i\sqrt{\frac{5}{256}} (P_6^1 - P_6^{-1})$ $u_{xy}^5$ $\sqrt{\frac{1}{2}} (P_6^2 - P_6^{-2})$
$\ell_\alpha = 6_2$	$u_{yz}^5$ $-\sqrt{\frac{3}{512}} (P_6^5 + P_6^{-5}) - \sqrt{\frac{55}{512}} (P_6^3 + P_6^{-3}) - \sqrt{\frac{99}{256}} (P_6^1 + P_6^{-1})$ $u_{zx}^5$ $i\sqrt{\frac{3}{512}} (P_6^5 - P_6^{-5}) - i\sqrt{\frac{55}{512}} (P_6^3 - P_6^{-3}) + i\sqrt{\frac{99}{256}} (P_6^1 - P_6^{-1})$ $u_{xy}^5$ $\sqrt{\frac{1}{2}} (P_6^6 - P_6^{-6})$

**Table B.9.:** Cubic bases transforming like  $\Gamma_5(\mathbf{O}_h)$  up to  $\ell = 6$ . The labelling of the rows agrees with the one used in Ref. [50].

$$\begin{aligned}
P_{12_b}^{\Gamma_1} &= \sum_{m=-6}^6 \sum_{m'=-8}^8 C_6^m C_8^{m'} \langle 6, m; 8, m' | 12, m+m' \rangle P_{12}^{m+m'} \\
&= \sqrt{\frac{175}{6912}} (P_{12}^{-12} + P_{12}^{12}) - \sqrt{\frac{2809}{291456}} (P_{12}^{-8} + P_{12}^8) \\
&\quad + \sqrt{\frac{2218783}{62760192}} (P_{12}^{-4} + P_{12}^4) + \sqrt{\frac{578773}{12837312}} P_{12}^0.
\end{aligned} \tag{B.11}$$

These two are indeed linearly independent and the only thing left is to orthonormalise the two components to ones liking. Requiring that for one of the bases the term  $\propto P_{12}^0$  vanishes, we arrive at the symmetrised bases

$$P_{12_1}^{\Gamma_1} = \sqrt{\frac{891}{47552}} (P_{12}^{12} + P_{12}^{-12}) - \sqrt{\frac{483}{1486}} (P_{12}^8 + P_{12}^{-8}) + \sqrt{\frac{7429}{47552}} (P_{12}^4 + P_{12}^{-4}), \tag{B.12}$$

$$\begin{aligned}
P_{12_2}^{\Gamma_1} &= \sqrt{\frac{676039}{4564992}} (P_{12}^{12} + P_{12}^{-12}) + \sqrt{\frac{46189}{760832}} (P_{12}^8 + P_{12}^{-8}) \\
&\quad + \sqrt{\frac{75075}{1521664}} (P_{12}^4 + P_{12}^{-4}) + \sqrt{\frac{743}{1536}} P_{12}^0,
\end{aligned} \tag{B.13}$$

which agree with those given in Ref. [152].

The cubic harmonics transforming like  $\Gamma_1^+$  are shown in Fig. B.1. They can be retrieved from Tab. B.5 and Eqs. (B.12, B.13) by replacing the  $P_\ell^m$  with the corresponding spherical harmonics  $Y_\ell^m(\mathbf{n})$ . Of course, only the cubic harmonics with even  $\ell$  transform like  $\Gamma_1^+$  while those with odd  $\ell$  transform like  $\Gamma_1^-$ .

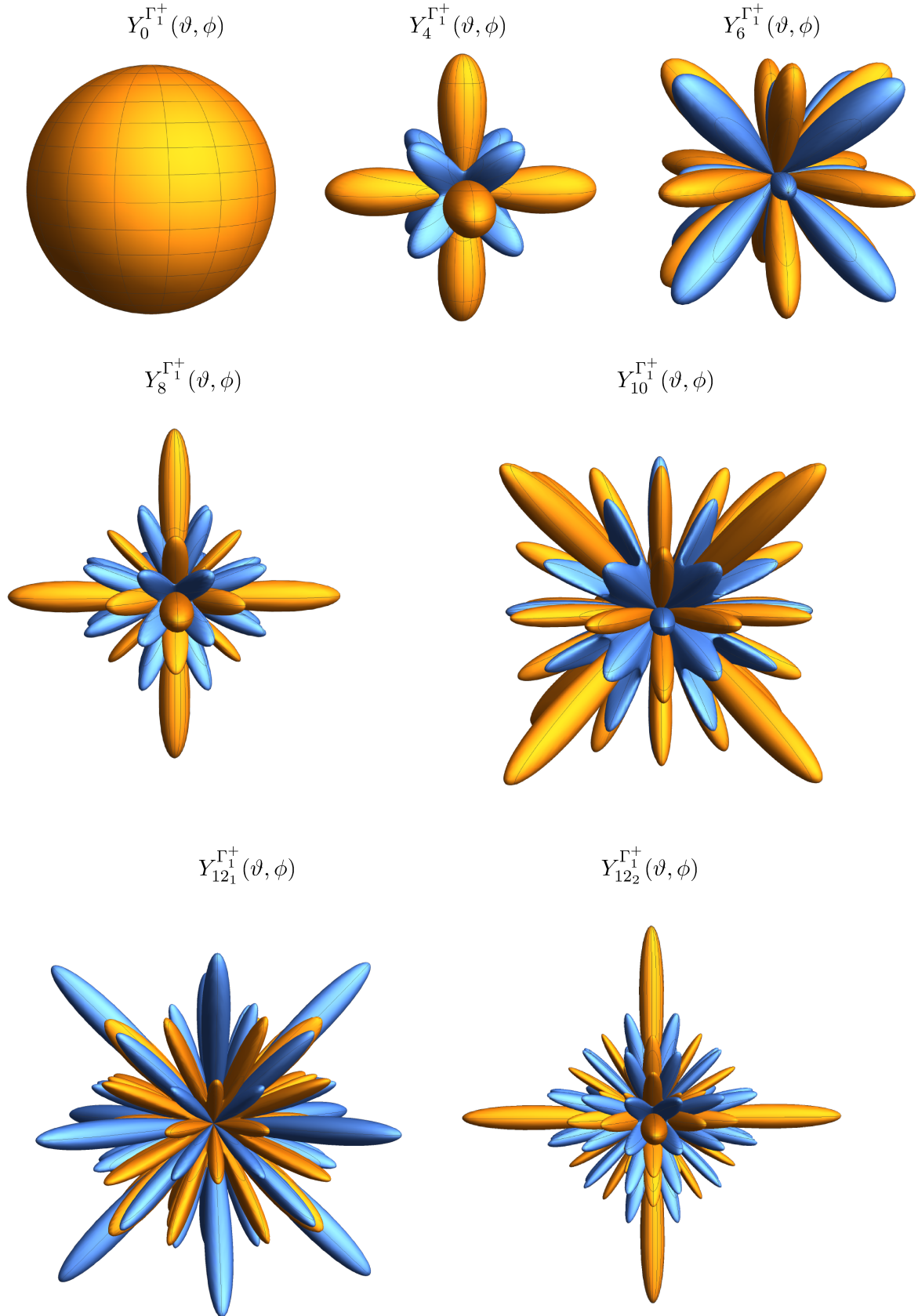


**Figure B.1.:** First seven cubic harmonics  $Y_{\ell_\alpha}^{\Gamma_1^+}(\vartheta, \phi)$  transforming like  $\Gamma_1^+$  (i. e. exhibiting full cubic symmetry), viewed from one of the main Cartesian axes. The colour indicates the phase (orange: positive, blue: negative).

### B.4.2. Compatibility of $D_{2h}$ with respect to $O(3)$

The point group  $D_{2h}$  is the symmetry group of a 3D ellipsoid and a subgroup of  $O_h$ . It contains three twofold rotation  $\{C_2, C'_2, C''_2\}$  around perpendicular axes (say,  $x$ ,  $y$  and  $z$ ) and an inversion, resulting in eight total symmetry operations  $\{E, C_2, C'_2, C''_2, I, \sigma_v, \sigma'_v, \sigma''_v\}$  [50]. Each of these operations makes up its own conjugacy class, giving eight irreducible representations of the single group labelled  $\Gamma_n^\pm$  with  $n \in \{1, 2, 3, 4\}$  which are all one-dimensional. Additionally, there are two irreducible representations  $\Gamma_5^\pm$  of the double group. The compatibility of  $D_{2h}$  with respect to  $O(3)$  is given in Tab. B.10.

$O(3)$	$D_{2h}$
$\Gamma_0$	$\Gamma_1$
$\Gamma_1$	$\Gamma_2 \oplus \Gamma_3 \oplus \Gamma_4$
$\Gamma_2$	$2\Gamma_1 \oplus \Gamma_2 \oplus \Gamma_3 \oplus \Gamma_4$
$\Gamma_3$	$\Gamma_1 \oplus 2\Gamma_2 \oplus 2\Gamma_3 \oplus 2\Gamma_4$
$\Gamma_4$	$3\Gamma_1 \oplus 2\Gamma_2 \oplus 2\Gamma_3 \oplus 2\Gamma_4$
$\Gamma_5$	$2\Gamma_1 \oplus 3\Gamma_2 \oplus 3\Gamma_3 \oplus 3\Gamma_4$
$\Gamma_6$	$4\Gamma_1 \oplus 3\Gamma_2 \oplus 3\Gamma_3 \oplus 3\Gamma_4$

**Table B.10.:** Compatibility table of  $D_{2h}$  with respect to  $O(3)$  [50]. The notation is equivalent to Tab. B.4. As  $D_{2h}$  possesses only one double-group representation  $\Gamma_5$  (ignoring parity), the double group representations are given by  $\Gamma_j(O(3)) \mapsto (j + \frac{1}{2}) \Gamma_5(D_{2h})$ , where  $j$  denotes some half-integer spin.

For even  $\ell$ , the lattice harmonics of  $D_{2h}$  are given by (with the obvious limits on  $\alpha$ )

$$P_{\ell_0}^{\Gamma_1} = P_\ell^0, \quad (B.14)$$

$$P_{\ell_\alpha}^{\Gamma_1} = \sqrt{\frac{1}{2}} \left( P_\ell^{2\alpha} + P_\ell^{-2\alpha} \right), \quad (B.15)$$

$$P_{\ell_\alpha}^{\Gamma_2} = \sqrt{\frac{1}{2}} \left( P_\ell^{2\alpha+1} - P_\ell^{-(2\alpha+1)} \right), \quad (B.16)$$

$$P_{\ell_\alpha}^{\Gamma_3} = i\sqrt{\frac{1}{2}} \left( P_\ell^{2\alpha} - P_\ell^{-2\alpha} \right), \quad (B.17)$$

$$P_{\ell_\alpha}^{\Gamma_4} = i\sqrt{\frac{1}{2}} \left( P_\ell^{2\alpha+1} + P_\ell^{-(2\alpha+1)} \right) \quad (B.18)$$

Correspondingly, those for odd  $\ell$  are given by

$$P_{\ell\alpha}^{\Gamma_1} = i\sqrt{\frac{1}{2}} \left( P_{\ell}^{2\alpha} - P_{\ell}^{-2\alpha} \right), \quad (\text{B.19})$$

$$P_{\ell\alpha}^{\Gamma_2} = i\sqrt{\frac{1}{2}} \left( P_{\ell}^{2\alpha+1} + P_{\ell}^{-(2\alpha+1)} \right), \quad (\text{B.20})$$

$$P_{\ell_0}^{\Gamma_3} = P_{\ell}^0, \quad (\text{B.21})$$

$$P_{\ell\alpha}^{\Gamma_3} = \sqrt{\frac{1}{2}} \left( P_{\ell}^{2\alpha} + P_{\ell}^{-2\alpha} \right), \quad (\text{B.22})$$

$$P_{\ell\alpha}^{\Gamma_4} = \sqrt{\frac{1}{2}} \left( P_{\ell}^{2\alpha+1} - P_{\ell}^{-(2\alpha+1)} \right). \quad (\text{B.23})$$

#### B.4.3. Compatibility of $C_{2h}$ with respect to $O(3)$

The point group  $C_{2h}$  is a subgroup of both  $O_h$  and  $D_{2h}$  which contains one two-fold rotation axis (assumed to be the  $z$ -axis) as well as the inversion resulting in four symmetry elements  $\{E, C_2, I, \sigma_h\}$ . The four corresponding single-group representations are all one-dimensional and usually labelled by  $\Gamma_{1/2}^{\pm}$ . In addition, four double group representations  $\Gamma_{3/4}^{\pm}$  exist, which are also one-dimensional. The compatibility of  $C_{2h}$  with respect to  $O(3)$  is given in Tab. B.11.

$O(3)$	$C_{2h}$
$\Gamma_0$	$\Gamma_1$
$\Gamma_1$	$\Gamma_1 \oplus 2\Gamma_2$
$\Gamma_2$	$3\Gamma_1 \oplus 2\Gamma_2$
$\Gamma_3$	$3\Gamma_1 \oplus 4\Gamma_2$
$\Gamma_4$	$5\Gamma_1 \oplus 4\Gamma_2$
$\Gamma_5$	$5\Gamma_1 \oplus 6\Gamma_2$
$\Gamma_6$	$7\Gamma_1 \oplus 6\Gamma_2$

**Table B.11.:** Compatibility table of  $C_{2h}$  with respect to  $O(3)$  [50]. The notation is equivalent to Tab. B.4. The double group representations are given by  $\Gamma_j(O(3)) \mapsto (j + \frac{1}{2}) (\Gamma_3(C_{2h}) \oplus \Gamma_4(C_{2h}))$ , where  $j$  denotes some half-integer spin.

The symmetrised bases for both odd and even  $\ell$  are given by (with the obvious limits on  $\alpha$ )

$$P_{\ell\alpha\pm}^{\Gamma_1} = P_{\ell}^{\pm 2\alpha}, \quad (\text{B.24})$$

$$P_{\ell_0}^{\Gamma_1} = P_{\ell}^0, \quad (\text{B.25})$$

$$P_{\ell\alpha\pm}^{\Gamma_2} = P_{\ell}^{\pm(2\alpha+1)}. \quad (\text{B.26})$$

## B.5. The continuous rotation group $O(3)$

$O(3)$  is the group of all orthogonal  $3 \times 3$  matrices and isomorphic to the group of all proper and improper rotations in  $\mathbb{R}^3$ . In fact, when applied to a vector in  $\mathbb{R}^3$ , all these rotations can be expressed as orthogonal matrices and one may claim that  $O(3)$  is the group of all rotations in  $3D$  space. It contains as a subgroup the special orthogonal group  $SO(3)$  which consists of all orthogonal  $3 \times 3$  matrices with determinant one and is the group of all proper rotations in  $3D$  space. In both classical and quantum mechanics, the invariance with respect to  $SO(3)$  is linked to the conservation of angular momentum by Noether's theorem [154].

Correspondingly, the irreducible representations  $\Gamma_{\ell}^{\pm}$  of  $O(3)$  can be labelled by parity and an orbital quantum number  $\ell \in \mathbb{N}_0$ . They are  $(2\ell + 1)$ -dimensional, respectively, with the rows often labelled by the magnetic quantum number  $m \in \{-\ell, \dots, 0, \dots, \ell\}$ . For the irreducible representations with parity  $(-1)^{\ell}$ , the basis functions can be chosen as the spherical harmonics  $Y_{\ell}^m(\mathbf{n})$ . For the other half with parity  $(-1)^{\ell+1}$ , basis operators can be chosen. Axial vector operators, such as the angular momentum operators  $\mathbf{L} = \mathbf{r} \times \mathbf{p}$ , for example, transform like  $\Gamma_1^+$ . The multiplication table of the irreducible representations (ignoring parity) is given by

$$\Gamma_{\ell} \otimes \Gamma_{\ell'} = \sum_{L=|\ell-\ell'|}^{\ell+\ell'} \Gamma_L. \quad (\text{B.27})$$

As each irreducible representation appears at most once, the Wigner-Eckart theorem for  $O(3)$  takes the well-known form

$$\langle R, \ell, m, p | T_L^{M,P} | R', \ell', m', p' \rangle = \left( R, \ell, p \parallel T_L^P \parallel R', \ell', p' \right) \langle \ell', m', p'; L, M, P | \ell, m, p \rangle, \quad (\text{B.28})$$

where  $p, p'$  and  $P$  denote the parity and

$$\langle \ell', m', p'; L, M, P | \ell, m, p \rangle = \delta_{pp'} \delta_{P,1} \langle \ell', m'; L, M | \ell, m \rangle, \quad (\text{B.29})$$

the coupling coefficients of  $O(3)$ , which are proportional to the Clebsch-Gordan coefficients  $\langle \ell', m'; L, M | \ell, m \rangle$ . Furthermore,  $T_L^{M,P}$  is a spherical tensor operator<sup>3</sup> and  $(R, \ell, p \| T_L^P \| R', \ell', p')$  the reduced matrix element which is independent of  $m, M$  and  $m'$ .

### B.5.1. Spherical harmonics

The spherical harmonics are defined as

$$Y_\ell^m(\mathbf{n}) = Y_\ell^m(\vartheta, \phi) = \sqrt{\frac{2\ell+1}{4\pi} \frac{(\ell-m)!}{(\ell+m)!}} P_\ell^m(\cos(\vartheta)) e^{im\phi}, \quad (\text{B.30})$$

where  $P_\ell^m(x)$  denotes the associated Legendre polynomials. The name “spherical harmonics” is motivated by the fact that  $r^\ell Y_\ell^m(\mathbf{n}) = H_\ell^m(\mathbf{r})$  are homogeneous, harmonic polynomials  $\nabla^2 H_\ell^m(\mathbf{r}) = 0$  [92]. In other words, the spherical harmonics can be understood as homogeneous, harmonic polynomials restricted to the unit sphere  $\mathbb{S}^2$ . The spherical harmonics are orthonormal

$$\oint d^2\mathbf{n} Y_\ell^{m\dagger}(\mathbf{n}) Y_{\ell'}^{m'}(\mathbf{n}) = \delta_{\ell, \ell'} \delta_{m, m'} \quad (\text{B.31})$$

and form a complete basis of  $L^2(\mathbb{S}^2)$  [92]. Under inversion and complex conjugation, the spherical harmonics follow the respective relations

$$Y_\ell^m(-\mathbf{n}) = (-1)^\ell Y_\ell^m(\mathbf{n}), \quad (\text{B.32})$$

$$Y_\ell^{m\dagger}(\mathbf{n}) = (-1)^m Y_\ell^{-m}(\mathbf{n}). \quad (\text{B.33})$$

Integrals over three spherical harmonics are called **Gaunt coefficients**

$$\begin{aligned} G(\ell, m; \ell', m'; \ell'', m'') &= \oint d^2\mathbf{n} Y_\ell^m(\mathbf{n}) Y_{\ell'}^{m'}(\mathbf{n}) Y_{\ell''}^{m''}(\mathbf{n}) \\ &= \sqrt{\frac{(2\ell+1)(2\ell'+1)(2\ell''+1)}{4\pi}} \begin{Bmatrix} \ell & \ell' & \ell'' \\ 0 & 0 & 0 \end{Bmatrix} \begin{Bmatrix} \ell & \ell' & \ell'' \\ m & m' & m'' \end{Bmatrix}, \end{aligned} \quad (\text{B.34})$$

where the terms in curly brackets are the **Wigner-3j** symbols [153]. The Gaunt coefficients vanish if one of the following conditions is not met:

- $|\ell - \ell'| \leq \ell'' \leq \ell + \ell'$  as well as  $|\ell' - \ell''| \leq \ell \leq \ell' + \ell''$  and  $|\ell'' - \ell| \leq \ell' \leq \ell'' + \ell$ ,
- $m + m' + m'' = 0$ ,
- $\ell + \ell' + \ell''$  is even.

<sup>3</sup>That is to say an operator that transform according to the row  $M$  of the irreducible representation  $\Gamma_L$  of  $SO(3)$  [153].



## Appendix C.

### Excitonic inter-series transitions

This Chapter contains additional information on the evaluation of the inter-series matrix-elements discussed in Sec. 5.1.

#### C.1. Yellow-green inter-band matrix elements

This appendix contains the derivation and the explicit expressions for the matrices  $M_{\sigma_h, \sigma'_h}$  and  $\tilde{N}_{\sigma_h, \sigma'_h}$  which appear in the theory of the yellow-green inter-series transitions laid out in Sec. 5.1. The symmetric matrices  $M_{\sigma_h, \sigma'_h}$  are defined by

$$\frac{m_0}{\hbar} \nabla_q \mathcal{H}_{\sigma_h, \sigma'_h}(\mathbf{q}) = \hbar \mathbf{M}_{\sigma_h, \sigma'_h} \cdot \mathbf{q}, \quad (\text{C.1})$$

and can easily be derived from the Suzuki-Hensel Hamiltonian  $\mathcal{H}(\mathbf{q})$  given in Eq. (2.45). When labelling the rows and columns of the Suzuki-Hensel Hamiltonian by the rows of  $\Gamma_7^+ \oplus \Gamma_8^+$  one could be tempted to use the eigenvalues of  $\mathbf{J}^2$  and  $J_z$ . This would, however, imply a basis  $\Gamma_4^- \otimes \Gamma_6^+ = \Gamma_6^- \oplus \Gamma_8^-$  compatible with the product of angular momentum  $\ell = 1$  and spin  $1/2$ . The actual states of  $\text{Cu}_2\text{O}$  are connected by a multiplication with the one-dimensional representation  $\Gamma_2^-$  and thereby the orthogonal transformation<sup>1</sup> [50]

$$\begin{aligned} |\Gamma_7^+, -1/2\rangle &= |\Gamma_6^-, -1/2\rangle |\Gamma_2^-\rangle, & |\Gamma_7^+, 1/2\rangle &= |\Gamma_6^-, 1/2\rangle |\Gamma_2^-\rangle, \\ |\Gamma_8^+, -3/2\rangle &= |\Gamma_8^-, 1/2\rangle |\Gamma_2^-\rangle, & |\Gamma_8^+, -1/2\rangle &= -|\Gamma_6^-, 3/2\rangle |\Gamma_2^-\rangle, \\ |\Gamma_8^+, 1/2\rangle &= -|\Gamma_8^-, -3/2\rangle |\Gamma_2^-\rangle, & |\Gamma_8^+, 3/2\rangle &= |\Gamma_6^-, -1/2\rangle |\Gamma_2^-\rangle. \end{aligned} \quad (\text{C.2})$$

---

<sup>1</sup>See also the discussion of the applicability of the Suzuki-Hensel Hamiltonian in Sec. 2.2.2.

Taking all of this into account, one arrives at

$$M_{\sigma, \sigma'} = \begin{pmatrix} \langle \Gamma_7^+, -1/2 | & \langle \Gamma_7^+, 1/2 | \\ M_{5,z} & M_{3,1} \\ M_{3,2} + M_{5,xy} & \sqrt{\frac{1}{3}} M_{5,z} \\ \sqrt{\frac{1}{3}} M_{5,z}^\dagger & -M_{3,2} + M_{5,xy} \\ -M_{3,1} & M_{5,z}^\dagger \end{pmatrix} \begin{matrix} |\Gamma_8^+, -3/2\rangle \\ |\Gamma_8^+, -1/2\rangle \\ |\Gamma_8^+, 1/2\rangle \\ |\Gamma_8^+, 3/2\rangle \end{matrix} \quad (C.3)$$

with

$$M_{5,z} = \frac{A_3 - B_3}{\sqrt{8}} \begin{pmatrix} 0 & 0 & 1 \\ 0 & 0 & i \\ 1 & i & 0 \end{pmatrix}, \quad M_{3,1} = \frac{A_2 - B_2}{\sqrt{18}} \begin{pmatrix} -1 & 0 & 0 \\ 0 & -1 & 0 \\ 0 & 0 & 2 \end{pmatrix}, \quad (C.4)$$

$$M_{3,2} = \frac{A_2 - B_2}{\sqrt{6}} \begin{pmatrix} 1 & 0 & 0 \\ 0 & -1 & 0 \\ 0 & 0 & 0 \end{pmatrix} \quad \text{and} \quad M_{5,xy} = \frac{A_3 - B_3}{\sqrt{6}} \begin{pmatrix} 0 & i & 0 \\ i & 0 & 0 \\ 0 & 0 & 0 \end{pmatrix}.$$

The matrices  $\tilde{N}_{\sigma_h, \sigma'_h}$  are defined as the antisymmetric part of the matrices  $N_{\sigma_h, \sigma'_h}$ , defined by Eq. (5.19). The application of the Wigner-Eckart theorem with a subsequent antisymmetrisation results in

$$\tilde{N}_{\sigma_h, \sigma'_h} = \begin{pmatrix} \langle \Gamma_7, -1/2 | & \langle \Gamma_7, 1/2 | \\ \sqrt{\frac{1}{3}} \tilde{N}_{4,xy} & \tilde{N}_{4,z} \\ \mathbf{0} & -\tilde{N}_{4,xy} \\ -\tilde{N}_{4,xy}^* & \mathbf{0} \\ \tilde{N}_{4,z} & \sqrt{\frac{1}{3}} \tilde{N}_{4,xy}^* \end{pmatrix} \begin{matrix} |\Gamma_8, -3/2\rangle \\ |\Gamma_8, -1/2\rangle \\ |\Gamma_8, 1/2\rangle \\ |\Gamma_8, 3/2\rangle \end{matrix} \quad (C.5)$$

where the  $*$  denotes a complex conjugation and

$$\tilde{N}_{4,xy} = F \sqrt{\frac{1}{2}} \begin{pmatrix} 0 & 0 & -1 \\ 0 & 0 & -i \\ 1 & i & 0 \end{pmatrix} \quad \text{as well as} \quad \tilde{N}_{4,z} = F \sqrt{\frac{2}{3}} \begin{pmatrix} 0 & i & 0 \\ -i & 0 & 0 \\ 0 & 0 & 0 \end{pmatrix}. \quad (C.6)$$

The parameter  $F$  is a free parameter that can be related to the parameters of the magnetic terms of the Suzuki-Hensel Hamiltonian via Eq. (5.20). By comparison with Eq. (2.47), we find  $F =$

$-(A_4 - 2B_4)/\sqrt{3}$ . A further comparison with the magnetic Hamiltonian and its parameters given in Ref. [42] yields

$$F = -\sqrt{\frac{3}{4}} \left( \kappa + \frac{g_s}{2} \right) = -0.43 \quad (\text{C.7})$$

where  $g_s \approx 2$  and  $\kappa \approx -0.5$  is the fourth Luttinger parameter [69].

## C.2. Extended Waters basis

This appendix lists the symmetrised exciton basis used in Sec. 5.1 and copied from Ref. [67]. This basis can be understood as an extension of the one derived by R. G. Waters *et al.* [127] for the yellow and green  $S$ -excitons.

The symmetrised yellow band states  $\Gamma_7^+ \otimes \Gamma_6^+ = \Gamma_2^+ \oplus \Gamma_5^+$  can be written as [75, 127, 50]

$$Y^{\Gamma_2^+} = \sqrt{\frac{1}{2}} \left( \psi_{1/2}^{\Gamma_6} \psi_{-1/2}^{\Gamma_7} - \psi_{-1/2}^{\Gamma_6} \psi_{1/2}^{\Gamma_7} \right), \quad (\text{C.8})$$

$$Y_{yz}^{\Gamma_5^+} = i\sqrt{\frac{1}{2}} \left( \psi_{1/2}^{\Gamma_6} \psi_{1/2}^{\Gamma_7} - \psi_{-1/2}^{\Gamma_6} \psi_{-1/2}^{\Gamma_7} \right), \quad (\text{C.9})$$

$$Y_{zx}^{\Gamma_5^+} = \sqrt{\frac{1}{2}} \left( \psi_{1/2}^{\Gamma_6} \psi_{1/2}^{\Gamma_7} + \psi_{-1/2}^{\Gamma_6} \psi_{-1/2}^{\Gamma_7} \right), \quad (\text{C.10})$$

$$Y_{xy}^{\Gamma_5^+} = -i\sqrt{\frac{1}{2}} \left( \psi_{1/2}^{\Gamma_6} \psi_{-1/2}^{\Gamma_7} + \psi_{-1/2}^{\Gamma_6} \psi_{1/2}^{\Gamma_7} \right), \quad (\text{C.11})$$

where the Bloch states are labelled by  $\psi_\sigma^\Gamma$ . The component  $Y^{\Gamma_2^+}$  corresponds to the paraexciton and the three  $Y^{\Gamma_5^+}$  components correspond to the orthoexcitons. The states visible in one-photon dipole absorption are the  $\Gamma_4^-$   $P$ -excitons arising from the orthoexciton component. With the cubic harmonics  $Y_1^{\Gamma_4^-, x_i}$  listed in Tab. B.8, the symmetrised exciton states can be written as

$$Y P_x^{\Gamma_4^-} = \frac{\phi_n}{\sqrt{2}} \left( i Y_{xy}^{\Gamma_5^+} \frac{Y_1^{-1} + Y_1^1}{\sqrt{2}} + Y_{zx}^{\Gamma_5^+} Y_1^0 \right), \quad (\text{C.12})$$

$$Y P_y^{\Gamma_4^-} = \frac{\phi_n}{\sqrt{2}} \left( Y_{xy}^{\Gamma_5^+} \frac{Y_1^{-1} - Y_1^1}{\sqrt{2}} + Y_{yz}^{\Gamma_5^+} Y_1^0 \right), \quad (\text{C.13})$$

$$Y P_z^{\Gamma_4^-} = \frac{\phi_n}{2} \left( Y_{zx}^{\Gamma_5^+} [Y_1^{-1} - Y_1^1] + i Y_{yz}^{\Gamma_5^+} [Y_1^{-1} + Y_1^1] \right), \quad (\text{C.14})$$

where  $Y_\ell^m$  denote the spherical harmonics and  $\phi_n$  is a placeholder for the radial envelope function. In the notational convention of Sec. 5.1, these states are labelled by  $|Y; \Gamma_4^-, x_i; nP; \mathbf{K}\rangle$  with  $x_i \in \{x, y, z\}$ .

Analogously, the symmetrised green band states  $\Gamma_8^+ \otimes \Gamma_6^+ = \Gamma_3^+ \oplus \Gamma_4^+ \oplus \Gamma_5^+$  are given by

$$G_1^{\Gamma_3^+} = -\sqrt{\frac{1}{2}} \left( \psi_{1/2}^{\Gamma_6^+} \psi_{-1/2}^{\Gamma_8^+} + \psi_{-1/2}^{\Gamma_6^+} \psi_{1/2}^{\Gamma_8^+} \right), \quad (\text{C.15})$$

$$G_2^{\Gamma_3^+} = -\sqrt{\frac{1}{2}} \left( \psi_{1/2}^{\Gamma_6^+} \psi_{3/2}^{\Gamma_8^+} + \psi_{-1/2}^{\Gamma_6^+} \psi_{-3/2}^{\Gamma_8^+} \right), \quad (\text{C.16})$$

$$G_x^{\Gamma_4^+} = i\sqrt{\frac{1}{8}} \left( \sqrt{3} \left[ \psi_{-1/2}^{\Gamma_6^+} \psi_{3/2}^{\Gamma_8^+} + \psi_{1/2}^{\Gamma_6^+} \psi_{-3/2}^{\Gamma_8^+} \right] - \left[ \psi_{-1/2}^{\Gamma_6^+} \psi_{-1/2}^{\Gamma_8^+} + \psi_{1/2}^{\Gamma_6^+} \psi_{1/2}^{\Gamma_8^+} \right] \right), \quad (\text{C.17})$$

$$G_y^{\Gamma_4^+} = \sqrt{\frac{1}{8}} \left( \sqrt{3} \left[ \psi_{-1/2}^{\Gamma_6^+} \psi_{3/2}^{\Gamma_8^+} - \psi_{1/2}^{\Gamma_6^+} \psi_{-3/2}^{\Gamma_8^+} \right] + \left[ \psi_{-1/2}^{\Gamma_6^+} \psi_{-1/2}^{\Gamma_8^+} - \psi_{1/2}^{\Gamma_6^+} \psi_{1/2}^{\Gamma_8^+} \right] \right), \quad (\text{C.18})$$

$$G_z^{\Gamma_4^+} = i\sqrt{\frac{1}{2}} \left( \psi_{1/2}^{\Gamma_6^+} \psi_{-1/2}^{\Gamma_8^+} - \psi_{-1/2}^{\Gamma_6^+} \psi_{1/2}^{\Gamma_8^+} \right), \quad (\text{C.19})$$

$$G_{yz}^{\Gamma_5^+} = -i\sqrt{\frac{1}{8}} \left( \left[ \psi_{-1/2}^{\Gamma_6^+} \psi_{3/2}^{\Gamma_8^+} + \psi_{1/2}^{\Gamma_6^+} \psi_{-3/2}^{\Gamma_8^+} \right] + \sqrt{3} \left[ \psi_{-1/2}^{\Gamma_6^+} \psi_{-1/2}^{\Gamma_8^+} + \psi_{1/2}^{\Gamma_6^+} \psi_{1/2}^{\Gamma_8^+} \right] \right), \quad (\text{C.20})$$

$$G_{zx}^{\Gamma_5^+} = \sqrt{\frac{1}{8}} \left( \left[ \psi_{-1/2}^{\Gamma_6^+} \psi_{3/2}^{\Gamma_8^+} - \psi_{1/2}^{\Gamma_6^+} \psi_{-3/2}^{\Gamma_8^+} \right] - \sqrt{3} \left[ \psi_{-1/2}^{\Gamma_6^+} \psi_{-1/2}^{\Gamma_8^+} - \psi_{1/2}^{\Gamma_6^+} \psi_{1/2}^{\Gamma_8^+} \right] \right), \quad (\text{C.21})$$

$$G_{xy}^{\Gamma_5^+} = i\sqrt{\frac{1}{2}} \left( \psi_{1/2}^{\Gamma_6^+} \psi_{3/2}^{\Gamma_8^+} - \psi_{-1/2}^{\Gamma_6^+} \psi_{-3/2}^{\Gamma_8^+} \right). \quad (\text{C.22})$$

The derivation of the symmetrised green  $S$ -states from these product states is trivial. The forty  $D$ -states will not be listed explicitly, but they can be constructed with the coupling coefficients given in Ref. [50] and the cubic harmonics  $Y_2^{\Gamma_3^+, i}$  given in Tabs. B.7 and B.9.

Finally, the symmetrised blue states  $\Gamma_7^+ \otimes \Gamma_8^- = \Gamma_3^- \oplus \Gamma_4^- \oplus \Gamma_5^-$  can be written as

$$B_1^{\Gamma_3^-} = -\sqrt{\frac{1}{2}} \left( \psi_{-1/2}^{\Gamma_7^+} \psi_{-3/2}^{\Gamma_8^-} + \psi_{1/2}^{\Gamma_7^+} \psi_{3/2}^{\Gamma_8^-} \right), \quad (\text{C.23})$$

$$B_2^{\Gamma_3^-} = \sqrt{\frac{1}{2}} \left( \psi_{-1/2}^{\Gamma_7^+} \psi_{1/2}^{\Gamma_8^-} + \psi_{1/2}^{\Gamma_7^+} \psi_{-1/2}^{\Gamma_8^-} \right), \quad (\text{C.24})$$

$$B_x^{\Gamma_4^-} = -i\sqrt{\frac{1}{8}} \left( \sqrt{3} \left[ \psi_{-1/2}^{\Gamma_7^+} \psi_{-1/2}^{\Gamma_8^-} + \psi_{1/2}^{\Gamma_7^+} \psi_{1/2}^{\Gamma_8^-} \right] + \left[ \psi_{-1/2}^{\Gamma_7^+} \psi_{3/2}^{\Gamma_8^-} + \psi_{1/2}^{\Gamma_7^+} \psi_{-3/2}^{\Gamma_8^-} \right] \right), \quad (\text{C.25})$$

$$B_y^{\Gamma_4^-} = \sqrt{\frac{1}{8}} \left( \sqrt{3} \left[ \psi_{1/2}^{\Gamma_7^+} \psi_{1/2}^{\Gamma_8^-} - \psi_{-1/2}^{\Gamma_7^+} \psi_{-1/2}^{\Gamma_8^-} \right] + \left[ \psi_{-1/2}^{\Gamma_7^+} \psi_{3/2}^{\Gamma_8^-} - \psi_{1/2}^{\Gamma_7^+} \psi_{-3/2}^{\Gamma_8^-} \right] \right), \quad (\text{C.26})$$

$$B_z^{\Gamma_4^-} = i\sqrt{\frac{1}{2}} \left( \psi_{1/2}^{\Gamma_7^+} \psi_{3/2}^{\Gamma_8^-} - \psi_{-1/2}^{\Gamma_7^+} \psi_{-3/2}^{\Gamma_8^-} \right), \quad (\text{C.27})$$

$$B_{yz}^{\Gamma_5^-} = -i\sqrt{\frac{1}{8}} \left( \left[ \psi_{-1/2}^{\Gamma_7^+} \psi_{-1/2}^{\Gamma_8^-} + \psi_{1/2}^{\Gamma_7^+} \psi_{1/2}^{\Gamma_8^-} \right] - \sqrt{3} \left[ \psi_{-1/2}^{\Gamma_7^+} \psi_{3/2}^{\Gamma_8^-} + \psi_{1/2}^{\Gamma_7^+} \psi_{-3/2}^{\Gamma_8^-} \right] \right), \quad (\text{C.28})$$

$$B_{zx}^{\Gamma_5^-} = \sqrt{\frac{1}{8}} \left( \left[ \psi_{-1/2}^{\Gamma_7^+} \psi_{-1/2}^{\Gamma_8^-} - \psi_{1/2}^{\Gamma_7^+} \psi_{1/2}^{\Gamma_8^-} \right] + \sqrt{3} \left[ \psi_{-1/2}^{\Gamma_7^+} \psi_{3/2}^{\Gamma_8^-} - \psi_{1/2}^{\Gamma_7^+} \psi_{-3/2}^{\Gamma_8^-} \right] \right), \quad (\text{C.29})$$

$$B_{xy}^{\Gamma_5^-} = i\sqrt{\frac{1}{2}} \left( \psi_{1/2}^{\Gamma_7^+} \psi_{-1/2}^{\Gamma_8^-} - \psi_{-1/2}^{\Gamma_7^+} \psi_{1/2}^{\Gamma_8^-} \right). \quad (\text{C.30})$$

Again the construction of the symmetrised blue  $S$ -exciton states is trivial and the blue  $P$ -exciton states can be constructed with the cubic harmonics  $Y_1^{\Gamma_4^-, x_i}$  listed in Tab. B.8 and the coupling coefficients given in Ref. [50].

### C.3. Evaluation of real-space integrals

The real-space integrals

$$O[\phi, \psi, \mathbf{q}] = \frac{\hbar}{i} \int_{\Omega} d^3\mathbf{r} e^{i\mathbf{q}\cdot\mathbf{r}} \phi^\dagger(\mathbf{r}) \nabla \psi(\mathbf{r}), \quad (\text{C.31})$$

$$W[\phi, \psi, \mathbf{q}] = \int_{\Omega} d^3\mathbf{r} e^{i\mathbf{q}\cdot\mathbf{r}} \phi^\dagger(\mathbf{r}) \psi(\mathbf{r}), \quad (\text{C.32})$$

introduced in Eqs. (5.25, 5.26) can be simplified for hydrogen-like wave functions  $\phi_{n,\ell,m}$  by the plane-wave expansion

$$e^{i\mathbf{q}\cdot\mathbf{r}} = 4\pi \sum_{\lambda=0}^{\infty} \sum_{\nu=-\lambda}^{\lambda} (-1)^\nu i^\lambda j_\lambda(qr) Y_\lambda^\nu(\mathbf{n}_q) Y_\lambda^{-\nu}(\mathbf{n}_r), \quad (\text{C.33})$$

where  $j_\lambda(x)$  denotes the spherical Bessel function. In this manner, the integration over the angular degrees of freedom can be carried out analytically, resulting in

$$\begin{aligned} W[\phi_{n,\ell,m}, \phi_{n',\ell',m'}, \mathbf{q}] &= 4\pi \sum_{\lambda=|\ell-\ell'|}^{\ell+\ell'} (-1)^{m'} i^\lambda Y_\lambda^{m'-m}(\mathbf{n}_q) \\ &\times G(\lambda, m-m'; \ell, -m; \ell', m') \int_0^\infty dr r^2 j_\lambda(qr) f_{n,\ell}^\dagger(r) f_{n',\ell'}(r), \end{aligned} \quad (\text{C.34})$$

where the  $G(\ell, m; \ell', m'; \ell'', m'')$  are the Gaunt coefficients introduced in Eq. (B.34) and the  $f_{n,\ell}(r)$  are just the radial wave functions corresponding to the  $\phi_{n,\ell,m}(\mathbf{r})$ . The primed sum symbol is supposed to indicate that the summation index  $\lambda$  can be incremented by 2 as the Gaunt coefficients vanish if  $\ell + \ell' + \lambda$  is not even (see App. B.5.1).

Equivalently the other integral can be expressed as

$$\begin{aligned}
& \mathcal{O} [\phi_{n,\ell,m}, \phi_{n',\ell',m'}, \mathbf{q}] = \\
& -4\pi\hbar \sum_{\mu=-1}^1 (-1)^{m'-\mu} \langle \ell' + 1, m' - \mu; 1, \mu | \ell', m' \rangle \sum_{\lambda=|\ell'+1-\ell|}^{\ell'+1+\ell} G(\ell, -m; \ell' + 1, m' - \mu; \lambda, m - m' + \mu) \\
& \quad \times i^{\lambda-1} Y_{\lambda}^{m'-\mu-m}(\mathbf{n}_q) \boldsymbol{\xi}_{\mu} \left[ \frac{\ell' + 1}{2\ell' + 1} \right]^{1/2} \int_0^{\infty} dr r^2 j_{\lambda}(qr) f_{n,\ell}^{\dagger}(r) \left( \frac{\partial}{\partial r} - \frac{\ell'}{r} \right) f_{n',\ell'}(r) \\
& +4\pi\hbar \sum_{\mu=-1}^1 (-1)^{m'-\mu} \langle \ell' - 1, m' - \mu; 1, \mu | \ell', m' \rangle \sum_{\lambda=|\ell'-1-\ell|}^{\ell'-1+\ell} G(\ell, -m; \ell' - 1, m' - \mu; \lambda, m + \mu - m') \\
& \quad \times i^{\lambda-1} Y_{\lambda}^{m'-\mu-m}(\mathbf{n}_q) \boldsymbol{\xi}_{\mu} \left[ \frac{\ell'}{2\ell' + 1} \right]^{1/2} \int_0^{\infty} dr r^2 j_{\lambda}(qr) f_{n,\ell}^{\dagger}(r) \left( \frac{\partial}{\partial r} + \frac{\ell' + 1}{r} \right) f_{n',\ell'}(r).
\end{aligned} \tag{C.35}$$

The Clebsch-Gordan coefficients are again labelled by  $\langle \ell, m; \ell', m' | L, M \rangle$ , and  $\boldsymbol{\xi}_{-1} = (1, -i, 0)^T / \sqrt{2}$ ,  $\boldsymbol{\xi}_0 = (0, 0, 1)^T$  and  $\boldsymbol{\xi}_1 = (-1, -i, 0)^T / \sqrt{2}$  are the spherical basis vectors.

## Appendix D.

### List of publications

#### D.1. Published papers

- (I) F. Schöne, S. O. Krüger, P. Grünwald, H. Stolz, S. Scheel, M. Aßmann, J. Heckötter, J. Thewes, D. Fröhlich, and M. Bayer  
“Deviations of the exciton level spectrum in  $\text{Cu}_2\text{O}$  from the hydrogen series”  
*Phys. Rev. B* **93**, 075203 (2016).
- (II) F. Schöne, S. O. Krüger, P. Grünwald, M. Aßmann, J. Heckötter, J. Thewes, H. Stolz, D. Fröhlich, M. Bayer, and S. Scheel  
“Coupled valence band dispersions and the quantum defect of excitons in  $\text{Cu}_2\text{O}$ ”  
*J. Phys. B: At. Mol. Opt. Phys* **49**, 134003 (2016).
- (III) S. O. Krüger and S. Scheel  
“Waveguides for Rydberg excitons in  $\text{Cu}_2\text{O}$  from strain traps”  
*Phys. Rev. B* **97**, 205208 (2018).
- (IV) V. Walther, S. O. Krüger, S. Scheel and T. Pohl  
“Interactions between Rydberg excitons in  $\text{Cu}_2\text{O}$ ”  
*Phys. Rev. B* **98**, 165201 (2018).
- (V) S. O. Krüger and S. Scheel  
“Interseries transitions between Rydberg excitons in  $\text{Cu}_2\text{O}$ ”  
*Phys. Rev. B* **100**, 085201 (2019).
- (VI) A. Konzelmann, S. O. Krüger and H. Giessen  
“Interaction of orbital angular momentum light with Rydberg excitons: Modifying dipole selection rules”  
*Phys. Rev. B* **100**, 115308 (2019).

- (VII) S. O. Krüger, H. Stolz and S. Scheel  
 “Interaction of charged impurities and Rydberg excitons in cuprous oxide”  
*Phys. Rev. B* **101**, 235204 (2020).

## D.2. Submitted papers

- (I) H. Stolz, R. Schwartz, J. Heckötter, M. Aßmann, D. Semkat, S. O. Krüger and M. Bayer  
 “Coherent transfer matrix analysis of the transmission spectra of Rydberg excitons in  $\text{Cu}_2\text{O}$ ”  
 submitted on the 19/09/2020 to *Phys. Rev. B*.

## D.3. Conference contributions

- (I) DPG Spring Meeting 2016 (Condensed Matter Section)  
 Regensburg, Germany, 06/03 – 11/03/2016  
 F. Schöne, S. O. Krüger, P. Grünwald, H. Stolz, and S. Scheel  
*Talk*: “Quantum Defects of Excitons in  $\text{Cu}_2\text{O}$ ”.
- (II) GiRyd Status Workshop 2016  
 Heidelberg, Germany, 14/11 – 15/11/2016  
 S. Scheel, P. Grünwald and S. O. Krüger  
*Poster*: “Coherent dynamics of interacting Rydberg excitons”.
- (III) DPG Spring Meeting 2017 (Condensed Matter Section)  
 Dresden, Germany, 19/03 – 24/03/2017  
 S. O. Krüger, P. Grünwald, F. Schöne and S. Scheel  
*Poster*: “Influence of strain on the binding energies of Rydberg excitons in  $\text{Cu}_2\text{O}$ ”.
- (IV) International Workshop on Atomic Physics 2017  
 Dresden, Germany, 27/11 – 01/12/2017  
 S. O. Krüger and S. Scheel  
*Poster*: “Rydberg excitons in strain-induced waveguide traps in cuprous oxide ( $\text{Cu}_2\text{O}$ )”.
- (V) DPG Spring Meeting 2018 (Condensed Matter Section)  
 Berlin, Germany, 11/03 – 16/03/2018  
 S. O. Krüger and S. Scheel  
*Talk*: “Trapping potentials for Rydberg excitons in cuprous oxide ( $\text{Cu}_2\text{O}$ )”
- (VI) International Workshop on Rydberg Excitons in Semiconductors 2018  
 Aarhus, Denmark, 03/05 – 04/05/2018



S. O. Krüger and S. Scheel

*Poster:* “Trapping potentials for Rydberg excitons in cuprous oxide”.

(VII) GiRyd Status Workshop 2018

Hamburg, Germany, 03/07 – 06/07/2018

S. O. Krüger and S. Scheel

*Poster:* “Trapping potentials for Rydberg excitons in cuprous oxide”.

(VIII) SRitp and GiRyd Advanced School 2018

Rehovot, Israel, 20/09 – 27/09/2018

S. O. Krüger and S. Scheel

*Poster:* “Trapping potentials for Rydberg excitons in cuprous oxide ( $\text{Cu}_2\text{O}$ )”.

(IX) DPG Spring Meeting 2019 (SAMOP)

Rostock, Germany, 10/03 – 15/03/2019

S. O. Krüger and S. Scheel

*Poster:* Interaction of Rydberg excitons in cuprous oxide ( $\text{Cu}_2\text{O}$ ) with a thin electron-hole plasma“.

(X) GiRyd Status Workshop 2019

Kaiserslautern, Germany, 25/03 – 27/03/2019

S. O. Krüger and S. Scheel

*Poster:* “Infrared transitions between the yellow and green exciton series in  $\text{Cu}_2\text{O}$ “.

(XI) International Workshop on Rydberg Excitons in Semiconductors 2019

Durham, United Kingdom, 15/07 – 16/07/2019

S. O. Krüger and S. Scheel

*Talk:* “Infrared inter-series transitions of Rydberg excitons in  $\text{Cu}_2\text{O}$ “.

(XII) International Conference on Optics of Excitons in Confined Systems 2019

St. Petersburg, Russia, 16/09 – 20/09/2019

S. O. Krüger and S. Scheel

*Poster:* “Infrared inter-series transitions of Rydberg excitons in  $\text{Cu}_2\text{O}$ “.







## Bibliography

- [1] A. Pfund, "The light sensitiveness of copper oxide," *Phys. Rev.*, vol. 7, no. 3, p. 289, 1916.
- [2] L. O. Grondahl, "The copper-cuprous-oxide rectifier and photoelectric cell," *Rev. Mod. Phys.*, vol. 5, p. 141, 1933.
- [3] K. C. Handel, *Anfänge der Halbleiterforschung und-entwicklung*. PhD thesis, RWTH Aachen, 1999.
- [4] J. Slepian, "Copper oxide rectifier." US Patent 1,844,928. Feb. 9 1932.
- [5] W. Schottky and W. Deutschmann, "Zum Mechanismus der Richtwirkung in Kupferoxydgleichrichtern," in *Electronic Structure of Metal-Semiconductor Contacts*, pp. 45–52, Springer, 1999.
- [6] W. Schottky, "Halbleitertheorie der Sperrschicht," *Naturwissenschaften*, vol. 26, pp. 843–843, 1938.
- [7] M. Hayashi and K. Katsuki, "Hydrogen-like absorption spectrum of cuprous oxide," *J. Phys. Soc. Jpn.*, vol. 7, no. 6, pp. 599–603, 1952.
- [8] E. F. Gross and N. A. Karryev, "Pogloshchenie sveta kristallom zakisi medi v infrakrasnoi i vidimoi chasti spektra," *Doklady Akademii Nauk SSSR*, vol. 84, no. 2, pp. 261–264, 1952.
- [9] E. F. Gross, "Optical spectrum of excitons in the crystal lattice," *Il Nuovo Cimento (1955-1965)*, vol. 3, no. 4, pp. 672–701, 2007.
- [10] J. Frenkel, "On the Transformation of light into Heat in Solids. I," *Phys. Rev.*, vol. 37, pp. 17–44, Jan 1931.
- [11] J. Frenkel, "On the Transformation of Light into Heat in Solids. II," *Phys. Rev.*, vol. 37, pp. 1276–1294, May 1931.
- [12] G. H. Wannier, "The Structure of Electronic Excitation Levels in Insulating Crystals," *Phys. Rev.*, vol. 52, pp. 191–197, Aug 1937.
- [13] S. Moskalenko, "Reversible optico-hydrodynamic phenomena in a nonideal exciton gas," *Soviet Physics-Solid State*, vol. 4, pp. 199–204, 1962.

- [14] J. M. Blatt, K. W. Böer, and W. Brandt, “Bose-Einstein Condensation of Excitons,” *Phys. Rev.*, vol. 126, pp. 1691–1692, Jun 1962.
- [15] D. W. Snoke, “When should we say we have observed Bose condensation of excitons?,” *physica status solidi (b)*, vol. 238, no. 3, pp. 389–396, 2003.
- [16] D. Semkat, S. Sobkowiak, F. Schöne, H. Stolz, T. Koch, and H. Fehske, “Multicomponent exciton gas in cuprous oxide: cooling behaviour and the role of Auger decay,” *Journal of Physics B: Atomic, Molecular and Optical Physics*, vol. 50, no. 20, p. 204001, 2017.
- [17] H. Matsumoto, K. Saito, M. Hasuo, S. Kono, and N. Nagasawa, “Revived interest on yellow-exciton series in  $\text{Cu}_2\text{O}$ : An experimental aspect,” *Solid State Communications*, vol. 97, no. 2, pp. 125 – 129, 1996.
- [18] T. Kazimierczuk, D. Fröhlich, S. Scheel, H. Stolz, and M. Bayer, “Giant Rydberg excitons in the copper oxide  $\text{Cu}_2\text{O}$ ,” *Nature*, vol. 514, no. 7522, pp. 343–347, 2014.
- [19] J. Heckötter, D. Janas, R. Schwartz, M. Aßmann, and M. Bayer, “Experimental limitation in extending the exciton series in  $\text{Cu}_2\text{O}$  towards higher principal quantum numbers,” *Phys. Rev. B*, vol. 101, p. 235207, Jun 2020.
- [20] J. Thewes, J. Heckötter, T. Kazimierczuk, M. Aßmann, D. Fröhlich, M. Bayer, M. A. Semina, and M. M. Glazov, “Observation of high angular momentum excitons in cuprous oxide,” *Phys. Rev. Lett.*, vol. 115, no. 2, p. 027402, 2015.
- [21] T. F. Gallagher, *Rydberg Atoms*. Cambridge University Press, UK, 1994.
- [22] J. Heckötter, M. Freitag, D. Fröhlich, M. Aßmann, M. Bayer, M. A. Semina, and M. M. Glazov, “Scaling laws of Rydberg excitons,” *Phys. Rev. B*, vol. 96, p. 125142, Sep 2017.
- [23] T. Peyronel, O. Firstenberg, Q.-Y. Liang, S. Hofferberth, A. V. Gorshkov, T. Pohl, M. D. Lukin, and V. Vuletic, “Quantum nonlinear optics with single photons enabled by strongly interacting atoms,” *Nature*, vol. 488, pp. 57–60, 2012.
- [24] Y. Zeng, P. Xu, X. He, Y. Liu, M. Liu, J. Wang, D. J. Papoular, G. V. Shlyapnikov, and M. Zhan, “Entangling Two Individual Atoms of Different Isotopes via Rydberg Blockade,” *Phys. Rev. Lett.*, vol. 119, p. 160502, Oct 2017.
- [25] F. Schöne, S. O. Krüger, P. Grünwald, H. Stolz, S. Scheel, M. Aßmann, J. Heckötter, J. Thewes, D. Fröhlich, and M. Bayer, “Deviations of the exciton level spectrum in  $\text{Cu}_2\text{O}$  from the hydrogen series,” *Phys. Rev. B*, vol. 93, no. 7, p. 075203, 2016.
- [26] F. Schöne, S. O. Krüger, P. Grünwald, M. Aßmann, J. Heckötter, J. Thewes, H. Stolz, D. Fröhlich, M. Bayer, and S. Scheel, “Coupled valence band dispersions and the quantum defect of excitons in  $\text{Cu}_2\text{O}$ ,” *J. Phys. B: At. Mol. Opt. Phys.*, vol. 49, no. 13, p. 134003, 2016.

- [27] M. A. Semina, “Fine Structure of Rydberg Excitons in Cuprous Oxide,” *Phys. Sol. State*, vol. 60, pp. 1527–1536, August 2018.
- [28] F. Schweiner, J. Main, G. Wunner, and C. Uihlein, “Even exciton series in  $\text{Cu}_2\text{O}$ ,” *Phys. Rev. B*, vol. 95, p. 195201, May 2017.
- [29] P. Grünwald, M. Aßmann, J. Heckötter, D. Fröhlich, M. Bayer, H. Stolz, and S. Scheel, “Signatures of quantum coherences in Rydberg excitons,” *Phys. Rev. Lett.*, vol. 117, no. 13, p. 133003, 2016.
- [30] J. Heckötter, M. Freitag, D. Fröhlich, M. Aßmann, M. Bayer, P. Grünwald, F. Schöne, D. Semkat, H. Stolz, and S. Scheel, “Rydberg excitons in the presence of an ultralow-density electron-hole plasma,” *Phys. Rev. Lett.*, vol. 121, no. 9, p. 097401, 2018.
- [31] D. Semkat, H. Fehske, and H. Stolz, “Influence of electron-hole plasma on Rydberg excitons in cuprous oxide,” *Phys. Rev. B*, vol. 100, p. 155204, 2019.
- [32] F. Schöne, H. Stolz, and N. Naka, “Phonon-assisted absorption of excitons in  $\text{Cu}_2\text{O}$ ,” *Phys. Rev. B*, vol. 96, p. 115207, Sep 2017.
- [33] H. Stolz, F. Schöne, and D. Semkat, “Interaction of Rydberg excitons in cuprous oxide with phonons and photons: optical linewidth and polariton effect,” *New J. Phys.*, vol. 20, no. 2, p. 023019, 2018.
- [34] F. Urbach, “The Long-Wavelength Edge of Photographic Sensitivity and of the Electronic Absorption of Solids,” *Phys. Rev.*, vol. 92, pp. 1324–1324, Dec 1953.
- [35] F. Moser and F. Urbach, “Optical Absorption of Pure Silver Halides,” *Phys. Rev.*, vol. 102, pp. 1519–1523, Jun 1956.
- [36] J. D. Dow and D. Redfield, “Toward a Unified Theory of Urbach’s Rule and Exponential Absorption Edges,” *Phys. Rev. B*, vol. 5, pp. 594–610, Jan 1972.
- [37] V. Walther, S. O. Krüger, S. Scheel, and T. Pohl, “Interactions between Rydberg excitons in  $\text{Cu}_2\text{O}$ ,” *Phys. Rev. B*, vol. 98, no. 16, p. 165201, 2018.
- [38] M. Kurz, P. Grünwald, and S. Scheel, “Excitonic giant-dipole potentials in cuprous oxide,” *Phys. Rev. B*, vol. 95, no. 24, p. 245205, 2017.
- [39] M. Kurz and S. Scheel, “Eigenenergies of excitonic giant-dipole states in cuprous oxide,” *Phys. Rev. B*, vol. 99, p. 075205, Feb 2019.
- [40] J. Heckötter, M. Freitag, D. Fröhlich, M. Aßmann, M. Bayer, M. A. Semina, and M. M. Glazov, “Dissociation of excitons in  $\text{Cu}_2\text{O}$  by an electric field,” *Phys. Rev. B*, vol. 98, no. 3, p. 035150, 2018.

- [41] P. Zielinski, P. Rommel, F. Schweiner, and J. Main, “Rydberg excitons in electric and magnetic fields obtained with the complex-coordinate-rotation method,” *J. Phys. B: At. Mol. Opt. Phys.*, vol. 53, no. 5, p. 054004, 2019.
- [42] F. Schweiner, J. Main, G. Wunner, M. Freitag, J. Heckötter, C. Uihlein, M. Aßmann, D. Fröhlich, and M. Bayer, “Magnetoexcitons in cuprous oxide,” *Phys. Rev. B*, vol. 95, no. 3, p. 035202, 2017.
- [43] S. O. Krüger, H. Stolz, and S. Scheel, “Interaction of charged impurities and Rydberg excitons in cuprous oxide,” *Phys. Rev. B*, vol. 101, p. 235204, Jun 2020.
- [44] D. Ziemkiewicz and S. Zielińska-Raczyńska, “Proposal of tunable Rydberg exciton maser,” *Opt. Lett.*, vol. 43, no. 15, pp. 3742–3745, 2018.
- [45] D. Ziemkiewicz and S. Zielińska-Raczyńska, “Solid-state pulsed microwave emitter based on Rydberg excitons,” *Opt. Exp.*, vol. 27, no. 12, pp. 16983–16994, 2019.
- [46] A. N. Poddubny and M. M. Glazov, “Topological spin phases of trapped Rydberg excitons in  $\text{Cu}_2\text{O}$ ,” *Phys. Rev. Lett.*, vol. 123, p. 126801, 2019.
- [47] W. Pauli Jr., “Zur Quantenmechanik des magnetischen Elektrons,” *ZS f. Phys.*, vol. 43, pp. 601–623, 1927.
- [48] H.-W. Streitwolf, *Group Theory in solid-state Physics*. Macdonald and Co., London, 1971.
- [49] M. S. Dresselhaus, G. Dresselhaus, and A. Jorio, *Group Theory: Application to the Physics of Condensed Matter*. Springer Verlag, Berlin, 2007.
- [50] G. F. Koster, J. O. Dimmock, R. G. Wheeler, and H. Statz, *Properties of the thirty-two point groups*. MIT press, 1963.
- [51] L. P. Bouckaert, R. Smoluchowski, and E. Wigner, “Theory of Brillouin Zones and Symmetry Properties of Wave Functions in Crystals,” *Phys. Rev.*, vol. 50, pp. 58–67, Jul 1936.
- [52] R. Gilmore, *Lie Groups, Physics, and Geometry: An Introduction for Physicists, Engineers and Chemists*. Cambridge University Press, 2008.
- [53] D. G. Bell, “Group Theory and Crystal Lattices,” *Rev. Mod. Phys.*, vol. 26, pp. 311–320, Jul 1954.
- [54] S. L. Altmann and C. J. Bradley, “Lattice Harmonics II. Hexagonal Close-Packed Lattice,” *Rev. Mod. Phys.*, vol. 37, pp. 33–45, Jan 1965.
- [55] F. C. von der Lage and H. A. Bethe, “A Method for Obtaining Electronic Eigenfunctions and Eigenvalues in Solids with An Application to Sodium,” *Phys. Rev.*, vol. 71, pp. 612–622, May 1947.



- [56] S. L. Altmann and A. P. Cracknell, “Lattice Harmonics I. Cubic Groups,” *Rev. Mod. Phys.*, vol. 37, pp. 19–32, Jan 1965.
- [57] P. Yu and M. Cardona, *Fundamentals of semiconductors: physics and materials properties*. Springer Verlag, Berlin, 2010.
- [58] G. L. Bir and G. E. Pikus, *Symmetry and Strain-induced Effects in Semiconductors*. Wiley New York, 1974.
- [59] L. C. L. Y. Voon and M. Willatzen, *The  $\mathbf{k} \cdot \mathbf{p}$  Method: Electronic Properties of Semiconductors*. Springer Verlag, Berlin, 2009.
- [60] H. Haug and S. W. Koch, *Quantum Theory of the Optical and Electronic Properties of Semiconductors*. World Scientific, Singapore, 4. ausgabe ed., 2004.
- [61] R. S. Knox, *Theory of Excitons*. Academic Press, 1963.
- [62] C. F. Klingshirn, *Semiconductor Optics*. Springer Verlag, Berlin, 2012.
- [63] W. Schäfer and M. Wegener, *Semiconductor Optics and Transport Phenomena*. Springer Verlag, Berlin, 2002.
- [64] F. Schweiner, *Theory of excitons in cuprous oxide*. PhD thesis, Universität Stuttgart, 2017.
- [65] W. Brauer and H.-W. Streitwolf, *Theoretische Grundlagen der Halbleiterphysik*. Reihe Wissenschaft, 2. überarbeitete Auflage, Vieweg, Braunschweig, 1977.
- [66] K. Suzuki and J. C. Hensel, “Quantum resonances in the valence bands of germanium. I. Theoretical considerations,” *Phys. Rev. B*, vol. 9, pp. 4184–4218, May 1974.
- [67] S. O. Krüger and S. Scheel, “Interseries transitions between Rydberg excitons in  $\text{Cu}_2\text{O}$ ,” *Phys. Rev. B*, vol. 100, p. 085201, Aug 2019.
- [68] G. E. Pikus and G. L. Bir, “Effect of deformation on the hole energy spectrum of germanium and silicon,” *Fiz. Tverd. Tela*, vol. 1, pp. 1642–1658, November 1959. [*Sov. Phys. Solid State* 1, 1502–1517 (1960)].
- [69] J. M. Luttinger, “Quantum Theory of Cyclotron Resonance in Semiconductors: General Theory,” *Phys. Rev.*, vol. 102, pp. 1030–1040, May 1956.
- [70] H. Kramers, “General theory of paramagnetic rotation in crystals,” in *Proc. Acad. Sci. Amsterdam*, vol. 33, p. 959, 1930.
- [71] E. Wigner, “Über die Operation der Zeitumkehr in der Quantenmechanik,” *Nachr. Ges. Wiss. Göttingen, Math.-Phys. Kl.*, vol. 1932, pp. 546–559, 1932.
- [72] J. Pollmann and H. Büttner, “Effective Hamiltonians and bindings energies of Wannier exci-

- tons in polar semiconductors,” *Phys. Rev. B*, vol. 16, pp. 4480–4490, Nov 1977.
- [73] F. Schweiner, J. Main, M. Feldmaier, G. Wunner, and C. Uihlein, “Impact of the valence band structure of  $\text{Cu}_2\text{O}$  on excitonic spectra,” *Phys. Rev. B*, vol. 93, p. 195203, May 2016.
- [74] G. M. Kavoulakis, Y.-C. Chang, and G. Baym, “Fine structure of excitons in  $\text{Cu}_2\text{O}$ ,” *Phys. Rev. B*, vol. 55, pp. 7593–7599, Mar 1997.
- [75] G. Dasbach, D. Fröhlich, R. Klieber, D. Suter, M. Bayer, and H. Stolz, “Wave-vector-dependent exchange interaction and its relevance for the effective exciton mass in  $\text{Cu}_2\text{O}$ ,” *Phys. Rev. B*, vol. 70, p. 045206, Jul 2004.
- [76] R. J. Elliott, “Intensity of Optical Absorption by Excitons,” *Phys. Rev.*, vol. 108, pp. 1384–1389, Dec 1957.
- [77] A. Werner and H. D. Hochheimer, “High-pressure x-ray study of  $\text{Cu}_2\text{O}$  and  $\text{Ag}_2\text{O}$ ,” *Phys. Rev. B*, vol. 25, no. 9, p. 5929, 1982.
- [78] J. Dahl and A. Switendick, “Energy bands in cuprous oxide,” *J. Phys. Chem. Sol.*, vol. 27, no. 6, pp. 931 – 942, 1966.
- [79] E. Ruiz, S. Alvarez, P. Alemany, and R. A. Evarestov, “Electronic structure and properties of  $\text{Cu}_2\text{O}$ ,” *Phys. Rev. B*, vol. 56, pp. 7189–7196, Sep 1997.
- [80] M. French, R. Schwartz, H. Stolz, and R. Redmer, “Electronic band structure of  $\text{Cu}_2\text{O}$  by spin density functional theory,” *J. Phys. Condens. Matter*, vol. 21, p. 015502, dec 2008.
- [81] F. Bruneval, N. Vast, L. Reining, M. Izquierdo, F. Sirotti, and N. Barrett, “Exchange and Correlation Effects in Electronic Excitations of  $\text{Cu}_2\text{O}$ ,” *Phys. Rev. Lett.*, vol. 97, p. 267601, Dec 2006.
- [82] J. Schmutzler, D. Fröhlich, and M. Bayer, “Signatures of coherent propagation of blue polaritons in  $\text{Cu}_2\text{O}$ ,” *Phys. Rev. B*, vol. 87, p. 245202, Jun 2013.
- [83] S. Nikitine, “Experimental investigations of exciton spectra in ionic crystals,” *Philos. Mag.*, vol. 4, no. 37, pp. 1–31, 1959.
- [84] F. Schöne, *Optical Properties of yellow Excitons in Cuprous Oxide*. PhD thesis, Universität Rostock, 2017.
- [85] G. Kuwabara, M. Tanaka, and H. Fukutani, “Optical absorption due to paraexciton of  $\text{Cu}_2\text{O}$ ,” *Solid State Communications*, vol. 21, no. 6, pp. 599 – 601, 1977.
- [86] Y. Toyozawa, “Interband effect of lattice vibrations in the exciton absorption spectra,” *J. Phys. Chem. Sol.*, vol. 25, no. 1, pp. 59 – 71, 1964.
- [87] K. E. O’Hara, *Relaxation Kinetics of Excitons in Cuprous Oxide*. PhD thesis, University of

Illinois, 1999.

- [88] R. Szmytkowski, "Alternative approach to the solution of the momentum-space schrödinger equation for bound states of the n-dimensional coulomb problem," *Annalen der Physik*, vol. 524, no. 6-7, pp. 345–352, 2012.
- [89] G. Dresselhaus, "Effective mass approximation for excitons," *J. Phys. Chem. Sol.*, vol. 1, no. 1, pp. 14 – 22, 1956.
- [90] M. Altarelli and N. O. Lipari, "Exciton dispersion in semiconductors with degenerate bands," *Phys. Rev. B*, vol. 15, pp. 4898–4906, May 1977.
- [91] C. Uihlein, D. Fröhlich, and R. Kenklies, "Investigation of exciton fine structure in  $\text{Cu}_2\text{O}$ ," *Phys. Rev. B*, vol. 23, pp. 2731–2740, Mar 1981.
- [92] K. Atkinson and W. Han, *Spherical Harmonics and Approximations on the Unit Sphere: An Introduction*. Lecture Notes in Mathematics, Springer, 2012.
- [93] M. Abramowitz and I. Stegun, *Handbook of Mathematical Functions: With Formulas, Graphs, and Mathematical Tables*. Applied mathematics series, US Government Printing Office, 10<sup>th</sup> printing with corrections ed., 1972.
- [94] C.-D. Kuo, "The uncertainties in radial position and radial momentum of an electron in the non-relativistic hydrogen-like atom," *Annals of Physics*, vol. 316, no. 2, pp. 431 – 439, 2005.
- [95] I. Hertel and C. Schulz, *Atoms, Molecules and Optical Physics 1: Atoms and Spectroscopy*. Graduate Texts in Physics, Springer, 2014.
- [96] S. Weber, C. Tresp, H. Menke, A. Urvoy, O. Firstenberg, H. P. Büchler, and S. Hofferberth, "Tutorial: Calculation of Rydberg interaction potentials," *J. Phys. B: At. Mol. Opt. Phys.*, vol. 50, no. 13, p. 133001, 2017.
- [97] K. Singer, J. Stanojevic, M. Weidemüller, and R. Côté, "Long-range interactions between alkali Rydberg atom pairs correlated to the  $ns$ – $ns$ ,  $np$ – $np$  and  $nd$ – $nd$  asymptotes," *J. Phys. B: At. Mol. Opt. Phys*, vol. 38, pp. 295–307, 2005.
- [98] R. J. Le Roy, "Long-Range Potential Coefficients From RKR Turning Points:  $C_6$  and  $C_8$  for  $B(3\Pi_{Ou}^+)$ -State  $\text{Cl}_2$ ,  $\text{Br}_2$ , and  $\text{I}_2$ ," *Can. J. Phys*, vol. 52, pp. 246–256, 1974.
- [99] R. Grimm, M. Weidemüller, and Y. B. Ovchinnikov, "Optical Dipole Traps for Neutral Atoms," *Advances in Atomic Molecular and Optical Physics*, vol. 42, pp. 95–170, 1999.
- [100] D. P. Trauernicht, J. P. Wolfe, and A. Mysyrowicz, "Thermodynamics of strain-confined paraexcitons in  $\text{Cu}_2\text{O}$ ," *Phys. Rev. B*, vol. 34, pp. 2561–2575, Aug 1986.
- [101] D. W. Snoke and V. Negoita, "Pushing the Auger limit: Kinetics of excitons in traps in  $\text{Cu}_2\text{O}$ ,"

- Phys. Rev. B*, vol. 61, pp. 2904–2910, Jan 2000.
- [102] N. Naka and N. Nagasawa, “Two-photon diagnostics of stress-induced exciton traps and loading of  $1s$ -yellow excitons in  $\text{Cu}_2\text{O}$ ,” *Phys. Rev. B*, vol. 65, p. 075209, Jan 2002.
- [103] N. Naka and N. Nagasawa, “Two-photon tomography of strain-induced potential wells of excitons in  $\text{Cu}_2\text{O}$ ,” *Phys. Rev. B*, vol. 70, p. 155205, Oct 2004.
- [104] K. Yoshioka, E. Chae, and M. Kuwata-Gonokami, “Transition to a Bose–Einstein condensate and relaxation explosion of excitons at sub-Kelvin temperatures,” *Nature communications*, vol. 2, p. 328, 2011.
- [105] C. Sandfort, J. Brandt, C. Finke, D. Fröhlich, M. Bayer, H. Stolz, and N. Naka, “Paraexcitons of  $\text{Cu}_2\text{O}$  confined by a strain trap and high magnetic fields,” *Phys. Rev. B*, vol. 84, p. 165215, Oct 2011.
- [106] H. Stolz, R. Schwartz, F. Kieseling, S. Som, M. Kaupsch, S. Sobkowiak, D. Semkat, N. Naka, T. Koch, and H. Fehske, “Condensation of excitons in  $\text{Cu}_2\text{O}$  at ultracold temperatures: experiment and theory,” *N. J. Phys.*, vol. 14, no. 10, p. 105007, 2012.
- [107] R. Schwartz, N. Naka, F. Kieseling, and H. Stolz, “Dynamics of excitons in a potential trap at ultra-low temperatures: paraexcitons in  $\text{Cu}_2\text{O}$ ,” *N. J. Phys.*, vol. 14, no. 2, p. 023054, 2012.
- [108] D. Fröhlich and M. Bayer, “Emission of  $\text{Cu}_2\text{O}$  Paraexcitons Confined by a Strain Trap: Hints of a Bose–Einstein Condensate?,” *Phys. Sol. State*, vol. 60, no. 8, pp. 1600–1605, 2018.
- [109] S. O. Krüger and S. Scheel, “Waveguides for Rydberg excitons in  $\text{Cu}_2\text{O}$  from strain traps,” *Phys. Rev. B*, vol. 97, p. 205208, May 2018.
- [110] A. C. Fischer-Cripps, *Introduction to contact mechanics*. Springer, 2007.
- [111] M. H. Manghnani, W. S. Brower, and H. S. Parker, “Anomalous elastic behavior in  $\text{Cu}_2\text{O}$  under pressure,” *physica status solidi (a)*, vol. 25, no. 1, pp. 69–76, 1974.
- [112] S. Axler, P. Bourdon, and R. Wade, *Harmonic function theory*. Springer Science & Business Media, 2001.
- [113] H. Hertz, “Über die Berührung fester elastischer Körper,” *J. reine angew. Math.*, vol. 92, pp. 156–171, 1882.
- [114] M. T. Huber, “Zur Theorie der Berührung fester elastischer Körper,” *Annalen der Physik*, vol. 319, no. 6, pp. 153–163, 1904.
- [115] E. M’Ewen, “Stresses in elastic cylinders in contact along a generatrix (including the effect of tangential friction),” *The London, Edinburgh, and Dublin Philosophical Magazine and Journal of Science*, vol. 40, no. 303, pp. 454–459, 1949.

- [116] K. L. Johnson, *Contact Mechanics*. Cambridge University Press, 1985.
- [117] R. S. Markiewicz, J. P. Wolfe, and C. D. Jeffries, “Strain-confined electron-hole liquid in germanium,” *Phys. Rev. B*, vol. 15, pp. 1988–2005, Feb 1977.
- [118] D. Wintgen, H. Marxer, and J. S. Briggs, “Efficient quantisation scheme for the anisotropic Kepler problem,” *J. Phys. A: Mat. Gen.*, vol. 20, pp. L965–L968, oct 1987.
- [119] E. A. Cerda-Méndez, D. N. Krizhanovskii, M. Wouters, R. Bradley, K. Biermann, K. Guda, R. Hey, P. V. Santos, D. Sarkar, and M. S. Skolnick, “Polariton Condensation in Dynamic Acoustic Lattices,” *Phys. Rev. Lett.*, vol. 105, p. 116402, Sep 2010.
- [120] P. V. Demekhin, “On the breakdown of the electric dipole approximation for hard x-ray photoionization cross sections,” *J. Phys. B: At. Mol. Opt. Phys.*, vol. 47, p. 025602, jan 2014.
- [121] N. H. List, J. Kauczor, T. Saue, H. J. A. Jensen, and P. Norman, “Beyond the electric-dipole approximation: A formulation and implementation of molecular response theory for the description of absorption of electromagnetic field radiation,” *The Journal of Chemical Physics*, vol. 142, no. 24, p. 244111, 2015.
- [122] M. Khazali, K. Heshami, and C. Simon, “Single-photon source based on Rydberg exciton blockade,” *J. Phys. B: At., Mol. Opt. Phys.*, vol. 50, p. 215301, oct 2017.
- [123] V. Walther, R. Johne, and T. Pohl, “Giant optical nonlinearities from Rydberg excitons in semiconductor microcavities,” *Nature Communications*, vol. 9, p. 1309, 2018.
- [124] M. Jörger, E. Tsitsishvili, T. Fleck, and C. Klingshirn, “Infrared absorption by excitons in  $\text{Cu}_2\text{O}$ ,” *phys. stat. sol. (b)*, vol. 238, no. 3, pp. 470–473, 2003.
- [125] P. Rommel, P. Zielinski, and J. Main, “Green exciton series in cuprous oxide,” *Phys. Rev. B*, vol. 101, p. 075208, Feb 2020.
- [126] T. Itoh and S.-i. Narita, “Analysis of wavelength derivative spectra of exciton in  $\text{Cu}_2\text{O}$ ,” *J. Phys. Soc. Jpn.*, vol. 39, no. 1, pp. 140–147, 1975.
- [127] R. G. Waters, F. H. Pollak, R. H. Bruce, and H. Z. Cummins, “Effects of uniaxial stress on excitons in  $\text{Cu}_2\text{O}$ ,” *Phys. Rev. B*, vol. 21, pp. 1665–1675, Feb 1980.
- [128] M. Takahata and N. Naka, “Photoluminescence properties of the entire excitonic series in  $\text{Cu}_2\text{O}$ ,” *Phys. Rev. B*, vol. 98, p. 195205, Nov 2018.
- [129] L. C. Lew Yan Voon and L. R. Ram-Mohan, “Tight-binding representation of the optical matrix elements: Theory and applications,” *Phys. Rev. B*, vol. 47, pp. 15500–15508, Jun 1993.
- [130] C. T. Schmiegelow and F. Schmidt-Kaler, “Light with orbital angular momentum interacting

- with trapped ions,” *Eur. Phys. J. D*, vol. 66, p. 157, Jun 2012.
- [131] C. T. Schmiegelow, J. Schulz, H. Kaufmann, T. Ruster, U. G. Poschinger, and F. Schmidt-Kaler, “Transfer of optical orbital angular momentum to a bound electron,” *Nat. Comm.*, vol. 7, p. 12998, Oct 2016.
- [132] A. Afanasev, C. E. Carlson, C. T. Schmiegelow, J. Schulz, F. Schmidt-Kaler, and M. Solyanik, “Experimental verification of position-dependent angular-momentum selection rules for absorption of twisted light by a bound electron,” *N. J. Phys.*, vol. 20, p. 023032, feb 2018.
- [133] S. A. Lynch, C. Hodges, W. W. Langbein, L. Gallagher, J. Rogers, C. S. Adams, M. P. Jones, and R. P. Singh, “Giant Rydberg Excitons in Synthetic and Artificial Cuprous Oxide,” in *2018 20th International Conference on Transparent Optical Networks (ICTON)*, pp. 1–4, IEEE, 2018.
- [134] S. Steinhauer, M. A. Versteegh, S. Gyger, A. W. Elshaari, B. Kunert, A. Mysyrowicz, and V. Zwiller, “Rydberg excitons in  $\text{Cu}_2\text{O}$  microcrystals grown on a silicon platform,” *Communications Materials*, vol. 1, no. 1, pp. 1–7, 2020.
- [135] J. Holtsmark, “Über die Verbreiterung von Spektrallinien,” *Ann. Phys.*, vol. 363, no. 7, pp. 577–630, 1919.
- [136] I. T. Iakubov, G. Kobzev, and M. Popovich, *Transport and optical properties of nonideal plasma*. Springer Science & Business Media, 2013.
- [137] A. K. Pradhan and S. N. Nahar, *Atomic astrophysics and spectroscopy*. Cambridge University Press, 2011.
- [138] C. Hooper Jr, “Electric microfield distributions in plasmas,” *Phys. Rev.*, vol. 149, no. 1, p. 77, 1966.
- [139] C. Hooper Jr, “Low-frequency component electric microfield distributions in plasmas,” *Phys. Rev.*, vol. 165, no. 1, p. 215, 1968.
- [140] D. G. Thomas, M. Gershenson, and F. A. Trumbore, “Pair Spectra and “Edge” Emission in Gallium Phosphide,” *Phys. Rev.*, vol. 133, pp. A269–A279, Jan 1964.
- [141] P. J. Dean, E. G. Schönherr, and R. B. Zetterstrom, “Pair Spectra Involving the Shallow Acceptor Mg in GaP,” *Journal of Applied Physics*, vol. 41, no. 8, pp. 3475–3479, 1970.
- [142] F. Biccari, *Defects and Doping in  $\text{Cu}_2\text{O}$* . PhD thesis, Universita di Roma, 2009.
- [143] J. Mund, D. Fröhlich, D. R. Yakovlev, and M. Bayer, “High-resolution second harmonic generation spectroscopy with femtosecond laser pulses on excitons in  $\text{Cu}_2\text{O}$ ,” *Phys. Rev. B*, vol. 98, no. 8, p. 085203, 2018.
- [144] J. Grimm, M. Stecker, M. Kaiser, F. Karlewski, L. Torralbo-Campo, A. Günther, and

- J. Fortágh, “Ionization spectra of highly Stark-shifted rubidium Rydberg states,” *Phys. Rev. A*, vol. 96, no. 1, p. 013427, 2017.
- [145] Sedlacek, J. A. and Schwettmann, A. and Kübler, H. and Pfau, T. and Shaffer, J. P., “Microwave electrometry with Rydberg atoms in a vapour cell using bright atomic resonances,” *Nature Physics*, vol. 8, pp. 819–824, 2012.
- [146] Facon, A. and Dietsche, E. K. and Grosso, D. and Haroche, S. and Raimond, J. M. and Brune, M. and Gleyzes, S., “A sensitive electrometer based on a Rydberg atom in a Schrödinger-cat state,” *Nature*, vol. 535, pp. 262–265, 2016.
- [147] Dietsche, E. K. and Larrouy, A. and Haroche, S. and Raimond, J. M. and Brune, M. and Gleyzes, S., “High-sensitivity magnetometry with a single atom in a superposition of two circular Rydberg states,” *Nature Physics*, vol. 15, pp. 326–329, 2019.
- [148] J. W. Hodby, T. E. Jenkins, C. Schwab, H. Tamura, and D. Trivich, “Cyclotron resonance of electrons and of holes in cuprous oxide,  $\text{Cu}_2\text{O}$ ,” *J. Phys. C: Sol. State Phys.*, vol. 9, pp. 1429–1439, apr 1976.
- [149] H.-R. Trebin, H. Z. Cummins, and J. L. Birman, “Excitons in cuprous oxide under uniaxial stress,” *Phys. Rev. B*, vol. 23, no. 2, p. 597, 1981.
- [150] C. Carabatos, A. Diffiné, and M. Sieskind, “Contribution à l’étude des bandes fondamentales de vibration du réseau de la cuprite ( $\text{Cu}_2\text{O}$ ),” *Journal de Physique*, vol. 29, no. 5-6, pp. 529–533, 1968.
- [151] M. O’Keeffe, “Infrared optical properties of cuprous oxide,” *J. Chem. Phys.*, vol. 39, no. 7, pp. 1789–1793, 1963.
- [152] J. Muggli, “Cubic harmonics as linear combinations of spherical harmonics,” *Zeitschrift für angewandte Mathematik und Physik ZAMP*, vol. 23, pp. 311–317, Mar 1972.
- [153] A. R. Edmonds, *Angular Momentum in Quantum Mechanics*. Princeton University Press, 1996.
- [154] E. Noether, “Invariant variation problems,” *Transport Theory and Statistical Physics*, vol. 1, no. 3, pp. 186–207, 1971.





# Acknowledgements

The work presented in this thesis would not have been possible without the support of several persons, whom I want to thank at this point.

First and foremost, I would like to thank Prof. Stefan Scheel for supervising this thesis and giving me the opportunity to work on this exciting, emerging field of physics. I would furthermore like to thank the Deutsche Forschungsgemeinschaft (DFG) for providing the funding under the umbrella of the Schwerpunktprogramm *SPP 1929: Giant Interactions in Rydberg Systems (GiRyd)*.

I am grateful to the supervisors of my master's thesis, Dr. Florian Schöne and Dr. Peter Grünwald, for introducing me to the physics of Rydberg excitons and entertaining my questions during my master's thesis and beyond. Furthermore, I have to thank my colleagues from Rostock Dr. Markus Kurz, Dr. Dirk Semkat, Prof. Heinrich Stolz, Prof. Wolf Dietrich Kraeft, PD Dr. Thomas Bornath and Ma. Sc. Johannes Block for the insightful discussions as well as Dr. Martin French for providing sDFT calculations of the band structure of  $\text{Cu}_2\text{O}$ .

This work would not have come to fruition without the support from our experimental collaborators at the TU Dortmund, specifically Prof. Manfred Bayer, Prof. Marc Aßmann and Dr. Julian Heckötter, as well as our theoretical collaborators from Aarhus (Dr. Valentin Walther and Prof. Thomas Pohl) and Stuttgart (Ma. Sc. Annika Konzelmann and Prof. Harald Giessen). Moreover, I would like to thank Dr. Marina Semina, Prof. Mikhail Glazov and his group as well as Ma. Sc. Patric Rommel, Prof. Jörg Main and his group for the hospitality and the insightful discussions during my respective visits.

Finally, I want to thank my friends and family, first and foremost my parents, for providing distraction when necessary and supporting me during my studies and the writing of this thesis.



## **Selbstständigkeitserklärung**

Ich versichere hiermit, dass ich die vorliegende Arbeit selbstständig verfasst und keine anderen als die angegebenen Quellen und Hilfsmittel benutzt habe. Ich versichere, dass die eingereichte elektronische Fassung mit den gedruckten Exemplaren übereinstimmt.

Sjard Ole Krüger  
Rostock, den 13. November 2020